

Experimental investigation and stochastic simulation of continuous spray agglomeration process in a horizontal fluidized bed

Dissertation

zur Erlangung des akademischen Grades

Doktoringenieur (Dr.-Ing)

von M.Sc. Jiajie Du
geb. am 15.07.1988 in Hebei, China

genehmigt durch die Fakultät für Verfahrens- und Systemtechnik
der Otto-von-Guericke-Universität Magdeburg

Promotionskommission: Prof. Dr. rer. nat. Nora Kulak (Vorsitz)
Prof. Dr.-Ing. habil. Evangelos Tsotsas (Gutachter)
Prof. Dr.-Ing. Andreas Bück (Gutachter)
Prof. Dr.-Ing. Themis Matsoukas (Gutachter)

eingereicht am: 28. September 2022

Promotionskolloquium am: 03. März 2023

Du, Jiajie:

Experimental investigation and stochastic simulation of continuous spray agglomeration process in a horizontal fluidized bed

Otto-von-Guericke University Magdeburg, 2022.

Declaration

I hereby declare that the dissertation with the title:

Experimental investigation and stochastic simulation of continuous spray agglomeration process in a horizontal fluidized bed

is my own work and effort and that it has not been submitted anywhere for any purpose. Where other sources of facts or ideas have been used, either directly or indirectly, they have been clearly stated.

The work has not been submitted in the same or a similar form to any other testing authority and has also not yet been published anywhere.

Magdeburg, 28.09.2022

M.Sc. Jiajie Du

Abstract

Spray fluidized bed agglomeration (SFBA) process is a size enlargement process widely used in the chemical, pharmaceutical and food industry to change the physical properties of powders to meet desired product specifications such as size, shape, flowability, density, solubility and porosity. It is used, for example, in the production of cleaning agents, powders to fill into capsules or compress to form tablets, food powders and detergents. In the SFBA process, fluidized particles are wetted by spraying a liquid; agglomeration occurs when a wet particle collides with another particle forming initially a liquid bridge which then solidifies by drying to form a blueberry-like structure. Due to the nature of fluidized beds, dispersion of binder, forming and drying of liquid bridges take place simultaneously, which results in highly efficient agglomeration.

In the present work, a continuously operated horizontal fluidized bed is employed to perform two series of experiments with glass beads as the primary particles and water-based binder hydroxypropylmethylcellulose (HPMC). The same glass beads are coated with sodium benzoate, and then they are used as tracers in the experiments to characterize the particle residence time distribution. In the first series, the process parameters such as air temperature, binder concentration and spray rate, and particle feed rate are varied to study their influence on the particle growth behavior. The results show that by the decrease in air temperature or particle feed rate and by the increase in binder concentration or spray rate, larger particles can be achieved. Larger particle size also results in higher bed mass and more fluctuations in the process. In the second series, the internal or outlet weir configurations are varied. The separation effect can be decreased, and the particle residence time can be optimized by the installation of internal weirs and lower height of outlet weir. The results show that the jets from the spray nozzles are increasing the motion and mixing of particles significantly.

To simulate the continuous SFBA process, the Monte Carlo method is used, which is a stochastic approach that can model different micro-mechanisms occurring in the process. At first, this method is extended to simulate the continuous SFBA process conducted in a cylindrical fluidized bed with a single process chamber. To simulate the feed of particles and discharge of products, the particle flow event that takes place periodically is added as an extra event. In the particle flow event, new particles are fed, and particles (primary particles or agglomerates) are randomly selected and removed according to the feed rate and the change in bed mass. To validate the model, experimental results achieved in a cylindrical fluidized bed are compared with simulation results. The ex-

perimental results show that the decrease in feed rate or bed mass increases the particle size. In the simulation, the collision frequency prefactor and the breakage probability are obtained by fitting to the reference experiment, and then the fitted values are used in all simulations. The comparison of experimental and simulation results shows that the new continuous Monte Carlo model can predict the evolution of the particle size distribution with collision frequency prefactor 0.05 and breakage probability 0.17 %. The evolution of particle size and particle size distribution (PSD) in simulations agrees well with experimental results. Meanwhile, the development of bed mass in experiments can be well reproduced in the simulations by controlling the number of particles in the simulation box.

Furthermore, the Monte Carlo model is developed to simulate the SFBA process performed in a pilot scale horizontal fluidized bed with multiple process chambers. Depending on the configuration of internal weirs, the Monte Carlo model with two or four simulation boxes is used. Besides the feed of particles and discharge of products, the exchange of particles between different simulation boxes is also included in the particle flow event. When the internal weirs are not installed, the process is simulated by the model with two simulation boxes. In each particle flow event, all the particles in simulation box 2 will reflux to simulation box 1 to simulate the rapid particle exchange rate between different process compartments in real experiments. When the internal weirs are installed, the process is simulated by the model with four simulation boxes. The exchange of particles between different simulation boxes is controlled by backflow cell model according to the particle residence time distribution (RTD) data. Due to the different shapes of the process chamber and different distances from nozzles to the distribution plate, the collision frequency prefactor is fitted to the reference experiment again, and the value 0.03 is used in all simulations. By comparing the simulation results and experimental results, it is shown that the model is able to correctly describe the influence of different process parameters, such as the air temperature, the particle feed rate and the binder spray rate. In all comparisons, the simulation and experimental results show the same trends. Meanwhile, the particle RTD can also be well reproduced in the simulation by controlling the particle exchange behavior.

Kurzzusammenfassung

Die Wirbelschicht-Sprühagglomeration (WSSA) ist ein in der chemischen, pharmazeutischen und Lebensmittelindustrie weit verbreitetes Verfahren zum Größenwachstum, mit dem die physikalischen Eigenschaften von Pulvern so verändert werden, dass sie die gewünschten Produktspezifikationen wie Größe, Form, Fließfähigkeit, Dichte, Löslichkeit und Porosität erfüllen. Es wird beispielsweise bei der Herstellung von Lebensmittelpulvern, Reinigungs- und Waschmitteln, sowie zur Vorbereitung der Verkapselung oder Tablettenpressung. Beim WSSA-Verfahren werden die fluidisierten Teilchen durch Versprühen einer Flüssigkeit benetzt. Die Agglomeration erfolgt, wenn ein benetztes Teilchen mit einem anderen zusammenstößt und zunächst eine Flüssigkeitsbrücke bildet. Durch Trocknung verfestigt sich die Brücke und es entsteht eine heidelbeerartige Struktur. Aufgrund der Beschaffenheit von Wirbelschichten finden die Dispersion des Bindemittels sowie die Bildung und Trocknung der Flüssigkeitsbrücken gleichzeitig statt, was zu einer hocheffizienten Agglomeration führt.

In der vorliegenden Arbeit werden in einer kontinuierlich betriebenen horizontalen Wirbelschicht zwei Versuchsreihen mit Glaskugeln als Primärteilchen und dem wasserbasierten Bindemittel Hydroxypropylmethylcellulose (HPMC) durchgeführt. Ein Teil der Glaskugeln wird mit Natriumbenzoat beschichtet und als Tracer in den Experimenten verwendet, um die Verteilung der Partikelverweilzeit zu charakterisieren. In der ersten Versuchsreihe werden die Prozessparameter wie Lufttemperatur, Bindemittelkonzentration, Sprühdrate und Partikelzufuhr rate variiert, um ihren Einfluss auf das Partikelwachstum zu untersuchen. Die Ergebnisse zeigen, dass durch die Verringerung der Lufttemperatur oder der Partikelzufuhr rate und durch die Erhöhung der Bindemittelkonzentration oder der Sprühdrate größere Partikel erzielt werden können. Größere Partikel führen auch zu einer höheren Bettmasse und mehr Schwankungen im Prozess. In der zweiten Serie werden die Konfigurationen der Innen- oder Auslasswehre variiert. Die Abscheidewirkung kann verringert und die Verweilzeit der Partikel durch den Einbau von Innenwehren und eine geringere Höhe des Auslasswehrs optimiert werden. Die Ergebnisse zeigen, dass die Zerstäubungsluft aus den Sprühdüsen die Bewegung und Vermischung der Partikel deutlich erhöht.

Zur Simulation des kontinuierlichen WSSA-Prozesses wird die Monte-Carlo Methode verwendet, ein stochastischer Ansatz, mit dem verschiedene im Prozess auftretende Mikromechanismen modelliert werden können. Zunächst wird diese Methode erweitert, um den kontinuierlichen WSSA-Prozess in einem zylindrischen Wirbelbett mit einer

einigen Prozesskammer zu simulieren. Um die Zufuhr von Partikeln und den Austrag von Produkten zu modellieren, wird das periodisch stattfindende Partikelflussereignis als zusätzliches Event hinzugefügt. Hier werden neue Partikel zugeführt, und Partikel (Primärpartikel oder Agglomerate) nach dem Zufallsprinzip ausgewählt und entsprechend der Zuführungsrate und der Änderung der Bettmasse entfernt. Zur Validierung des Modells werden experimentelle Ergebnisse aus einem zylindrischen Wirbelbett mit den Simulationsergebnissen verglichen. Die experimentellen Ergebnisse zeigen, dass die Verringerung der Zulaufgeschwindigkeit oder der Bettmasse die Partikelgröße erhöht. In der Simulation werden der Kollisionsfrequenz-Vorfaktor und die Bruchwahrscheinlichkeit durch Anpassung an das Referenzexperiment ermittelt. Die angepassten Werte werden dann in allen Simulationen verwendet. Der Vergleich von experimentellen und Simulationsergebnissen zeigt, dass das neue kontinuierliche Monte-Carlo Modell die Entwicklung der Partikelgrößenverteilung mit einem Kollisionsfrequenz-Vorfaktor von 0,05 und einer Bruchwahrscheinlichkeit von 0,17 % vorhersagen kann. Die Entwicklung der Partikelgröße und der Partikelgrößenverteilung in den Simulationen stimmen gut mit den experimentellen Ergebnissen überein. Die Entwicklung der Bettmasse in den Experimenten kann in den Simulationen gut reproduziert werden, indem die Anzahl der Partikel in der Simulationsbox kontrolliert wird.

Außerdem wurde das Monte-Carlo Modell ausgebaut, um den WSSA-Prozess in einer horizontalen Wirbelschicht im Pilotmaßstab mit mehreren Prozesskammern zu simulieren. Abhängig von der Konfiguration der internen Wehre wird das Monte-Carlo Modell mit zwei oder vier Simulationsboxen verwendet. Neben der Einspeisung von Partikeln und dem Austrag von Produkten wird auch der Austausch von Partikeln zwischen verschiedenen Simulationsboxen in das Partikelflussereignis einbezogen. Wenn keine internen Wehre installiert sind, wird der Prozess durch das Modell mit zwei Simulationsboxen simuliert. Bei jedem Partikelflussereignis fließen alle Partikel aus Simulationsbox 2 in Simulationsbox 1 zurück, um den schnellen Partikelaustausch zwischen verschiedenen Prozesskompartimenten in realen Experimenten zu simulieren. Wenn die internen Wehre installiert sind, wird der Prozess durch das Modell mit vier Simulationsboxen simuliert. Der Austausch von Partikeln zwischen den verschiedenen Simulationsboxen wird durch das Rückflusszellenmodell entsprechend der Partikelverweilzeitverteilung gesteuert. Aufgrund der unterschiedlichen Formen der Prozesskammer und der verschiedenen Abstände zwischen den Düsen und der Verteilerplatte wird der Kollisionsfrequenz-Vorfaktor erneut an das Referenzexperiment angepasst, und der Wert 0,03 wird in allen Simulationen verwendet. Der Vergleich der Simulations- und der Versuchsergebnisse zeigt, dass das Modell in der Lage ist, den Einfluss verschiedener Prozessparameter wie der Lufttemperatur, der Partikelzufuhr und der Bindemittel-Sprührate korrekt zu beschreiben. Bei allen Vergleichen zeigen die Simulations- und die Versuchsergebnisse die gleichen Tendenzen. Auch die Partikelverweilzeitverteilung kann in der Simulation gut wiedergegeben werden, indem das Partikelaustauschverhalten kontrolliert wird.

Contents

List of Figures	xv
List of Tables	xvii
Normenclature	xxiv
1 Introduction	1
1.1 Motivation and objectives	1
1.2 Outline	2
2 Size enlargement processes in fluidized beds	5
2.1 Fluidized bed systems	5
2.2 Size enlargement processes in spray fluidized beds	7
2.3 Spray fluidized bed agglomeration processes	11
2.4 Continuous processes in fluidized beds	14
2.5 Modeling of spray fluidized bed agglomeration processes	19
2.5.1 Population balance equations	19
2.5.2 Monte Carlo method	21
3 Experimental and measurement methods	23
3.1 Materials	23
3.1.1 Solid properties	23
3.1.2 Binder properties	24
3.1.3 Preparation of tracers	24
3.2 Plant description	25
3.3 Measurement methods	27
3.3.1 Particle size distribution	27
3.3.2 Average particle growth rate	29
3.3.3 Separation effect in particle size	30
3.3.4 Determination of steady state	30
3.3.5 Calculation of particle residence time distribution	32
4 Modeling of spray fluidized bed agglomeration process by Monte Carlo method	37
4.1 General algorithm of Monte Carlo method	37
4.1.1 Simulation box and flow chart	37

4.1.2	Scaling and regulation of the system	39
4.1.3	Concept of positions	42
4.1.4	Event frequency and selection	42
4.2	Micro-processes	45
4.2.1	Droplet deposition and drying	45
4.2.2	Particles collisions	48
4.2.3	Breakage	49
4.2.4	Equivalent particle size	51
4.3	Particle flow event in continuous process	53
5	Experimental study of continuous agglomeration process in a horizontal fluidized bed	55
5.1	Experimental plan	55
5.2	Results and discussion	56
5.2.1	Reference experiment	56
5.2.2	Effect of air temperature	61
5.2.3	Effect of particle feed rate	64
5.2.4	Effect of binder concentration	68
5.2.5	Effect of binder spray rate	74
5.2.6	Effect of outlet weir height	75
5.2.7	Effect of internal weirs	78
5.3	Conclusions	87
6	Modeling of continuous spray agglomeration in a cylindrical fluidized bed	89
6.1	Structure of the algorithm	89
6.1.1	Equivalent simulation box	89
6.1.2	Particle flow event	90
6.1.2.1	Discharge of products	92
6.1.2.2	Feed of primary particles	93
6.2	Plant and experimental plan	94
6.3	Simulation results	97
6.3.1	Batch-wise process	97
6.3.2	From batch-wise to continuous process	99
6.3.3	Influence of bed mass development	99
6.3.4	Influence of primary particle feed rate	101
6.4	Conclusions	106
7	Modeling of continuous spray agglomeration in a horizontal fluidized bed	107
7.1	Structure of the algorithm	107
7.1.1	Equivalent simulation box	107
7.1.2	Particle flow event	108
7.1.2.1	Discharge of products	108
7.1.2.2	Particle exchange without internal weirs	111
7.1.2.3	Particle exchange with internal weirs	111

7.1.2.4	Feed of primary particles	112
7.1.3	Particle residence time distribution	112
7.2	Simulation plan	113
7.3	Simulation results	115
7.3.1	Simulation of the reference experiment	115
7.3.2	Effect of air temperature	119
7.3.3	Effect of particle feed rate	121
7.3.4	Effect of binder spray rate	121
7.3.5	Effect of binder concentration	123
7.3.6	Effect of outlet weir height	125
7.3.7	Effect of internal weirs	125
7.3.8	Conclusions	130
8	Summary and outlook	131
8.1	Summary	131
8.2	Outlook	132
	References	135
	Appendices	147
A	Material properties	149
A.1	Properties of dry air	149
A.2	Properties of water	150
B	Additional experimental results	153
B.1	Measured and calculated RTD	153
B.2	Results of experiment with air temperature at 60 °C	154
B.3	Results of experiment with binder mass fraction at 6%	155
C	Additional simulation results	157
C.1	Comparison of the development of bed mass in simulation and experiment	157

List of Figures

2.1	The principal flow regimes of fluidization with increasing gas velocity [13].	6
2.2	The Geldart classification of particles for air at ambient conditions [14].	6
2.3	Illustration of different spray systems: a. top spray, b. bottom spray c. side spray.	9
2.4	Schematic representation of spray fluidized bed processes: a. agglomeration, b. granulation, c. coating.	10
3.1	SEM image of primary particles.	23
3.2	Primary particle size distribution.	24
3.3	Scheme of cylindrical fluidized bed with side spray.	25
3.4	Particle size distribution of tracers.	26
3.5	Scheme of horizontal fluidized bed plant.	28
3.6	Process chamber of horizontal fluidized bed a. without internal weir, b. with internal weirs.	28
3.7	Conductivity measurement of tracers.	34
3.8	Conductivity measurement of uncoated particles.	35
4.1	Scheme of simulation box in Monte Carlo model: a. simulation box with spray; b. simulation box without spray.	38
4.2	Flow chart of Monte Carlo simulation.	40
4.3	Influence of initial primary particle number on the relative computation time [86].	41
4.4	Division of particle surface into sections and positions (24 positions).	43
4.5	Deposition of droplet on the particle surface.	47
4.6	Breakage of an agglomerate with three primary particles.	52

4.7	Relation of particle size and primary particle number for Exp. Ref. . . .	53
5.1	Evolution of particle size.	58
5.2	Development of bed and product mass.	59
5.3	PSDs of selected samples.	60
5.4	Steady state determination from the evolution of particle size: Samples from bed (top), samples from products (bottom).	62
5.5	Steady state determination from the development of bed mass.	63
5.6	Measured and calculated RTD	63
5.7	Results of Exp. T1: a. evolution of particle size; b. development of bed and product mass; c. PSDs of selected samples.	65
5.8	Results of Exp. T2: a. evolution of particle size; b. development of bed and product mass; c. PSDs of selected samples.	66
5.9	Comparison of particle Sauter mean diameter and standard deviation for Exp. Ref, T1 and T2.	67
5.10	Results of Exp. F1: a. evolution of particle size; b. development of bed and product mass; c. PSDs of selected samples.	69
5.11	Results of Exp. F2: a. evolution of particle size; b. development of bed and product mass; c. PSDs of selected samples.	70
5.12	Comparison of particle Sauter mean diameter and standard deviation for Exp. Ref, F1 and F2.	71
5.13	Results of Exp. B1: a. evolution of particle size; b. development of bed and product mass; c. PSDs of selected samples.	72
5.14	Results of Exp. B2: a. evolution of particle size; b. development of bed and product mass; c. PSDs of selected samples.	73
5.15	Comparison of particle Sauter mean diameter and standard deviation for Exp. Ref, B1 and B2.	74
5.16	Results of Exp. S1: a. evolution of particle size; b. development of bed and product mass; c. PSDs of selected samples.	76
5.17	Results of Exp. S2: a. evolution of particle size; b. development of bed and product mass; c. PSDs of selected samples.	77
5.18	Comparison of particle Sauter mean diameter and standard deviation for Exp. Ref, S1 and S2.	78
5.19	Results of Exp. Ref-L: a. evolution of particle size; b. development of bed and product mass; c. PSDs of selected samples.	79

5.20	Comparison of particle Sauter mean diameter and standard deviation for Exp. Ref and Ref-L.	80
5.21	Results of Exp. W1: a. evolution of particle size; b. development of bed and product mass; c. PSDs of selected samples; d. measured and calculated RTDs.	82
5.22	Results of Exp. W2: a. evolution of particle size; b. development of bed and product mass; c. PSDs of selected samples; d. measured and calculated RTDs.	83
5.23	Results of Exp. W1-L: a. evolution of particle size; b. development of bed and product mass; c. PSDs of selected samples; d. measured and calculated RTDs.	84
5.24	Comparison of particle Sauter mean diameter and standard deviation for Exp. Ref, W1 and W2.	85
6.1	Modeling of SFBA process in different plants: a. batch-wise cylindrical fluidized bed, b. continuous cylindrical fluidized bed.	90
6.2	Flow chart of particle flow event for continuous cylindrical fluidized bed.	91
6.3	Scheme of the pilot-scale cylindrical fluidized bed with internal classifier.	96
6.4	Comparison of Exp. C-Ref-Batch and Sim. C-Ref-Batch: a. evolution of particle size with different breakage rates, b. evolution of particle size with different collision prefactors, c. PSDs of selected samples.	98
6.5	Comparison of Exp. C-Ref-BMC and Sim. C-Ref-BMC: a. evolution of particle size, b. development of bed mass, c. PSDs of selected samples.	100
6.6	Comparison of Exp. C-Ref and Sim. C-Ref: a. evolution of particle size, b. development of bed mass, c. PSDs of selected samples.	102
6.7	Comparison of Exp. C-F1 and Sim. C-F1: a. evolution of particle size, b. development of bed mass, c. PSDs of selected samples.	104
6.8	Comparison of Exp. C-F2 and Sim. C-F2: a. evolution of particle size, b. development of bed mass, c. PSDs of selected samples.	105
7.1	Modeling of continuous process in different plants: a. continuous horizontal fluidized bed without internal weirs; b. continuous horizontal fluidized bed with internal weirs.	109
7.2	Flow chart of particle flow event for continuous horizontal fluidized bed.	110
7.3	Evolution of particle size with different collision frequency prefactor: a. $F_{coll} = 0.025$, b. $F_{coll} = 0.030$, c. $F_{coll} = 0.035$	116
7.4	PSDs of bed samples from experiment and simulation.	117

7.5	Development of bed mass in experiment and simulation.	118
7.6	RTD results from experiment, dispersion model and simulation.	119
7.7	Comparison of Exp. T1 and Sim. T1: a. evolution of particle size, b. PSDs of selected samples.	120
7.8	Comparison of Exp. T2 and Sim. T2: a. evolution of particle size, b. PSDs of selected samples.	120
7.9	Comparison of Exp. F1 and Sim. F1: a. evolution of particle size, b. PSDs of selected samples.	121
7.10	Comparison of Exp. F2 and Sim. F2: a. evolution of particle size, b. PSDs of selected samples.	122
7.11	Comparison of Exp. S1 and Sim. S1: a. evolution of particle size, b. PSDs of selected samples.	122
7.12	Comparison of Exp. S2 and Sim. S2: a. evolution of particle size, b. PSDs of selected samples.	123
7.13	Comparison of Exp. B1 and Sim. B1: a. evolution of particle size, b. PSDs of selected samples.	124
7.14	Comparison of Exp. B2 and Sim. B2: a. evolution of particle size, b. PSDs of selected samples.	124
7.15	Comparison of Exp. Ref-L and Sim. Ref-L: a. evolution of particle size, b. PSDs of selected samples.	125
7.16	Comparison of Exp. W1 and Sim. W1: a. evolution of particle size, b. PSDs of selected samples, c. simulated RTD.	127
7.17	Comparison of Exp. W2 and Sim. W2: a. evolution of particle size, b. PSDs of selected samples, c. simulated RTD.	128
7.18	Comparison of Exp. W1-L and Sim. W1-L: a. evolution of particle size, b. PSDs of selected samples, c. simulated RTD.	129
B.1	Measured and calculated RTD.	153
B.2	Results of experiment with air temperature at 60 °C: a. evolution of particle size; b. development of bed and product mass; c. PSDs of selected samples.	154
B.3	Results of experiment with binder mass fraction at 6%: a. evolution of particle size; b. development of bed and product mass; c. PSDs of selected samples.	155
C.1	Development of bed mass with varied air temperature.	157

C.2	Development of bed mass with varied particle feed rate.	158
C.3	Development of bed mass with varied binder spray rate.	158
C.4	Development of bed mass with varied binder concentration.	159
C.5	Development of bed mass with lower outlet weir.	159
C.6	Development of bed mass with varied internal weirs.	160

List of Tables

2.1	Selected publications focusing on spray fluidized bed agglomeration process.	13
2.2	Selected publications focusing on continuous processes in fluidized bed.	16
3.1	Parameters used in the preparation of tracers.	26
5.1	Experimental plan.	57
5.2	Overview of bed mass and Bo number.	85
5.3	Overview of calculated values and process dynamics.	86
6.1	Experimental parameters.	95
6.2	Varied experimental parameters.	96
6.3	Additional simulation parameters.	97
7.1	Varied simulation parameters.	114
7.2	Additional simulation parameters.	115

Nomenclature

Symbols

a	coefficient	-
A	area	m^2
B_p	particle birth rate	$\text{m}^{-3}\text{s}^{-1}$
Bo	Bodenstein number	-
c	molar concentration	molm^{-3}
C	concentration	kgm^{-3}
COR	coefficient of restitution	-
CoV	coefficient of variation	-
CoV_{back}	coefficient of variation (backwards)	-
d	diameter	m
Dou	number of doubling	-
D	dispersion coefficient	m^2s^{-1}
D_f	fractal dimension	-
D_p	particle death rate	$\text{m}^{-3}\text{s}^{-1}$
d_{32}	Sauter mean diameter	m
d_o	diameter of discharge orifice in nozzle	m
E	normalized mass fraction of tracer	s^{-1}
E_{break}	kinetic energy of collision	J
f	frequency	s^{-1}
F_{coll}	collision frequency prefactor	-
G	particle size growth rate	ms^{-1}
GR	bed mass growth rate	kgs^{-1}
h	height	m
h_a	height of asperities	m
i	control variable	-
j	control variable	-

k	control variable	-
K	fractal prefactor	-
$K(v)$	separation function	-
l	control variable	-
L	length	m
m	weight	kg
\dot{m}	mass flow rate	kg s^{-1}
\tilde{M}	molar mass	kg kmol^{-1}
MCN	mean coordination number	-
\dot{n}_{in}	volumetric number flux of newly fed particles	$\text{m}^{-3}\text{s}^{-1}$
\dot{n}_{out}	volumetric number flux of removed fed particles	$\text{m}^{-3}\text{s}^{-1}$
n	number of particles per unit volume	m^{-3}
N	number	-
\dot{N}	particle or droplet number flow rate	s^{-1}
N_{geo}	geometric number of tanks in geometry	-
N_{pos}	number of positions in each section	-
N_{tank}	number of tanks	-
\tilde{N}_{pp}	number of primary particles in the simulation box	-
P	pressure	Pa
Pe	Péclet number	-
Pr	Prandtl number	-
P_v^*	saturation vapor pressure	Pa
q_r	normalized particle size distribution density regarding quantity	-
Q_r	normalized particle size sum distribution regarding quantity r	-
r	type of quantity (0: number, 1: length, 2: area, 3: volume)	-
r_{cap}	radius of spherical cap	m
r_n	normally distributed random number	-
R	reflux factor	-
\tilde{R}	specific gas constant	$\text{J kmol}^{-1}\text{K}^{-1}$
R_1, R_2	random number in the open interval (0,1)	-

R^2	coefficient of determination	-
Re	Reynolds number	-
s	specific heat capacity	$\text{Jkg}^{-1}\text{K}^{-1}$
S	scaling factor	-
SE	separation effect	-
St	Stokes number	-
St^*	critical Stokes number	-
St_{def}	Stokes deformation number	-
St_{def}^*	critical Stokes deformation number	-
t	time	s
T	temperature	$^{\circ}\text{C}$
u	velocity	ms^{-1}
u_r	air to liquid relative velocity	ms^{-1}
v, v'	particle volume	m^3
V	volume	m^3
\dot{V}	volume flow rate	m^3s^{-1}
w	control variable	-
W_{bridge}	adhesive energy of bridge	J
We	Weber number	-
X	mass fraction	kgkg^{-1}
\tilde{y}^*	molar fraction at saturation condition	-
\tilde{y}	molar fraction	-
\tilde{y}_p	dynamic plastic yield stress	Pa
z	spatial coordinate (longitudinal direction)	m

Greek symbols

β'	agglomeration efficiency	depending on $\beta'(v, v')$
$\beta'(t, v, v')$	agglomeration kernel	s^{-1}
$\beta'(v, v')$	volume-dependent agglomeration kernel	various
ε	agglomerate porosity, voidage	-
θ	contact angle	$^{\circ}$
κ	conductivity	Sm^{-1}
Λ	molar conductivity	$\text{Sm}^2\text{mol}^{-1}$
μ	dynamic viscosity	Pa s

ν	kinematic viscosity	m^2s^{-1}
τ	mean residence time	s
ρ	density	kgm^{-3}
σ	standard deviation	various
σ^2	variance of particle residence time distribution	s^2
σ_s	strength	Pa
σ_{ten}	surface tension	Nm^{-1}
σ_{ts}	tensile strength	Pa

Subscripts

0	initial value
a	air
acc	accumulated
agg	agglomerate
b	binder
ca	classifier air
coll	collision
d	droplet
dis	discharge
g	gas
int	interval
MC	Monte Carlo model
ori	discharge orifice
p	particle
pd	product
pos	position
pp	primary particle
r	relative
res	residence time
s	sample
sat	saturated
sb	simulation box
t	tracer
tot	total
u	velocity

v	vapor
w	water

Abbreviations

3D	three-dimensional
CFD	computational fluid dynamics
CNMC	constant-number Monte Carlo model
CSTR	continuous stirred tank reactor
CVMC	constant-volume Monte Carlo model
DCS	distributed control system
DEM	discrete element method
HPMC	hydroxy-propyl-methyl-cellulose
PBE	population balance equation
PSD	particle size distribution
PTV	particle tracking velocimetry
RTD	residence time distribution
SEM	scanning electron microscopy
SFBA	spray fluidized bed agglomeration
SFBC	spray fluidized bed coating
SFBG	spray fluidized bed granulation
TIS	tank-in-series

Chapter 1

Introduction

1.1 Motivation and objectives

Particulate products are widely used almost everywhere in the industry because they have a number of advantages, such as low transport and handling costs, high physical and chemical stability and good product performance [1]. Since the 1980s, industrialists, equipment suppliers and scientists have become increasingly aware of a global engineering approach to the production and the use of particulate products for different applications [2]. In the chemical industry alone, it has been estimated that 60 % of products are manufactured as particulates and a further 20 % use powders as ingredients. Besides the chemical industry, particles are also widely used in agriculture, pharmaceutical and food industries; for example, fertilizers, pills and tablets containing an active pharmaceutical ingredient, beverage powders and milk powders.

After years of development, plenty of processes are available for handling particulate materials according to the properties of raw materials and the production purposes. They can be sorted into size enlargement processes, such as crystallization, granulation and agglomeration, and size reduction processes, such as milling, comminution and emulsification. Among them, size enlargement processes are used to enhance the flowability, compressibility, stability and solubility of powders. To achieve the size enlargement, especially for the production of free-flowing, low-dust and low-attrition particles, spray fluidized beds are widely used [3]. Spray fluidized beds can be either employed to produce particulate products from suspensions or from dry powders by spray drying, granulation, coating or agglomeration. In the spray drying process, a liquid is atomized into droplets; then the water is vaporized by hot air to get solid particles. The granulation and coating process share a similar size enlargement mechanism called layering. In layering, particles grow by applying a layer of the sprayed solid material around the initial particles. If the material of the new layer is identical to the core material, it is called granulation. If the material of the new layer and the core material are different, it is called coating. In the agglomeration process, a liquid is atomized into droplets; then particles are wetted by the droplets; agglomeration occurs

when a wet particle collides with another particle forming initially a liquid bridge which is then solidified by drying into a solid bridge.

Fluidized beds can be either operated batch-wise or continuously. Compared to continuous processes, batch processes have the advantages of easier control, predefined process time, better traceability and lower equipment cost. However, if large quantities of products are needed, the continuous mode becomes a better option. Continuous processes can increase the output, decrease labor and reduce the processing and holding time. The difficulty lies in the dynamic of the continuous process, for example, the operation strategy, the stability of the process and the uniformity of products. Among these two operational modes, the continuous processes in fluidized beds have not been investigated as widely as the batch ones. In literature, some investigations focusing on continuously operated processes in fluidized bed can be found, for example, drying [4], coating [5] and granulation [6, 7]. Regarding continuous agglomeration, the first patent was registered by Uhlemann et al. [8] in 1996. However, it was rarely studied or reported in the last two decades. In the last years, however, there has been a resurgent interest in this process. Schmidt et al. [9] and Strenzke et al. [10] studied the continuous agglomeration process performed in a cylindrical fluidized bed. Regarding the continuous agglomeration process performed in the horizontal fluidized bed, there is still no work available.

The goal of the present work is to investigate the continuously operated SFBA process performed in a horizontal fluidized bed with varied process parameters such as air temperature, particle feed rate and binder spray rate, as well as for different plant configurations with, for example, different heights of outlet weir. Variations shall be analyzed in terms of evolution of particle size, particle size distribution (PSD), development of bed mass, particle residence time distribution (RTD) and process stability. Meanwhile, two stochastic models based on the Monte Carlo method are developed to simulate the continuous SFBA process in a cylindrical fluidized bed and in a horizontal fluidized bed. By adding the particle flow event that takes place periodically to the model, feed of new particles, flow of particles between different simulation boxes and discharge of products are simulated. Finally, the simulation results are compared to corresponding experimental data with different process parameters to validate the model.

1.2 Outline

This thesis contains six main chapters, which cover a detailed literature survey on fluidized beds and particle formation processes in fluidized beds, the materials and measurement methods used in experiments, microscopic modeling by using the Monte Carlo method, experimental results regarding continuous spray agglomeration process in a horizontal fluidized bed, and presentation of the simulation results for spray agglomeration conducted in a cylindrical and a horizontal fluidized bed.

Chapter 2 gives an overview of theoretical knowledge of spray fluidized bed processes for a better understanding of this work. At first, the definition and fundamentals of

fluidized bed systems are introduced briefly. Then, the mechanisms and applications of particle formation processes in a fluidized bed, as well as the types of spray systems, are described. Afterward, the continuous processes conducted in a fluidized bed from previous work are presented. Finally, the modeling methods available in the literature are introduced.

In Chapter 3, the materials, plants and measurement methods used in experiments are introduced in detail. At first, the solid materials, binder solution and the preparation of tracer particles are explained. Then, the horizontal fluidized bed used in the experiments is described. In the last section, the measurement method employed is introduced, which includes the calculation of particle size, the definition of average particle growth rate, the separation effect and the determination of steady state.

Chapter 4 describes the Monte Carlo model used for the continuous spray fluidized bed agglomeration process. At first, the general algorithm of the Monte Carlo method is introduced, which includes the flow chart, the definition of the simulation box, the scaling and regulation procedure, the concept of positions and the event selection and time step calculation. Then, the micro-processes and events such as the deposition and drying of droplets, the particle collisions and the estimation of particle size are shown.

Chapter 5 shows the experimental results regarding the continuous spray fluidized bed agglomeration conducted in a horizontal fluidized bed with varied parameters and weir configurations. At first, the experimental plan and procedures are described in detail. Then, the evolution of particle size, the change in bed mass and the PSDs of selected samples are used to characterize the process behavior. For better comparison, some quantitative indicators such as the growth rate and separation effect are calculated and summarized. Additionally, the particle RTD is measured in some experiments and explained.

Chapter 6 presents the Monte Carlo model for the continuous spray agglomeration process conducted in a cylindrical fluidized bed. Meanwhile, experimental results and simulation results are compared to validate the model. Firstly, the algorithm for equivalent simulation box and particle flow event is described in detail. Then, the experimental plan and procedures of the process conducted in the cylindrical fluidized bed are introduced briefly. In the last section, the simulation and experimental results regarding the evolution of particle size, the change in bed mass and the PSDs of selected samples are compared.

Chapter 7 focuses on the Monte Carlo model used to simulate the continuous spray agglomeration process conducted in a horizontal fluidized bed. At first, the algorithm for equivalent simulation box and particle flow event (includes the feed of primary particles, discharge of products, and flow and reflux of particles between different simulation boxes) is detailed and described. Then, the simulation results are compared with the experimental results presented in Chapter 5. In addition, the simulated particle RTDs are also compared with experimental results.

Chapter 8 summarizes the conclusions achieved from experiments and simulations and gives outlooks for future work.

Chapter 2

Size enlargement processes in fluidized beds

This chapter gives an overview of the size enlargement processes in spray fluidized beds through a detailed literature review. At first, the principles of the fluidization phenomenon and the applications of fluidized beds are briefly explained. Afterward, the mechanisms of spray fluidized agglomeration are briefly described followed by a comparison of different size enlargement processes in fluidized beds, i.e., coating, granulation, and spray drying. The applications of continuous processes that have been conducted in fluidized beds are introduced. Then, the modeling methods including population balance equations (PBE) from the macroscopic and Monte Carlo method from the microscopic point of view are introduced.

2.1 Fluidized bed systems

Fluidization refers to the contact of a bed of solids and flowing fluid (gas or liquid). When the fluid reaches a certain velocity (minimum fluidization velocity) and passes through the solid particles via a distributor plate, the solid particles are transformed into a fluid-like state that is named fluidization. Since the first fluidized bed gas generator was developed in Germany by Fritz Winkler in the 1920s, the use of fluidized beds has been one of the most important technologies for gas-solid heterogeneous operations in both chemical and physical processes [11]. For example, for chemical processes like catalytic cracking, gasification, combustion, absorption, and for physical processes like particle drying, particle mixing, filtering of particles and size enlargement [12]. In some of the chemical processes, the flowing fluid can either be liquid or gas. The size enlargement process is investigated in this work, which uses gas as the fluidization medium. Thus, the focus lies on the gas-solid fluidized beds.

A common gas-solid fluidized bed consists of a process chamber where the interactions occur, a distributor plate to distribute the gas evenly, a relaxation zone to reduce the entrainment and some other accessories such as ventilators and heaters to achieve the required process parameters. The fluidization behavior is directly dependent on the gas velocity when the gas enters the bed through the distributor plate. As shown in

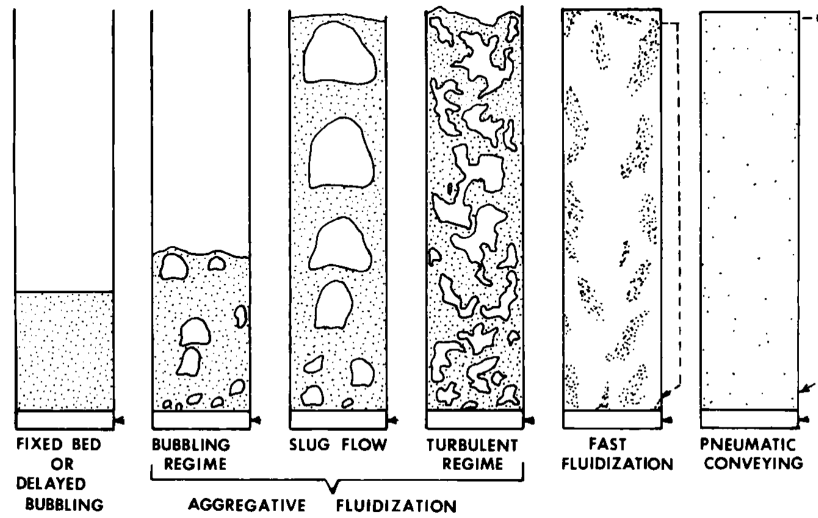


Figure 2.1: The principal flow regimes of fluidization with increasing gas velocity [13].

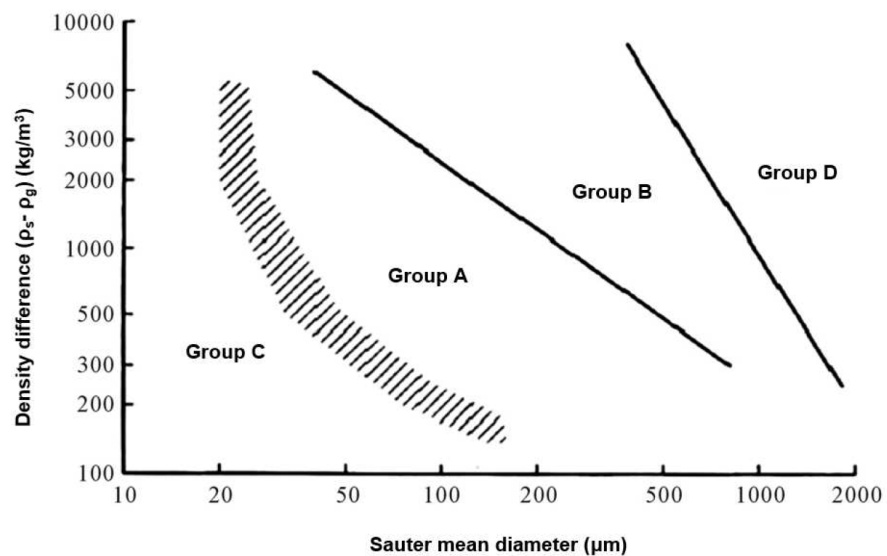


Figure 2.2: The Geldart classification of particles for air at ambient conditions [14].

Figure 2.1, with increasing gas velocity, the bed develops from a fixed bed to aggregative fluidization, finally to pneumatic transport [13].

Meanwhile, the fluidization behavior of gas-solids systems depends very much on the types of particles employed. The types of particles can be classified regarding their properties and their functionalities. By carefully observing the fluidization of all sorts and sizes of solid particles, the particles were classified by Geldart [14] into four groups characterized by the density difference and the mean particle size, which is shown in Figure 2.2. They are categorized as follows:

- Group A is called “aeratable” particles. The particles have a small mean diameter (typically between 50 and 200 μm [15]) and/or a low particle density (less than 1400 kg/m^3). They can be fluidized easily, in smooth way at low gas velocity without the formation of bubbles.
- Group B is called “sandlike” particles. Those particles have a mean diameter roughly between 40 μm and 500 μm and densities between 1400 kg/m^3 and 4000 kg/m^3 . These solids start bubbling at minimum fluidization velocity and behave similarly at higher velocities, whereas the bed expansion is rather small. Glass beads and coarse sand are examples of this group.
- Group C is called “cohesive” particles. Particles in this group are very fine (typically less than 50 μm [15]), and often very difficult to fluidize. Starch and flour are examples of this group.
- Group D is called “spoutable” particles. Particles in this group are rather large and / or dense particles, and are often difficult to fluidize in deep beds. Grains and coffee beans are examples of this group.

2.2 Size enlargement processes in spray fluidized beds

Size enlargement processes in spray fluidized beds are widely used in various industries such as pharmaceuticals, fertilizers and foods. These processes have the purpose of changing the physical properties of particles to meet desired product specifications such as size, shape, flowability, density, solubility or porosity [16]. For different applications and based on different mechanisms, the three main processes are granulation, coating and agglomeration. During the size enlargement processes in spray fluidized beds, liquid or suspension is usually sprayed on fluidized particles by a nozzle. Schematic spray fluidized beds with nozzle installed at different positions are shown in Figure 2.3. According to the position of the nozzle, the types of spray system can be divided as: top spray, bottom spray and side spray. The applications and differences of the spray systems are briefly introduced below:

- Top spray: In this configuration, the nozzle is installed at the top or in the upper part of the process chamber. The spray liquid is sprayed from above onto

the fluidized particles. Top spray is widely used for coating, granulation and agglomeration (for example, see Saleh et al. [17], Schmidt et al. [18] and Tan et al. [19]). It has the advantages of easy nozzle access, good mixing and high throughput. Limitations are higher overspray and that the solid-liquid contact area is not well defined. In coating and granulation processes, the top spray promotes the formation of large agglomerates, which is normally undesired in such processes [20].

- **Bottom spray:** In this configuration, the nozzle is installed at the bottom or in the lower part of the process chamber. The liquid is sprayed from below upwards. It is commonly used in the coating and granulation process (for example, see Bachmann et al. [5] and Er et al. [21]). Bottom spray has the advantages of a well-defined contact area of solid and liquid, low overspray and less formation of agglomerates. Whereas the bottom spray makes the nozzle access tedious, decreases the particle growth rate in granulation, and increases the risk of over-wetting [20, 22]. Based on bottom spray, a new air-suspension technique named Wurster process was developed, which divides the process chamber into two sections by a partition tube and a segmented distributor [23]. The particles are moved with the fluidizing air and the atomizing air through the spray zone, which induces a cyclic upward flow of the particles. Then, the particles circulate back to the bed when their velocity is reduced. The Wurster process has been used commercially for coating and granulation for years [24].
- **Side spray:** In this configuration, the nozzle is installed at the side wall of the process chamber. The liquid is usually sprayed from the side tangentially near the bottom of the process chamber, so the side spray is also named tangential spray. It is commonly used in agglomeration and coating process (for example, see Wong et al. [20], Xu et al. [25] and Elsergany et al. [26]). This type of fluidized bed can also be combined with a rotatory distributor plate for coating and agglomeration processes [27, 28]. The side spray fluidized bed has the advantage of a higher spray rate and can produce even coating layers of high quality. However, the disadvantages are higher over-wetting risk and difficulty of scale-up.

Size enlargement processes in spray fluidized beds are complex due to the integration of various sub-processes such as spraying, particle wetting, drying and solidifying. In the literature, different names and definitions have been used to define and describe the spray fluidized bed processes. Here, these processes are distinguished to spray fluidized bed granulation (SFBG), spray fluidized bed coating (SFBC) and spray fluidized bed agglomeration (SFBA) according to Peglow et al. [29]. The basic principles of these processes are schematically shown in Figure 2.4. Principles and applications of different processes are as follows:

- (a) The SFBG process can also be described as a particle layering process. The liquid that consists of the same material as the core particles is atomized and sprayed. If

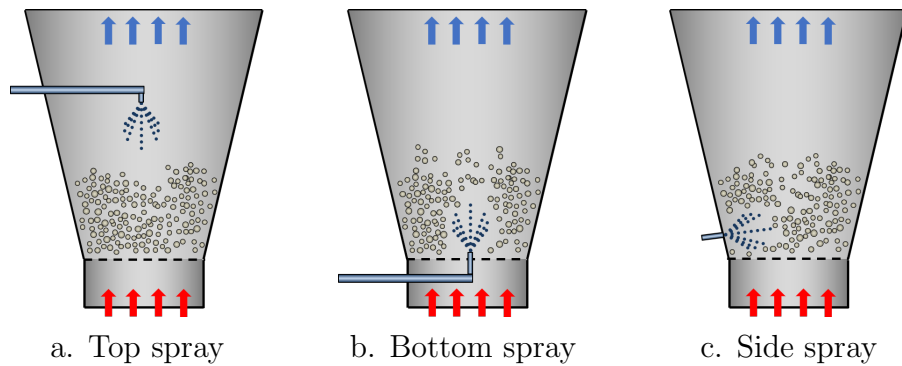


Figure 2.3: Illustration of different spray systems: a. top spray, b. bottom spray c. side spray.

the sprayed droplets hit the core particles in the bed and don't rebound, they will partially cover the surface of the particles and get dried. With the accumulation of these droplets, a closed layer is formed on the surface of core particles (see Figure 2.4a). Thus, layer-wise growth of the particles can be achieved. The main goal of this process is to change the particle size distribution (PSD). The main application of the SFBG process is to transform a solid-containing liquid to the solid state, such as in the production of fertilizers from an aqueous solution of ammonium sulfate [30] and urea [31].

- (b) The SFBC process has similar principles to the SFBG process (see Figure 2.4b). However, the material of the core particle is different from the solids in the sprayed liquid. Compared to the SFBG process, the thickness of the layer is normally small. The main goal of this process is to protect the core particle, enhance its functionality, or create a new functionality by means of the coating. It is widely used in the chemical, pharmaceutical and food industries. For example, to coat membranes onto catalytic particles to increase reaction yield and selectivity [32], to protect the active ingredients from oxidation and thermal degradation [33], to control the release of active ingredients [34] and to achieve superior aesthetic quality (e.g., color, texture, mouth feel, and taste masking) of drugs [35], to retain aroma during storage and increase flavors shelf-life of foods [36].
- (c) In the SFBA process, liquid binder (for non-amorphous materials) or pure water (for amorphous materials) is usually dispersed on the surface of particles by an atomizer. The agglomeration occurs when a wet particle collides with another particle forming initially a liquid bridge that is viscous enough to dissipate the collision energy. The liquid bridge is then solidified by the hot air and forms the agglomerate. The mechanism is briefly shown in Figure 2.4c. The main goal of this process is to enhance the properties of particles by increasing particle size. SFBA process is also widely used in various industries. In the pharmaceutical industry, this process is used to produce solid dosage forms directly or for the preparation of tableting and encapsulating [37, 38]. In the food industry, it is

used to produce various instant products such as coffee, milk, soymilk and cocoa, as well as dehydrated convenience products such as instant soups and sauces of enhanced wettability, sinkability, dispersibility and solubility [38, 39]. This process is also used to produce laundry powders and some fine chemicals such as vitamin mixtures [38, 40].

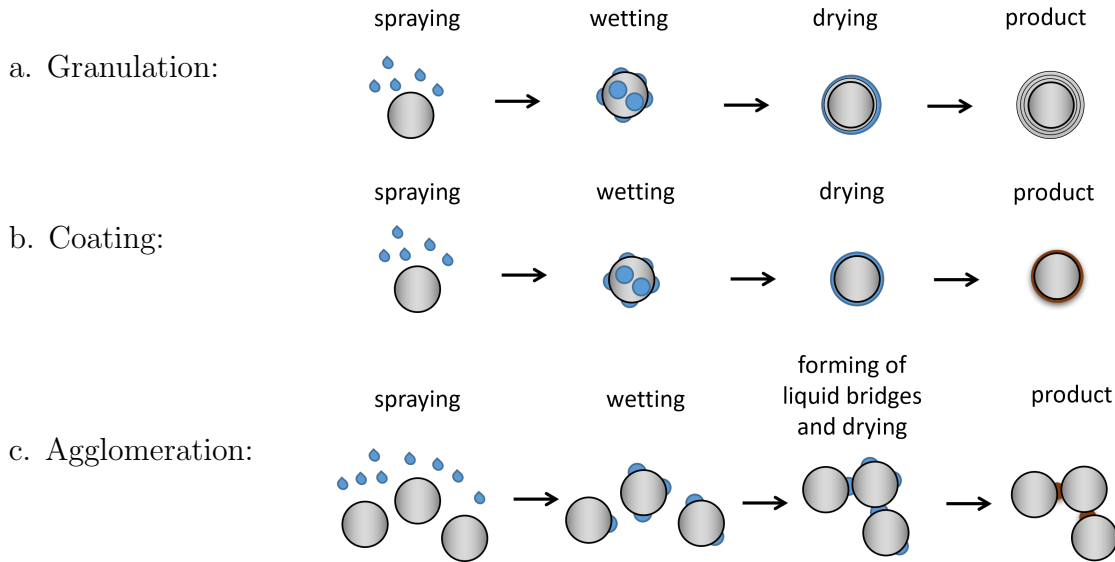


Figure 2.4: Schematic representation of spray fluidized bed processes: a. agglomeration, b. granulation, c. coating.

In spray fluidized bed size enlargement processes, layering (granulation or coating) and agglomeration may occur simultaneously due to the similarities of operation conditions in these processes. However, the quality of products can be significantly affected by the undesired process. Depending on the applications, only one main process is normally desired in practice. For example, some agglomeration tendency is frequently seen in the layering process, especially for small particles. It leads to non-well-defined product qualities and mechanical resistance or even bed collapses in producing process [41]. In contrast, layering tendency may be seen in the agglomeration process. It leads to a decrease in the efficiency of sprayed binder and the change of particle surface properties [42]. To investigate the boundary between layering and agglomeration process, some studies have been conducted in previous work. Different process parameters such as the particle size, gas velocity, gas temperature, droplet size and porosity of particles have been studied in layering experiments [17, 41, 43]. Their results show that smaller particle size, lower gas temperature, larger droplet size and smaller porosity of particles promote the agglomeration tendency in the layering process. Meanwhile, theoretical studies on the boundary between layering and agglomeration are also available in the literature. Based on the work of Barnocky and Davis [44], Ennis et al. classified the results (rebound or agglomeration) of particle binary collisions at the micro-level by using the viscous Stokes number. The Stokes number is a dimensionless number that

is determined by parameters such as the liquid film height, binder viscosity, collision velocity and weight of particles [45]. In their approach, the colliding particles coalesce only when the viscous Stokes number is lower than a critical Stokes number. By calculating the Stokes number and comparing it with the critical Stokes number, the result of each collision is determined. Thus, the behavior of the process is determined. Another dimensionless number called Akkermans or flux number appears in a patent by Akkermans et al. [46]. The flux number depends on the particle density, the excess gas velocity and the binder mass flow rate. Under this concept, Boerefijn and Hounslow [40] studied the melt agglomeration process in a top spray fluidized with different process parameters. They suggested that when the flux number is below 3.5, agglomeration is the dominant size enlargement process. This concept was used in the scale-up of a coating process by Hede et al. [47]. They found that when the flux number was below 4.5, the bed collapsed during processing, which means that the agglomeration process became dominant. Additionally, a simulation model based on population balances was proposed by Rieck et al. [48], who suggested that exceeding a probability of successful collisions of 0.001 is sufficient for agglomeration to become dominant.

2.3 Spray fluidized bed agglomeration processes

Compared to the other particle size enlargement processes, the agglomeration process is a unit operation in which several small, individual particles are combined to form larger porous structures in a way that the original particles can still be distinguished [2]. The inter-particle bonding mechanisms were firstly described by Rumpf [49] in 1958. Particles can be bound together by material bridges or without material bridges. The material bridges can be further divided into liquid bridges and solid bridges. With liquid bridges, particles stick together due to the cohesive force (viscous binder) and the capillary force. Solid bridges can be formed due to sintering, chemical reactions, and drying of viscous liquid bridges. Without material bridges, the particles can stick together by van der Waals forces, electrostatic forces or interlocking, when fibrous [50, 51]. The size of primary particles varies in typical applications from a few nanometers to several millimeters; the size of the formed agglomerates ranges typically from several micrometers to several centimeters [52]. Depending on the desired agglomerate structure of final products, different processes can be applied for the manufacturing of the agglomerates: agitation agglomeration, pressure agglomeration and sintering/heat agglomeration, which are described briefly as follows [53]:

- **Agitation agglomeration:** Agitation agglomeration is also named tumble or growth agglomeration. In this process, small particles collide during their irregular motions in a particle bed and coalesce to form a new entity that is held together by binding forces. A liquid binder (water) is usually used in this process. The particles are temporarily bonded by the effects of surface tension and capillary forces of the liquid binder. To a smaller degree, other binding mechanisms, such as van der Waals force, may also participate [54]. Agitation equipment can be operated

batch-wise or continuously, distinguishing mainly three types of equipment: disc and drum agglomerators, mixer agglomerators and fluidized bed agglomerators.

- Pressure agglomeration: In pressure agglomeration, new enlarged entities are formed by applying external forces to particulate solids using, e.g., punch-and-die presses, roller presses and extrusion machines. The principal binding force is the van der Waals force. Compared to agitation agglomeration, pressure agglomeration is usually binderless and mainly used to achieve products with high density, high strength, low porosity and specific shape.
- Sintering/heat agglomeration: In the sintering/heat agglomeration, the atoms and molecules move at elevated temperatures across the interface at the contact points between two solid particles and form a bridge that can hold the particles together. As a post-treatment, this process is carried out to provide strength to agglomerates or to modify the porosity.

Spray fluidized beds are suitable apparatuses to produce agglomerates with high porosity and good mechanical resistance for handling and packaging [55]. Compared to other apparatuses, fluidized beds have a simple equipment design and can combine different micro-level processes such as dispersion of binder, and forming and drying of liquid bridges. The combination of different micro-level processes results in high operational efficiency. However, it also increases the complexity of the agglomeration process and makes it difficult to describe, design and operate. As described above, the mechanism of spray agglomeration is the dissipation of kinetic energy by viscous force in the collisions. To determine if a collision is successful or not, the Stokes number St derived by Ennis et al. [45] can be used. It is defined as:

$$St = \frac{2m_p u_{coll}}{3\pi\mu d_p^2}, \quad (2.1)$$

where m_p and d_p are mass and the diameter of colliding particles, respectively; μ is the viscosity of the colliding wet spot, u_{coll} is the collision velocity.

For agglomeration of the colliding particles to occur, the Stokes number must be below a critical value

$$St^* = \left(1 + \frac{1}{COR}\right) \ln \frac{h}{h_a}, \quad (2.2)$$

where COR is the particle restitution coefficient, h is the height of liquid at the colliding wet spot, and h_a is the height of asperities on the surface of the primary particles.

The amount of available experimental investigations on the SFBA process is relative large. Some of the previous works are partially summarized in Table 2.1. They found the particle growth behavior and product properties to depend on the configuration of the apparatus and the process parameters, such as the properties of materials, temperature and velocity of fluidization air, properties and spray rate of binder, pressure of atomizing air, droplet size and primary particle properties.

Table 2.1: Selected publications focusing on spray fluidized bed agglomeration process.

Year	Author	Remark
1991	Ennis et al. [45]	Classification of granulation mechanisms based on particle kinetic energy; study of dimensionless binder Stokes number St and critical Stokes number St^*
1996	Watano [56]	Investigations with various binder flow rates and inlet air temperatures; prediction of particle growth rate by using heat transfer and moisture balance measurements
1999	Turton et al. [57]	Microscopic considerations about wetting and spreading rates of the liquid binder and the critical binder/particle ratio; evaluation of the strength of the particles produced in agglomeration process; modeling of agglomeration by population balance equation (PBE)
2003	Hemati et al. [41]	Investigations with process-related and physicochemical variables, such as gas velocity, atomizer location, liquid flow rate and concentration, atomizing air flow rate, wettability of granulating liquid on solid particle surfaces, initial particle mean size
2003	Saleh et al. [58]	Effect of particle size on the coating and agglomeration behavior; simulations with population balance model taking into account the simultaneous growth by layering and agglomeration
2005	Turchiuli et al. [55]	Influences of the operating conditions on the physical and end-use properties, such as the size, shape, wettability, friability and flowability, of zein particles agglomerated with maltodextrin introduced as a liquid solution or as a powder
2005, 2006	Tan et al. [19, 59]	Investigations on the kinetics of fluidized melt agglomeration process with different parameters; identification of overall kinetics during the process by a combination of particle aggregation, binder solidification and granule breakage; influences of granule size and age on breakage kinetics for the fluidized melt agglomeration process

2007	Peglow et al. [60]	Simulation of spray agglomeration process with population balance model to predict the size distribution, the moisture content and the temperature of particles
2008	Thielmann et al. [61]	Effect of primary particle surface wettability on the particle size growth behavior and agglomerate structure; simulation of agglomeration process by population balance model solved using the Monte Carlo method
2010	Hampel [62]	Experimental study of spray agglomeration processes with varied air temperature, air velocity binder concentration, binder spray rate and materials; comparison of experimental results and simulation results done by PBE model
2012 - 2014	Dadkhah et al. [63–65]	Internal structure of non-porous glass agglomerates measured by X-ray micro-computed tomography and analyzed by different morphological descriptors; investigations on product properties with different primary materials (non-porous glass, porous ceramic) and varying inlet gas temperatures and binder concentrations; investigations on solidified binder morphology
2016, 2018	Pashminehazar et al. [66, 67]	Evaluation of particle size, internal porosity and spatial distribution of the pores inside the maltodextrin agglomerates produced in a fluidized bed by X-ray micro-computed tomography; study of the morphology of maltodextrin agglomerates by simplified spherical primary particle model and real structure model
2019	Atalar and Yazici [68]	Investigation on the influence of different binders (distilled water, ionic, and sugar-based solutions) on agglomeration growth mechanism, particle morphology, and chemical bonds with spray-dried yogurt powders as primary particles

2.4 Continuous processes in fluidized beds

To achieve a continuous process in fluidized beds, the raw materials need to be fed and products need to be discharged continuously. In general, raw materials are fed at the upper part of the bed directly or via a branch pipe which is isolated from the

atmosphere by a rotary valve or a double sluice gate. Depending on the desired feed rate and the properties of the materials, different devices can be used to control the feed rate, such as the rotary feeder and vibratory feeder. Moreover, there are normally three approaches to achieve the continuous discharging of the products: internally classifying discharge, non-classifying discharge and externally classifying discharge [69]. In the internally classifying discharge approach, the size of discharged particles is controlled by adjusting the airflow rate in the internal classifier, which is normally directly connected to the fluidized bed. In ideal conditions, only the particles with sinking velocity higher than the air velocity in the classifier can be discharged from the bed. This approach is used to control the size of products in coating, granulation and agglomeration processes [7, 10, 70]. The discharging rate is also controlled by adjusting the air velocity in the classifier, which makes it difficult to keep a constant bed mass, especially with changing particle size in the bed. In the non-classifying approach, the particles are discharged directly from the bed without classification by a rotary discharger or a sluice gate. The bed mass is usually controlled by controlling the rotational speed or the frequency of the sluice gate. In the externally classifying discharge approach, the particles can be discharged like in the non-classifying approach. However, the discharged particles are then transported to an external classifier (e.g., centrifugal classifier, vibrating sieve) for further separation. Compared to the internal classifier, the external classifier has the possibility to be combined with other particle handling devices. For example, Schmidt et al. [6] used an external classifier combined with a mill in a continuously operated SFBG process. The oversize particles were milled and then returned to the bed along with the undersize particles to serve as seed particles.

There are several investigations of continuous processes in fluidized bed reported in the literature (partially summarized in Table 2.2). For the fluidized drying process, the early studies focused on the application of pilot scale plants, which used the advantage of high throughput [71–73]. Due to the direct connection of the particle residence time distribution (RTD) and the drying behavior of these particles, different correlation equations and modeling approaches have been proposed; for example, see Nilson and Wimmerstedt [71], Bachmann et al. [74, 75], Chen et al. [4, 76] and Pietsch et al. [77]. For the continuous SFBG process, studies focused more on the process oscillation behavior and the control strategies by experiments and simulations, for example, see Heinrich et al. [78], Bück et al. [79] and Schmidt et al. [6, 7]. For the continuous SFBC process, only a few studies focused on the process control strategy [80] and produce quality [5, 70] are available in the literature. For the continuous SFBA process, although the first patent was registered by Uhlemann et al. [8] in 1996, little work has been done in the last two decades. In recent years, there is a resurgent interest in this process. Schmidt et al. [9] conducted experiments with maltodextrin as primary particles in a continuous cylindrical fluidized bed that was equipped with an internal classifier or external classifier. They achieved the steady state successfully in some of the experiments and showed the influence of primary particle feed rate and classifying method on the process behavior and product properties. For a better understanding of this process, Strenzke et al. [10] performed a series of experiments by using the same

apparatus as in Schmidt's work equipped with an internal classifier. In their study, glass beads were employed as primary particles, and process parameters, e.g., primary particle feed rate, fluidizing air temperature, binder spray rate, binder fraction, atomizing air pressure, etc., were varied to study the process behavior in detail. Du et al. [81] used a horizontal fluidized bed with non-classifying discharge, alongside with glass beads as primary particles. They studied the influence of air temperature, binder fraction and the configuration of internal and outlet weirs on the evolution of particle size, as well as the RTD of particles.

Table 2.2: Selected publications focusing on continuous processes in fluidized bed.

Year	Author	Process	Remark
1987	Nilson and Wimmerstedt [71]	drying	Study of particle drying behavior in a vibrating horizontal fluidized bed, description of particle movement by dispersion model
1996	Uhlemann et al. [8]	SFBA	US patent, agglomeration of particles in a cylindrical fluidized bed with internal classifier
2000	Wetchacama et al. [72]	drying	Drying of paddy in a horizontal vibro-fluidized bed with rotary discharger
2012	Khanali et al. [73]	drying	Drying of rough rice in a horizontal fluidized bed, study of particle RTD
2013	Hampel et al. [70]	SFBC	Coating of micro-crystalline-cellulose in a continuous Wurster fluidized bed with an internal classifier for different process parameters
2015	Schmidt et al. [6, 7]	SFBG	Granulation of sodium benzoate in a continuous cylindrical fluidized bed with internal and external classifier, study of process oscillations with different process parameters
2017	Chen et al. [4]	drying	Modeling of particle moisture distribution of drying process in a continuous horizontal fluidized bed by using a two-dimensional population balance (PB) model
2018	Schmidt [9]	SFBA	Study of process behaviors and product properties with maltodextrin in a continuous cylindrical fluidized bed with an internal or external classifier

2018	Diez et al. [82]	SFBG	Granulation of sodium benzoate in a continuous horizontal fluidized bed with an external classifier, study of product properties with different process parameters
2019	Müller et al. [80]	SFBG	Development of process control strategies for diverse desired particle growth ratios and various separation sharpnesses in a continuous Wurster fluidized bed with an internal classifier
2020	Bachmann et al. [5]	SFBC	Modeling of particle size and layer-thickness distributions of coating process in a continuous horizontal fluidized bed with PB equations
2020	Strenzke et al. [10]	SFBA	Study of process behaviors and product properties with glass beads in a continuous cylindrical fluidized bed with an internal classifier
2020	Du et al. [81]	SFBA	Study of process behaviors with glass beads and particle RTD in a continuous horizontal fluidized bed

Regarding the continuous processes in the fluidized bed, the particle RTD is an important factor that can either determine the product quality directly (e.g., in drying, coating and granulation processes) or influence the product quality indirectly (e.g., for heat-sensitive products). Therefore, a comprehensive understanding of particle RTD in different types of fluidized beds is helpful to the control of process and to the improvement of product quality. In reality, the convection of particles in the fluidized bed is disturbed by the dispersion of particles, which leads to a distribution of particle residence time. According to this factor, the horizontal fluidized bed can also be called back-mixing flow fluidized bed [83]. To measure the residence time distribution, the stepwise and pulse input method of tracers are commonly used. In the stepwise method, the flow of particles is switched to the same materials with a specific fraction of tracer with an unchanged flow rate. In the pulse method, a small amount of tracer is instantaneously injected into the flow, which makes it enter like a pulse. In both methods, the tracer concentration is then observed at the outlet and used for further analysis. In this work, the pulse method is employed in the experiments, and further calculation is introduced briefly. The tracer mass fraction X_t of a sample taken at a certain time t is calculated as:

$$X_t(t) = \frac{m_t(t)}{m_s(t)}, \quad (2.3)$$

where $m_t(t)$ is the weight of tracers in the taken sample and $m_s(t)$ is the total weight of sample. Then, the concentration $X_t(t)$ can be converted into a normalized value $E(t)$ by the following calculations:

$$E(t) = X_t(t) \frac{\dot{m}_p}{m_{t,tot}}, \quad (2.4)$$

where $m_{t,tot}$ is the total weight of the injected tracers and \dot{m}_p is the feed rate of primary particles at inlet.

To compare and indicate the degree of dispersion, different calculation methods and models have been proposed in previous work, which are briefly described as follows:

- Method of moments: This method is a general way to calculate the mean residence time τ and the variance of the residence time distribution σ^2 , which can indicate the time of particles stay within the bed and the spread of the time distribution, respectively. These two parameters can be calculated by the method of moments as follows:

$$\tau = \frac{\sum_{i=1}^N tE(t)\Delta t}{\sum_{i=1}^N E(t)\Delta t} \quad (2.5)$$

and

$$\sigma^2 = \frac{\sum_{i=1}^N t^2 E(t)\Delta t}{\sum_{i=1}^N E(t)\Delta t} - \tau^2, \quad (2.6)$$

where N is the number of intervals.

- The tank-in-series (TIS) model: In this model, the system is assumed to be a certain number of connected ideal continuously stirred tank reactors (CSTR). The number of tanks N_{tank} can be simply calculated by [84]:

$$N_{tank} = \frac{\tau^2}{\sigma^2}, \quad (2.7)$$

and the normalized RTD is calculated as:

$$E(t) = \frac{1}{\tau} \left(\frac{t}{\tau} \right)^{N_{tank}-1} \frac{N_{tank}^{N_{tank}}}{(N_{tank}-1)!} e^{-tN_{tank}/\tau}. \quad (2.8)$$

where N_{tank} is the number of tanks.

- Backflow cell model: By considering a mechanism whereby material can move and mix upstream, the backflow cell model was proposed by Roemer and Durbin [85]. It is calculated as:

$$\sigma^2 = \frac{1+2R}{N_{geo}} - \frac{2R(1+R)}{N_{geo}^2} \left[1 - \left(\frac{R}{1+R} \right)^{N_{geo}} \right] \quad (2.9)$$

where N_{geo} is the number of geometrical stirred tank reactors, and R is the reflux factor. In the present work, this model is used to calculate the reflux factor in the Monte Carlo simulation, which is introduced in detail in Chapter 7.

- Dispersion model: This empirical model is widely used to describe the axial solid mixing in fluidized beds, in which the dispersion coefficient D is determined by fitting the analytical solution to the experimental data. It is written as:

$$\frac{\partial E(t)}{\partial t} = D \frac{\partial^2 E(t)}{\partial z^2} - u_{bed} \frac{\partial E(t)}{\partial z}, \quad (2.10)$$

with

$$u_{bed} = \frac{L_{bed}}{\tau}, \quad (2.11)$$

where L_{bed} is the length of fluidized bed, u_{bed} is the bed velocity and z is the axial location.

In order to compare the residence time distribution and show the ratio of solid convection to dispersion from the inlet to the outlet, the dimensionless Bodenstein number Bo is used:

$$Bo = \frac{u_{bed} L_{bed}}{D}. \quad (2.12)$$

When Bo is zero, the solid flow is a well-mixed flow. On the contrary, when Bo goes to infinity, the solid flow is an ideal plug flow. In this work, Bo is calculated and used to indicate to dispersion behavior of the particles in the bed. The variance of the residence time distribution σ^2 can be calculated from Bo by:

$$\sigma^2 = \frac{2}{Bo^2} [Bo - 1 + e^{-Bo}]. \quad (2.13)$$

2.5 Modeling of spray fluidized bed agglomeration processes

Modeling spray fluidized bed agglomeration processes has drawn significant interest in the last few years. **An appropriate** and validated model can either be used to predict the process behavior and product characteristics or help us to understand the mechanisms of the process better. Compared to the other processes (e.g., drying, coating and granulation) that take place in the fluidized bed, the kinetics of agglomeration process can not be calculated directly, which makes it more difficult to be modeled. Regardless of the difficulty, different methods at different scales, e.g., the macroscopic PBE and the microscopic Monte Carlo model [86–88], have been proposed and successfully applied.

2.5.1 Population balance equations

Using PBE is a traditional approach to describe how the properties of a group of particles change with time and position. These properties are usually measured by the PSD [89]. Since it was proposed by Hulburt and Katz [90] in 1964, this approach has been

used in the modeling of many relevant fluidized beds processes, such as drying [4], coating [5, 91], granulation [92, 93] and agglomeration [60, 62, 94]; moreover, for breakage during milling [95], polymerization [96] and crystallization [97] processes. According to Randolph and Larson [98], a general approach for modeling the particle number density function n by PBE is:

$$\frac{\partial n}{\partial t} = -\nabla(Gn) + B_p(t, v) - D_p(t, v) + \dot{n}_{in}(t, v) - \dot{n}_{out}(t, v), \quad (2.14)$$

where $\partial n/\partial t$ describes the change in particle number density over time, G is the particle growth rate, $B_p(t, v)$ stands for the ‘‘birth’’ of new particles by nucleation, coalescence or breakage, $D_p(t, v)$ stands for the ‘‘death’’ of particles by coalescence or breakage, $\dot{n}_{in}(t, v)$ is the feed rate of particles to the system, and $\dot{n}_{out}(t, v)$ is the removal rate of particles from the system.

In the agglomeration process, the change in particle volume by the deposition of binder is always neglected due to the small thickness of the binder film. Therefore, the particle growth $-\nabla(Gn)$ can be removed from the equation. The equation is governed by four terms, which can be classified into two groups:

$$\begin{aligned} \text{Agglomeration term: } & B_p(t, v) - D_p(t, v) \\ \text{Feed and discharge term: } & \dot{n}_{in}(t, v) - \dot{n}_{out}(t, v) \end{aligned} \quad (2.15)$$

The agglomeration term is described by binary agglomeration, where two particles with the volumes v and v' are combined to form a new particle with the volume $v + v'$ [99]:

$$\begin{aligned} B_p(t, v) - D_p(t, v) = & \frac{1}{2} \int_0^v \beta'(t, v - v', v') n(t, v - v') n(t, v') dv' \\ & - n(t, v) \int_0^\infty \beta'(t, v, v') n(t, v') dv'. \end{aligned} \quad (2.16)$$

In the Equation 2.16, $\beta'(t, v, v')$ is called the agglomeration kernel, used to describe the kinetics of the process. It can be further divided into a time-dependent pre-factor and a volume-dependent factor as:

$$\beta'(t, v, v') = \beta'(t) \beta'(v, v'), \quad (2.17)$$

where $\beta'(t)$ is the agglomeration efficiency that depends on all parameters involved in the agglomeration process except the size of the particles, e.g., the materials and the process conditions; $\beta'(v, v')$ is the volume-dependent factor, which is assumed to reflect the influence of the flow field on the probability of collision between particles of different size [100].

To derive the agglomeration kernel, different methods, including empirical [101], semi-empirical [102] and mechanistic [103] methods have been proposed. However, it is

still the most difficult part of the application of a PBE to analyze and understand the agglomeration process [104]. The selection and correlation of the kernels heavily depend on experimental results, which restrict the usage of the kernels to specific materials and process parameters [51].

The feed and discharge terms are used in continuous processes, where the feed of new particles and the discharge of products occur simultaneously during the process [92, 105, 106]. Their combination can be calculated as:

$$\dot{n}_{in}(t, v) - \dot{n}_{out}(t, v) = \dot{N}_{feed}q_{0,feed}(v) - \dot{N}_{dis}K(v)n(t, v). \quad (2.18)$$

In Equation 2.18, \dot{N}_{feed} and \dot{N}_{dis} are the feed rate of new particles and the discharge rate of products, respectively. $q_{0,feed}(v)$ is the normalized number density of new particles. $K(v)$ is the separation function of the classifier, which can be either calculated from other models depending on the properties of particles and the classifying air velocity or achieved from experimental results.

Besides the difficulty in the selection of agglomeration kernel, another problem arises in the discretization and solving the PBE due to the complexity of the equations [107–109]. Especially when the agglomeration kernel is involved, the PBE turns to an integro-differential equation which cannot be solved analytically. Numerical schemes have to be used to obtain an approximate solution [100].

2.5.2 Monte Carlo method

The Monte Carlo method is a kind of stochastic approach based on the use of random numbers and probabilities to simulate the underlying micro-scale processes directly. The idea of Monte Carlo method can be traced back to the eighteenth century, but it came into its modern form in the push to develop nuclear weapons during World War II [110]. After a few decades of development and with the rapid development of computers, Monte Carlo method has been used in various areas such as statistical physics [111], chemical reaction [112], crystallization [113], particulate systems [86], and finance and business [114, 115].

According to the treatment of time steps, Monte Carlo methods can be divided into time-driven and event-driven methods [116]. If the time step is fixed first, the method is called time-driven method. All possible events may occur or not within the time step. If the event is fixed first, the method is called event-driven method, in which only one event per time step can occur. The times of events are linked to the time in reality by event frequency. Compared to the time-driven method, the event-driven method increases the computational efficiency by eliminating the eventless time steps.

Apart from the treatment of time steps, Monte Carlo methods can be divided into constant-volume Monte Carlo (CVMC) method and the constant-number Monte Carlo (CNMC) method according to the size regulation technique [116]. In the CVMC method, when the number of individuals (which may be primary particles or agglomerates) in the simulation box becomes lower than half of the initial number, an extra

copy of the particle population is introduced to the simulation box to restore the initial number. In the CNMC method, the number of particles is kept constant by random duplication or deletion of particles in each time step.

The Monte Carlo method has been applied to simulate the coating and agglomeration processes in fluidized bed. Rieck et al. [117] used this method to simulate the coating process conducted in a lab-scale fluidized bed. The model has been coupled by Jiang et al. [118] with a computational fluid dynamics-discrete element method (CFD-DEM) simulation to achieve more information such as cycle time distribution, residence time distribution, coating coverage, uniformity of porosity, and layer thickness distributions on individual particles and in the particle population. For the spray fluidized bed agglomeration process, Terrazas-Velarde et al. [86, 119, 120] used this method to simulate the particle size growth of non-porous (glass beads) and porous (alumina) particles. To improve the model, Dervedde et al. [121] considered the pre-drying process of droplets by implementing a single-droplet drying model that considers the change in droplet diameter and in the radial concentration profile of binder in the droplet. To trace the three-dimensional (3D) structure of the agglomerates in the simulation, Dervedde et al. [87] then proposed a cluster-cluster ballistic aggregation model that allows a complete, unrestricted description of the spatial evolution of particles related to physical micro-processes. Furthermore, Rieck et al. [88] extended the usage of Monte Carlo model to amorphous particles (maltodextrin) by adding a particle surface wetting routine. Based on experimental results achieved with the help of X-ray tomography by Dadkhah and Tsotsas [64], Singh and Tsotsas [122, 123] developed a tunable structure formation model to reconstruct morphological descriptors of SFB agglomerates computationally. The Monte Carlo method can also be used to solve the PBE and to improve the PBE by analyzing the effect of microscopic events [124, 125].

Chapter 3

Experimental and measurement methods

3.1 Materials

3.1.1 Solid properties

In this work, all the experiments were conducted with non-porous glass beads (Sigmund Lindner GmbH, Germany). A scanning electron microscopy (SEM) image of the primary particles is shown in Figure 3.1. The primary particles have high sphericity of 0.89 and density of 2500 kg/m^3 . As shown in Figure 3.2, the particles have a narrow range size distribution between 0.15 and 0.40 mm with a Sauter mean diameter $d_{32,pp}$ of 0.20 mm.

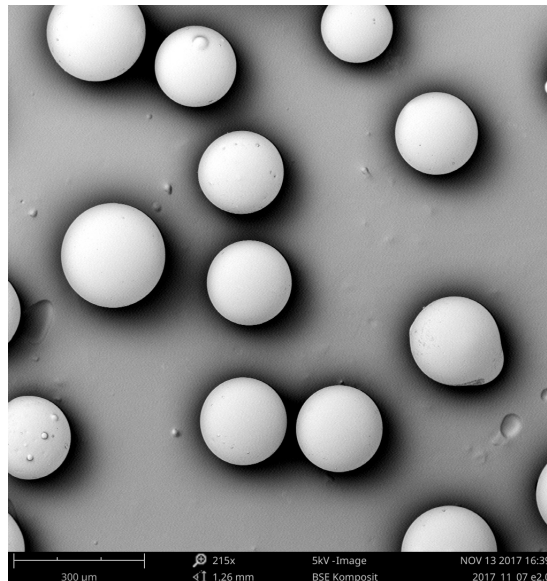


Figure 3.1: SEM image of primary particles.

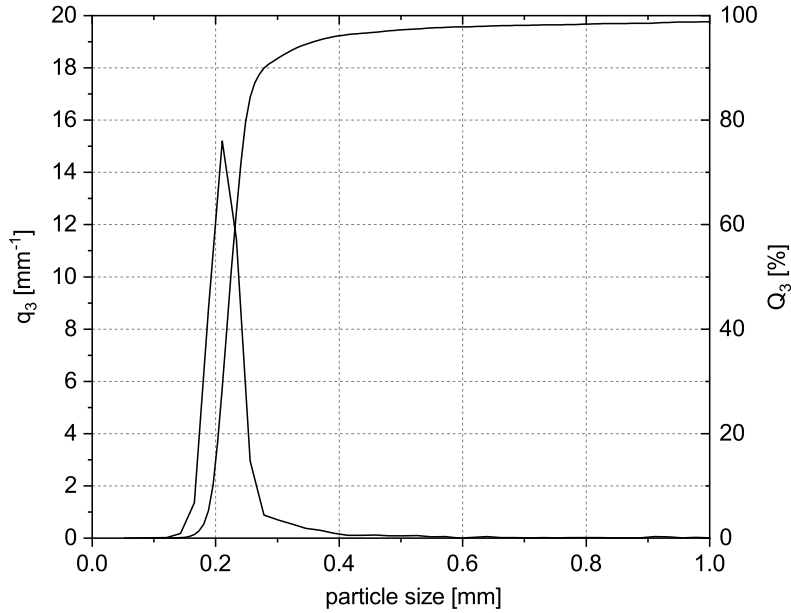


Figure 3.2: Primary particle size distribution.

3.1.2 Binder properties

The binder used was hydroxy-propyl-methyl-cellulose (HPMC, trade name Pharmacoat 606, from Shin-Etsu, Japan) water solution. HPMC is white powder when it is in an undissolved state. The water solution was prepared according to producer instructions with tap water in different mass fractions from 3 % to 6 %. HPMC can form flexible and tough bridges, which makes it suitable for the agglomeration of excipients and coating of active substances in the pharmaceutical industry. The viscosity of binder solution highly depends on the fraction of HPMC. In previous work, the relationship between solution viscosity and binder mass fraction was measured by Terrazas-Velarde with a falling ball viscometer. The results were empirically correlated as [126]:

$$\mu_b = 7.23 \times 10^{-4} X_b^3 - 6.42 \times 10^{-3} X_b^2 + 0.0265 X_b - 0.0246 \quad (3.1)$$

where μ_b is the viscosity in Pa · s and X_b is the mass fraction of binder in percentage. The correlation is only valid in the range of 2 % to 30 % of binder.

3.1.3 Preparation of tracers

To measure the particle residence time distribution, the same glass beads used in the agglomeration experiments were coated with sodium benzoate and then used as tracer. Due to the small size of the particles, it is difficult to measure the amount of tracer in each sample directly. Therefore, the samples that contained tracer were mixed with deionized water, and the conductivity was then measured to achieve the amount of tracer in each sample. The detailed calculation is described in Section 3.3.5.

To coat the glass beads, a cylindrical fluidized bed with a side spray nozzle was used (shown in Figure 3.3). The inner diameter of the process chamber was 200 mm with a two-fluid nozzle (Düsen-Schlick, Mod.946 S1, liquid orifice diameter: 2.3 mm) installed at the side of the bed. The air velocity and pressure in the bed can be controlled by the two fans installed at the inlet and outlet.

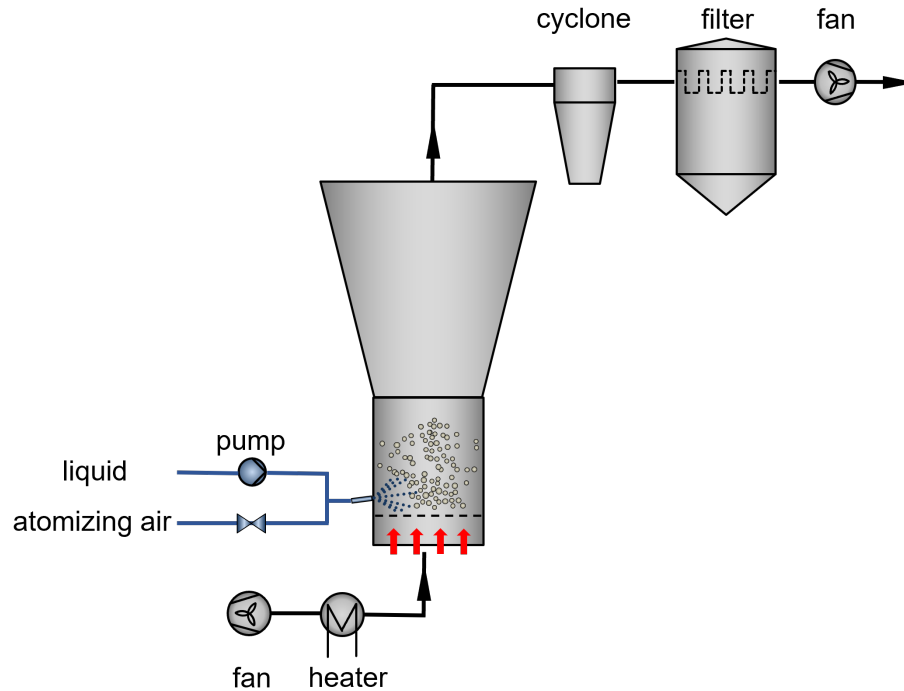


Figure 3.3: Scheme of cylindrical fluidized bed with side spray.

The main parameters used in the coating process are summarized in Table 3.1. The sprayed liquid is a water solution of sodium benzoate with a mass fraction of 30 % and HPMC with a mass fraction of 0.3 %. HPMC is used to increase the strength of the coating layer. To see the coated layer more clearly, a small amount of water-soluble yellow dye was also mixed with the solution. To reduce the agglomeration of particles, the atomizing air pressure was set at 2.5 bar, and the air temperature was set at 90 °C. The plant was heated to the desired temperature, and then the glass beads were fed in. The spray was started when the glass beads were in good fluidization condition. The process was run for about 10 min; then, all the particles were discharged from the bed simultaneously. Moreover, the coated glass beads were sieved by a wire mesh with a mesh size of 0.355 mm to remove large agglomerates. The size distribution of tracer particles was measured by Camsizer and is shown in Figure 3.4. After coating, the Sauter mean diameter of tracers increases from 0.20 mm to 0.22 mm.

3.2 Plant description

In the present work, a series of agglomeration experiments were performed in a continuously operated horizontal fluidized bed (GF/Procell 20, Glatt Ingenieurtechnik GmbH,

Table 3.1: Parameters used in the preparation of tracers.

Parameter	Value
Bed mass	7 kg
Primary particles size	0.20 mm
Sprayed liquid	water solution of 30 % sodium benzoate and 0.3 % HPMC
Spray rate	80 g/min
Atomizing air pressure	2.5 bar
Fluidizing air velocity	2 m/s
Fluidizing air temperature	90 °C
Process time	10 min

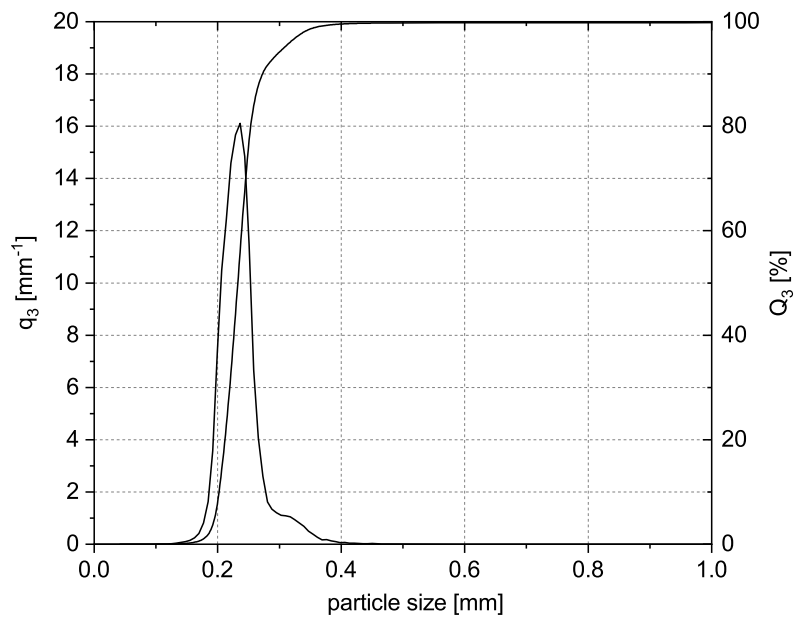


Figure 3.4: Particle size distribution of tracers.

Weimar, Germany). A schematic flow diagram of the experimental fluidized bed is shown in Figure 3.5. This apparatus can be used for different processes such as drying [4], coating [5] and granulation [82]. The dimensions of this horizontal fluidized bed are 1 m in length and 0.20 m in width. As shown in Figure 3.6, by the installation of internal weirs, the bed can be separated into four process compartments. With different settings of internal weirs, underflow, overflow and sideflow can be achieved. The height of underflow weirs is same as the height of the bed in order to prevent the overflow of particles. To control the bed height, outlet weirs of different heights can be installed. The feed rate of particles was controlled by a twin screw feeder together with a rotary valve at the end of the feeding pipe, which was used to isolate the bed from the atmosphere. At the inlet, a filling tube was installed to enable the pulse injection of particles during the process. The outlet was controlled by a rotary valve with constant rotation speed. The fluidization air was provided by two fans; one was at the inlet and one at the outlet. By adjusting the power of the two fans, the pressure inside the bed can be controlled. The fluidization air was heated by an electrical heater. Then, it was separated into four pipes and entered the bed through a distributor, which is a combination of a perforated plate and a 100 mesh stainless steel screen. The air velocity and temperature in each pipe can be separately controlled by the opening ratio of two valves, respectively. Process parameters such as the fluidization air velocity, the heater temperature, the opening ratio of valves, the spraying rate etc. were controlled by a distributed control system (DCS). The cross-section of the upper side of the process chamber was expanded to reduce gas velocity and, thus, enforce the return of entrained particles in the fluidized bed. For spraying, bottom or top spray systems are possible. When the top spray is applied, a maximum of three spray nozzles (Düsen-Schlick GmbH, Untersiemau, Germany, model 940/3 with orifice diameter 0.8 mm, two-fluid nozzle) can be used. The nozzles are placed at a height of 320 mm from the distributor. The spray rate was controlled by a peristaltic pump and the atomizing air pressure was controlled by an adjustable valve. Depending on the spray condition, process chambers 1-3 are called spray compartments (with spray), and process chamber 4 is called conditioning compartment (without spray). The spray compartments are where the main agglomeration process take place, whereas the conditioning compartment is used to further dry and discharge the particles. In order to take samples from the bed during the process, a sampling probe is installed on the back wall of the bed at a height of 100 mm from the distributor in chamber 4.

3.3 Measurement methods

3.3.1 Particle size distribution

Particle size distribution (PSD) is one of the most important features of particulate systems. The particle size influences many properties of powders and is a valuable indicator of quality and performance to the end user. The PSD of a powder, or granular material, is a list of values or a mathematical function that defines the relative amount of particles present according to size. The cumulative density in PSD can be defined by

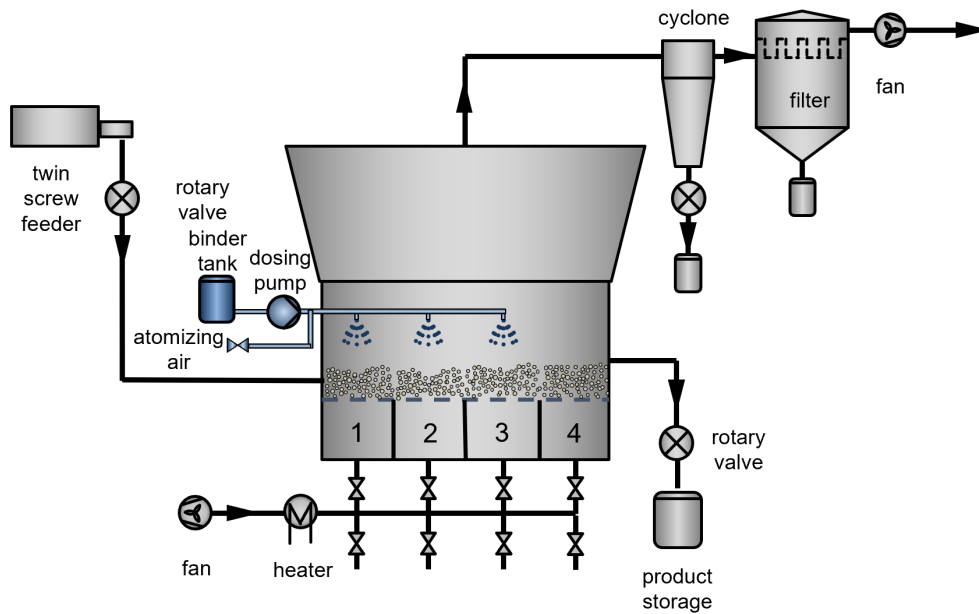
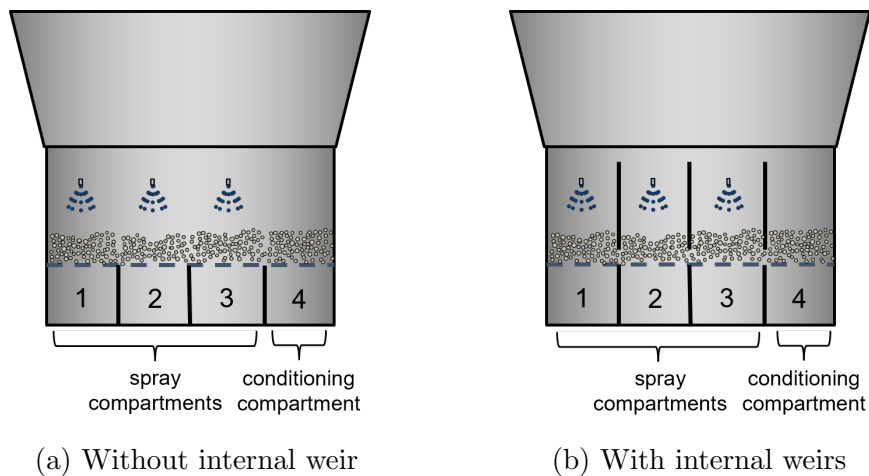


Figure 3.5: Scheme of horizontal fluidized bed plant.



(a) Without internal weir

(b) With internal weirs

Figure 3.6: Process chamber of horizontal fluidized bed a. without internal weir, b. with internal weirs.

number $Q_0(d)$, length $Q_1(d)$, area $Q_2(d)$ or volume $Q_3(d)$. Normally, the number and volume-based distributions are the most frequently used. The normalized distribution density is calculated by:

$$q_r(d) = \frac{dQ_r(d)}{dd}, \quad (3.2)$$

where $q_r(d)$ is the normalized distribution density with the index r ranging from zero to three; d is the particle size.

The measurement PSD of a sample can be performed using various techniques, for example, sieve analysis, laser diffraction, dynamic light scattering and optical analysis. Depending on the properties of particulate solids, different techniques show their advantages and disadvantages [127].

In this work, the device called Camsizer (Retsch Technology, Germany) is used in the measurement. Camsizer is an optical analysis device that can reliably analyze a wide range of particles from 0.02 mm to 30 mm. It works on the measuring principle of dynamic image analysis to count the number of particles. The sample is fed in from the feed channel with a vibrating chute, so that all particles fall through the measurement area uniformly. There, a planar light source is used to create projections of the falling particles. The particle images are recorded as shadow projections by two cameras at a high frequency. The recorded data are then further analyzed by the computer. After the measurement, $Q_0(d)$ and $Q_3(d)$ can be exported. Due to the discrete nature of the measured values, the calculation of normalized distribution density is done in intervals:

$$q_r(\bar{d}_i) \approx \frac{Q_r(d_i) - Q_r(d_{i-1})}{d_i - d_{i-1}}, \quad (3.3)$$

where d_i is the size and $Q_r(d_i)$ is the cumulative frequency of class i .

To show the evolution of particle size with process time, the measured particle size distribution is converted to the corresponding Sauter mean diameter:

$$d_{32} = \frac{\sum_{i=1}^n d_i^3 q_0(i)}{\sum_{i=1}^n d_i^2 q_0(i)}. \quad (3.4)$$

Sauter mean diameters are plotted versus process time to show the particle size evolution in the agglomeration process.

3.3.2 Average particle growth rate

For better comparison, particle growth rates which also take the size of inlet particles in consideration are used. The calculated particle size growth rate G is:

$$G = \frac{\bar{d}_{32,pd} - d_{32,pp}}{\tau}, \quad (3.5)$$

where $\bar{d}_{32,pd}$ is the average Sauter mean diameter of product samples taken after the process has been determined to have reached the steady state, $d_{32,pp}$ is the Sauter mean diameter of primary particles, and τ is the particle mean residence time.

3.3.3 Separation effect in particle size

Only the particles that are fluidized higher than the outlet weir can be discharged from the bed. This leads to a separation effect of the particles between bed and products. To indicate the separation effect SE , differences of the samples taken from bed and at the outlet are used:

$$SE = \frac{\bar{d}_{32,bed} - \bar{d}_{32,pd}}{\bar{d}_{32,bed}}. \quad (3.6)$$

Where $\bar{d}_{32,bed}$ is the average Sauter mean diameter of samples taken from the bed at steady state, and $\bar{d}_{32,pd}$ is the average Sauter mean diameter of samples taken from the outlet at steady state.

3.3.4 Determination of steady state

In an ideal steady state, all variables such as particle size and bed mass should stay constant over time. However, the variables are permanently fluctuating in real experiments. To determine the steady state in a continuous process, the evolution of particle size and the change in bed mass during the process are used as indicators. The particle size is the main factor in such a size enlargement process, which influences the properties of particles significantly. Meanwhile, the change in bed mass during the process should also be considered as an indicator to show the stability of the process. If the bed mass increases continually during the process, the risk of bed collapse increases with ongoing of process time, which can finally terminate the process. In the steady state, both the evolution of particle size and the development of bed mass should meet the criterion.

Regarding the particle size, the coefficient of variation CoV is used. This approach was proposed by Schmidt and has been used in continuous granulation and agglomeration processes [9] to determine the steady state stage in experiments. First, the average Sauter mean diameter of each three samples from the beginning of the process is calculated as follows:

$$\bar{d}_{32,i} = \frac{\sum_{j=i}^{j+2} d_{32,j}}{3} \quad i = 1..(l-2), \quad j = 1..l, \quad (3.7)$$

where l is the total number of samples.

Then, the standard deviation σ_i for each average set of Sauter mean diameter is calculated by:

$$\sigma_i = \sqrt{\frac{\sum_{j=i}^{j+2} (d_{32,j} - \bar{d}_{32,i})^2}{2}}. \quad (3.8)$$

Finally, the CoV_i for each sample is calculated as follows:

$$CoV_i = \frac{\sigma_i}{\bar{d}_{32,i}}. \quad (3.9)$$

Since the average value is calculated from $d_{32,i}$ to $d_{32,i+2}$, it needs two successor values. Therefore, the data of the last two samples have to be dropped in the calculation. In order to determine CoV of the samples at the end of the process, the same calculation is done backwards with the values starting from $d_{32,l}$ to $d_{32,l-2}$, and CoV_{back} is achieved. These calculations are conducted for bed samples and product samples, respectively.

Regarding the change in bed mass, the accumulation of bed mass growth rate $GR_{k,acc}$ from process time t_k to the end of the process t_w is used. The bed mass achieved from experiments is calculated from the bed pressure drop, which is recorded by the DCS each minute. The average bed mass of every three minutes is calculated as:

$$\bar{m}_{bed,k} = \frac{\sum_{k-2}^k m_{bed,k}}{3} \quad k = 3..w, \quad (3.10)$$

where k is the number of recorded bed mass, and w is the total number of recorded bed mass. Then, the bed mass growth rate GR_k in a period of process time from t_{k-1} to t_k is calculated by:

$$GR_k = \frac{\bar{m}_{bed,k} - \bar{m}_{bed,k-1}}{\bar{m}_{bed,k}(t_k - t_{k-1})} \quad k = 4..w. \quad (3.11)$$

Then, the accumulation of bed mass growth rate is calculated by:

$$GR_{k,acc} = \left| \sum_k^k GR_k \right| \quad k = 4..w. \quad (3.12)$$

The accumulation of bed mass growth rate can be used to indicate the growth behavior of bed mass. When the bed mass increases continuously during the process, a higher value is achieved.

Only when both the coefficient of variation CoV and the accumulation of bed mass growth rate $GR_{k,acc}$ are under specific values, the process can be determined to have reached the steady state. In Section 5.2.1, the calculation for the reference experiment Exp. Ref is presented in detail as an example.

3.3.5 Calculation of particle residence time distribution

In this work, the conductivity method is used in the measurement of RTD due to the small size of particles used in experiments. In the experiment, a pulse of tracer was inserted into the bed to measure the particle RTD. After the tracer had been injected, samples were taken periodically at the outlet. The collected samples were then separated with a rotary cone sample divider (Laborette 27, Fritsch GmbH, Germany) into eight parts. Depending on the amount of each sample, two or three of separated parts were selected randomly for conductivity measurement. The weight of the selected parts was determined by a scale, and then they were mixed with a specific volume of deionized water. To ensure all coated sodium benzoate can be dissolved in the water, the mixture was stirred with a glass stick, then the conductivity of the mixture was measured with a conductivity meter (LF 323/SET, WTW, Germany) thrice. Between each pair of measurements, the time interval was 5 minutes. Then, the average value was used in the calculation to determine the tracer concentration for each sample.

The measured conductivity can be separated into two parts:

$$\kappa = \kappa_t + \kappa_p, \quad (3.13)$$

where κ_t is the conductivity caused by tracers due to the coated sodium benzoate, and κ_p is caused by the uncoated glass beads due to their uncleanness. Because sodium benzoate is a strong electrolyte that can completely dissociate in water, the molar conductivity was considered constant. For the conductivity caused by tracer it holds:

$$\kappa_t = c_t \Lambda_t, \quad (3.14)$$

where

$$c_t = \frac{C_t}{\tilde{M}_t}. \quad (3.15)$$

Here, c_t is the molar concentration of the tracer in water; Λ_t is the molar conductivity of tracer; C_t is the tracer mass concentration in water; \tilde{M}_t is the molar mass of tracer.

Similarity, the molar conductivity of the uncoated glass beads is also considered constant. Then, the conductivity caused by these particles is:

$$\kappa_p = C_p \frac{\Lambda_p}{\tilde{M}_p}, \quad (3.16)$$

where C_p is the mass concentration of particles in water; formally, Λ_p is the molar conductivity of particles and \tilde{M}_p is the molar mass of particles.

Then, Equation 3.13 becomes:

$$\kappa = C_t \frac{\Lambda_t}{\tilde{M}_t} + C_p \frac{\Lambda_p}{\tilde{M}_p}. \quad (3.17)$$

In the measurement, selected samples are mixed with deionized water. The tracer mass concentration C_t and particle mass concentration C_p are calculated by:

$$C_t = \frac{m_t \rho_w}{m_w}, \quad (3.18)$$

and

$$C_p = \frac{(m_s - m_t) \rho_w}{m_w}, \quad (3.19)$$

respectively.

Here, m_s is the weight of the sample; m_t is the weight of tracer; and m_w is the weight of deionized water used in the measurement. By substituting Equations 3.18 and 3.19 into Equation 3.17, the weight of tracer in the sample is achieved by:

$$m_t = \frac{m_w \kappa - m_s \Lambda_p \tilde{M}_p^{-1} \rho_w}{\rho_w (\Lambda_t \tilde{M}_t^{-1} - \Lambda_p \tilde{M}_p^{-1})}. \quad (3.20)$$

Then the mass fraction of tracer X_t is calculated by:

$$X_t = \frac{m_s^{-1} m_w \kappa - \Lambda_p \tilde{M}_p^{-1} \rho_w}{\rho_w (\Lambda_t \tilde{M}_t^{-1} - \Lambda_p \tilde{M}_p^{-1})}. \quad (3.21)$$

By using Equation 2.4, the mass fraction of tracer in each sample is converted into a normalized value as:

$$E = \frac{(m_s^{-1} m_w \kappa - \Lambda_p \tilde{M}_p^{-1} \rho_w) \dot{m}_p}{\rho_w m_{t,tot} (\Lambda_t \tilde{M}_t^{-1} - \Lambda_p \tilde{M}_p^{-1})}. \quad (3.22)$$

The value of factor $(\tilde{M}_t \Lambda_t^{-1})$ depends on the properties of tracer. Since all tracers used in experiments were prepared in the same batch, the factor $(\Lambda_t \tilde{M}_t^{-1})$ is considered as a constant value in all measurements. The conductivity caused by tracer is in linear positive correlation with the mass concentration of tracer, and the factor $(\Lambda_t \tilde{M}_t^{-1})$ can be correlated by measuring the conductivity of solution in different concentrations. To reduce the error, three groups (denotes by T.1 to T.3) of mixtures were used to achieve this value. In each group, five samples were prepared in different mass concentrations of tracer from around 10^{-3} to 0.03 gml^{-1} . In the preparation, pure tracers were randomly

taken and mixed with deionized water. Then, the mixtures were well stirred to make sure all sodium benzoate can dissolve, and their conductivity values were measured. Finally, all values are plotted in Figure 3.7, and a correlation line is achieved. The value of $(\Lambda_t \tilde{M}_t^{-1})$ is $15691.08 \text{ Sm}^2\text{kg}^{-1}$ with the coefficient of determination $R^2 = 0.998$.

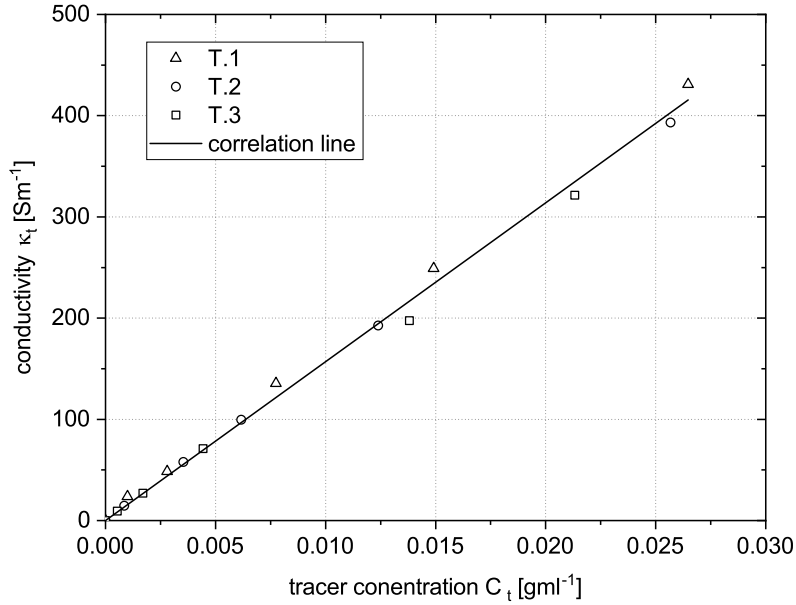


Figure 3.7: Conductivity measurement of tracers.

The value of factor $(\tilde{M}_p \Lambda_p^{-1})$ depends on the cleanness of the glass beads used in each experiment. To achieve this value, the last two samples (denotes by S.1 and S.2) taken at the outlet before the injection of tracers in the corresponding experiment are used. Here, the calculation of this value for the reference experiment (Exp. Ref) is shown as an example. The particles from each sample are mixed with deionized water in different concentrations from around 0.05 to 0.23 gml⁻¹. Finally, the measured values are plotted and illustrated in Figure 3.8. The value of $(\Lambda_p \tilde{M}_p^{-1})$ is $351.02 \text{ Sm}^2\text{kg}^{-1}$ with the coefficient of determination $R^2 = 0.985$.

By substituting Equation 2.12 into Equation 2.10, the derived dispersion-convection equation is:

$$\frac{\partial E(t)\tau}{\partial t} = \frac{1}{Bo} \frac{\partial^2 E(t)}{\partial \xi^2} - \frac{\partial E(t)}{\partial \xi}, \quad (3.23)$$

with

$$\xi = \frac{z}{L_{bed}}, \quad (3.24)$$

where ξ is the relative axial location.

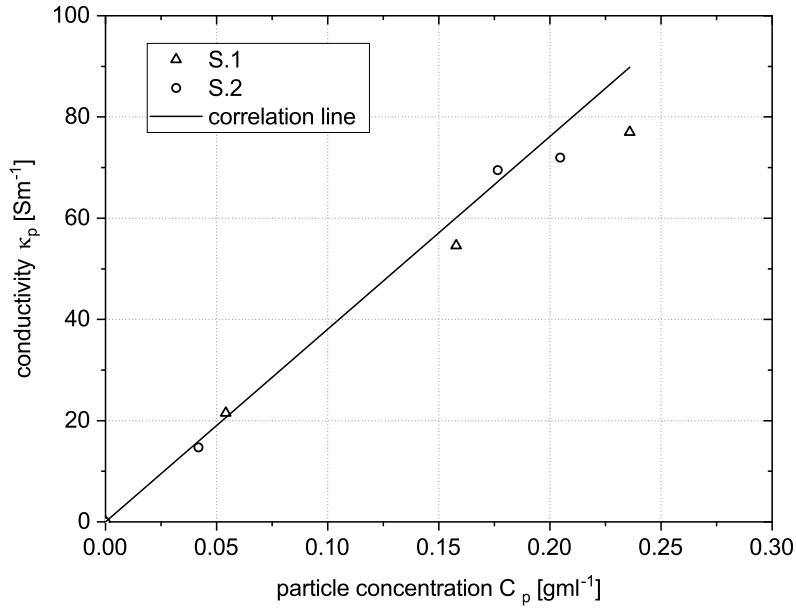


Figure 3.8: Conductivity measurement of uncoated particles.

To determine the Bo number, Equation 3.23 was solved with the software MATLAB (MathWorks Inc., R2021a) using the ode15s solver, an equidistant grid (1500 cells) and a flux limiter function with an initial pulse condition and Danckwerts boundary conditions for a closed-closed system [128]. Finally, the Bodenstein number is determined by fitting to the experimental results by the least squares method to find its nearest value [129].

The particle mean residence time τ is calculated according to the average bed mass \bar{m}_{bed} at steady state and the feed rate of primary particles at inlet by:

$$\tau = \frac{\bar{m}_{bed}}{\dot{m}_p}. \quad (3.25)$$

Chapter 4

Modeling of spray fluidized bed agglomeration process by Monte Carlo method

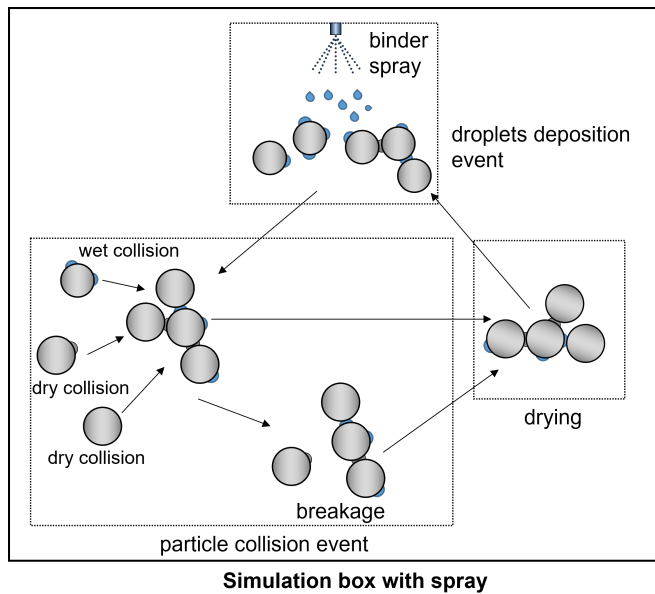
4.1 General algorithm of Monte Carlo method

4.1.1 Simulation box and flow chart

As discussed in [Chapter 2](#), Monte Carlo methods can be distinguished into event-driven and time-driven methods according to the treatment of time steps and divided into constant volume and constant number methods according to the size regulation technique. Compared to the time-driven variant, the event-driven method shows higher accuracy and simulation speed [116]. Therefore, the event-driven method is selected in this work. Regarding the size regulation method, particles in the simulation box are randomly deleted or replicated to maintain the number of particles in the CNMC method, which makes it difficult to determine the number of particles that need to be fed and discharged in a continuous process. Therefore, the CVMC method is a better option for the simulation of the continuous process. Consequently, the event-driven CVMC method is used in this work to simulate the continuous agglomeration process.

[Figure 4.1](#) shows a scheme of the simulation box used in the Monte Carlo simulations. The simulation box is considered as a simplification and a scaled-down version of the real system. It only contains a limited number of particles and implements the main micro-scale events and processes involved. In this work, two kinds of simulation boxes are used to simulate different kinds of process compartments: the simulation box with spray and the simulation box without spray. In the Monte Carlo simulation, the main events consider the interactions between droplets and particles and particles with other particles. Thus, droplet deposition events and particle collision events are considered as the two main events. The drying of deposited droplets takes place simultaneously with the main events. In the simulation box with spray, the real process is simplified into droplet deposition events, particle collision events and droplet drying. In the simulation box without spray, the droplet deposition event is removed, and only particle collision events and droplet drying are considered.

a.



b.

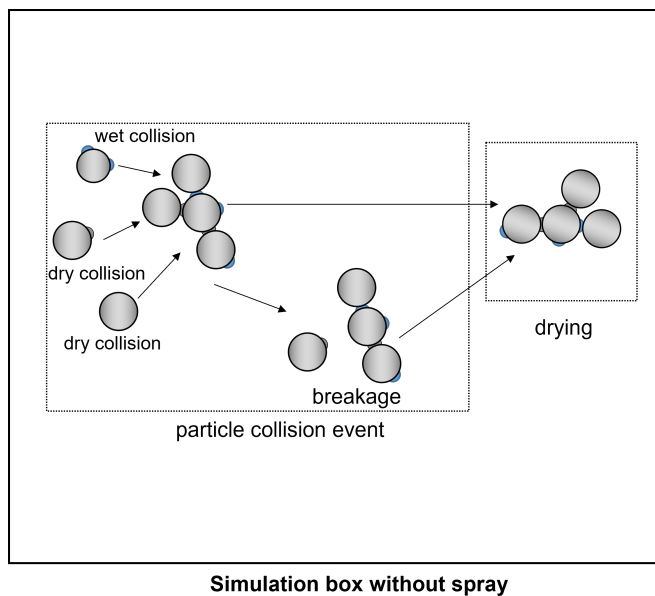


Figure 4.1: Scheme of simulation box in Monte Carlo model: a. simulation box with spray; b. simulation box without spray.

The flow chart of this model is shown in Figure 4.2. In the model, the simulation starts with real process time $t_{real} = 0$. First, the system is scaled down, and the primary particles are generated in the simulation box according to the set parameters. As mentioned above, the droplet deposition event and particle collision event are the two main events. These two events take place in a random sequence in the simulation box according to their frequencies. Therefore, a random number is generated to decide which event will take place in each iteration. If the droplet deposition event is chosen, the number of droplets to be deposited is calculated, and then the droplets are deposited randomly. If the particle collision event takes place, two particles are chosen randomly, and the Stokes criterion is checked to determine the status of the collision. Afterward, the drying of deposited droplets proceeds, and the heights of the deposited droplets are calculated and updated. The real process time, calculated according to the frequency, is then updated. If the defined process time has been reached, the simulation will be finished. If not, the simulation will continue until the defined process time is reached. When the model is applied to continuous processes, extra particle flow events need to be considered, which include the periodic feed and discharge of particles and the exchange of particles between different simulation boxes (for processes in the plant with multiple compartments). The algorithms for the particle flow events in plants with a single process chamber or multiple process chambers are described in detail in Chapter 6 and Chapter 7, respectively. Before the simulation goes to the next event selection iteration, the particle number is checked. If the number is lower than half of the initial particle number, the particle number is doubled, and the relevant parameters are updated as well.

4.1.2 Scaling and regulation of the system

Due to the huge number of particles in the real process, a direct simulation requires unacceptable computation ability and time. Therefore, the particle system in the simulation has to be scaled down. With this idea, the particle population in the simulation box can be thought of as a sample of the particles in the real system, which can stand for the properties of particles in the real system. The scaling factor S_0 at the starting of simulation is calculated as:

$$S_0 = \frac{N_{p,0}}{N_{p,0,real}}, \quad (4.1)$$

where $N_{p,0}$ and $N_{p,0,real}$ are the initial number of primary particles in the simulation and in the real system, respectively.

In the simulation, $N_{p,0}$ is one of the major factors that can influence the simulation speed significantly, as well as the simulation accuracy. $N_{p,0,real}$ is the number of particles in the real system that depends on the starting bed mass $m_{bed,0,real}$ and the size of primary particles $d_{32,pp}$, which is calculated as:

$$N_{p,0,real} = \frac{6m_{bed,0,real}}{\pi\rho_{pp}d_{32,pp}^3}. \quad (4.2)$$

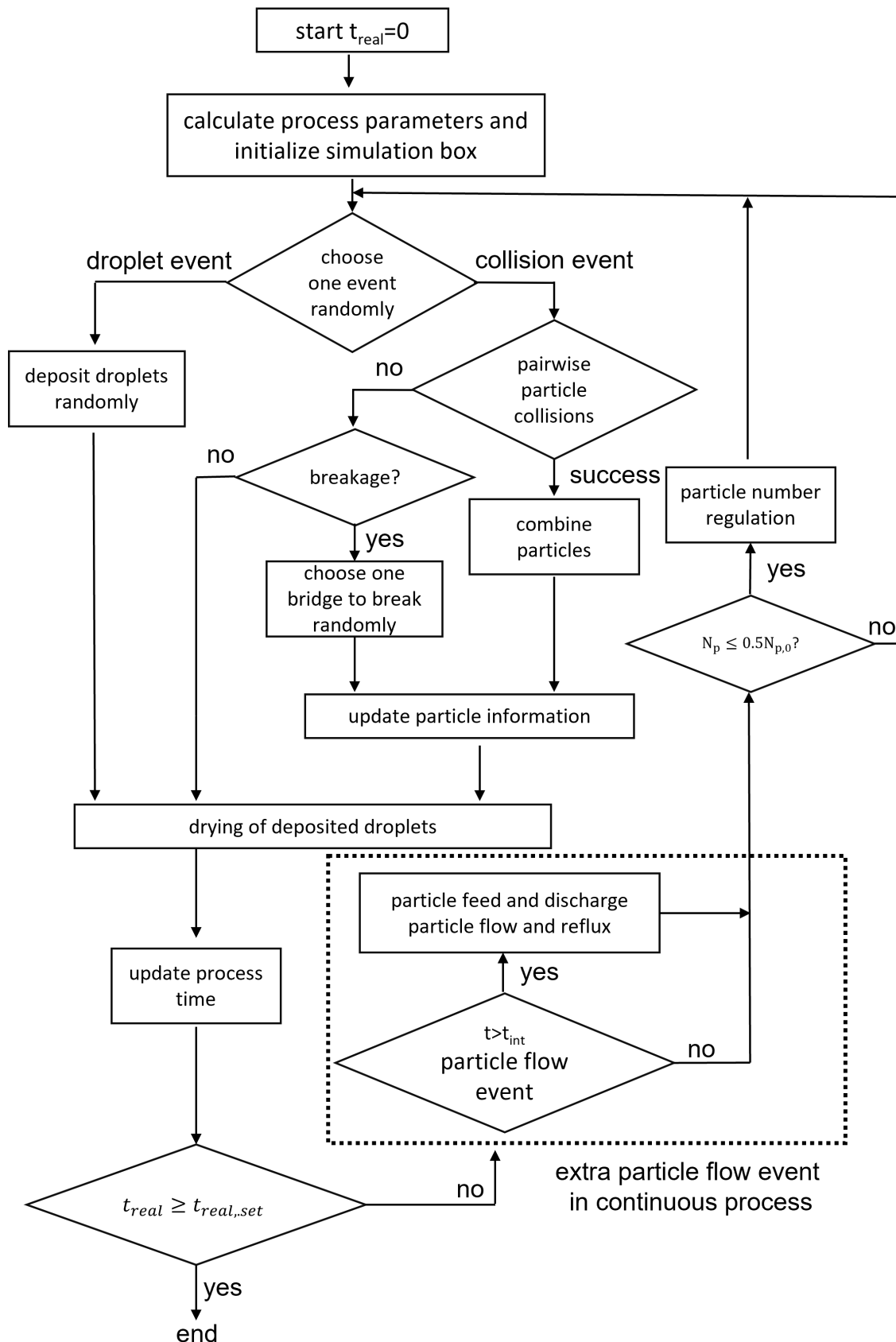


Figure 4.2: Flow chart of Monte Carlo simulation.

where ρ_{pp} is the density of primary particles.

To decide about an appropriate initial primary particle number in the simulation box, the relationship between initial primary particle number and computation time was studied by Terrazas-Velarde et al. [86]. As shown in Figure 4.3, the relative computation time with 1000 primary particles is set to 1. They suggested that 1000–2000 primary particles in the simulation box are an appropriate choice for achieving a balance between accuracy and simulation speed. Meanwhile, 1000-2000 primary particles have been also widely used in relevant work [87, 88, 117, 121]. Considering that the continuous process in this study has a longer process time compared to the batch-wise process in previous work [19, 62, 86], 1000 primary particles initially put in each simulation box are used to decrease the computation time.

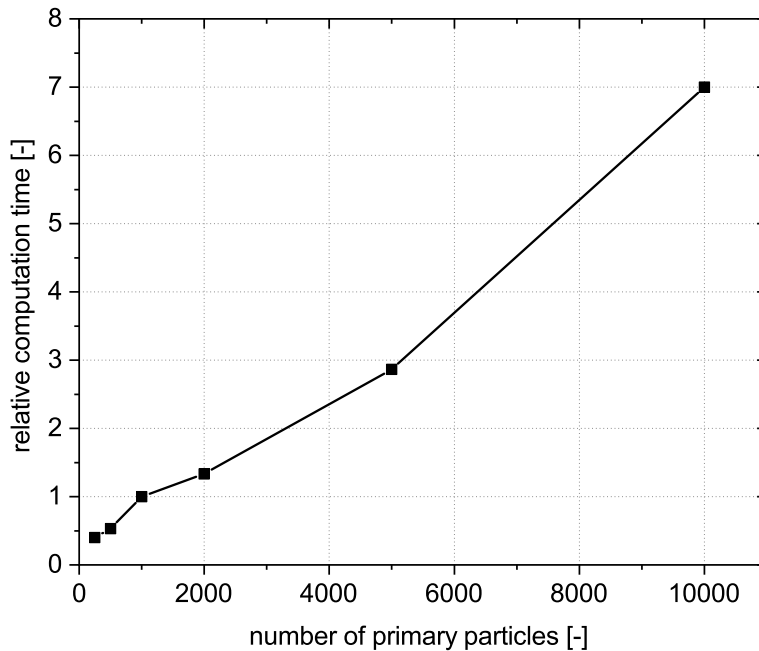


Figure 4.3: Influence of initial primary particle number on the relative computation time [86].

As mentioned above, the CVMC method is used for the regulation of particles in the simulation box. When the number of particles (include primary particles and agglomerates) in the simulation box has dropped to lower than half of the initial value, the particle population is copied and the replicate is introduced to the simulation box, which means that the number of primary particles $N_{pp,MC}$ is doubled. As shown in Figure 4.2, this information is checked and updated after the particle flow event when the model is applied for continuous process. To indicate the regulation times, the doubling number Dou that starts from zero is advanced by one after each regulation. Meanwhile, the scaling factor S is updated according to the doubling number and calculated as:

$$S = 2^{D_{ou}} S_0. \quad (4.3)$$

Once the scaling factor is changed, the other parameters related to the scaling factor are recalculated and applied in the next iteration.

4.1.3 Concept of positions

In order to describe the structure of agglomerates generated in the simulation box, the concept of positions and an algorithm for the evolution of 3D structures have been proposed in previous work [86, 87]. In the first approach (concept of positions), the surface of particle is assumed to be divided into six sections. On each section, a maximum of one other particle can be attached. It means that the neighbors of any primary particle in agglomerates are limited in the range of one to six. In the second approach (algorithm for the 3D structure), the unrestricted spatial development of agglomerates in 3D is considered, and the evolution of particle morphology can be tracked. Compared to the algorithm for the 3D structure, the concept of positions enables a fast and effective geometrical discretization to follow properties such as primary particle number per agglomerate [87]. Considering the long process time in continuous processes, the concept of positions is used in this work. As shown in Figure 4.4, the surface of a particle is divided into six sections on average. Depending on the size of droplets, each section is further divided into several positions where the droplets can be deposited. The number of positions $N_{pos,each}$ in each section is calculated by:

$$N_{pos,each} = \frac{d_{32,pp}^2}{6r_{cap}^2}. \quad (4.4)$$

where r_{cap} is the diameter of the spherical cap after the droplet has been deposited. It can be calculated by Equation 4.22.

If $N_{pos,each}$ is not an integer, it will be rounded to the nearest integer.

In the model, two matrices are used to store the information of each section and position for every particle. The initial state of the sections and positions is marked by zero. Once the section is occupied, which means there is another particle attached to the section, the corresponding sections on both particles are marked by one to show the occupation of the section. Meanwhile, the positions in the corresponding section are blocked, which means no further droplets can be deposited on that positions.

4.1.4 Event frequency and selection

In the Monte Carlo model, droplet deposition and particle collision are considered as the two main events, which take place in a random sequence according to their frequencies in each iteration. If the model is used for a continuous process, an extra event named particle flow event is used in this work. The particle flow event takes place periodically to control the particle flow behavior in the simulation.

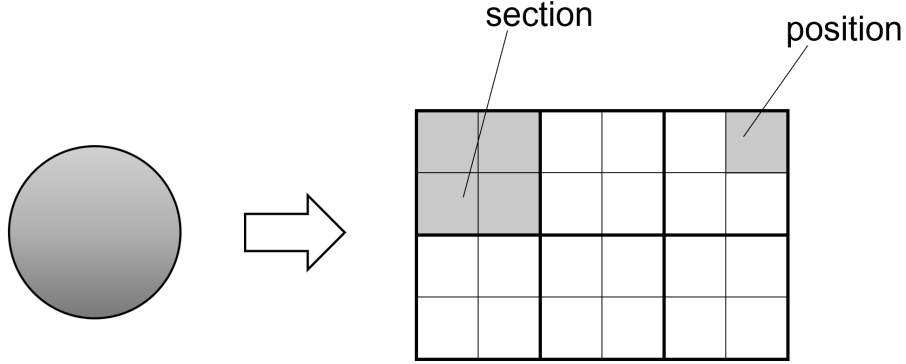


Figure 4.4: Division of particle surface into sections and positions (24 positions).

In droplet deposition events, droplets are generated and deposited on the surface of either primary particles or agglomerates randomly. For simplification, the droplets are assumed spherical and mono-dispersed. The droplet deposition rate $\dot{N}_{d,MC}$ in the simulation box is calculated as:

$$\dot{N}_{d,MC} = S\dot{N}_{d,real} \quad (4.5)$$

with

$$\dot{N}_{d,real} = \frac{6\dot{m}_{spray,real}}{\pi\rho_d d_d^3}, \quad (4.6)$$

where $\dot{m}_{spray,real}$ is binder spray rate in real process, ρ_d is the density of droplet, and d_d is the diameter of droplets.

Thus, the droplet frequency $f_{d,MC}$ is calculated by

$$f_{d,MC} = S \frac{6\dot{m}_{spray,real}}{\pi\rho_d d_d^3}. \quad (4.7)$$

In collision events, a pairwise collision between two randomly chosen particles (primary particles or agglomerates) in the simulation box is considered as one collision event. Therefore, the inter-particle collision rate is defined as the total number of collisions per unit time and calculated as:

$$f_{coll,MC} = \frac{1}{2} f_{coll} N_{p,MC}, \quad (4.8)$$

where f_{coll} is the number of collisions of a single particle per unit time and $N_{p,MC}$ is the particle number in the simulation box.

In order to calculate the single particle collision frequency, different correlations have been proposed, based on different experimental and computational approaches in previous work [130–133]. Here, the same method used by Rieck et al. [88] and Dervede [134] in the simulation of spray agglomeration process is used. The model was originally proposed by Oesterle and Petitjean [130], based on the introduction of simulated particle-to-particle collisions with a predicted probability during the trajectory calculation. This probability depends on the local concentration and velocity and is predicted through an iterative process. The collision frequency f_{coll} is:

$$f_{coll} = F_{coll}\sqrt{2}d_p^2n\bar{u}, \quad (4.9)$$

where F_{coll} is a defined prefactor to adjust the value of collision frequency. This value is obtained by fitting simulation results to experimental results done for a certain combination of plant and materials, then applied in all simulations. \bar{u} and n are the mean relative velocity of the particles in the fluidized bed and the particle number concentration in the bed, respectively.

Latter is defined as the number of particles per unit volume:

$$n = \frac{N_{p,0,real}}{V_{bed}}. \quad (4.10)$$

Here, V_{bed} is the total volume of the fluidized bed which can be calculated from the total volume of particles and the bed porosity ε :

$$V_{bed} = \frac{N_{p,0,real}V_p}{1 - \varepsilon}, \quad (4.11)$$

with the volume of a single particle as:

$$V_p = \frac{\pi}{6}d_p^3. \quad (4.12)$$

Substituting in Equation 4.11 and Equation 4.10, yields for number concentration:

$$n = \frac{6(1 - \varepsilon)}{\pi d_p^3}. \quad (4.13)$$

The mean relative velocity of the particles \bar{u} is calculated from a correlation that was obtained from a pseudo-two-dimensional fluidized bed using particle tracking velocimetry (PTV) [134]:

$$\bar{u} = -0.00001669Re^2 + 0.00444290Re, \quad (4.14)$$

with

$$Re = \frac{u_g d_p}{\nu_g}, \quad (4.15)$$

where u_g and ν_g are the gas velocity and kinematic viscosity, respectively.

Finally, the total frequency $f_{tot,MC}$ is the summation of droplet deposition frequency and collision frequency:

$$f_{tot,MC} = f_{d,MC} + f_{coll,MC}. \quad (4.16)$$

Due to the discrete nature of the events, the length of the time step Δt_{step} is calculated assuming exponentially distributed time steps, as it has also been done similarly in previous Monte Carlo simulations [87, 88, 135]:

$$\Delta t_{step} = -\frac{1}{f_{tot,MC}} \ln R_1, \quad (4.17)$$

where 1 represents uniformly distributed random numbers in the open interval (0,1) generated in each event selection.

To determine which event will occur in the current iteration, one more random number R_2 from an open interval (0,1) is defined, then the event to take place in the corresponding iteration is chosen by the rule:

$$\begin{aligned} \text{Collision event: } & f_{tot,MC} R_2 \leq f_{coll,MC} \\ \text{Droplet event: } & f_{coll,MC} \leq f_{tot,MC} R_2 \leq f_{tot,MC} \end{aligned} \quad (4.18)$$

4.2 Micro-processes

4.2.1 Droplet deposition and drying

Atomization of binder and deposition of droplets on the particle surfaces are complex processes. In the atomization process, the liquid binder is atomized by compressed air into fine droplets and then sprayed in the bed. The size of droplets is determined by various parameters e.g., the pressure and flow rate of atomizing air, the viscosity and flow rate of binder and the type of nozzle. Here, the atomized droplets are assumed mono-dispersed, and the size of droplets is estimated by [136]:

$$d_d = 51 d_{ori} Re^{-0.39} We^{-0.18} \left(\frac{\dot{m}_b}{\dot{m}_a} \right)^{0.29}, \quad (4.19)$$

with

$$Re = \frac{\rho_b u_r d_{ori}}{\mu_b}, \quad (4.20)$$

and

$$We = \frac{\rho_b u_r^2 d_{ori}}{\sigma_{ten,b}}. \quad (4.21)$$

where d_{ori} is the discharge orifice diameter of nozzle, u_r is the air to liquid relative velocity, $\sigma_{ten,b}$ is the surface tension of binder, and \dot{m}_b and \dot{m}_a are the mass flow rates of binder and atomizing air, respectively.

There are three possibilities after the droplets leave the nozzle: overspray, rebound and successful deposition. Overspray describes the situation of droplets entrained by the fluidization gas flow before entering the bed. During the flight of droplets from the nozzle to the bed, the droplets undergo drying by the hot air, which may lead to overspray. The second possibility is the rebound of droplets. During the flight, the outer shell of droplets is solidified and may inhibit the deposition of droplets on the particle surface [121]. For simplification, the overspray and rebound of droplets are neglected, which means that all droplets are successfully deposited on the particle surfaces. It is also assumed that the equilibrium shape of droplets is attained immediately after the collision of droplets and particles. As shown in Figure 4.5, a deposited droplet should form a spherical cap with the equilibrium contact angle θ , the radius of spherical cap r_{cap} and the initial height of spherical cap $h_{cap,0}$. The equilibrium contact angle θ depends on the interfacial tensions between the contact surface and the sprayed liquid. When the contact angle is fixed, the radius and the initial height of the spherical cap are:

$$r_{cap} = \left(\frac{3V_d}{\pi} \frac{\sin^3 \theta}{2 - 3 \cos \theta + \cos^3 \theta} \right)^{1/3}, \quad (4.22)$$

with

$$V_d = \frac{\pi}{6} d_d^3. \quad (4.23)$$

Finally, the initial height of spherical cap $h_{cap,0}$ is

$$h_{cap,0} = r_{cap} \left(\frac{1 - \cos \theta}{\sin \theta} \right). \quad (4.24)$$

In the random droplet deposition process, three random numbers are generated and used to determine which particle, which sector on the selected particle and which position in the selected sector shall be used to deposit the droplet, respectively. Similar to previous work, the selection of particles is based on the surface area, which means the particles having a larger diameter are more likely to obtain a droplet than the smaller particles [88]. The selected position is marked as one to show the existence of the droplet, which is used to determine the type of collision. Meanwhile, two matrices are generated and used to record the height of deposited droplets and the age of deposited droplets, respectively.

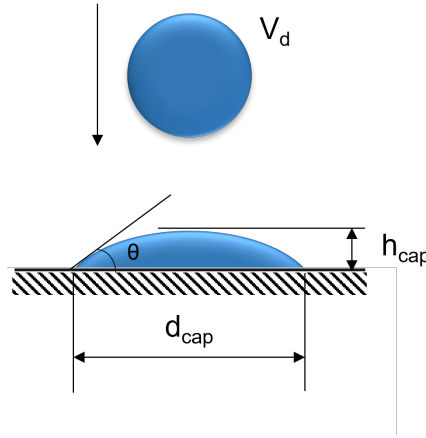


Figure 4.5: Deposition of droplet on the particle surface.

As mentioned above, the overspray is neglected. Therefore, the droplets drying takes place only after the deposition has finished. With the proceeding of the fluidization process, the deposited droplets undergo drying with time t . The height of spherical caps shrinks until they solidify. From the mass balance, the molar amount of water N_w contained in the droplet holds:

$$\frac{dN_w}{dt} = A_{cap}\beta\frac{\rho_g}{\tilde{M}_g}(\tilde{y}^* - \tilde{y}_g) \quad (4.25)$$

with

$$A_{cap} = \frac{2\pi h_{cap}^2}{1 - \cos\theta}, \quad (4.26)$$

and

$$\tilde{y}^* = \frac{P_v^*}{P}, \quad (4.27)$$

where A_{cap} is the area of deposited cap, β is the gas-side mass transfer coefficient calculated as shown in Appendix A, ρ_g is the mass density of gas, \tilde{M}_g is the molecular weight of gas, \tilde{y}^* is the vapor molar fraction at saturation condition, \tilde{y}_g is the actual vapor molar fraction in the gas and P_v^* is the saturation vapor pressure of the gas calculated from the adiabatic saturation temperature as shown in Appendix A.

Meanwhile, the number of moles of water N_w can be also described by:

$$N_w = \frac{\rho_w}{\tilde{M}_w}V_{cap}, \quad (4.28)$$

with

$$V_{cap} = \pi h_{cap}^3 \left[\frac{1}{1 - \cos \theta} - \frac{1}{3} \right], \quad (4.29)$$

where ρ_w is the mass density of water, \tilde{M}_w is the molecular weight of water and V_{cap} is the volume of the deposited cap.

By combining Equation 4.28 and Equation 4.29 and taking the first derivative, it holds:

$$- \frac{dN_w}{dt} = 3 \frac{\rho_w}{\tilde{M}_w} \pi \left[\frac{1}{1 - \cos \theta} - \frac{1}{3} \right] h_{cap}^2 \frac{dh_{cap}}{dt}. \quad (4.30)$$

Then, the complete mass balance is derived by combining the Equations 4.25 to 4.27 and Equation 4.30:

$$- \left[\frac{1}{1 - \cos \theta} - \frac{1}{3} \right] \frac{dh_{cap}}{dt} = \frac{2}{3} \frac{\rho_g}{\rho_w} \frac{\tilde{M}_w}{\tilde{M}_g} \beta \left(\frac{P_v^*}{P} - \tilde{y}_g \right). \quad (4.31)$$

Finally, the change of this height with time is calculated by:

$$h_{cap} = h_{cap,o} - \frac{2}{3} \frac{\rho_g}{\rho_w} \frac{\tilde{M}_w}{\tilde{M}_g} \frac{\beta}{1 - \cos \theta} \left(\frac{P_v^*}{P} - \tilde{y}_g \right) \left[\frac{1}{1 - \cos \theta} - \frac{1}{3} \right]^{-1} t. \quad (4.32)$$

4.2.2 Particles collisions

In a collision event, two individuals are selected randomly to execute the binary collision. In order to decide the colliding sections, two random numbers are generated according to the available section number of each particle. After the sections have been selected, two more random numbers are generated to decide the colliding positions according to the number of positions in each section. To save simulation time, the type of colliding is first checked with the status of positions stored in the matrix. Only when the collision is a wet-dry or wet-wet collision, which means at least one selected position contains a droplet, the Stokes criterion is checked to determine if the collision is successful or not. As discussed in Chapter 2, the Stokes number St and the critical value St^* are:

$$St = \frac{2m_{agg}u_{coll}}{3\pi\mu d_{agg}^2}, \quad (4.33)$$

and

$$St^* = \left(1 + \frac{1}{COR} \right) \ln \frac{h}{h_a}. \quad (4.34)$$

The collision usually takes place between two particles of different sizes. The harmonic mean values of the masses and diameters are used in the calculation. The harmonic mean values are:

$$m_{agg} = \frac{2m_{agg1}m_{agg2}}{m_{agg1} + m_{agg2}}, \quad (4.35)$$

and

$$d_{agg} = \frac{2d_{agg1}d_{agg2}}{d_{agg1} + d_{agg2}}, \quad (4.36)$$

where m_{agg1} , m_{agg2} and d_{agg1} , d_{agg2} are the masses and diameters of the selected particles in the collision, respectively.

Another key factor in the Stokes criterion is the collision kinetic energy, or rather the collision velocity. To estimate the collision velocity, the same method presented by Dervede is used in this work [134]. The collision velocity u_{coll} is calculated as:

$$u_{coll} = u_{agg,1} + u_{agg,2}, \quad (4.37)$$

where $u_{agg,1}$ and $u_{agg,2}$ are the velocities of the two collision partners. By assuming a normal distribution of the velocity, the relative velocity is calculated as:

$$u_{p,j} = |\bar{u} + \sigma_u r_n|, \quad (4.38)$$

where \bar{u} is the mean relative velocity calculated from Equation 4.14; r_n is a normally distributed random number in the open interval (0,1) and σ_u is the standard deviation of the velocity set to $10\bar{u}$. The same setting was used in previous work by Rieck [88].

4.2.3 Breakage

Breakage of formed agglomerates is a typical phenomenon, which can significantly decrease the particle growth rate in an agglomeration process. In a collision event, if the solid or liquid bridge is not strong enough to withstand the kinetic energy of collision, the agglomerates can break. According to Tan et al. [137], the breakage mechanisms can be classified into three types: fragmentation, attrition and binary breakage. In the fragmentation breakage, the agglomerate is completely reduced to its primary particles, which means all brigades in the agglomerate break. In the attrition breakage, the agglomerate breaks to give a single particle of size comparable to that of the primary particles, reducing the agglomerate diameter slightly. In the binary breakage, the agglomerate breaks into two smaller agglomerates that may contain several primary particles each. In previous work, different binary breakage models have been used in the Monte Carlo model. Terrazas-Velarde [126] used the Stokes deformation number to predict the limit size of the agglomerates, which was developed by Tardos et al. [138]. The Stokes deformation number St_{def} is the ratio of the externally applied kinetic energy to the energy required for deformation:

$$St_{def} = \frac{\rho_{agg} u_{coll}^2}{2\sigma_s}, \quad (4.39)$$

with

$$\rho_{agg} = (1 - \varepsilon_{agg})\rho_{pp}. \quad (4.40)$$

where σ_s is the agglomerate strength, and ρ_{agg} is the density of agglomerate.

In work presented by Terrazas-Velarde, it is assumed that the agglomerate breaks when the Stokes deformation number St_{def} is beyond the critical Stokes deformation number St_{def}^* . Therefore, the growth limit of particle size is characterized by $St = St^*$ while the rupture limit by $St_{def} = St_{def}^*$. Here, the critical Stokes deformation number St_{def}^* is set to be equal to the critical Stokes number St^* . Finally, the maximum diameter of agglomerates $d_{agg,coal}^*$ is calculated as

$$d_{agg,def}^* = \frac{9\mu}{(1 - \varepsilon_{agg})\rho_{pp}u_{coll}}St^*, \quad (4.41)$$

where ε_{agg} is the porosity of agglomerate.

Furthermore, Dervedde improved this breakage model by considering the orientations of collisions and the distinction between liquid and solid bridges [134]. In an unsuccessful collision, the kinetic energy of the collision is denoted by ΔE_{break} . The binding energy W_{bridge} of each solid bridge is

$$W_{bridge} = \sigma_{ts}V_{bridge}, \quad (4.42)$$

where σ_{ts} is the tensile strength of the bridge, and V_{bridge} is the volume of the bridge.

The binding energy of each bridge in both colliding particles is sorted from the smallest to the largest with number from 1 to N_{bridge} . When the following criterion is reached, the bridges from 1 to j break:

$$\Delta E_{break} > \sum_{j=1}^{N_{bridge}} W_{bridge,j}. \quad (4.43)$$

Depending on the morphology of agglomerates, Singh and Tsotsas [139] proposed a breakage model which considers the mean coordination number MCN and the porosity of agglomerates. In the model, the agglomerate strength is calculated directly by:

$$\sigma_s = \frac{9\mu u_{coll}MCN(1 - \varepsilon_{agg})^2}{4d_{agg}\varepsilon_{agg}}. \quad (4.44)$$

The MCN and porosity of the agglomerates can be influenced by process parameters (e.g. fluidization air temperature, mass fraction of binder) and the properties of agglomerates (e.g. number of primary particles) and lead to different breakage behaviors. In their work, the critical Stokes deformation number St_{def}^* is assumed to be equal to twice the critical Stokes number St^* .

However, there are restrictions of above breakage models. The first restriction is that the breakage of agglomerates only takes place when the particle size grows above a specific value, which is obviously inconsistent with the real processes. Another restriction is that all the agglomerates are limited to a specific size, which means that no agglomerate can grow larger than the maximum size.

Another method, used by Rieck et al. [88], assumes a constant breakage rate in the course of collisions, which is a simple and fast method. For an unsuccessful collision, a random number is generated. If the generated random number is below the pre-set breakage rate, one of the colliding particles is randomly selected, and then a bridge (wet or dry) on the selected particle is selected randomly to break. The corresponding droplet of the broken bridge is assigned to the particle it was deposited in the droplet deposition event. If the selected particle is a primary particle, no breakage will occur. Figure 4.6 shows the fragments (one wet and one dry) of an agglomerate with three primary particles (marked by particle 1, 2 and 3) and two bridges (marked by bridge 1 and 2) as an example. In the breakage, the bridge is randomly chosen by using a uniformly distributed random number generated according to the number of bridges. Depending on the selected bridge, different particles are formed. For the agglomerate with three primary particles, there are two scenarios. If bridge 1 is selected, a single particle (particle 1) and an agglomerate (consisting of particle 2 and 3) are formed. The single particle has three dry spots on its surface, and the agglomerate has one wet bridge, one wet spot on the surface of particle 2 and a dry spot on the surface of particle 3. If bridge 2 is selected, particle 3 becomes a single particle that has one wet spot and one dry spot on its surface. The agglomerate consists of particle 1 and 2, which has two dry spots on the surface of particles 1 and a wet spot on the surface of particle 2. In both scenarios, if the bridge is wet, the deposited droplet information is preserved, and the drying of the droplet continues, which means that the wet spot may still contribute to a new successful collision event before it has been finally dried. The information about the broken particle will be updated, keeping the newly produced particles in the simulation box. By using this method, the breakage of agglomerates can also occur when the agglomerates are small, and the maximum size is not limited to a specific value. However, the distinction of particle size, bridges and collision velocity is not considered in this approach. Regardless of the number of primary particles (above one) in the selected particle, only one bridge breaks in each collision. The dry and wet bridge selection has equal probability in the selection of bridges.

In the present work, we use the constant breakage rate method. The value of the breakage rate is obtained by visually fitting simulation results to experimental results for the batch reference experiment (shown in Chapter 6). It is then kept constant and applied to all simulations of this work.

4.2.4 Equivalent particle size

The growth rate of particle size is the main feature of an agglomeration process, which is used to characterize particle growth behavior. However, the information about particles in the Monte Carlo simulation is stored and processed in numbers (i.e., number of

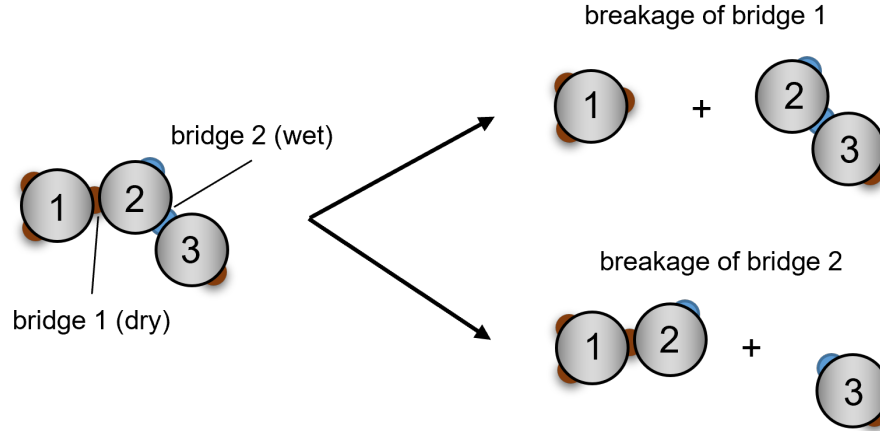


Figure 4.6: Breakage of an agglomerate with three primary particles.

primary particles in each agglomerate), which cannot be compared with the experimental results directly. Therefore, the relationship between the number of primary particles per entity and the particle diameter is required to convert the information from particle number into particle size. In previous work, this relationship was established by assuming a constant porosity of the agglomerates regardless of the primary particle number and process parameters [86, 88]. In order to improve it, a model proposed by Singh and Tsotsas [122] is used in this work. Instead of assuming a constant porosity, the model considers the change in agglomerate porosity with different sizes and process parameters:

$$d_{agg} = 1.291 d_{pp} \left(\frac{N_{pp,agg}}{K} \right)^{1/D_f}, \quad (4.45)$$

with

$$K = 5.323 - 1.4802 D_f, \quad (4.46)$$

where D_f is the fractal dimension, and $N_{pp,agg}$ is the number of primary particles in a single agglomerate.

The fractal dimension D_f was correlated by the experimental data achieved from X-ray tomography by Dadkhah et al. [63]:

$$D_f = 0.0105 T_g - 0.067 X_b + 2.13, \quad (4.47)$$

where T_g is inlet gas temperature in °C, and X_b is the sprayed binder mass fraction.

The relation of particle size and primary particle number for Exp. Ref is shown in Figure 4.7 as an example. It can be seen that, due to the discrete nature of the particle system and the assumed mono-dispersity of the primary particles in the simulation, the calculated diameter of the agglomerates can only be specified at values above 0.20 mm.

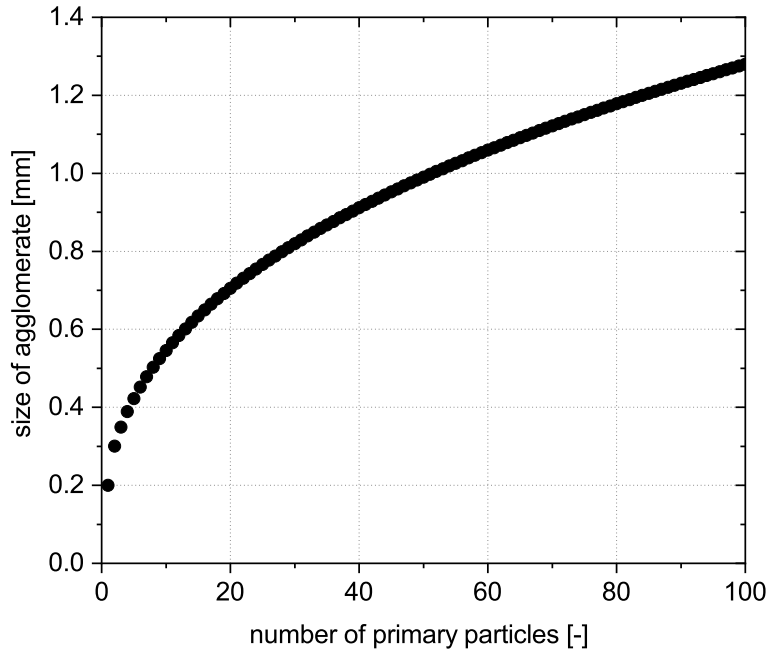


Figure 4.7: Relation of particle size and primary particle number for Exp. Ref.

With the size of each agglomerate in the simulation box, the cumulative density related to the particle volume Q_3 and particle number Q_0 can be obtained. Then, these data can be further calculated into the Sauter mean diameter d_{32} by Equation 3.4 and the normalized PSD by Equation 3.3 for better comparison.

4.3 Particle flow event in continuous process

As shown in Figure 4.2, the particle flow event is a necessary event in a continuous process. Depending on the types of fluidized beds used in experiments, different sub-events take place in the particle flow event. When the model is used to simulate the continuous agglomeration process in the cylindrical fluidized bed with a single process chamber, the feed of primary particles and discharge of products (primary particles or agglomerates) are the sub-events considered (detailed in Chapter 6). When the model is used to simulate the continuous agglomeration process conducted in a horizontal fluidized bed with multiple process chambers, the feed of primary particles and discharge of products, as well as the particle exchange between different simulation boxes, are the sub-events that need to be considered (detailed in Chapter 7).

Chapter 5

Experimental study of continuous agglomeration process in a horizontal fluidized bed

This chapter is an extended version of Du et al. [81]. In this chapter, the results of the continuously operated agglomeration process in a horizontal fluidized bed with different parameters are presented. The conducted experiments were divided into two series. In the first series, the fluidization air temperature, the feed rate of primary particles, and the binder mass fraction and spray rate were varied to study the influence of each parameter on the process behavior. In the second series, the configuration of internal and outlet weirs was changed to study the influence of different weir configurations. The samples were characterized by Camsizer, and then the Sauter mean diameter and PSDs were compared to show the process behaviors. The change in bed mass was calculated by the pressure drop and presented. Meanwhile, the RTDs of some experiments were measured and compared to show the influences of internal and outlet weir configurations.

5.1 Experimental plan

As listed in Table 5.1, two series of experiments were conducted. In the first series, the process parameters were changed. To be specific, the fluidization air temperature (Exp. T1 and T2), primary particle feed rate (Exp. F1 and F2), binder flow rate (Exp. S1 and S2) and binder mass fraction (Exp. B1 and B2) were varied. The experiment with air temperature 80 °C, feed rate 400 g/min, spray rate 77 g/min and binder mass fraction 4 % is considered as the reference experiment. All the experimental results are then compared with the reference experiment Exp. Ref to study the influence of each process parameter on the process behavior. In the second series, the process parameters were kept the same as Exp. Ref and only the internal and outlet weir configurations were changed. By the installation of internal weirs (Exp. W1 and W2) with different gaps, the fluidized bed was divided into four separated process compartments, which can significantly change the particle flow behavior in the bed. Similar approaches have been used in previous work for different processes, for example, see Satija and Zucker [140] and Bachmann et al. [75]. By the installation of outlet weirs at different heights

(Exp. Ref-L and W1-L), the bed mass and the separation effect were changed. Besides the particle growth behavior, the particle RTD in the second series was studied. For all experiments, the atomizing pressure was kept constant at 1 bar. The peristaltic pump was set according to the desired spray rate, and the actual spray rate was determined by weighing the binder tank after the experiment had been finished. The superficial gas velocity was set to 1.0 m/s for all experiments.

At the start of the experiment, the empty plant was heated up for at least 30 minutes until the pre-set temperature was reached. Then, the atomizing air used by the nozzles was switched on and adjusted to the desired pressure. The jet flow from nozzles can influence the particle flow behavior and the bed mass significantly. Therefore, the atomizing air was started prior to the feed of particles to avoid its sudden influence on the bed mass. Depending on the height of the outlet weir, 5-7 kg of primary particles were fed into the bed simultaneously from the rotary valve to promote the establishment of the starting bed mass. At the same time, the feeder was started together with the inlet and outlet rotary valve. The particle flow rate at the outlet was continuously measured with a balance (Sartorius AG, Sartorius IS 150 IGG-H). When the particle flow rate at the outlet became equal to the feed rate and remained stable, steady state without binder spray had been reached. Bed mass at this moment was considered as the starting bed mass. When this steady state had been reached, the binder pump was turned on to start the binder spray. After the spray had been started, the particle flow rate at the outlet decreased suddenly due to the fast growth of particle size in the first few minutes. With increased bed mass and particle size, the outlet flow rate increased gradually. Finally, when the steady state was reached according to the criteria presented in Section 3.3.4, both the bed mass and particle size fluctuated in a small range. During the experiment, samples were taken periodically from the outlet in bottles, as well as from the sampling probe installed in the bed. To measure the particle residence time distribution, tracer particles were injected into the bed via the filling tube after 80-90 minutes of spray time, and samples were taken at the outlet more frequently. Depending on process behavior and operability, experiments were run for 140-180 minutes. After the last sample had been taken, the binder spray and feed were stopped together with the heater and ventilators. Afterward, the samples were measured offline with Camsizer to determine the PSD. The samples taken after the tracer injection were measured for the particle RTD by using the method described in Section 3.3.5.

5.2 Results and discussion

5.2.1 Reference experiment

In Figure 5.1, the evolution of particle size for Exp. Ref is illustrated. The particle size is one of the most important indicators to show the particle growth behavior in an agglomeration process. Similar to a batch-wise process shown in previous work, almost a linear growth of particle size of bed samples and product samples at a high rate is seen in the first 20 min after the process was started. However, the following growth

Table 5.1: Experimental plan.

Experiment	$T_{g,in}$	\dot{M}_f	Spray rate	X_b	Internal weir	Gap height	Outlet weir height
[-]	[°C]	[kg/min]	[g/min]	[%]	[-]	[mm]	[mm]
Ref	80	0.4	77	4	-	-	200
T1	70	0.4	78	4	-	-	200
T2	100	0.4	78	4	-	-	200
F1	80	0.3	78	4	-	-	200
F2	80	0.5	79	4	-	-	200
S1	80	0.4	98	4	-	-	200
S2	80	0.4	53	4	-	-	200
B1	80	0.4	77	5	-	-	200
B2	80	0.4	76	3	-	-	200
Ref-L	80	0.4	78	4	-	-	135
W1	80	0.4	80	4	underflow	5	200
W2	80	0.4	79	4	underflow	10	200
W1-L	80	0.4	78	4	underflow	5	135

58

pattern of the continuous process is different from a batch-wise process after 20 min. The particle growth rate decreases gradually from 20 min until approximately 110 min of process time. Afterward, the particle size fluctuates in a small range with the mean size of bed samples around 0.64 mm and product samples around 0.53 mm, but it does not increase significantly. We can see that the size of product particles is always smaller than that of bed samples, which shows the separation effect between bed samples and product samples. During the continuous process, only particles fluidized over the top of the outlet weir can be discharged from the bed. The fluidization height of large particles is lower than that of small particles, which makes the larger particles more difficult to be discharged. Another reason is that the jets from the nozzles can bring newly fed primary particles from the inlet to the outlet directly. Especially when no internal weir is installed, some of the primary particles travel fast from the inlet to the outlet without finding an opportunity to get a droplet or collide with other particles. This is also observed in the PSDs (shown in Figure 5.3) and particle residence time distributions (shown in Figure 5.6).

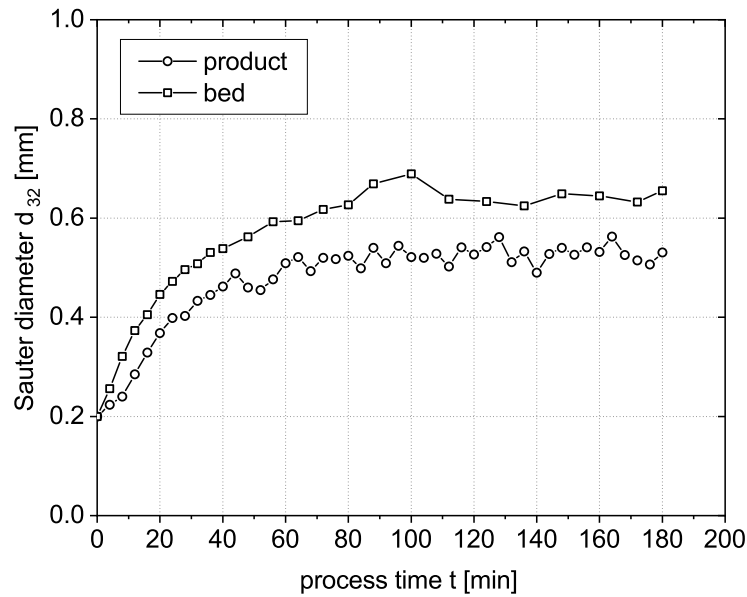


Figure 5.1: Evolution of particle size.

In Figure 5.2, the change in bed mass and the weight of products during the process are shown. The starting bed mass is around 8.30 kg. Similar to the particle growth pattern, the bed mass increased fast in the first 20 min to about 10.90 kg. Since the fluidization height of larger particles is lower, the fast increase in particle size leads to the increase of bed mass. From 20 min until the end of the process, bed mass increased slowly with fluctuations to 11.80 kg of final bed mass. The continuous but slow increase of bed mass is caused by the accumulation of large particles in the bed. In the course of this process, more large particles stay in the bed, which increase the risk of bed collapse. Due to the high viscosity of the binder, wet particles may stick on chamber walls and nozzle caps, and they need to be frequently removed. This can prevent the

formation of large chunks of particles and the blockage of nozzles, which would lead to the bed collapse and increase the fluctuations of bed mass. The total process time was 180 minutes, and about 66.64 kg of products were achieved at the outlet.

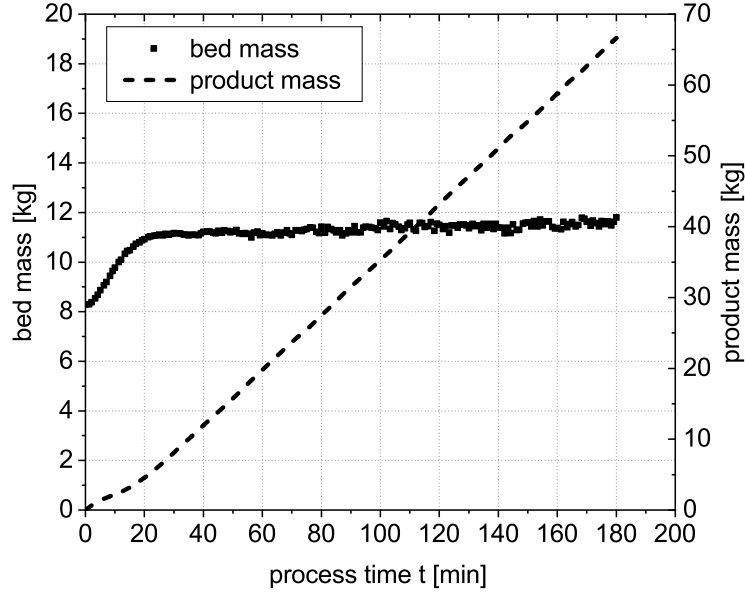


Figure 5.2: Development of bed and product mass.

The PSDs of selected bed and product samples that were taken at different process times are shown in Figure 5.3. For each of the selected samples, especially the samples taken in the early period of the process, two peaks can be seen. The first peak is at a size of around 0.20 mm, which equals the size of primary particles, meaning that a certain amount of primary particles are still in the samples both from bed and product. In the first agglomeration stage, agglomerates were formed by primary particles, and a fast initial growth rate was seen due to the fast agglomeration of primary particles. After a few agglomerates had been formed, the growth rate decreased, and the process went to a secondary stage of slower growth. The coexistence of primary particles (0.20 mm), agglomerates (0.20-1.0 mm), and large agglomerates (> 1.0 mm) leads to a very wide particle size distribution. Compared to the bed samples, product samples always have a higher peak at a size of 0.20 mm, which shows the separation effect clearly. With the growth of particles, the height of peaks at 0.20 mm in product samples decreases fast until 64 min of process time. After this, the height of the peak keeps almost constant. As mentioned above, this is partially led by the jets from nozzles, which bring new primary particles from the inlet to the outlet directly. The PSDs at 148 min and 180 min are almost identical, which means that the PSD is also kept stable when the process is in the steady state.

As described in Section 3.3.4, the coefficient of variation CoV of particle size and the accumulation of bed mass growth rate $GR_{k,acc}$ from process time t_k to the end of the process are used to determine the steady state. All steady state data for the experiments

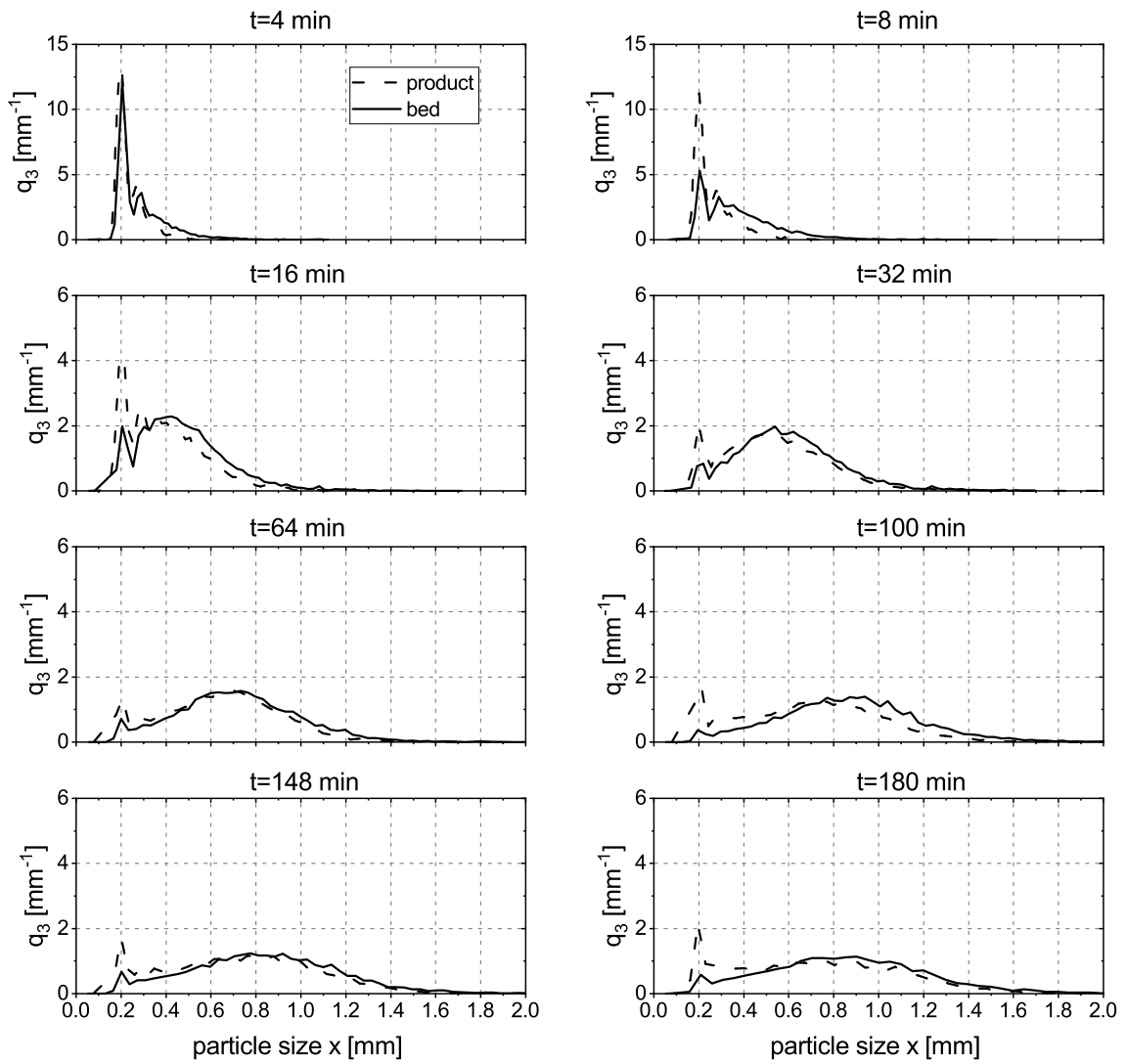


Figure 5.3: PSDs of selected samples.

in this chapter are listed in Table 5.3. For the reference experiment, the steady state criteria $CoV < 5\%$ and $GR_{k,acc} < 3\%$ are used. Only when the CoV of both product samples and bed samples is lower than 5% and $GR_{k,acc}$ of bed mass is lower than 3%, it is considered that the process has reached the steady state. As shown in Figure 5.4, according to the calculated CoV , the size of product samples reaches the steady state after 136 min of process time, whereas the size of bed samples reaches the steady state after 72 min of process time. Furthermore, according to the calculated $GR_{k,acc}$, the bed mass reaches the steady state after 98 min of process time (shown in Figure 5.5). Finally, it is determined that this process reaches the steady state at 136 min.

By using the method described in Section 3.3.5, the particle RTD of Exp. Ref was measured (shown in Figure 5.6). Here, we see that the peak of tracer concentration reaches the highest point after 3 min of the tracer injection, which shows the fast movement of some particles from the inlet to the outlet. After fitting to the experimental results, the final Bo number is 0.00930 with the coefficient of determination $R^2 = 0.983$. A lower Bo number means higher dispersion in the system and a wider particle residence time distribution, which is closer to a well-mixed reactor. Similar results were observed in all experiments without internal weirs. Due to the similarities of these RTDs, only part of the experiments (Exp. T1, T2, F1 and F2) conducted without internal weirs were analyzed by respective measurements. Beside Exp. Ref, the figures are shown in Appendix B.1. Only the final calculated values are summarized in Table 5.2.

5.2.2 Effect of air temperature

In this series of experiments, the influence of fluidizing air temperature was studied. In order to compare with Exp. Ref, Exp. T1 and T2 were performed with reduced air temperature (70 °C) and increased air temperature (100 °C), respectively. Besides the fluidizing air temperature, the other parameters in Exp. T1 and T2 were kept the same as that used in Exp. Ref.

Exp. T1 was performed at a lower fluidizing gas temperature (70 °C). As depicted in Figure 5.7, the evolution of particle size, the change in bed mass and the PSDs of selected samples are used to describe the process behavior. Compared to Exp. Ref, we see that a higher growth rate with larger particle size was achieved from the beginning of the experiment with lower air temperature; fluctuations of particle size are large (shown in Figure 5.7a). After 100 minutes of process time, some increase in particle size is still observed. The process was stopped at 180 minutes with fluctuating particle size of approximately 0.84 mm in the bed and 0.66 mm in the product. An increase in particle size, as shown in Figure 5.7b, results in higher bed mass. The process was started with bed mass at about 8.30 kg, similar to Exp. Ref, a fast increase took place in the first 20 min to approximately 11.40 kg. But here, a continuous increase in bed mass is observed from 100 to 140 min, caused by the continual growth of particle size. Determined by the criteria, this process reached the steady state after 143 min. Finally, the process was stopped at 180 min with about 12.50 kg of bed mass. In the experiments, it was observed that the outlet mass flow rate could be used as an indicator of particle growth

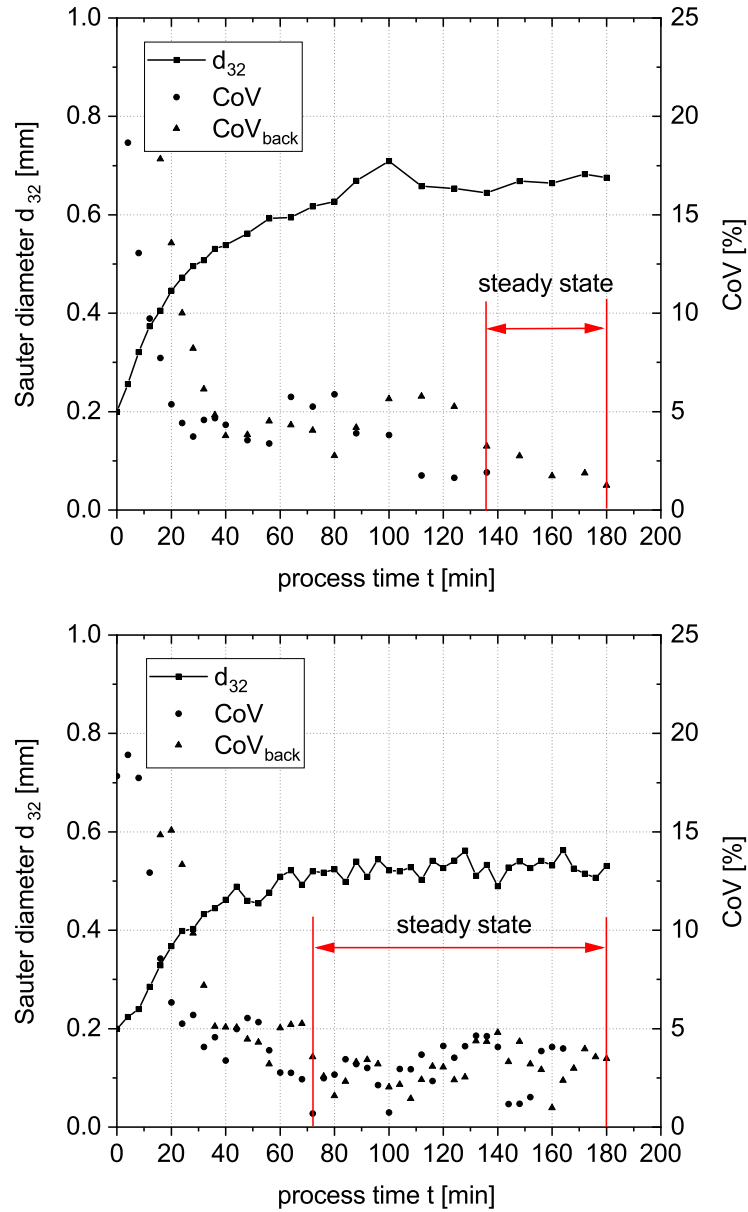


Figure 5.4: Steady state determination from the evolution of particle size: Samples from bed (top), samples from products (bottom).

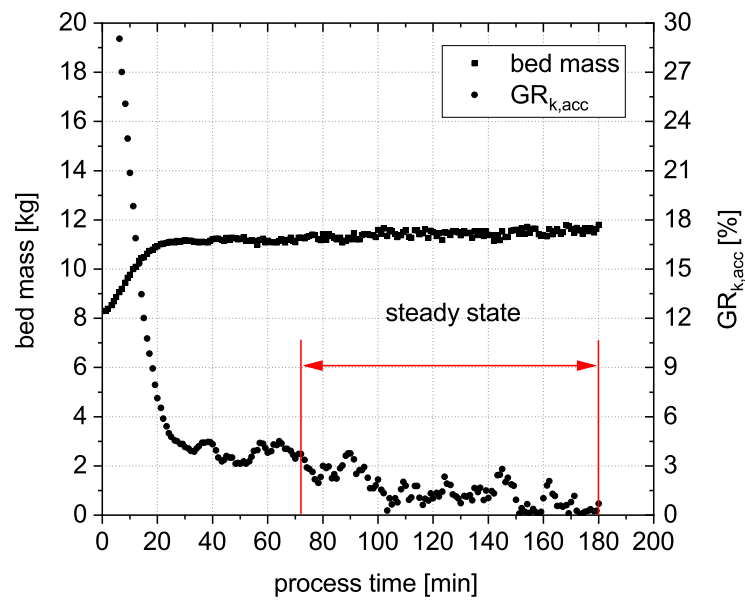


Figure 5.5: Steady state determination from the development of bed mass.

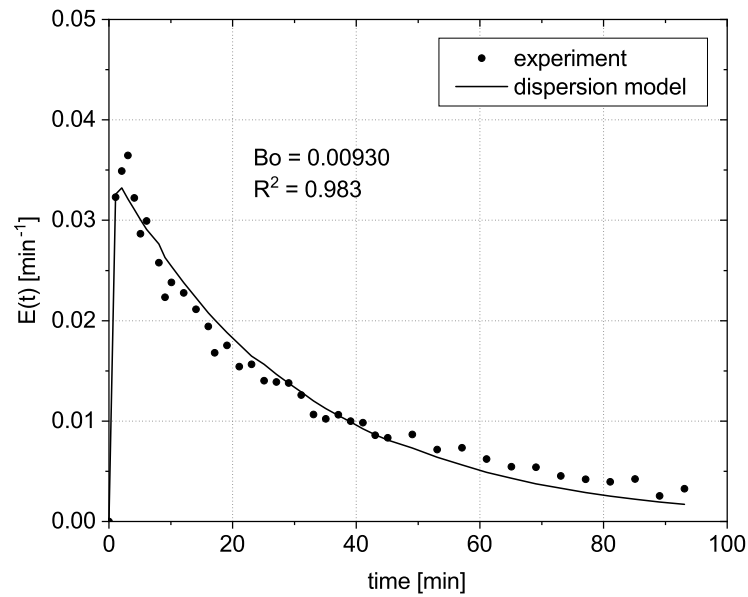


Figure 5.6: Measured and calculated RTD

and process stability. The continuous growth of bed mass bears the risk of defluization before the attainment of a stable steady state. PSDs at 16 min and 180 min are shown in Figure 5.7c. Compared to Exp. Ref, we can see a much lower peak at 0.20 mm, but a wider PSD. Corresponding to the higher agglomeration rate, more primary particles undergo successful collisions.

Exp. T2 was performed at a higher fluidizing gas temperature (100 °C). In Figure 5.8a, it is clear that smaller particles (bed: 0.51 mm, product: 0.39 mm) were achieved in the steady state, which reached faster (after 95 min) and with less fluctuations in particle size. As illustrated in Figure 5.8c, higher peaks that stand for the original particles are observed. In this case, the higher air temperature decreased the agglomeration rate, resulting in fewer opportunities for primary particles to agglomerate with others. As shown in Figure 5.8b, the process was started with about 6.80 kg and stopped with 10.60 kg after 160 minutes. Compared to Exp. Ref and T1, a lower bed mass was seen from the beginning (due to stronger electrostatic effects) to the end (due to smaller particle size) in this experiment. Compared to Exp. T1, it can be seen that there is only minor increase in the bed mass from 100 min to the end of the process. The smaller particles are easier to be discharged from the bed. This decreases the accumulation of large particles and the risk of bed collapse.

Experiments were also conducted with the air temperature further reduced to 60 °C (results shown in Appendix B.2). A strong and continuous growth of particle size and bed mass was observed in the experiment, which finally led to defluization. Over-wetted particle chunks usually start to form at the center of spray cones right under the spray nozzles where the most binder is deposited.

The influence of air temperature has been studied before in batch operated agglomeration processes [64, 86]. In these investigations, a similar influence of air temperature is seen, that higher air temperature decreases the particle size. As reported in Table 5.3, the growth rate increases with the decrease of temperature in Exp. T1 to 0.0215 mm/min, and it decreases with the increase of temperature in Exp. T2 to 0.0148 mm/min. For better comparison, the average Sauter mean diameter in the steady state and its standard deviation are plotted in Figure 5.9. At higher temperatures, binder droplets evaporate and shrink faster after having been sprayed from the nozzle, which decreases the height of sessile droplets. Some spray droplets may not even find a chance to hit the particle surface, which means that overspray is also increased at higher air temperatures. In both cases, the number of particle collisions leading to agglomeration decreases. Moreover, the bed mass is also influenced by particle size. With smaller particles, the bed mass is lower, which means that the bed mass can become steady faster when the feed rate is fixed. In turn, it can promote the stability of particle size, which finally leads the process to steady state.

5.2.3 Effect of particle feed rate

In this series of experiments, the influence of particle feed rate was studied. In order to compare with Exp. Ref, Exp. F1 and F2 were performed with a reduced particle feed

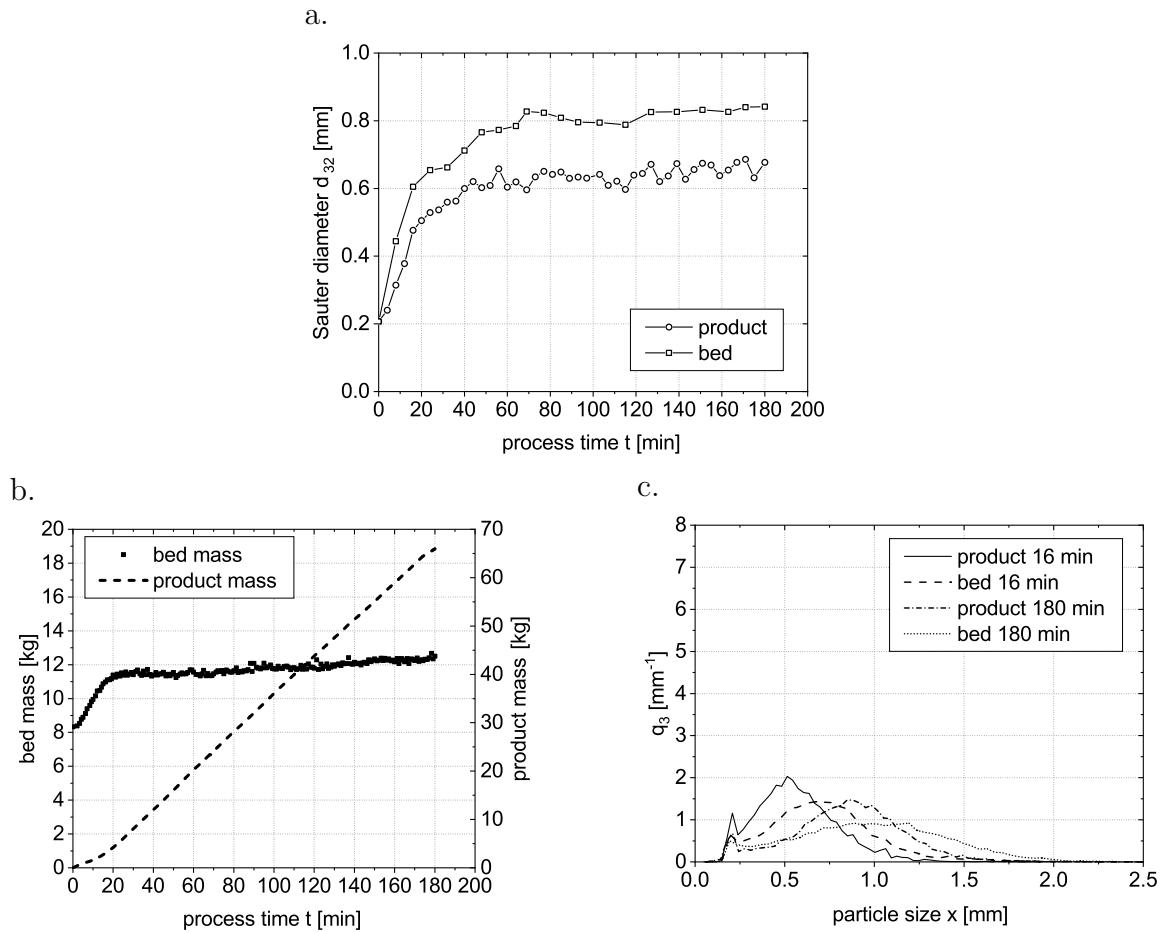


Figure 5.7: Results of Exp. T1: a. evolution of particle size; b. development of bed and product mass; c. PSDs of selected samples.

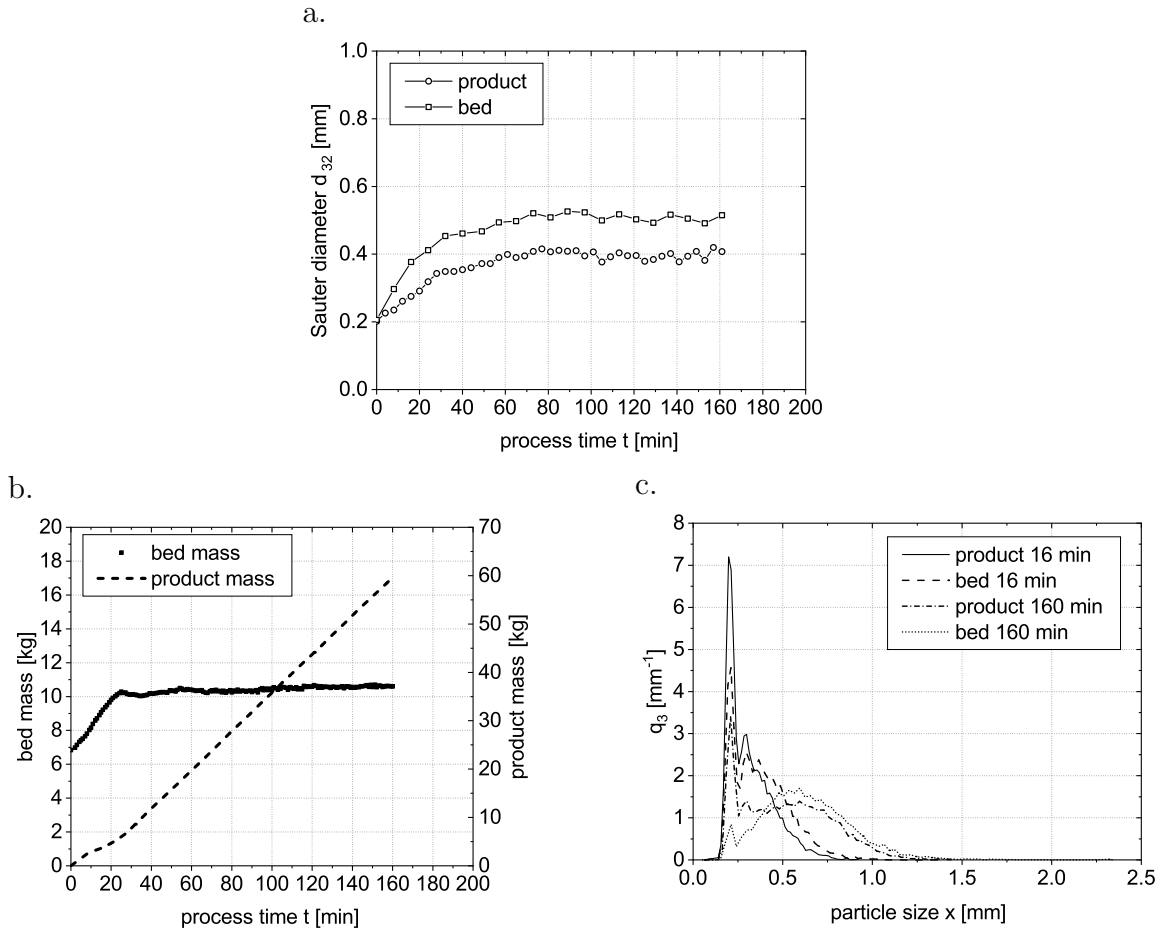


Figure 5.8: Results of Exp. T2: a. evolution of particle size; b. development of bed and product mass; c. PSDs of selected samples.

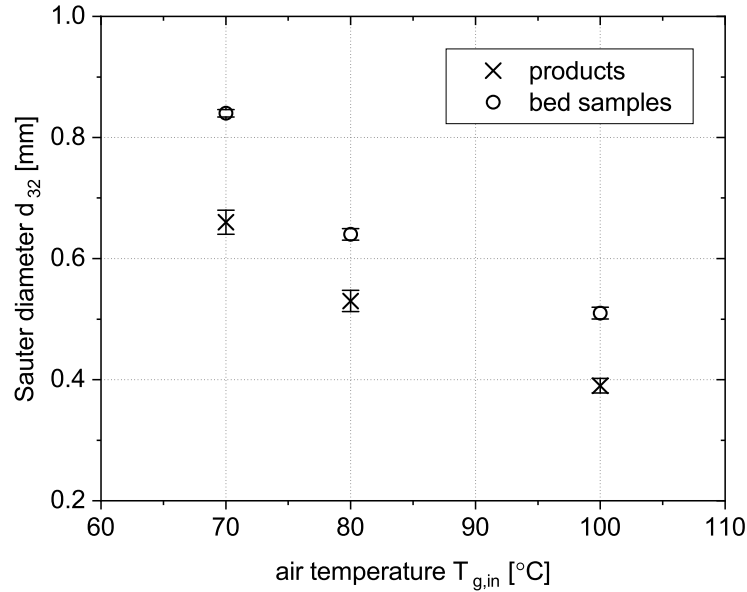


Figure 5.9: Comparison of particle Sauter mean diameter and standard deviation for Exp. Ref, T1 and T2.

rate of 300 g/min and an increased feed rate of 500 g/min, respectively. Besides the particle feed rate, the other parameters in Exp. F1 and F2 were kept the same as that used in Exp. Ref.

Compared to Exp. Ref, we can see for Exp. F1 in Figure 5.10a a similar growth pattern, but with larger particles in both bed and product samples. After 120 min of process time, a trend of increasing particle size could still be seen. The steady state was reached after 150 of process time. Finally, the experiment was stopped at 178 min with a particle size of approximately 0.70 mm in the bed and 0.59 mm in the product. The change in bed mass during the process is shown in Figure 5.10b. Compared to Exp. Ref, the starting bed mass is lower due to the lower feed rate. At the start of the process, a lower feed rate brings lower starting bed mass in the steady state before spraying. After the spray had been started, a lower increase rate but a longer period of growth was seen because of the larger particle size. Consequently, the bed mass ended at approximately 12.60 kg, which is even higher than in Exp. Ref. Similar to the trend of particle size growth, a slight but continual increase in bed mass was seen until the end of the experiment. In this situation, the risk of bed collapse increases with process time. The separation effect of the outlet weir exacerbates the accumulation of large particles, which results in a longer residence time of large particles. The PSDs of the selected samples are depicted in Figure 5.10c. Due to the larger particle size, lower peaks of the primary particles at 0.20 mm in all samples were seen, meaning that fewer primary particles were discharged directly from the bed. Meanwhile, the larger particle sizes lead to broader size distributions.

Exp. F2 was conducted with particle feed rate increased to 500 g/min. As shown in Figure 5.11a, slower growth of the particle size was seen from the beginning of the process. The final particle size is about 0.56 mm in bed and about 0.46 mm in the product, which is significantly lower than in Exp. Ref. Meanwhile, this process reached the steady state (after 95 min) faster than in Exp. Ref and T1. Finally, the process was run for 144 min. Compared to Exp. Ref, the starting bed mass is 9.18 kg, which is higher due to the higher feed rate (shown in Figure 5.11b). Despite the higher feed rate and starting bed mass, the bed mass of Exp. F2 at the end of the process is 11.27 kg, which is lower than in Exp. Ref. This results from the smaller particle size. Meanwhile, we see much higher peaks at 0.2 mm for the samples taken at 16 min and 144 min in Figure 5.11c than in Figure 5.10c. When the feed rate is increased, more particles are discharged directly without finding the opportunity to get a droplet.

As presented in Figure 5.12, the final particle size is decreased with increased feed rate and increased with decreased feed rate. When particle feed rate is decreased, the ratio of new particles to the binder is decreased, and particle mean residence time increases. Thus, there are more liquid bridges, and the particles should have more opportunities of colliding to form new agglomerates. However, the growth rate reported in Table 5.3 decreases with the decrease of feed rate from 0.0210 mm/min in Exp. F2 to 0.0140 mm/min in Exp. F1, respectively. The reason is that even though the feed rate was decreased, bed mass did not decrease much because of the larger particle size. This resulted in a much longer particle mean residence time, in which unsuccessful collisions with breakage of liquid and solid bridges decrease the efficiency of the binder. That is why a lower growth rate was achieved at the lower feed rate, even though larger particles were produced.

5.2.4 Effect of binder concentration

In order to study the influence of binder concentration (viscosity) on the process behavior, Exp. B1 and B2 were conducted with 5 wt. % and 3 wt. % HPMC water solutions, respectively. As mentioned in Chapter 3, binder viscosity is highly dependent on the concentration of dissolved HPMC. Besides the concentration of binder, the other parameters in Exp. B1 and B2 were kept the same as that used in Exp. Ref.

First, a binder mass fraction of 6 % was used. In that experiment, particle growth was very fast from the beginning of the process, and the process was terminated by bed defluidization in 30 minutes (results shown in Appendix B.3). Because of the rapid growth of the particles in the bed, the particle discharge rate at the outlet was too low, which means that most newly fed particles remained in the bed and grew fast. This resulted in an unbalance between particle feed rate and growth rate. For better operation, the binder mass fraction was decreased to 5 %, with other parameters kept constant. As shown in Figure 5.13a, with 5 % HPMC, we got a faster particle growth rate and larger particle size compared to Exp. Ref. The process was successfully run and stopped after 180 minutes with particle size at ca. 0.84 mm in the bed and 0.67 mm at the outlet. However, the steady state was not reached until the end of process. Seen

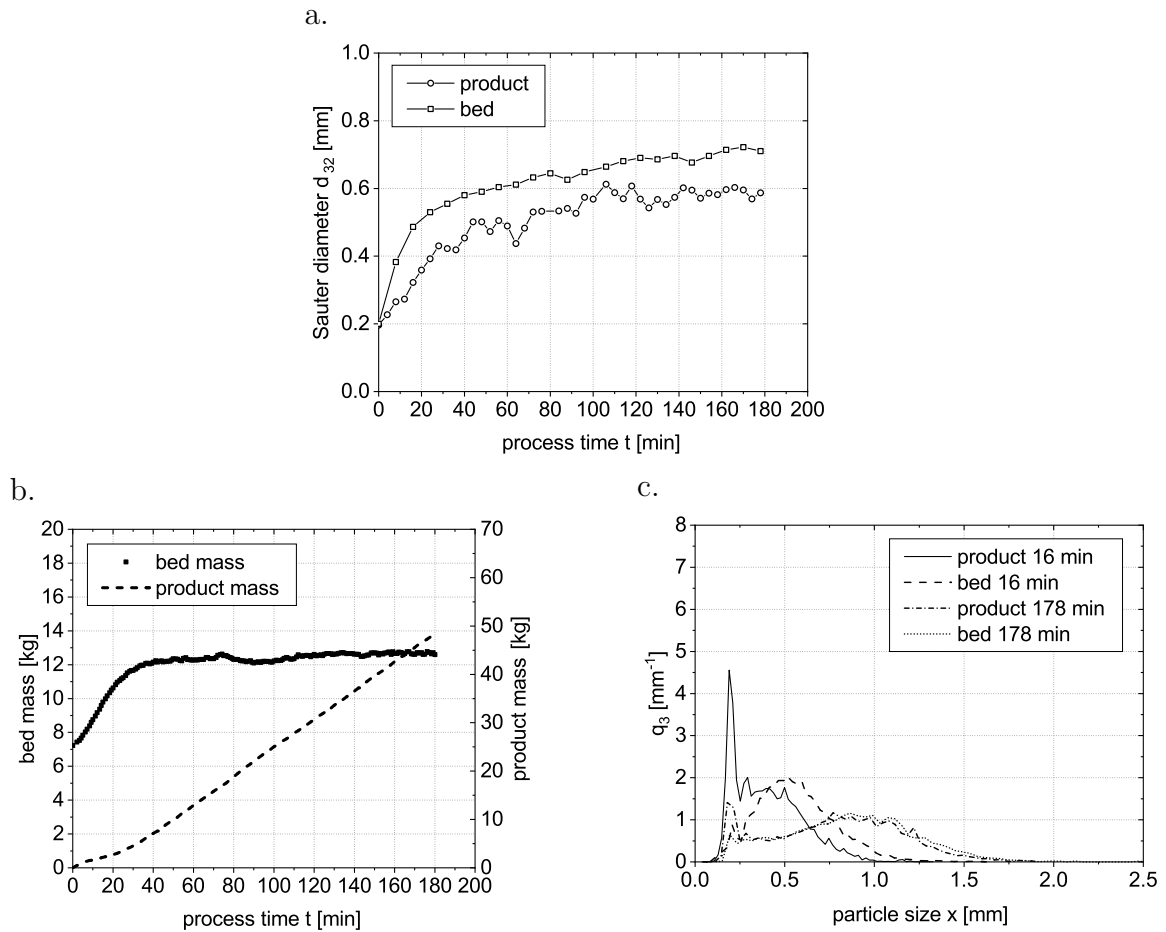


Figure 5.10: Results of Exp. F1: a. evolution of particle size; b. development of bed and product mass; c. PSDs of selected samples.

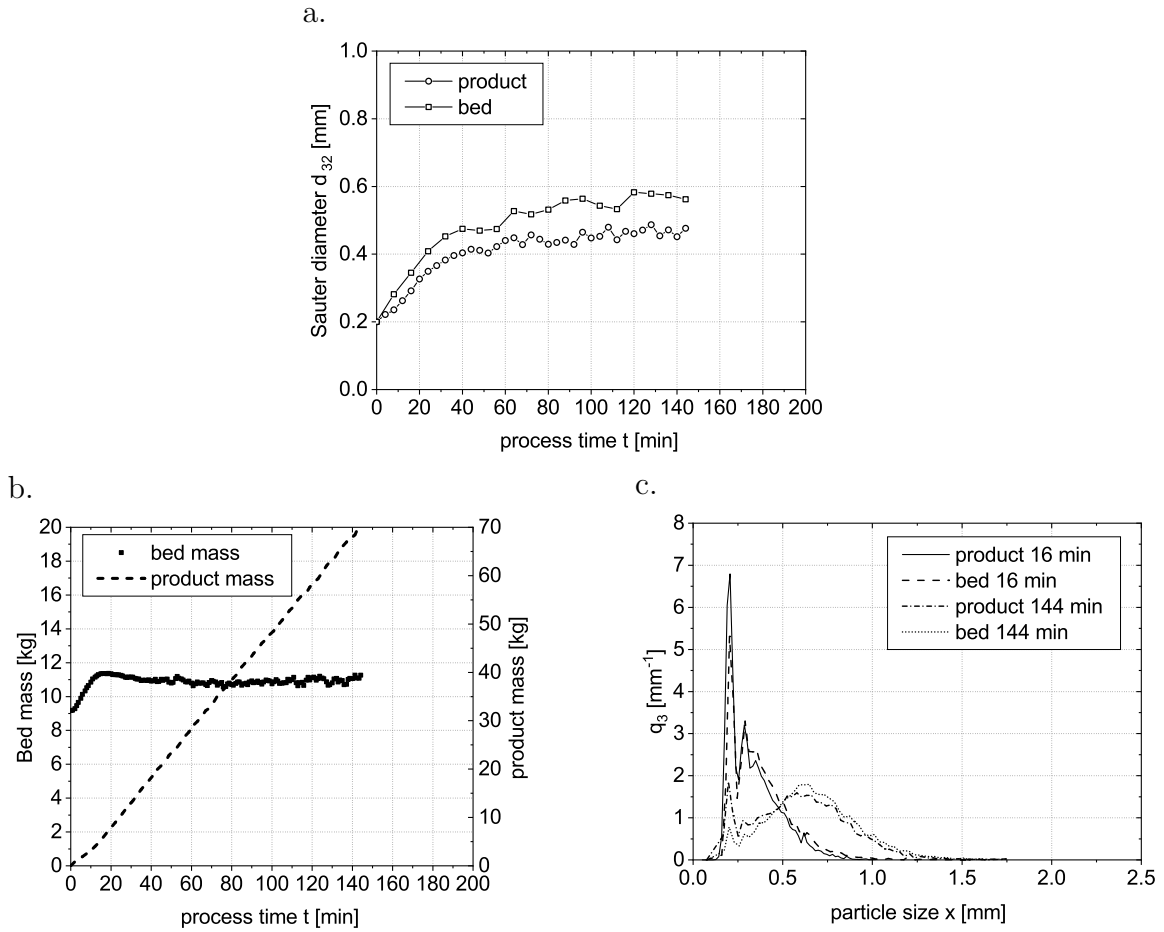


Figure 5.11: Results of Exp. F2: a. evolution of particle size; b. development of bed and product mass; c. PSDs of selected samples.

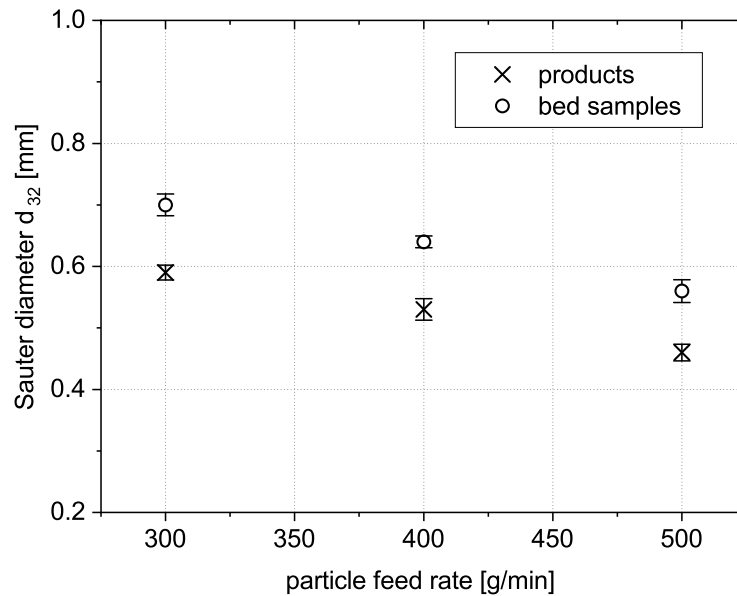


Figure 5.12: Comparison of particle Sauter mean diameter and standard deviation for Exp. Ref, F1 and F2.

from Figure 5.13b, the starting bed mass is 7.48 kg, which is similar to Exp. Ref due to the same feed rate. However, the bed mass at the end of the process is continuously increasing, even if slowly. Under this condition, with fixed air velocity, larger particles bring more defluidization risks to the system, as it is more difficult for larger particles to overcome the outlet weir and exit from the chamber. That is why we can observe a larger particle size difference between samples taken from the bed and the outlet with the growth of the particles. Seen in Figure 5.13c, larger particles and wider PSDs were achieved. The higher growth rate also resulted in fewer primary particles at the outlet (compared to Exp. Ref) when the process was stopped.

Figure 5.14a illustrates the evolution of particle size with binder at 3 % for Exp. B2. In this experiment, a much more moderate particle growth rate was achieved compared to Exp. Ref. Finally, the lower binder concentration resulted in a smaller particle size as well as a shorter time to steady state (120 min). The process was stopped after 180 minutes with a particle size of 0.52 mm and 0.43 mm in samples from the bed and the outlet, respectively. The starting bed mass is 7.42 kg which is almost equal to that of Exp. B1. However, due to the smaller particle size, the bed mass at the end of the process is 11.88 kg. In Figure 5.14c, smaller particles after 16 min and 180 min are apparent, as well as narrow particle size distribution. A high peak in the sample taken at 16 min from the outlet indicates that many newly fed particles come out from the outlet without having formed agglomerates due to a lower growth rate. After 30-40 min, bed mass enters the steady state with hardly any fluctuations.

For better comparison, the average Sauter mean diameters of the samples in steady state are presented in Figure 5.15. Since the steady state for Exp. B1 was not reached,

the sizes of the last taken samples are used in the figure. When the binder mass fraction is increased, the more viscous liquid layer can dissipate more collision energy. Meanwhile, the higher binder viscosity leads to larger droplets when the binder is atomized. These cause more collisions that can fulfill the Stokes criterion and, therefore, more agglomerates and higher growth rates are achieved. As shown in Table 5.3, the growth rates for Exp. B1 and B2 are 0.0211 and 0.0146 mm/min, respectively. But larger particles bring more defluidization risks to the system with fixed air velocity, as it is more difficult for bigger particles to overcome the outlet weir and exit from the chamber. That is why we have observed a larger particle size difference between samples taken from the bed and the outlet with the growth of the particles in Exp. B1. Meanwhile, higher binder viscosity results in a more serious partial clogging of spray nozzles by the glass beads, which usually leads to atomizing problems such as larger droplets and off-center spray. More fluctuations are also seen when the higher binder concentration is used.

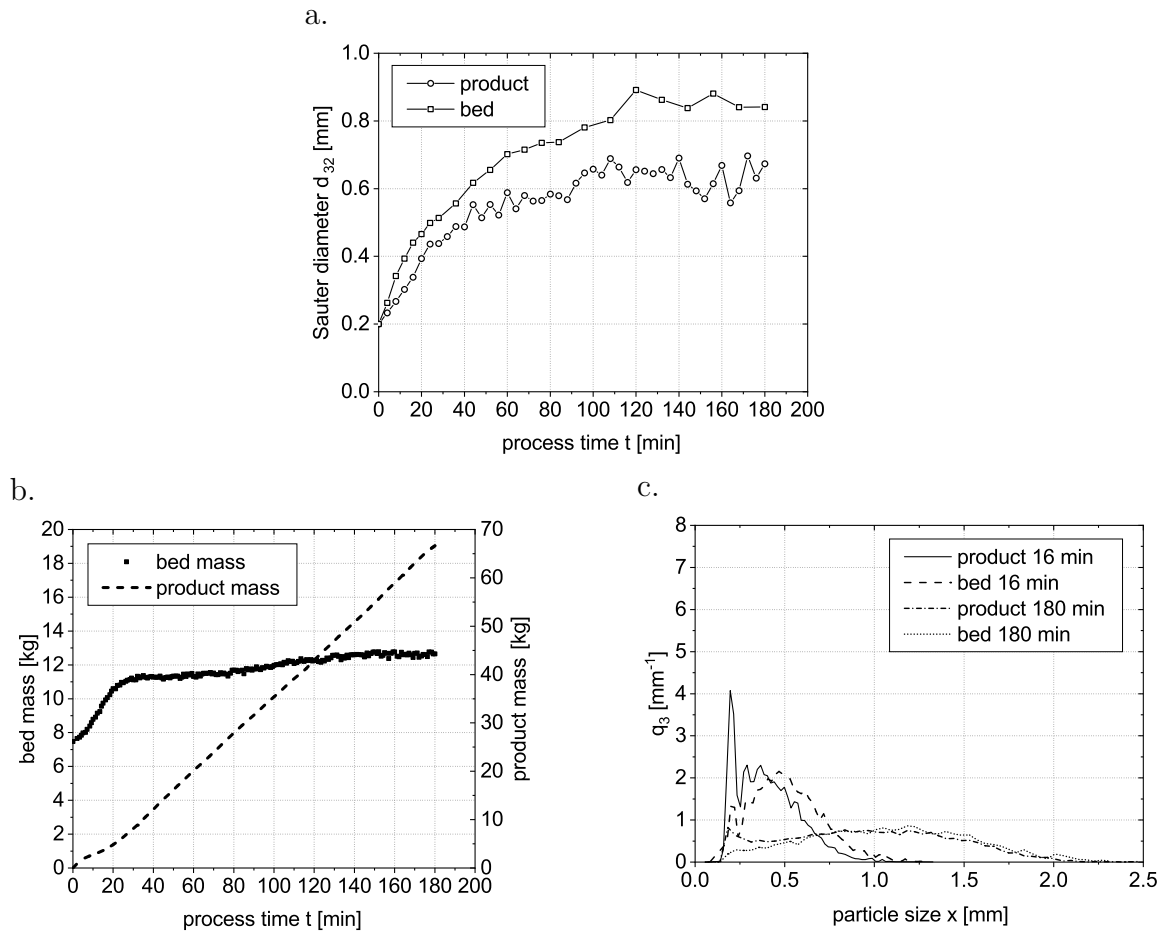


Figure 5.13: Results of Exp. B1: a. evolution of particle size; b. development of bed and product mass; c. PSDs of selected samples.

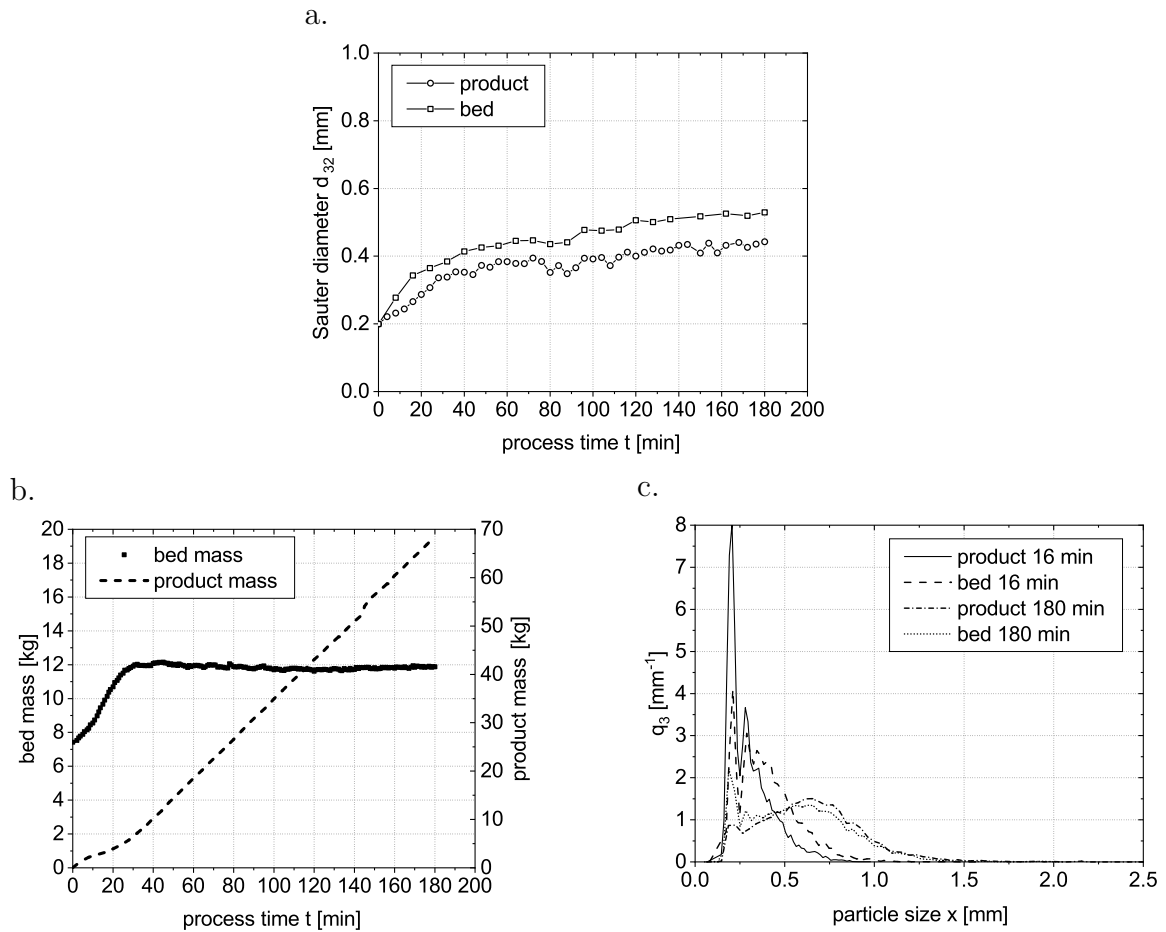


Figure 5.14: Results of Exp. B2: a. evolution of particle size; b. development of bed and product mass; c. PSDs of selected samples.

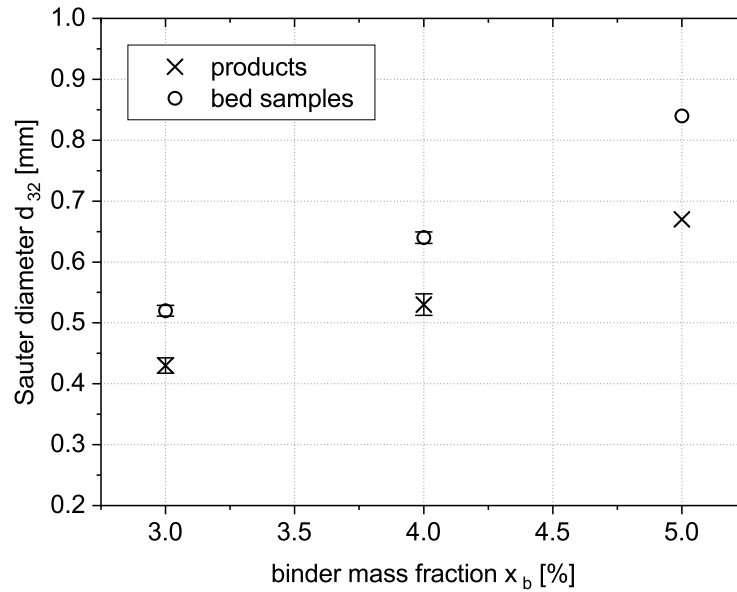


Figure 5.15: Comparison of particle Sauter mean diameter and standard deviation for Exp. Ref, B1 and B2.

5.2.5 Effect of binder spray rate

To investigate the influence of binder spray rate on the process behavior, Exp. S1 and S2 were conducted with the spray rate of 98 g/min and 53 g/min, respectively. The change in spray rate changes the ratio of binder to primary particles. Beside the spray rate, the other parameters for Exp. S1 and S2 were kept the same as that used in Exp. Ref.

In Figure 5.16a for Exp. S1, speedy growth of particle size was visible from the beginning of the process. From about 30 min to 60 min of process time, we see strong fluctuations of the particle size, which is caused by the partial clogging of the spray nozzles and the sticking of particles on the inner surface of the process chamber. Finally, due to defluidization, the process was terminated after 88 min of process time with the final particle size of 0.82 mm in the bed and 0.63 mm at the outlet. Similar to other bed defluidization situations, partial over-wetting in the spray area resulted in caking and bed collapse. As shown in Figure 5.16b, the starting bed mass is about 7.32 kg. With the growth of particle size, the bed mass increased fast in the first 30 min after the process was started. From 30 min to the end of the process, only a slight increase is seen. However, the particle size still grows fast. About 3 min before the end of the process, a sudden decrease in bed mass was seen in Figure 5.16b. The bed mass is calculated from the measured bed pressure drop. At defluidization, the pressure drop is significantly lower than the weight of bed mass. Therefore, the caking had already started 3 min before it was observed in this experiment. As shown in Figure 5.16c, due to the fast growth rate, the product sample taken at 16 min has a much lower height of the peak at 0.20 mm (primary particle size) compared to Exp. Ref. At 88 minutes,

when the process was terminated by defluidization, we see a notable decrease in outlet sample particle size. Because of fast agglomeration in the bed, only small particles which are still in fluidized status can be discharged. This also leads to a fast decrease in the discharge rate at the outlet.

When the binder feed rate was decreased to 53 g/min in Exp. S2, a much lower particle growth rate was seen. As illustrated in Figure 5.17a, the process was stopped after 138 min with a particle size of 0.37 mm in the bed and 0.32 mm at the outlet. After about 40 min of process time, no further significant increase in particle size was seen. Finally, it is determined to have reached a steady state after 80 min. Due to the smaller particle size, the final bed mass is 11.14 kg (Figure 5.17b). Though the particle size is smaller, a fast increase of bed mass in the first 20 min was observed, which is similar to Exp. Ref. Seen from Figure 5.17c, all selected samples contain a lot of primary particles with a size of 0.2 mm. With the decreased spray rate, fewer particles have the opportunity to get droplets deposited, and thus there are less successful collisions. Hence, more primary particles are seen in the bed samples and products.

The average Sauter mean diameters of the samples in steady state are presented in Figure 5.18. Since the steady state for Exp. S1 was not reached, the sizes of the last taken samples are used in the figure. When the binder spray rate is increased, the ratio of binder to particles is increased as well, which results in more particles having opportunities to get droplets on their surface and agglomerate with other particles. When the growth rate of the particle size is too high, the balance of agglomeration, breakage and feed of primary particles cannot be reached. At the given fluidization air velocity, too large particles cannot be fluidized. The caking typically starts from the area under the nozzles where most of the binder is deposited. The particle overwetting is exacerbated by the caking, and then it grows very fast. In a short time, the bed collapses. After the process had been terminated, we could see the formation of chunks right under the nozzles. A similar phenomenon was also observed in the batch operated processes. Bed collapse is one of the biggest challenges in running a continuous agglomeration process for a long period of time. In contrast, when the spray rate is decreased, much slower growth of particle size is achieved.

5.2.6 Effect of outlet weir height

In the previous series of experiments, we have seen a strong separation effect with the outlet weir at a height of 200 mm in all experiments. To investigate the influence of outlet weir height on the process behavior, Exp. Ref-L with outlet weir height decreased to 135 mm was conducted. Besides the outlet weir height, the other process parameters were kept the same as that used in Exp. Ref.

As depicted in Figure 5.19a, a similar growth pattern to Exp. Ref was observed. It is determined that the experiment reached the steady state after 100 min. Finally, the average Sauter mean diameter of bed samples and products are 0.62 mm and 0.56 mm, respectively (shown in Figure 5.20). Compared to Exp. Ref, we see a larger particle size at outlet, however, a smaller particle size for the bed samples. The differences

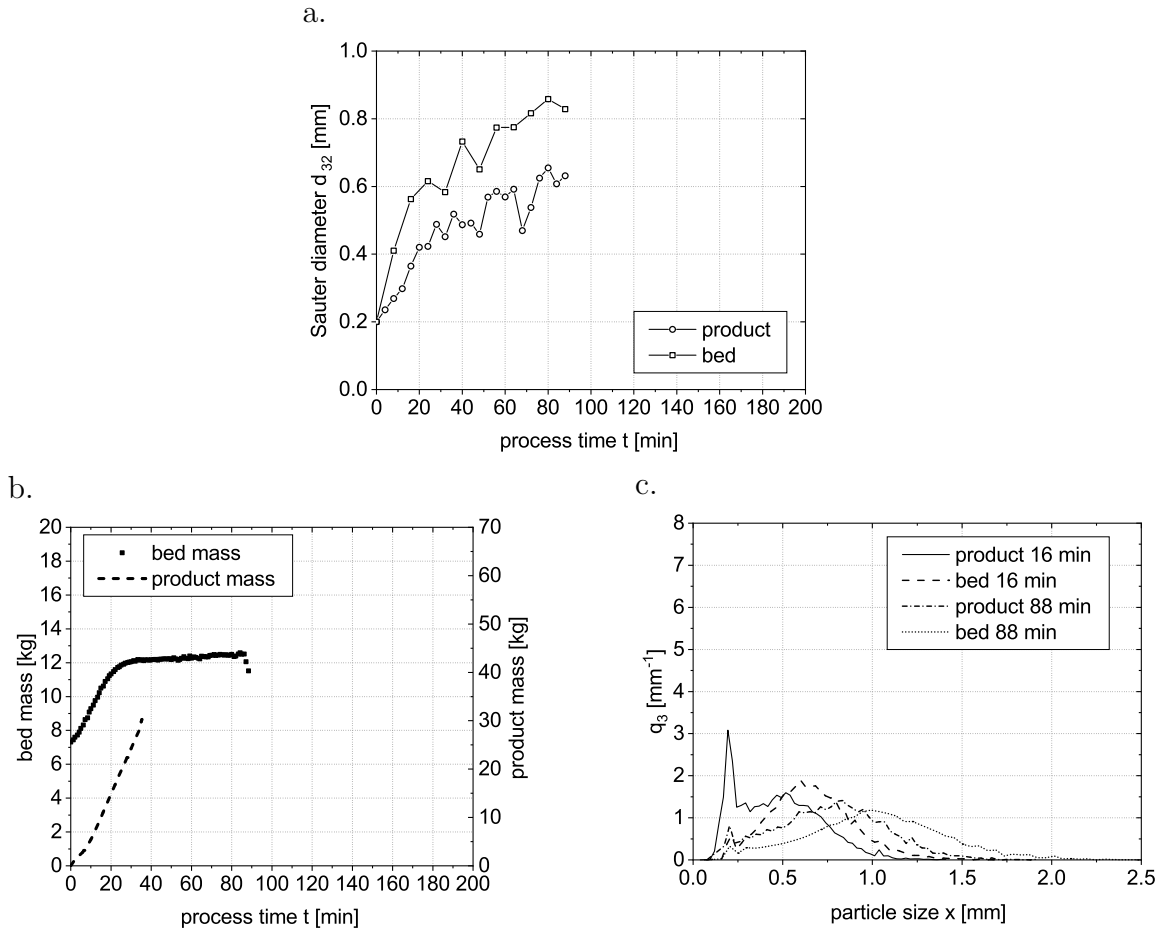


Figure 5.16: Results of Exp. S1: a. evolution of particle size; b. development of bed and product mass; c. PSDs of selected samples.

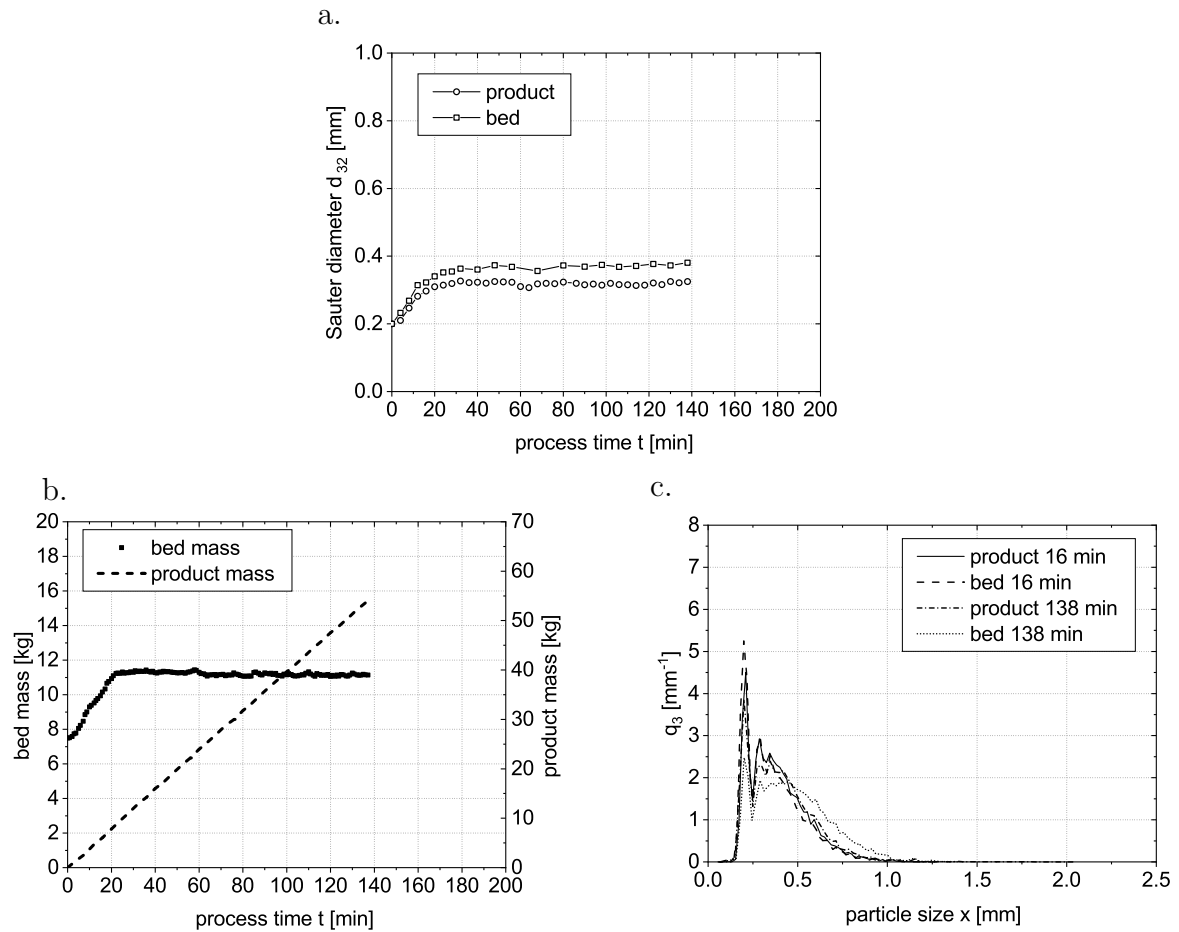


Figure 5.17: Results of Exp. S2: a. evolution of particle size; b. development of bed and product mass; c. PSDs of selected samples.

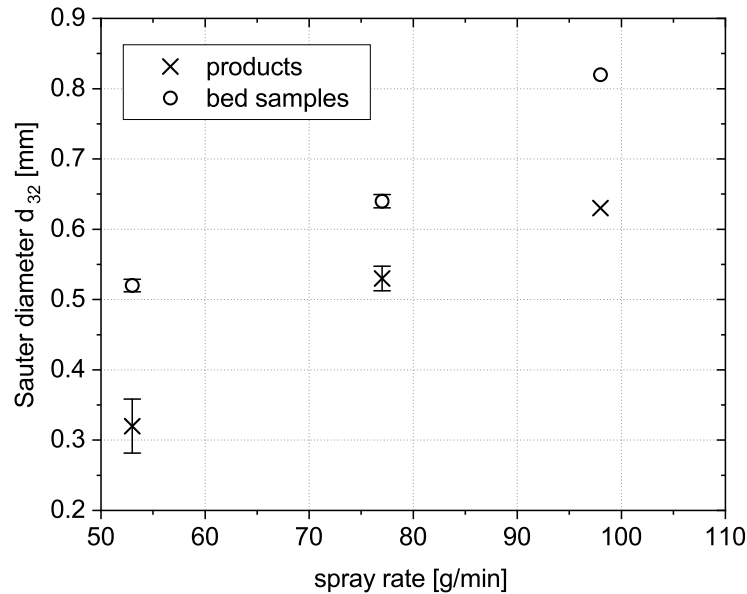


Figure 5.18: Comparison of particle Sauter mean diameter and standard deviation for Exp. Ref, S1 and S2.

in particle size between products and bed samples are smaller, which means the lower outlet weir height resulted in a weaker separation effect. Exp. Ref-L had a much lower bed mass at both the beginning (6.62 kg) and the end (7.96 kg) of the process (shown in Figure 5.19b). Because the bed height is set by the outlet weir, the bed mass was significantly decreased due to the decrease in bed height. The lower starting bed mass can explain why Exp. Ref-L had a higher growth rate at the beginning compared to Exp. Ref, but finally had similar a particle size at steady state. The weaker separation effect also can be seen in Figure 5.19c. Comparing the samples taken at the outlet and from the bed, we see a similar PSD, but the peak of primary particles was reduced a lot. When the lower outlet weir is employed, there is less difference between the starting bed mass and final bed mass, which results in a short time to reach the feed and discharge balance. This also helps the process to reach steady state faster. Meanwhile, the lower bed mass yields a shorter particle residence time. Compared to Exp. Ref, the size of product samples is increased slightly from 0.53 mm to 0.56 mm. However, due to a much shorter mean residence time, a much higher growth rate of 0.0286 mm/min is achieved in this experiment.

5.2.7 Effect of internal weirs

In all experiments, we have observed that the spray from nozzles has a strong influence on the flow behavior of particles in the process chamber. The nozzles are two-fluid nozzles, using compressed air to atomize the liquid into fine droplets. The high-speed air from nozzles enhances the axial movement of the particles significantly. Moreover, small particles can move very fast from the inlet to the outlet with the jets. To decrease

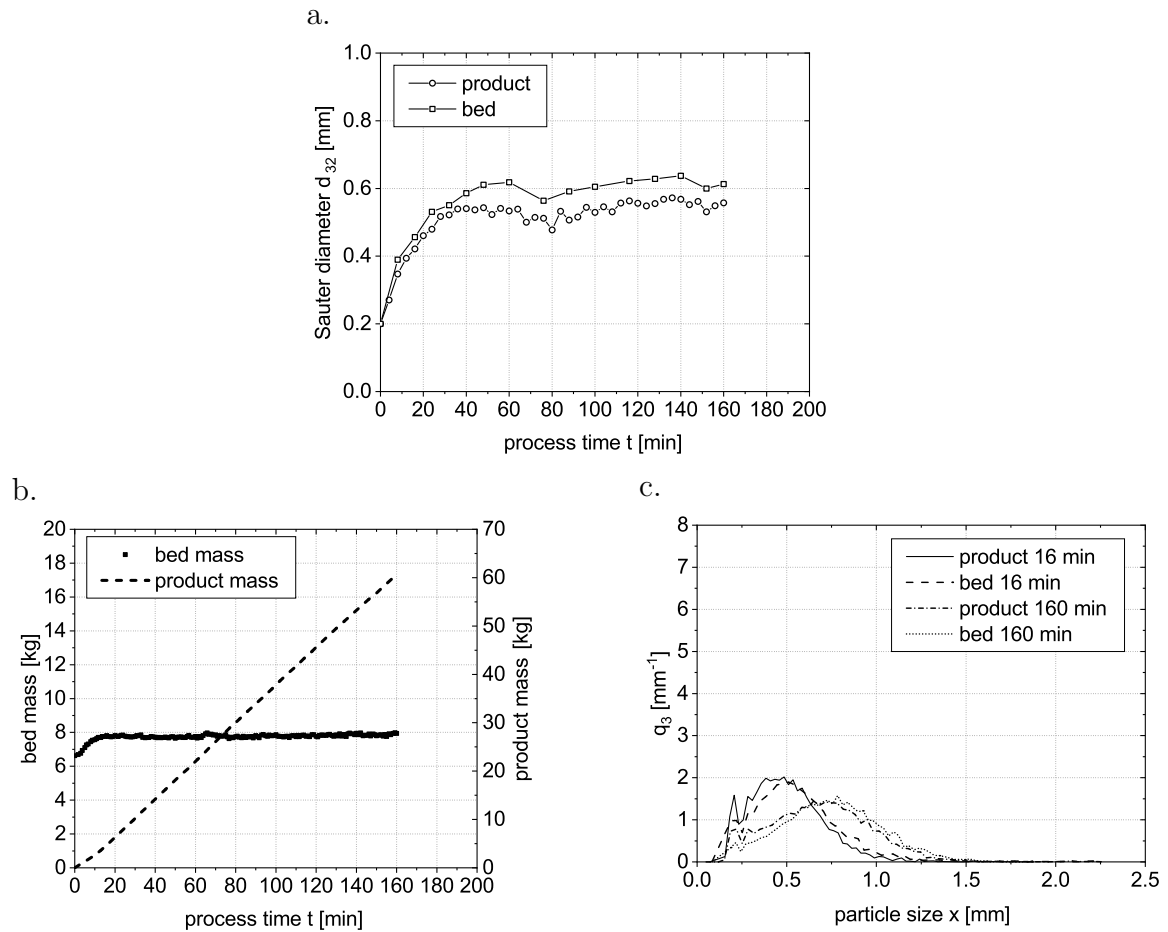


Figure 5.19: Results of Exp. Ref-L: a. evolution of particle size; b. development of bed and product mass; c. PSDs of selected samples.

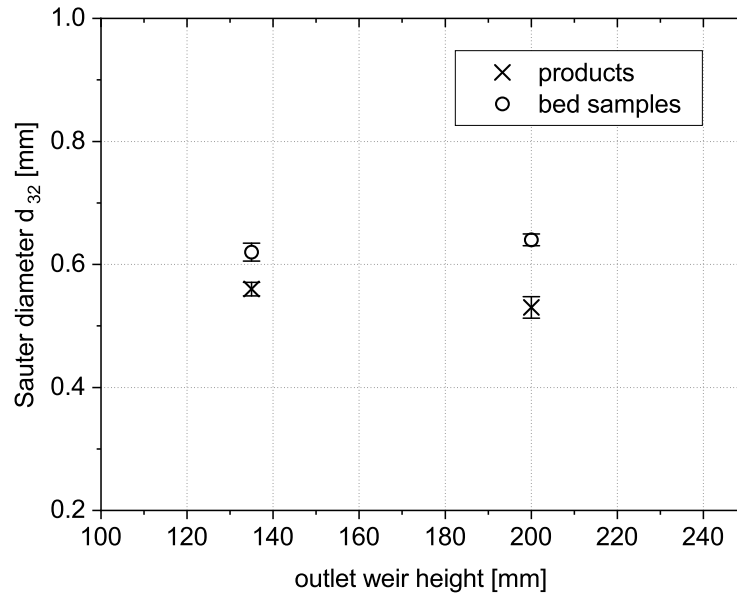


Figure 5.20: Comparison of particle Sauter mean diameter and standard deviation for Exp. Ref and Ref-L.

this effect, internal underflow weirs that have different gaps to the distribution plate were installed. Exp. W1 and W2 were conducted with internal weirs with 5 mm and 10 mm gap, respectively, with outlet weir at 200 mm, whereas other parameters were kept the same as that used in Exp. Ref.

From Figure 5.21a and Figure 5.22a, we see a similar growth behavior of both bed and outlet samples compared to Exp. Ref. However, as illustrated in Figure 5.24, more fluctuations were seen in Exp. W1 with a smaller particle size. This may be due to the smaller gap between the internal weirs and the distribution plate, which results in the larger agglomerates being more difficult to go through the gap. Compared to Exp. Ref, the separation effect of Exp. W1 and W2 was reduced significantly from 0.17 to 0.13 and 0.14. This also can be observed from the PSDs of selected samples shown in Figure 5.21c and Figure 5.22c. The peaks at 0.20 mm, which stand for the primary particles are decreased in the outlet samples. The values of starting bed masses and final bed mass of Exp. W1 and W2 are close (Figure 5.21b and Figure 5.22b). Compared to Exp. Ref, the starting bed masses of Exp. W1 and W2 are higher. When the process chamber is not separated, the fluidization of particles in chamber 4 is influenced by the jet from the other three chambers. Many small particles are blown up by the jets, which then have the possibility to be discharged directly from the outlet. Therefore, a higher starting bed mass was observed with internal weirs. With the growth of particles, the larger particles are more difficult to be entrained by the jets. Finally, we see a similar bed mass to Exp. Ref at the end of the process due to their similar particle size.

Comparing Exp. W1, W2 and Ref, we see that the separation effect is affected by the height of outlet weir and the high-speed atomizing air from nozzles. To eliminate these

influences, Exp. W1-L was conducted with a lower outlet weir at 135 mm and internal weirs. As depicted in [Figure 5.23a](#) and [Figure 5.24](#), respectively, the process reached the steady state after 92 min with a final particle size of about 0.56 mm both in the bed and at the outlet, which indicates that the separation effect is reduced to zero with this configuration. The process chamber compartments were separated by the internal weirs, and the outlet separation effect was further decreased by the lower outlet weir. Consequently, we see identical particle size in samples taken from the bed and from the outlet. Though the separation of the process compartments led to a higher starting bed mass at 7.08 kg, a similar final bed mass was achieved (shown in [Figure 5.23b](#)). In [Figure 5.23c](#), almost identical PSDs of the selected samples are seen, which also indicates the very weak separation effect.

Nozzle air flows fast in form of a jet to the distribution plate. Once the jet hits the plate, it turns its direction suddenly and can blow more small particles rather than large particles that may rise very high and be discharged directly from the bed. When the process chamber is separated by internal weirs, those can prevent the particles from overflowing. In this way, the internal weirs decrease the influence of the jets. Meanwhile, the height of the outlet weir affects the separation effect significantly. With a higher outlet weir, large particles are more difficult to be discharged, which leads to a stronger separation effect.

As mentioned above, all the experiments without internal weirs have a very small Bo value (summarized in [Table 5.2](#)), which means the process chamber is very close to a well-mixed reactor. There are some literature data and correlations available about particle residence time distribution in horizontal fluidized beds [[73–75](#), [141](#)], but none of them have been determined with spray jets. Without internal weirs, the jets from the nozzles spread the small particles used in the present work over the whole fluidization chamber. That is why a peak of the tracer concentration curve is observed in a very short period after the tracer has been injected; see, for example, Exp. Ref in [Figure 5.6](#). This also explains why we got a lot of particles at the outlet in their original size when the experiments were conducted without internal weirs. When internal weirs are installed, the process chamber is divided into four compartments. The internal weirs are high enough to prevent the particles from overflowing. Therefore, the axial movement of the particles is significantly restricted. Moving forward or backward, all particles need to go through the gap left open between the weir and distributor. In this case, axial dispersion decreases, and the Bodenstein number increases significantly. Comparing Exp. W1 and W2, we see a small increase in Bo when the smaller gap is applied. Further decrease in gap height would decrease the stability of the process even more.

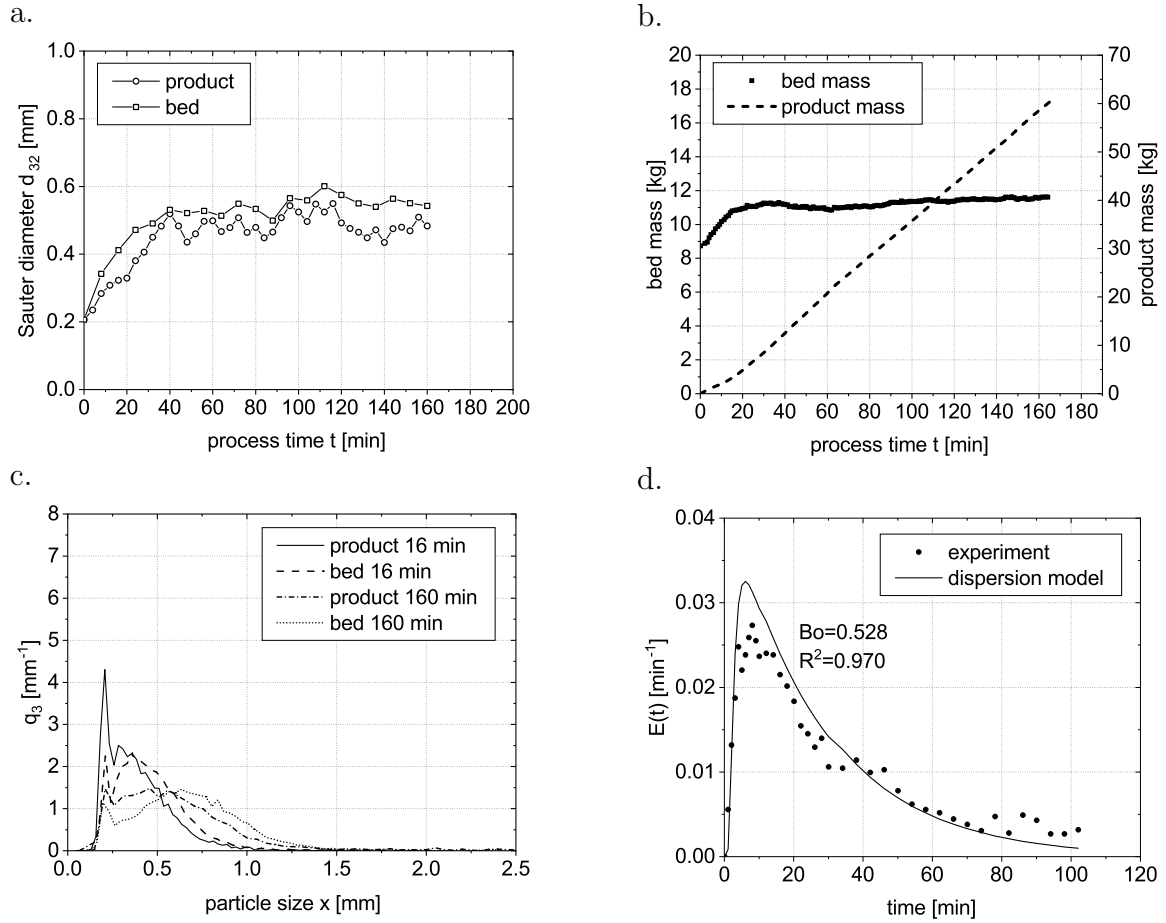


Figure 5.21: Results of Exp. W1: a. evolution of particle size; b. development of bed and product mass; c. PSDs of selected samples; d. measured and calculated RTDs.

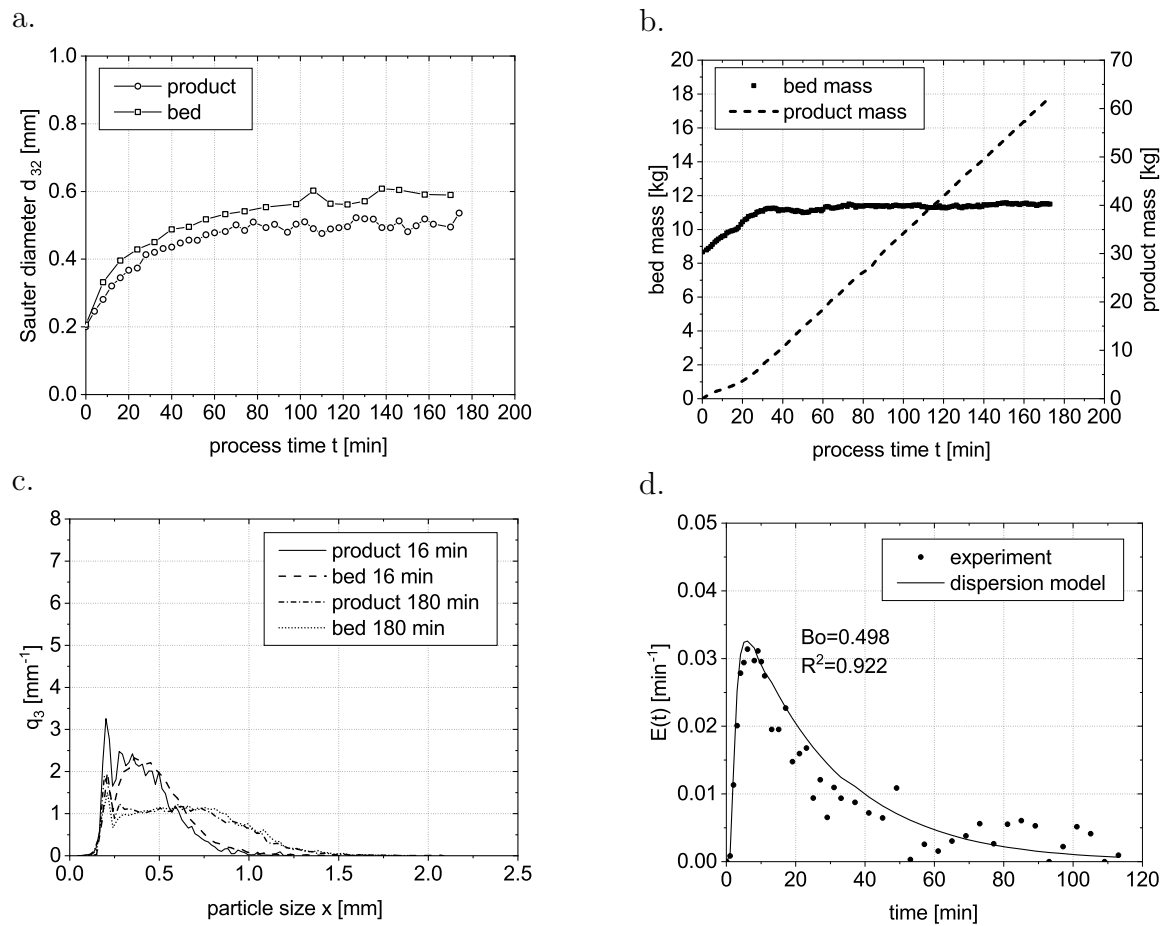


Figure 5.22: Results of Exp. W2: a. evolution of particle size; b. development of bed and product mass; c. PSDs of selected samples; d. measured and calculated RTDs.

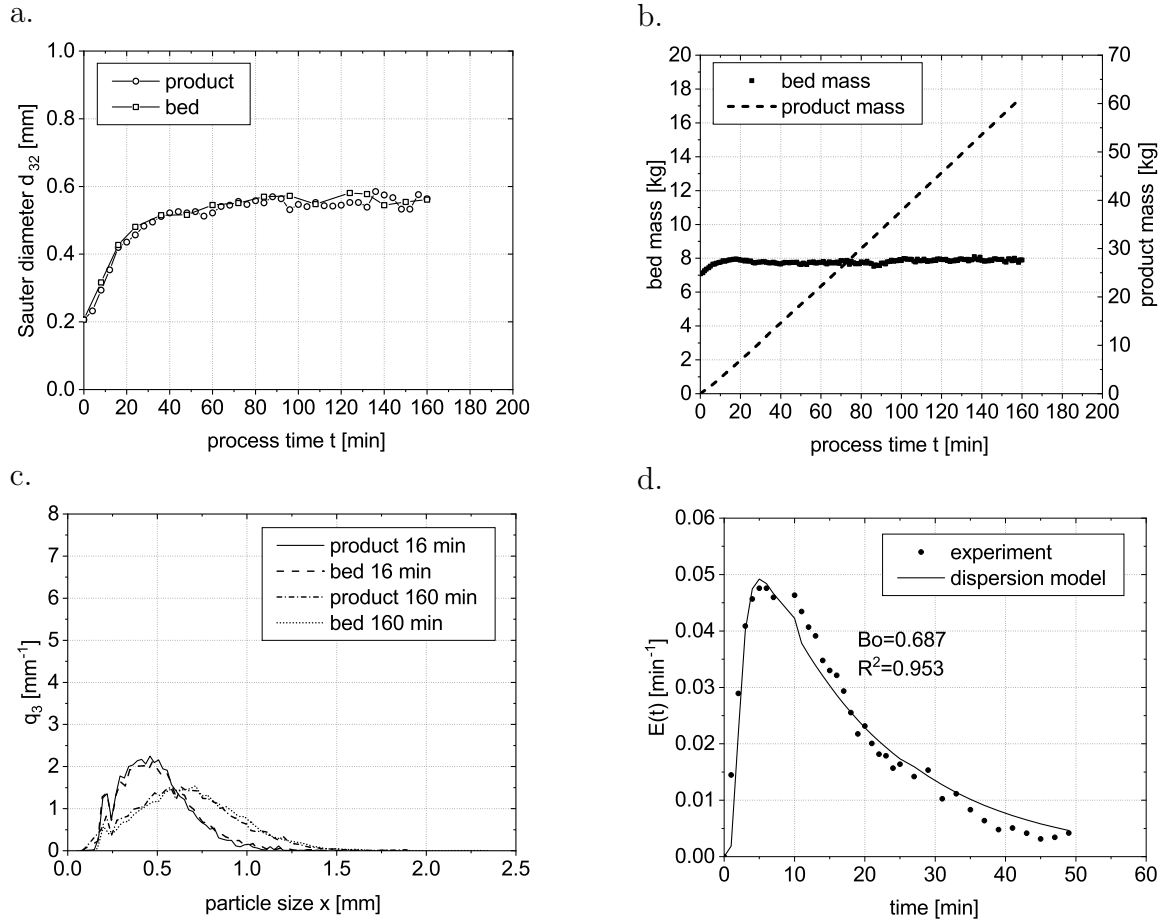


Figure 5.23: Results of Exp. W1-L: a. evolution of particle size; b. development of bed and product mass; c. PSDs of selected samples; d. measured and calculated RTDs.

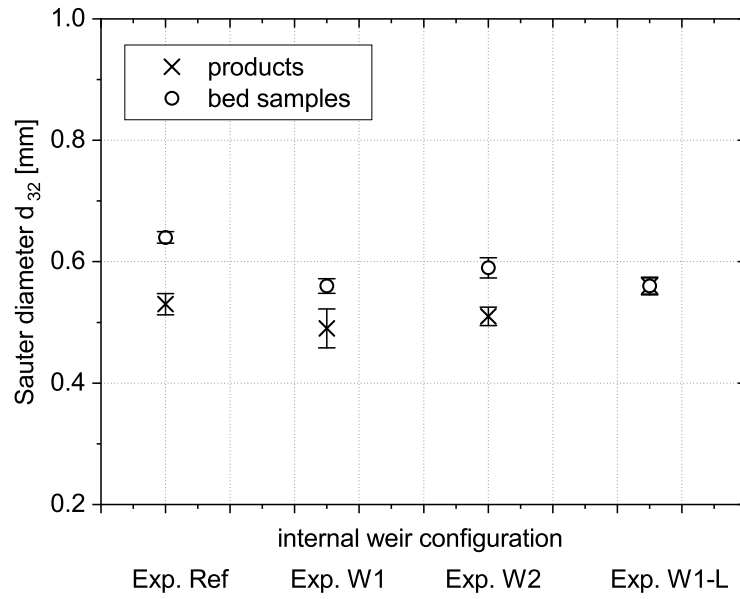


Figure 5.24: Comparison of particle Sauter mean diameter and standard deviation for Exp. Ref, W1 and W2.

Table 5.2: Overview of bed mass and Bo number.

Exp.	$m_{\text{bed,start}}$ [kg]	$m_{\text{bed,final}}$ [kg]	\bar{m}_{bed} [kg]	m_{product} [kg]	τ [min]	Bo [—]
Ref	8.30	11.80	11.56	66.64	28.90	0.00930
T1	8.33	12.50	12.30	65.98	30.75	0.0116
T2	6.84	10.10	10.56	10.61	26.40	0.00580
F1	7.23	12.66	12.68	47.82	42.27	-
F2	9.18	11.27	10.94	69.80	21.88	-
B1	7.48	12.69	-	66.64	31.72*	-
B2	7.42	11.88	11.80	68.46	29.50	0.0710
S1	7.32	11.53*	-	30.28*	28.83*	-
S2	7.50	11.14	11.15	54.37	27.88	-
Ref-L	6.62	7.96	7.83	60.67	19.58	0.122
W1	8.74	11.64	11.52	61.08	28.80	0.528
W2	8.67	11.52	11.47	61.99	28.68	0.498
W1-L	7.08	7.86	7.90	60.61	19.75	0.687

* When the process was stopped.

Table 5.3: Overview of calculated values and process dynamics.

Exp.	Product sample		Chamber sample		SE	Time to steady state [min]	CoV, CoV _{back} [%]	GR _{k,acc} rate [mm/min]	Operability	
	$\bar{\sigma}_{pd}$ [mm]	σ_{pd} [mm]	\bar{d}_{bed} [mm]	σ_{bed} [mm]						
Ref	0.53	0.0176	0.64	0.0096	0.17	136	5	3	0.0183	stable
T1	0.66	0.0199	0.84	0.0062	0.21	143	4	3	0.0215	stable
T2	0.39	0.0121	0.51	0.0097	0.24	95	4	3	0.0148	stable
F1	0.59	0.0121	0.70	0.0176	0.17	150	4	3	0.0140	stable
F2	0.46	0.0134	0.56	0.0185	0.18	95	4	3	0.0210	stable
B1	0.67*	-	0.84*	-	0.25*	-	-	-	0.0211*	growing
B2	0.43	0.0127	0.52	0.0089	0.17	120	4	3	0.0146	stable
S1	0.63*	-	0.82*	-	0.23*	-	-	-	0.0218*	defluidization
S2	0.32	0.0386	0.37	0.0033	0.14	80	2	3	0.0115	stable
Ref-L	0.56	0.0110	0.62	0.0144	0.10	100	4	3	0.0286	stable
W1	0.49	0.0320	0.56	0.0120	0.13	120	5	3	0.0168	stable
W2	0.51	0.0151	0.59	0.0167	0.14	130	4	3	0.0170	stable
W1-L	0.56	0.0146	0.56	0.0134	0	92	5	3	0.0284	stable

* When the process was stopped.

5.3 Conclusions

A continuously operated agglomeration process in a pilot horizontal fluidized bed has been presented in this chapter. It has been shown by experiments that different operation parameters (air temperature, feed rate, binder concentration, binder spray rate, height of outlet weir and configuration of internal weirs) have an influence on the particle growth behavior, particle size distribution, bed mass as well as the process operability. Main quantified results such as the final particle size, process stability, growth rate, bed mass and mean particle residence time are summarized in [Table 5.2](#) and [Table 5.3](#).

Due to the small size of particles at the beginning of the process, the particles have higher collision frequency and lower particle weight. Therefore, the highest particle size growth rate is seen at the beginning in all continuously operated experiments. Over time, the growth rate decreases slowly till a steady state (if there is one). Oscillations in the evolution of particle size are not observed for the investigated parameter regime. With the growth of particle size, the bed mass increases fast at the beginning. When a low outlet weir is used, less difference between starting bed mass and final bed mass is seen, which also accelerates the transition to steady state. The experiments with larger particle sizes usually show more fluctuations in both particle size and bed mass. There is a stronger trend of particles sticking on chamber walls and nozzle caps; hence, nozzle blockage and chunk formation add more fluctuations and defluidization risk to the process. Similar to the batch operated process, a decrease in air temperature, decrease in particle feed rate, increase in binder concentration or increase in binder spray rate will increase the particle growth rate as well as the particle size. The separation effect at high outlet weir is strong, and a significant difference between samples from the bed and the outlet can be seen. Large particles are more difficult to remove from the chamber, which results in an accumulation of large particles that may break again, thereby decreasing the agglomeration efficiency. With lower outlet weir, the separation effect is less pronounced. Outlet and chamber particles have almost the same size distribution. In this case, a higher agglomeration efficiency is achieved. The jets from the two-fluid nozzles have a significant influence on the particle residence time distribution. If the process chamber is not separated and small particles are used, the air jets act like a stirrer that can mix the particles in the axial direction very fast. Without internal weirs, the horizontal fluidized beds behaves like a well-stirred reactor. The wide residence time distribution results in partial short-circuiting, meaning that some particles leave the process chamber in a very short time after they have entered. These particles have hardly any opportunity to form agglomerates. When the chamber is separated by internal weirs, the particle residence time distribution can be better controlled. In this way, the number of primary particles at the outlet can also be decreased.

Chapter 6

Modeling of continuous spray agglomeration in a cylindrical fluidized bed

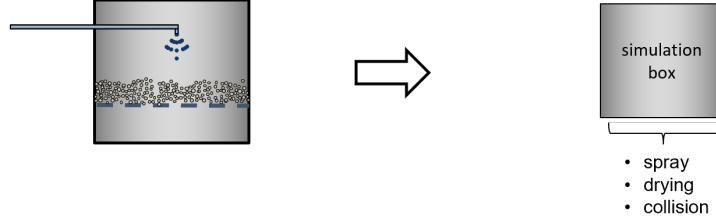
This chapter is an extended version of Du et al. [142]. The model in this chapter has been developed by the author and Gerd Strenzke together. The conduction of the experiments in this chapter and the analysis of the experimental results have been done by Gerd Strenzke. The implementation and running of the model have been done by the author. In this chapter, the usage of the Monte Carlo model is extended from batch-wise to continuous SFBA process conducted in a cylindrical fluidized bed with a single process chamber by adding particle flow event. The algorithm of the particle flow event is presented in a flow chart, and the strategy of particle selection is explained. By fitting the simulation results to the experimental results from one batch-wise experiment, the collision frequency prefactor and breakage rate used in all simulations are achieved. The simulations are then conducted with the same parameters as used in corresponding experiments. Finally, the results are compared with experimental results regarding the evolution of particle size, PSDs and bed mass to validate the model.

6.1 Structure of the algorithm

6.1.1 Equivalent simulation box

In the Monte Carlo model, the real process chamber is usually converted into a simulation box that contains a limited number of particles and simplified micro-processes. As shown in Figure 4.1a, a cylindrical fluidized bed operated in batch is simulated by a simulation box where spraying of binder, drying of droplets and particle collisions take place in a given sequence and at a given frequency as shown in Figure 4.2. Furthermore, when a cylindrical fluidized bed is equipped with a feed tube and a discharge classifier, it can be operated continuously. To simulate the continuous process, the particle flow event is added to the simulation box, which then includes the feed of primary particles and the discharge of products (shown in Figure 4.1b).

a. Batch-wise operated cylindrical fluidized bed:



b. Continuously operated cylindrical fluidized bed:

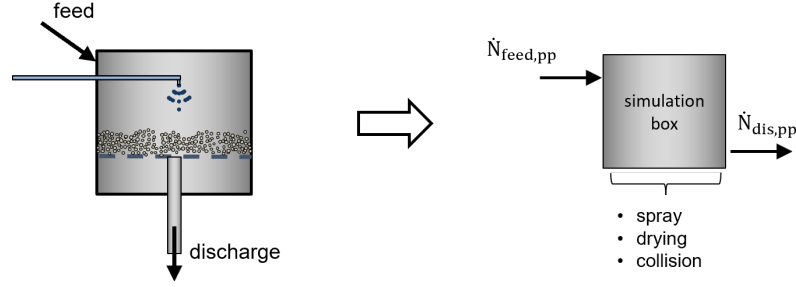


Figure 6.1: Modeling of SFBA process in different plants: a. batch-wise cylindrical fluidized bed, b. continuous cylindrical fluidized bed.

6.1.2 Particle flow event

As mentioned above, when the model is used to simulate the continuous process in a cylindrical fluidized bed, the particle flow event, which includes the discharge of products and the feed of primary particles needs to be considered. In the simulation, the continuous feed of primary particles and the discharge of products are simulated by periodically introducing new primary particles to and randomly selecting and removing particles from the simulation box. The structure of the algorithm for the particle flow event is shown in Figure 6.2. First, particles in the simulation box are selected randomly and then removed from the simulation box to simulate the discharge of products in the real process. Afterward, primary particles are generated and added to the simulation box according to the real feed rate to simulate the feed of new particles.

In experiments, the feed of primary particles is controlled by a vibration feeder. Although the feed rate is not exactly constant during the process, it is considered steady for simplification. The average feed rate of the real process $\dot{m}_{feed,real}$ is obtained from the weight of added particles and overall process time. With the scaling factor S , the feed rate of new primary particles $\dot{N}_{feed,pp}$ in the simulation is calculated by:

$$\dot{N}_{feed,pp} = S \frac{6\dot{m}_{feed,real}}{\pi\rho_{pp}d_{pp}^3}. \quad (6.1)$$

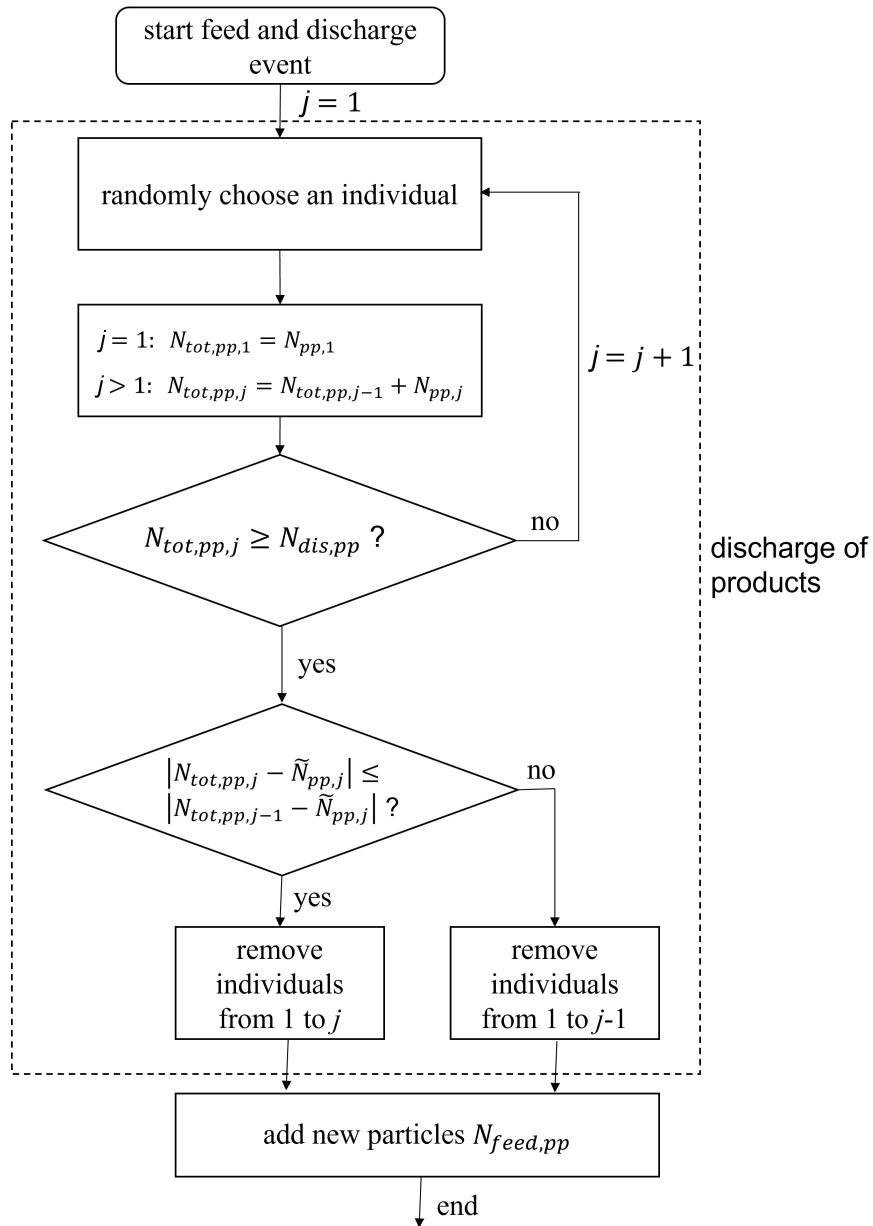


Figure 6.2: Flow chart of particle flow event for continuous cylindrical fluidized bed.

The primary particle discharge rate $\dot{N}_{dis,pp}$ in the simulation is calculated as follows:

$$\dot{N}_{dis,pp} = S \frac{6\dot{m}_{dis,real}}{\pi\rho_{pp}d_{pp}^3}, \quad (6.2)$$

with

$$\dot{m}_{dis,real} = \dot{m}_{feed,real} - \frac{\Delta m_{bed,real}}{\Delta t}, \quad (6.3)$$

where $\Delta m_{bed,real}$ is the change in bed mass that is obtained from experiments. This value is negative, if the bed mass decreases.

6.1.2.1 Discharge of products

In the real process, the particle flow event takes place uninterrupted during the whole process. However, due to the limited particle number in the simulation box and the discrete nature of the particulate system, a time interval t_{int} between two events has to be set long enough to accumulate enough particles to be added or removed. Due to the discrete nature of the particulate system, only a natural number of particles can be handled, which means the number of particles must be an integer in the simulation.

If the bed mass is kept constant, which means there is no change in bed mass during the process, the discharge rate should be equal to the feed rate. However, considering that the selection of discharged particles is random, means that the number of primary particles contained in the selected particles cannot be predicted before the selection has been finished. This uncertainty always brings fluctuations to the particle number in the simulation box. In order to keep the particle number constant during the simulation, the desired number of primary particles contained in the discharged particles, $N_{dis,pp}$, is calculated before each particle flow event as:

$$N_{dis,pp} = N_{feed,pp} + N_{pp,i} - 2^{Dou} N_{pp,0}. \quad (6.4)$$

Here, $N_{pp,i}$ is the current number of primary particles in the simulation box and $N_{feed,pp}$ is the number of particles fed in each particle flow event.

If the bed mass changes during the process, this model can replicate the change in bed mass by controlling the number of particles in the simulation box. A change in bed mass is commonly seen in continuous mode experiments, especially during start-up, or when the bed mass is not controlled. Since the feed rate is constant, the development and fluctuations of bed mass are only caused by the change in discharge rate. The change in bed mass during the process is obtained from experiments, then the desired number of primary particles $\tilde{N}_{pp,i}$ at any given time i in the simulation box is

$$\tilde{N}_{pp,i} = S \frac{6m_{bed,real,i}}{\pi\rho_{pp}d_{pp}^3}, \quad (6.5)$$

where $m_{bed,real,i}$ is the bed mass obtained from experiments.

The number of primary particles that should be contained in the discharged particles in one particle flow event is then calculated as:

$$N_{dis,pp} = N_{feed,pp} + N_{pp,i} - \tilde{N}_{pp,i}. \quad (6.6)$$

The particles that need to be discharged are selected randomly by an iterative method from the simulation box. Due to the weak separation effect of the classifier in the plant, the size difference between the discharged particles and the particles in the simulation box is neglected, which means the particles from the simulation box can be randomly selected regardless of particle size. In each iteration, only one particle (primary particle or agglomerate) is selected. Then the number of primary particles $N_{pp,j}$ contained in the selected individual is checked and summed up to the number of primary particles that have been selected in previous iterations to obtain the actual total number of primary particles $N_{tot,pp,j}$. When the number of primary particles has overcome the expected number $N_{dis,pp}$, the iteration will be stopped. Afterward, the number of primary particles reached in iteration j is compared with the number reached in iteration $j - 1$ to check which one is closer to the expected value $\tilde{N}_{pp,i}$. If $N_{tot,pp,j}$ is closer to that value, the individuals selected from iteration 1 to j will be removed from the simulation box. If not, the individuals selected in the last iteration will be dropped, then only the individuals selected in the iterations from 1 to $j - 1$ will be removed. Due to the random selection of the individuals, it is not possible to predict the number of primary particles contained in them before they have been selected. This may lead to an excessive discharge of primary particles when an individual that contains a large number of primary particles is selected at the end of the iteration. It results in a difference between the actual number of discharged primary particles and the expected number, which brings fluctuations of the simulated bed mass. With this algorithm, the fluctuations of simulated bed mass can be controlled in a small range and follow the experimental results well.

6.1.2.2 Feed of primary particles

As mentioned above, particle flow events take place periodically, with a time interval t_{int} between two events. To avoid numerical errors introduced by direct rounding of the calculated feed rate, a random number R from the open interval (0,1) is used to decide the actual number of primary particles $N_{feed,pp}$ to be fed in one particle flow event. It is calculated as follows:

$$N_{feed,pp} = \lceil (R - 1 + \dot{N}_{feed,pp} t_{int} - \lfloor \dot{N}_{feed,pp} t_{int} \rfloor) \rceil. \quad (6.7)$$

This value is re-calculated at the beginning of each particle flow event.

Compared to the discharge of products, the feed of primary particles to the simulation box is simple. After the discharged particles have been removed from the simulation box, the new particles are generated according to the predefined properties and put into the simulation box to simulate the feed of particles in the real process.

6.2 Plant and experimental plan

The experimental results used to compare with the simulation results were retrieved by Strenzke et al. [10] with a continuously operated cylindrical fluidized bed. The scheme of the plant is shown in Figure 6.3.

The plant is of pilot scale and has a cylindrical process chamber with an inner diameter of 300 mm. Similar to the horizontal fluidized bed, the operation parameters are controlled and recorded by a DCS. In order to discharge particles during the process, the plant is equipped with an internal classifier at the bottom of the bed. The inner diameter of the internal classifier is 44 mm. Independent from the bed, the airflow rate in the classifier can be either controlled manually at a fixed flow rate or controlled automatically by a bed mass controller.

If the flow rate is controlled manually, the airflow rate can be set to a fixed value and controlled by the DCS via a mass flow meter. If the bed mass controller is used, the DCS of the plant calculates the bed mass from the measured pressure drop continuously during the process. Hence, the airflow rate in the classifier is controlled automatically and continuously by the DCS to maintain the pre-set bed mass. The temperature of the classifying air in the tube can be controlled separately. In this series of experiments, the temperature was set to the same value as the temperature of the fluidizing air. The fluidizing air in this plant is circulated and cooled by a condenser to remove the moisture from the air. After most of the moisture has been removed, the air is heated up again to the desired temperature by an electrical heater and enters the bed through a distributor plate. The air is exhausted from the bed through a relaxation zone to reduce the entrainment of particles. In the process, the moisture contents of the inlet and outlet air are measured and recorded by an optical dew point meter (Optidew Vision, Michell Instruments Ltd.) and an infrared instrument (NGA 2000 MLT, Rosemount Analytical Inc., Emerson Process Management), respectively. By closing the discharge tube, the discharge of particles during the process is disabled, and the plant can be operated batch-wise. The binder is stored in an external tank and supplied by a peristaltic pump, then sprayed by a two-fluid nozzle (Düsen-Schlick, model 940/6 with a hemispheric cap, liquid orifice diameter: 0.8 mm) which is installed at the top of the bed, in a distance of 420 mm from the distributor plate. As mentioned in Chapter 3, the binder is an aqueous solution of HPMC, and the particles are glass beads with a Sauter mean diameter of 0.20 mm.

In this chapter, five of experiments performed by Strenzke et al. [10] are used, which includes one batch-wise experiment and four continuously operated experiments. Among them, Exp. C-Ref-Batch is the batch-wise experiment with the same process parameters as the continuous reference experiment (Exp. C-Ref). It is conducted to obtain the prefactor F_{coll} of collision frequency and the breakage rate. Then, these values are used in all simulations of this work. A similar method has been used in previous work by Terrazas-Velarde et al. [86] and Rieck et al. [88].

In all experiments, the fluidizing air temperature was set to 90 °C, and the mass flow rate was 275 kg/h. The atomizing air pressure was 1.7 bar with the air cap position at

Table 6.1: Experimental parameters.

Bed diameter	d_{bed}	300 mm
Starting bed mass	$M_{bed,0,real}$	8 kg
Sauter mean diameter of primary particles	$d_{32,pp}$	0.20 mm
Density of primary particles	ρ_{pp}	2400 kg/m ³
Binder mass fraction	X_b	4 wt. %
Binder density	ρ_b	1020 kg/m ³
Fluidizing air mass flow rate	\dot{m}_g	275 kg/h
Classifier air volume flow rate	\dot{V}_{ca}	415 l/min
Fluidizing air inlet temperature	$T_{g,in}$	90 °C

120°. When the bed mass controller was not used, the volume flow rate of classifier air was set to 415 l/min. The main experimental parameters are summarized in Table 6.1. Exp. C-Ref-BMC is an experiment conducted with a bed mass controller to keep the bed mass constant during the process, which is used to study the influence of bed mass. Exp. C-F1 and Exp. C-F2 are experiments with different feed rates to study the influence of primary particle feed rate. The varied parameters are listed in Table 6.2. The target binder spray rate was set to 45 g/min. But due to the indirect control of this value (by the rotation speed of the peristaltic pump), the achieved values were calculated by the weight difference of the binder tank. The target values of primary particle feed rate were 150 g/min, 250 g/min and 350 g/min for Exp. C-F1, C-Ref and C-F2, respectively. Similar to the binder spray rate, this value is controlled by adjusting a vibratory feeder and is difficult to meet precisely. The real feed rate was calculated by recording the total weight of fed particles and process time.

When the plant was used for batch experiments, 8 kg of primary particles were initially added to the fluidized bed. Then, the heater and ventilators were started to heat the plant to the set temperature. After the temperature had been reached, the peristaltic pump was started at the pre-set rotation speed. Meanwhile, the compressed air was switched on in order to atomize and spray the binder. Samples were collected periodically through a sample taker from the bed during the process. The batch-wise experiment was run for 45 min. Different from the batch-wise experiment, the continuous experiments need the continuous discharge of product by the internal classifier and continuous feed of primary particles by the vibratory feeder. The starting bed mass was also 8 kg. Then the plant was heated to the set temperature. When the temperature was reached, the binder spray was started, as well as the discharge of particles and the feed of primary particles. This moment is considered as the starting of the continuous experiments (time zero). During the experiments, samples were taken periodically (more frequently in the transient stage and less frequently during the steady state) from the bed via the sample taker. The processes were run for 120 min, then the binder spray and feeder, as well as the heater, were stopped to terminate the process.

Table 6.2: Varied experimental parameters.

Experiment	$\dot{m}_{feed,real}$ (g/min)	$\dot{m}_{b,real}$ (g/min)
C-Ref-Batch	-	43
C-Ref-BMC	263	48
C-Ref	226	45
C-F1	138	46
C-F2	333	47

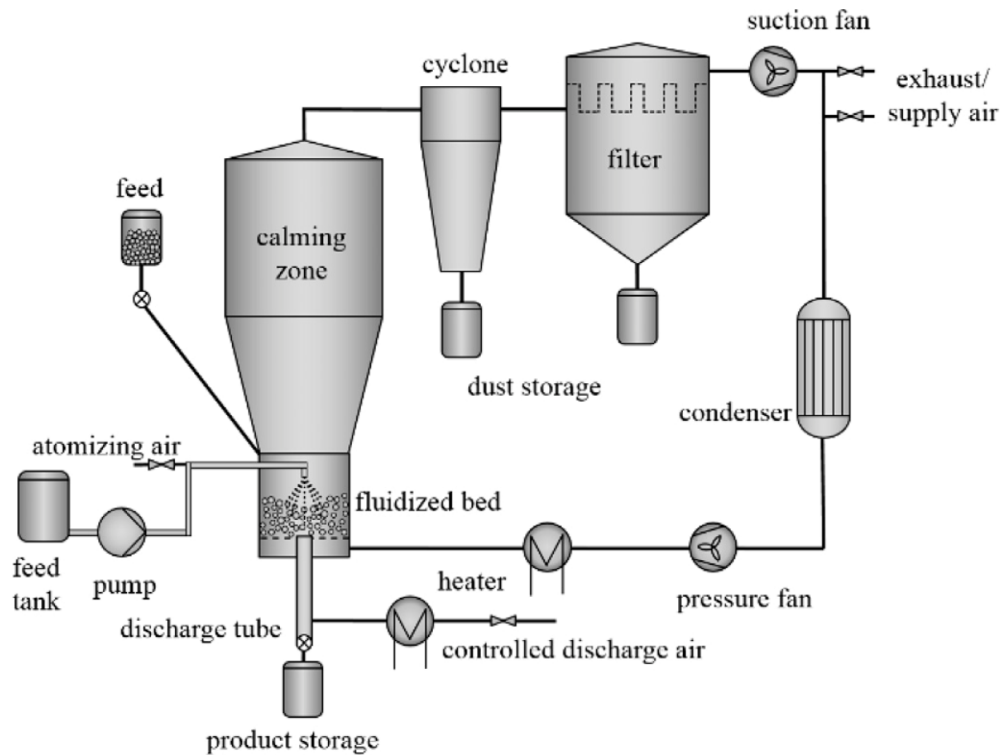


Figure 6.3: Scheme of the pilot-scale cylindrical fluidized bed with internal classifier.

Table 6.3: Additional simulation parameters.

Starting bed mass	$m_{bed,0,sim}$	8 kg
Starting number of particles in simulation box	$N_{pp,0}$	1000
Particle surface asperities height	h_a	1 μm
Collision prefactor	F_{coll}	0.05
Particle restitution coefficient	COR	0.8
Breakage rate	-	0.17 %
Droplet diameter	d_d	30 μm
Particle-binder contact angle	θ	40°

6.3 Simulation results

In order to compare with the experimental results, one simulation for each experiment was performed. In the simulation, the same process parameters and plant configuration as in the corresponding experiment were used. The main parameters used in the simulations are summarized in [Table 6.3](#).

6.3.1 Batch-wise process

As described before, the new model can be applied to either batch-wise or continuous processes. To get the collision prefactor and the breakage rate, the batch-wise experiment run for 45 min with the same process parameters as Exp. C-Ref, but without primary particle feed, is used. As shown in [Figure 6.4a](#), the Sauter mean diameter of the particles increases from 0.2 mm to 0.86 mm after 45 min with a particle size growth rate of about 14.7 $\mu\text{m}/\text{min}$ in the batch-wise experiment. An almost linear growth of the particle size is seen, which has also been observed in previous works [[19](#), [62](#), [86](#)].

To show the influence of different breakage rates in the model, simulations with a fixed collision frequency prefactor 0.05 and different breakage rates of 0.15 %, 0.17 % and 0.19 % were conducted. The results of the simulations are shown in [Figure 6.4a](#). Here, we see the significant influence of the breakage rate on the particle growth behavior. An increasing breakage rate leads to smaller particle size. When the breakage rate is increased further, the equivalence of agglomeration and breakage will be reached early, which means the growth of particles will stop at smaller particle sizes. To show the influence of collision frequency prefactor, simulations with a fixed breakage rate of 0.17 % and different collision frequency prefactors 0.04, 0.05 and 0.06 were conducted. Since the process time and collision times are linked directly by the collision frequency, the change of this prefactor will change the particle growth rate directly. After visually fitting the simulation results to the experimental results by means of breakage rate and collision frequency prefactor, it was found that when the breakage rate is 0.17 %, and the collision frequency prefactor is 0.05, both the evolution of particle Sauter mean diameter and PSDs (shown in [Figure 6.4c](#)) are reproduced satisfactorily.

However, compared to the experimental results, the PSDs from simulations are steeper, with more peaks, and narrower (less large agglomerates). As shown in Figure 4.7, the calculated diameter of the agglomerates can only be specified for values above 0.20 mm, which may lead to more steep peaks. In the real process, partial over-wetting can lead to the sticking of binder on the inner surface of the process chamber with the formation of large deposits, which are then removed from the wall by knocking the outer wall during the process after they have been solidified. These large deposits are more difficult to break into small particles before they are discharged. Another reason may be the simplified breakage mechanism, in which the distribution of particle size, bridges and collision velocity are ignored, and the breakage rate is assumed constant for all particles.

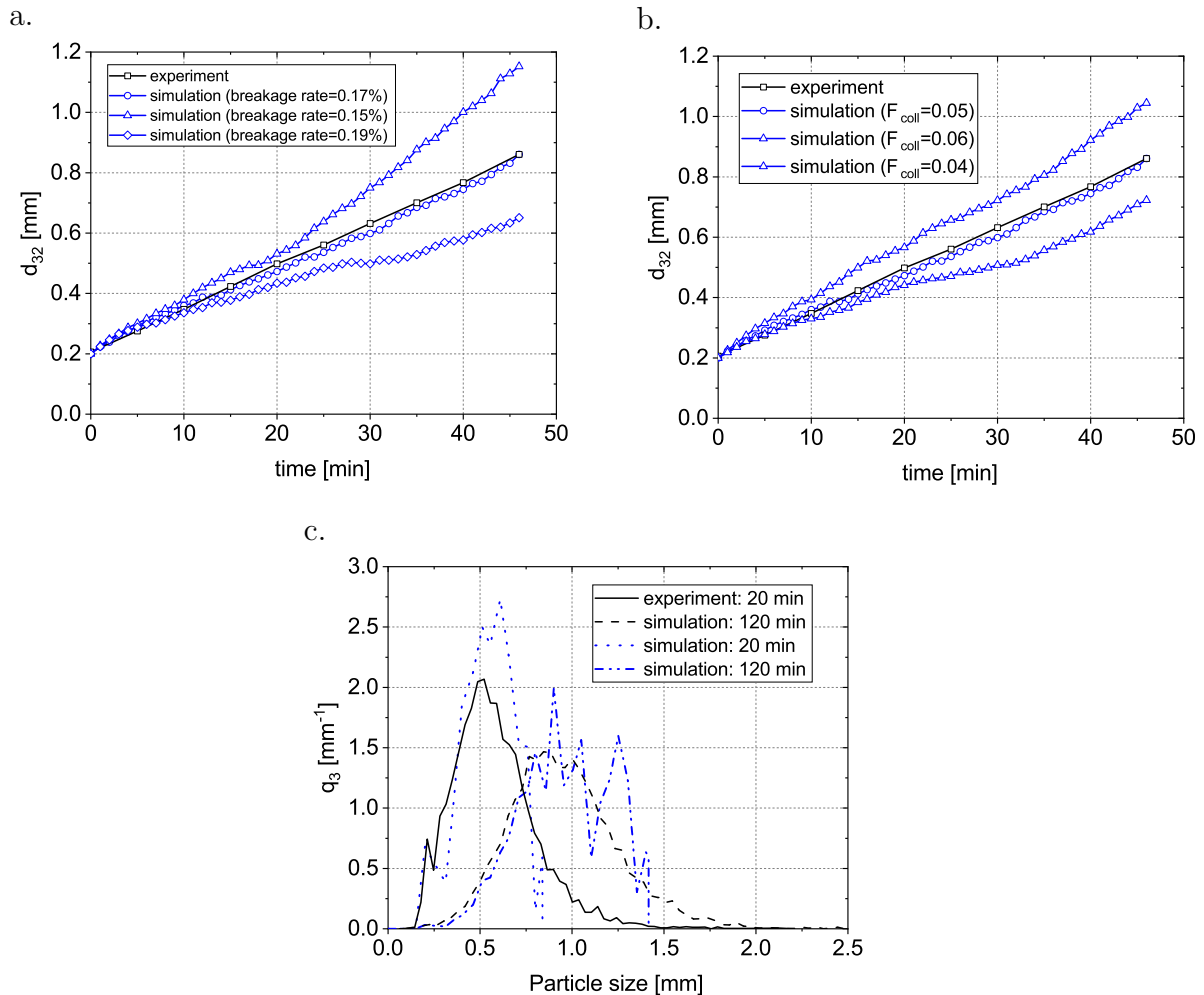


Figure 6.4: Comparison of Exp. C-Ref-Batch and Sim. C-Ref-Batch: a. evolution of particle size with different breakage rates, b. evolution of particle size with different collision prefactors, c. PSDs of selected samples.

6.3.2 From batch-wise to continuous process

After it has been applied to the batch-wise process, the model is extended to be used to simulate the continuous process by activating the particle flow event. In order to study the influence of primary particle feed, Sim. C-Ref-BMC is performed and compared with the experimental results. In Exp. C-Ref-BMC, a bed mass controller was employed to control the bed mass at the starting bed mass of 8 kg by automatically and continually adjusting the air flow rate in the classifier throughout the process. Although the bed mass in the experiment was not perfectly kept constant, much smaller fluctuations were seen compared to the experiments done without the bed mass controller. For simplification, the bed mass is kept constant at 8 kg in the simulation, which means the discharge rate is set same as the feed rate to 263 g/min. As illustrated in Figure 6.5a, we see a much slower growth of the particles and a totally different growth pattern compared to Exp. C-Ref-Batch. Instead of linear growth, the particle size increases to around 0.58 mm after 40 min of process time, then reaches to a steady state with slight fluctuations. The average standard deviation of particle size in steady state is 0.018 mm. For the evolution of particle size, the simulation result agrees well with the experimental results in both the transient period and the steady state. The actual bed mass in the simulation is shown in Figure 6.5b. With the feed and discharge strategy, the bed mass is kept at around 8 kg with fluctuations in a small range. The actual average primary feed rate in the simulation is 263.16 g/min, which is quite close to the set value of 263 g/min. The PSDs of selected samples are shown in Figure 6.5c. In these plots, one sees peaks at a size of around 0.2 mm, showing the continuously fed primary particles. However, compared to the PSDs from the experiment, the PSDs from the simulation have higher peaks and narrower size distribution at both 20 min and 120 min of process time. As described before, perfect bed mass control is not possible in the simulation. For all simulations in this chapter, the change in bed mass achieved from experiments is well reproduced. However, for better explanation of the particle growth behavior, the developments of bed mass are shown for all experiments.

The simulation was run on a 64-bit PC (10-core Intel(R) Core(TM) i9-10900K with 64 GB of RAM), and the total computational time for this Sim. C-Ref-BMC is about 6 hours. Considering that the process time is 120 min, the computational time is acceptable. However, the computational speed is strongly dependent on the primary particle number and the number of doublings in the simulation, which means the computational time will be longer with more primary particles and larger particle size.

6.3.3 Influence of bed mass development

Instead of using the bed mass controller, the volume flow rate of classifying air is often controlled manually or set to a constant value during this experiment. This results in a significant change in bed mass during the process (compared to the initial mass). In order to elucidate the influence of bed mass fluctuations during the process, Exp. C-Ref was performed, which has the same parameters as Exp. C-Ref-BMC, except that the air volume flow rate in the classifier was set to 415 l/min. Figure 6.6b depicts the

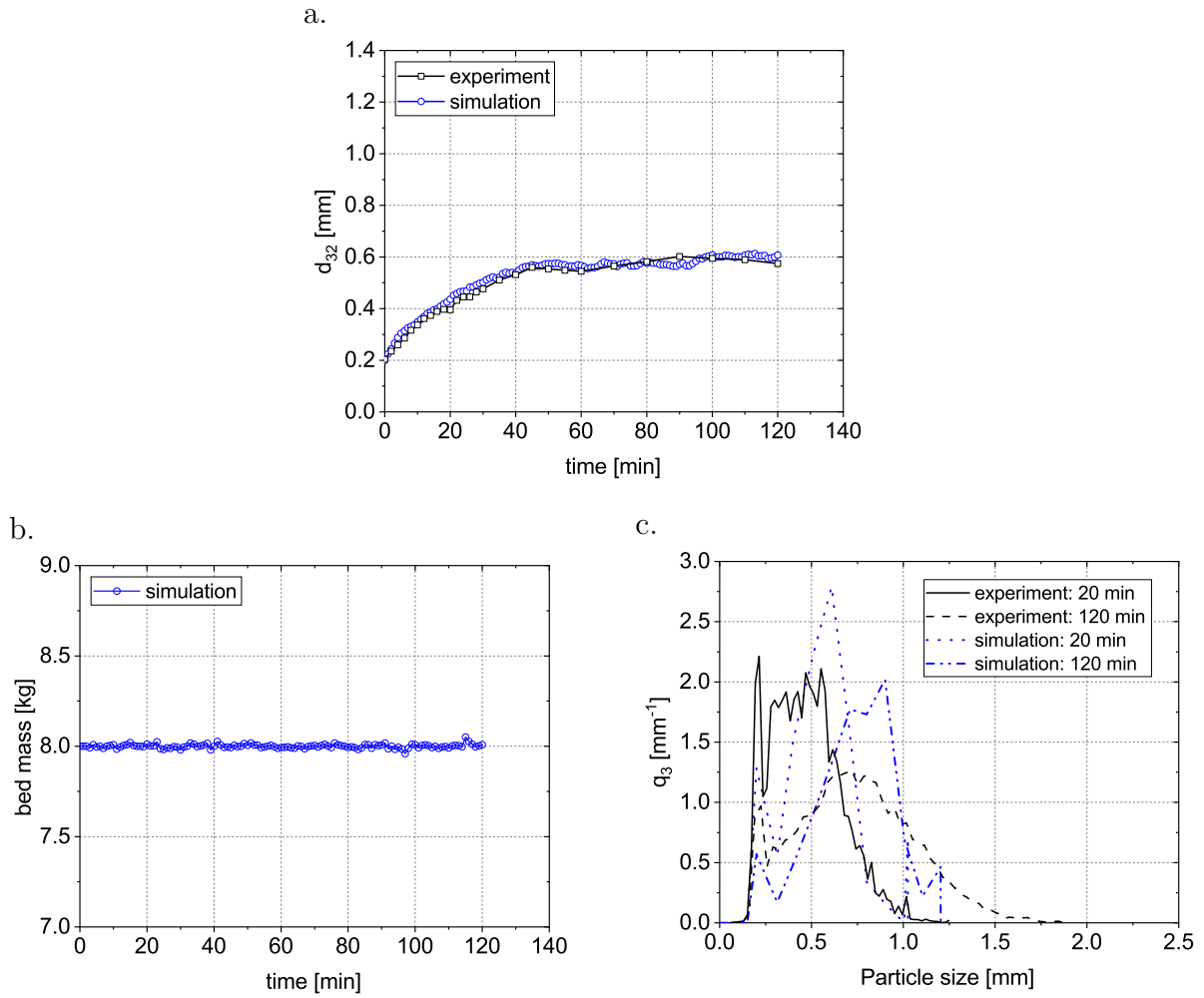


Figure 6.5: Comparison of Exp. C-Ref-BMC and Sim. C-Ref-BMC: a. evolution of particle size, b. development of bed mass, c. PSDs of selected samples.

development of bed mass during the experiment. In the first 5 min, we see a slight increase in bed mass from 8 kg to 8.5 kg. Afterward, the bed mass starts to decrease quickly and reaches the lowest value of about 6.2 kg after 23 min, which may be caused by the growth of particles and the intense extraction of samples from the bed in the first 30 min. From 38 min until 60 min of process time, the bed mass increases again to about 7.7 kg. The final bed mass is around 7 kg, which is distinctly lower than the starting bed mass. The fluctuations of bed mass during the experiment influence the growth behavior of the particles. As shown in Figure 6.6a, the particle growth rate in this experiment is significantly higher than that of Exp. C-Ref-BMC in the first 30 min. Due to the decreased bed mass, the ratio of binder to particles in Exp. C-Ref is higher than that in Exp. C-Ref-BMC, which leads to a higher particle growth rate. The increase in bed mass from 40 min to 60 min promotes the transition from a high growth rate to a steady state of almost zero growth in time. The process has then reached a balance between the feed of new particles, the breakage of agglomerates, and the agglomeration. Finally, the process was stopped with a Sauter mean diameter of around 0.62 mm with the average standard deviation of 0.015 mm in the steady state.

As can be observed in Figure 6.6a, the simulation result underestimates the particle size slightly in the transient period but still agrees well with the experimental results in the steady state period. The fast decrease of bed mass in the first 30 min increases the growth rate of particles in the simulation (compared to Exp. C-Ref-Batch and C-Ref-BMC). In general, the simulation results have a similar trend to the experimental results when the bed mass changes during the process. An increase in bed mass leads to slower growth, while a decrease in bed mass leads to a higher growth rate. Again, simulated PSDs match the measured PSDs of samples from the experiment (Figure 6.6c). However, one still sees a narrower span of PSDs achieved by simulation. Figure 6.6b illustrates the development of bed mass in the simulation compared to the experimental values. Excellent agreement during the whole process is observed, which means that the algorithm is capable of controlling the bed mass according to the experimental result. Finally, the average feed rate in this simulation is 226.01 g/min.

6.3.4 Influence of primary particle feed rate

To elucidate the influence of primary particle feed rate on the particle size growth behavior and to evaluate the performance of the model, experiments and simulations with different feed rates were used. As shown in Table 6.2, Exp. C-F1 has an average feed rate of 138 g/min, whereas Exp. C-F2 has an average feed rate of 333 g/min.

With a lower feed rate, the ratio of binder to particles and the particle mean residence time is higher, which can lead to more successful collisions (via increased wetted surface area). As presented in Figure 6.7a, higher growth rate and larger particles are obtained in Exp. C-F1 compared to Exp. C-Ref. The final particle size achieved is about 1.1 mm in this experiment, which is significantly larger than that in Exp. C-Ref. In Figure 6.7c, the PSDs of selected samples are shown. The average standard deviation of particle size in steady state is 0.038 mm, which shows it has more fluctuations than Exp. C-Ref in

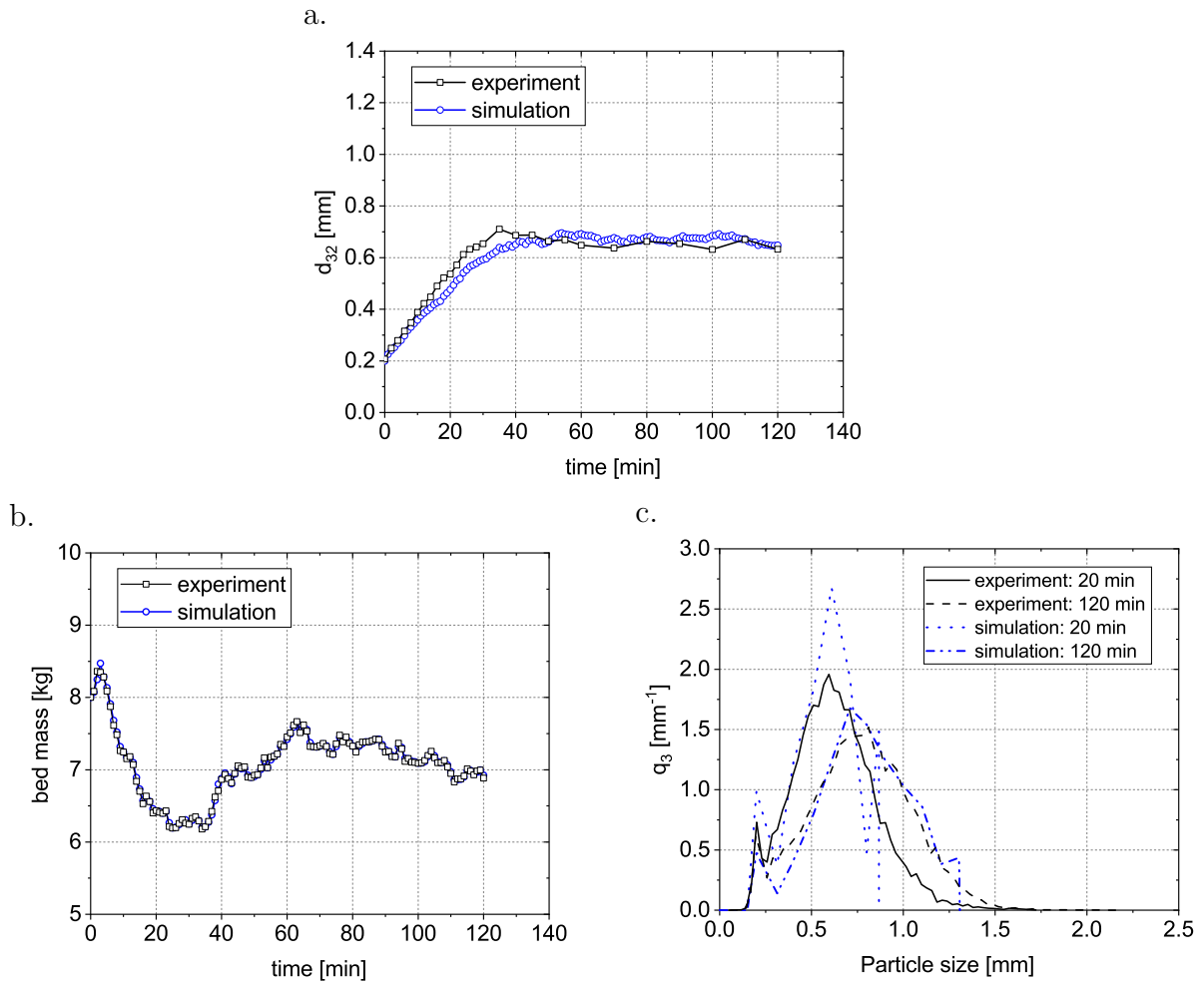


Figure 6.6: Comparison of Exp. C-Ref and Sim. C-Ref: a. evolution of particle size, b. development of bed mass, c. PSDs of selected samples.

the steady state. Compared to Exp. C-Ref, much fewer primary particles (lower peaks at 0.2 mm) are seen. The bed mass decreases to about 5.8 kg after 20 min of process time, and the final bed mass of about 5.6 kg (Figure 6.7b) is lower than in Exp. C-Ref. Due to the larger particle size and lower feed rate, the fixed air flow rate in the classifier is not capable of keeping the bed mass constant. Therefore, a continuous decrease in bed mass is seen towards the end of this experiment, which increases the risk of bed collapse that would break down the continuous process.

As shown in Figure 6.7a, the simulation reproduces the trend of experimental results at a lower feed rate. It agrees well with the experiment until 80 min of process time but overestimates the particle size from 80 min until the end of the process. The particle size in the simulation increases fast from about 100 min to 115 min, whereas it stays almost constant in the experiment. With the decrease in bed mass, the probability of successful collisions increases, while the breakage rate is still kept constant in the simulation. The growth rate of particle size results from the difference in successful agglomeration and breakage events. This difference is increased by the rapid and significant decrease in bed mass, which yields an overestimation of the particle size in this model. Moreover, the separation effect of the classifier is ignored in the simulation, which means that the size of discharged particles is similar to the size of particles in the bed. However, due to an even weak separation effect, discharged particles should be larger than the particles left in bed in experiments. When more large particles are discharged, the overall size of the particles in the bed is, though, more difficult to increase. The PSDs shown in Figure 6.7c give similar results. More large agglomerates are observed in the simulation after 120 min of the process. The change in bed mass is reproduced well in the simulation with a final average feed rate of 138.13 g/min (Figure 6.7b).

When the feed rate is further increased to 333 g/min, lower particle size growth rate and smaller agglomerates size (Figure 6.8a) are observed. The process ends up with an average agglomerate size of about 0.50 mm. Compared to Exp. Ref, the growth of particle size reaches the steady state faster. The average standard deviation of particle size in the steady state is 0.016 mm. The higher feed rate decreases the ratio of binder to particles, which results in less successful collisions. In Figure 6.8c, higher peaks at around 0.2 mm are seen for both samples taken from the experiment, indicating a larger amount of primary particles. As shown in Figure 6.8b, the bed mass decreases from 8 kg to around 6.7 kg after 20 min of process time, which shows a similar development as in the other experiments. However, due to the higher feed rate, the bed mass starts to grow fast from 8 kg after 100 min, then ends up at 9.5 kg. Compared to Exp. C-F1, smaller particle size and higher feed rate bring the continuous increase in bed mass until the end of the process. The fast increase in bed mass from $t = 100$ min leads to the decrease in particle size seen in Figure 6.8a. The simulation result agrees well with the experimental result for the evolution of particle size in both the transient period and at steady state (Figure 6.8a). From $t = 100$ min to the end of the process, the decrease in particle size is also seen. Again, the development of the bed mass is well reproduced in the simulation, with an average feed rate of 332.87 g/min.

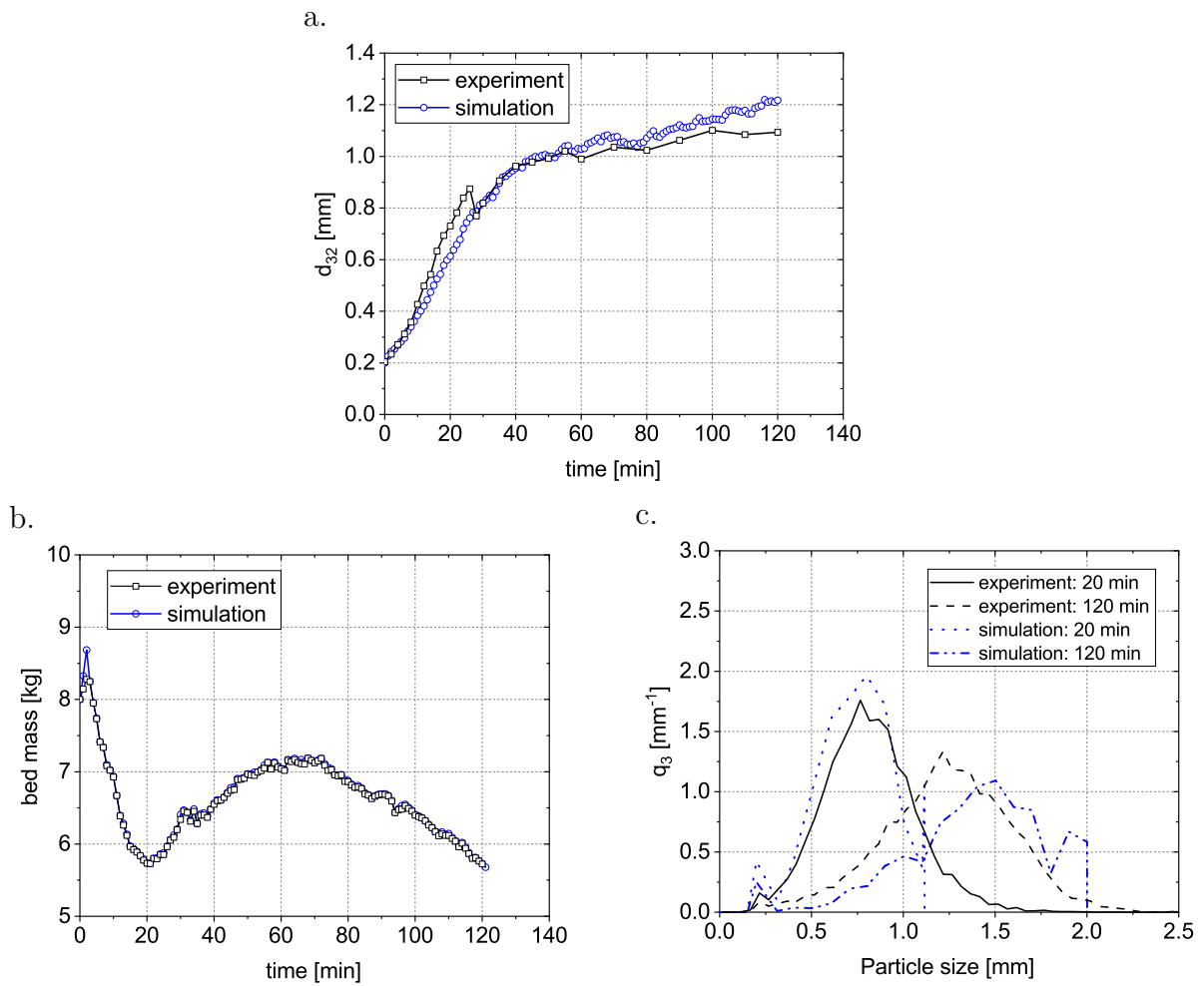
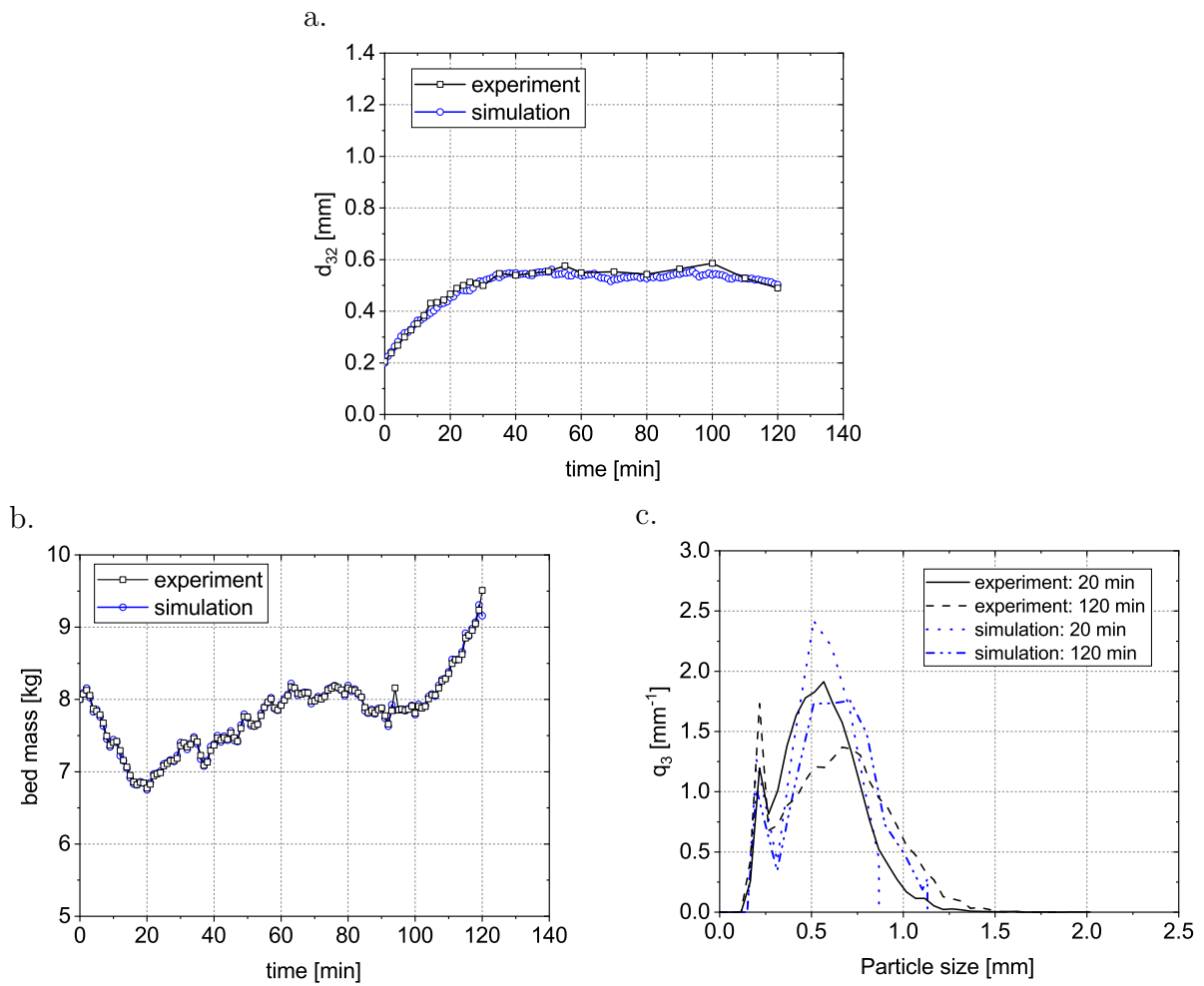


Figure 6.7: Comparison of Exp. C-F1 and Sim. C-F1: a. evolution of particle size, b. development of bed mass, c. PSDs of selected samples.



6.4 Conclusions

In this chapter, the usage of the Monte Carlo method has been successfully extended to simulate the continuous agglomeration process conducted in a cylindrical fluidized bed with a single process chamber. In the model, the continuous feed and discharge of particles in the real process are simulated by introducing the particle flow event. There, particles are randomly removed from the simulation box according to a predetermined value. Simultaneously, new primary particles are added to the simulation box according to the real feed rate in experiments. With this strategy, the bed mass in the simulation can be either made to fluctuate in a small range around a constant value or to follow any change according to the experimental results.

To validate the model, both batch-wise and continuous experiments have been used. Firstly, one batch experiment has been used to retrieve the collision frequency prefactor and the particle breakage rate by visually fitting the simulation results to the experimental results. Then a series of continuous experiments have been utilized to show the influence of the fluctuant bed mass and the varied feed rate on the particle growth behavior. The experiments show that a higher feed rate leads to smaller particles. It was also observed that the change in bed mass has a considerable influence on the growth behavior of particle size. The presented model shows good agreement with the experimental results in terms of the evolution of particle size and of PSDs for both the batch-wise and continuous experiments. This model is capable of reproducing any change in bed mass in the experiments and simulates the influence of bed mass on particle growth behavior.

Chapter 7

Modeling of continuous spray agglomeration in a horizontal fluidized bed

In this chapter, the usage of the Monte Carlo method is further extended to simulate the continuous spray agglomeration process conducted in a horizontal fluidized bed with multiple process compartments. When no internal weirs are installed, just two simulation boxes with a rapid exchange of particles between them are used. When three internal weirs are installed, the four resulting process compartments are simulated by four simulation boxes. To control the exchange of particles between the simulation boxes, the backflow cell model [85] is combined with the Monte Carlo model by using the RTD data achieved from experiments. To validate the model, the simulation results are then compared with experimental results in terms of the evolution of particle size and PSDs of selected samples with different plant configurations and process parameters. For simulations performed with internal weirs, particle RTD is also compared with experimental results.

7.1 Structure of the algorithm

7.1.1 Equivalent simulation box

As described in [Chapter 6](#), the simulation box is considered as a simplification of the real process chambers. When the Monte Carlo model is used to simulate the agglomeration process conducted in the horizontal fluidized bed, this conversion becomes more complex since the horizontal fluidized bed can have up to four distinguishable process chambers, three of which are equipped with nozzles. Depending on the installation of internal weirs, the equivalent simulation box can be divided into two types:

- When the internal weirs are not installed, according to the RTD results measured in experiments (summarized in [Table 5.2](#)), the particles in the bed can be assumed well-mixed. As illustrated in [Figure 7.1a](#), the horizontal fluidized bed is simulated by two simulation boxes. The process chambers 1-3 in the bed with spray are

considered as one large compartment simulated by simulation box 1. In simulation box 1, the spray of binder, drying of droplets and particle collisions take place. The process chamber 4 is simulated by simulation box 2. In simulation box 2, the spray of binder is excluded, which means that droplet deposition events are not considered in this simulation box. The particles flowing from simulation box 1 may contain wet though droplets; therefore, the drying of droplets and particle collisions still need to be considered. The particle number in each simulation box is determined by the relative volume of the corresponding process chamber. In this case, the ratio of particle number in simulation box 1 and simulation box 2 is 3:1. Besides the feed of primary particles and the discharge of particles (primary particles or agglomerates), the exchange of particles between these two simulation boxes is necessary.

- When the horizontal fluidized bed is further divided by internal weirs, each process chamber needs to be considered as a separated simulation box to simulate the particle flow behavior. Therefore, the whole bed is divided into four simulation boxes (shown in Figure 7.1b). Similar to the continuous horizontal fluidized bed without internal weirs, the spray of binder, drying of droplets and particle collisions take place in simulation boxes 1-3, whereas the drying of droplets and particle collisions take place in simulation box 4. The particle number in each simulation box is determined by the volume of the corresponding process chamber. With this configuration, the separation of process chambers restricts the flow and reflux of particles, which decreases the dispersion in particle residence time. To control the exchange of particles between different simulation boxes, the backflow cell model proposed by Roemer and Durbin [85] is used with measured RTDs from experiments.

7.1.2 Particle flow event

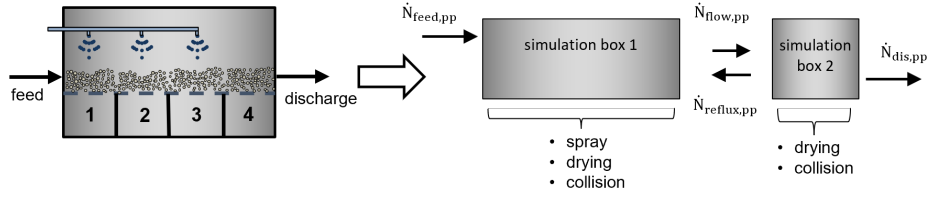
When the Monte Carlo model is used to simulate the process conducted in the horizontal fluidized bed, the feed of primary particles, discharge of products and exchange of particles between different simulation boxes take place in a given sequence in each particle flow event. Figure 7.2 shows the flow chart of the particle flow event. First, the discharge of products is conducted. Second, the exchange of particles between different simulation boxes is conducted according to the RTD data measured in experiments. Finally, new particles are added to simulation box 1.

7.1.2.1 Discharge of products

Similar to the model used for the continuous process in the cylindrical fluidized bed, the particle flow event occurs periodically with a time interval t_{int} . Therefore, the number of primary particles contained in the discharged particles is calculated by:

$$N_{dis,pp} = N_{feed,pp} + N_{pp,i} - \tilde{N}_{pp,i}. \quad (7.1)$$

a. Continuous horizontal fluidized bed without internal weirs:



b. Continuous horizontal fluidized bed with internal weirs:

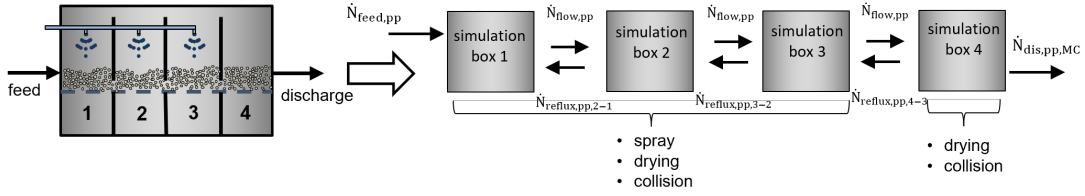


Figure 7.1: Modeling of continuous process in different plants: a. continuous horizontal fluidized bed without internal weirs; b. continuous horizontal fluidized bed with internal weirs.

with

$$\tilde{N}_{pp,i} = S \frac{6m_{bed,real,i}}{\pi \rho_{pp} d_{pp}^3}, \quad (7.2)$$

where $M_{bed,real,i}$ is the bed mass at time i obtained from experiments.

Due to the weak separation effect of the classifier in the cylindrical fluidized bed, the size differences between the bed particles and the products were not considered in the simulation. Hence, the discharged particles were selected randomly from the simulation box directly. When the model is used for the experiments in the horizontal fluidized bed, the discharged products shall be selected from simulation box 2 (without internal weirs) or simulation box 4 (with internal weirs). However, a strong separation effect was seen in most of the experiments conducted in the horizontal fluidized bed, which means that the error of the model is large (especially in the size of products), if this effect is neglected. In order to simulate the separation effect, the separation effect value achieved from experiments is used in the simulation. At first, the particles in simulation box 2 (without internal weirs) or simulation box 4 (with internal weirs) are sorted upon the number of primary particles from least to most, and then stored in a new matrix. Then, particles are selected from the beginning of the matrix by the method of iteration, and the size of the selected particles is calculated in each iteration. Once the ratio of the size of selected particles to the size of particles in the simulation box becomes larger than SE , the iteration is stopped. Finally, the discharged products are selected randomly by the same method shown in Figure 7.2.

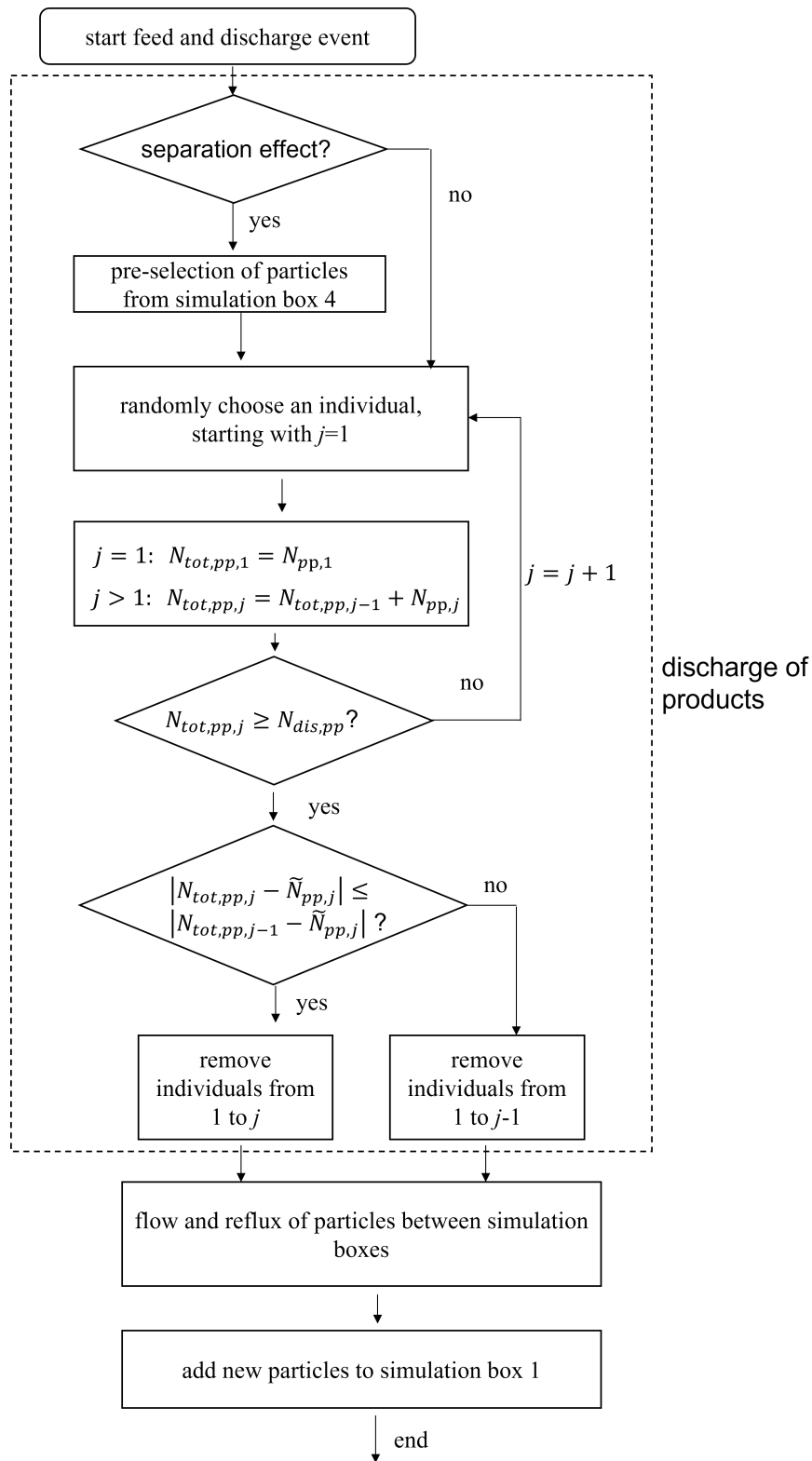


Figure 7.2: Flow chart of particle flow event for continuous horizontal fluidized bed.

7.1.2.2 Particle exchange without internal weirs

When the Monte Carlo model is used to simulate the process conducted in the horizontal fluidized bed without internal weirs, the fluidized bed is simulated by two separated simulation boxes. As listed in Table 5.2, all the experiments conducted without internal weirs have very low Bodenstein numbers, which means that the particle exchange rate between these two simulation boxes is very high. In order to simulate this rapid particle exchange, all particles in simulation box 2 are refluxed to simulation box 1 in each particle flow event. Therefore, the number of primary particles contained in the refluxed particles in each particle flow event is:

$$N_{reflux,pp,2-1} = N_{pp,2}, \quad (7.3)$$

where $N_{pp,2}$ is the number of primary particles in simulation box 2 after the discharged particles have been removed.

Meanwhile, the number of particles that flow from simulation box 1 to simulation box 2 is calculated according to the total number of primary particles in both simulation boxes,

$$N_{flow,pp,1-2} = 0.25\tilde{N}_{pp,i}. \quad (7.4)$$

If the calculated values are not integers, the values are rounded to the nearest integers.

7.1.2.3 Particle exchange with internal weirs

When the Monte Carlo model is used to simulate the process conducted in the horizontal fluidized bed with internal weirs, the fluidized bed is simulated by four separate simulation boxes. The backflow cell model proposed by Roemer and Durbin [85] is used to control the flow and reflux of the particles between different simulation boxes. With the data of measured RTD in experiments, the reflux factor R is calculated by Equation 2.9. The flow and reflux rate of the primary particles is calculated by:

$$\dot{N}_{flow,pp} = (R + 1)\dot{N}_{feed,pp} \quad (7.5)$$

and

$$\dot{N}_{reflux,pp} = R\dot{N}_{feed,pp}. \quad (7.6)$$

With the time interval t_{int} between two particle flow events, the numbers of primary particles contained in the advected particles $N_{flow,pp}$ and the recycled particles $N_{reflux,pp}$ are calculated by:

$$N_{flow,pp} = \dot{N}_{flow,pp}t_{int} \quad (7.7)$$

and

$$N_{reflux,pp} = \dot{N}_{reflux,pp} t_{int}. \quad (7.8)$$

These values are rounded to the nearest integer if they are not integers.

When the bed mass is constant during the simulation, the number of refluxed particles is the same between different simulation boxes. However, a significant change in bed mass with time is usually seen in these continuous processes. Since the feed rate is kept constant in the simulation, the change in bed mass (particle number) is only due to the fluctuations in discharge rate. To uniformly distribute the particles in all four simulation boxes, the number of refluxed particles needs to be calculated according to the bed mass and the actual particle number in each simulation box. If the bed mass increases, which means that fewer particles are discharged from simulation box 4, more particles need to be refluxed from simulation box 4 to the previous simulation boxes. On the contrary, if the bed mass decreases, fewer particles need to be refluxed. By this approach, the numbers of primary particles contained in the refluxed particles need to be calculated for each simulation box separately by:

$$\begin{aligned} \text{From simulation box 4 to 3: } N_{reflux,pp,4-3} &= N_{pp,4} + N_{reflux,pp} - 0.25\tilde{N}_{pp,t} \\ \text{From simulation box 3 to 2: } N_{reflux,pp,3-2} &= N_{pp,3} + N_{reflux,pp,4-3} - 0.25\tilde{N}_{pp,t} \\ \text{From simulation box 2 to 1: } N_{reflux,pp,2-1} &= N_{pp,2} + N_{reflux,pp,3-2} - 0.25\tilde{N}_{pp,t} \end{aligned} \quad (7.9)$$

where $N_{pp,2}$, $N_{pp,3}$ and $N_{pp,4}$ are the numbers of primary particles in simulation box 2, 3 and 4, respectively.

7.1.2.4 Feed of primary particles

Similar to the model used for the continuous cylindrical fluidized bed, the calculation of particle number $N_{feed,pp}$ fed in each particle flow event uses a random number R from the open interval $(0,1)$. It is calculated at the beginning of each particle flow event as:

$$N_{feed,pp} = \lceil (R - 1 + \dot{N}_{feed,pp} t_{int} - \lfloor \dot{N}_{feed,pp} t_{int} \rfloor) \rceil. \quad (7.10)$$

In experiments, the primary particles are fed via a tube to process chamber 1. Therefore, the new particles are added to simulation box 1 in the simulation.

7.1.3 Particle residence time distribution

In order to track the residence time of each particle, the times when particles are added and when they are discharged are recorded in the simulation. By using this method, the residence time of each primary particle can be calculated by:

$$t_{res,n} = t_{dis,n} - t_{feed,n}, \quad (7.11)$$

where $t_{dis,n}$ and $t_{feed,n}$ are the discharge time and the feed time of primary particle. Since the residence time of each particle can be calculated, the mean residence time τ of the discharged particles can be obtained as:

$$\tau = \frac{\sum_{n=1}^{N_{tot,pp}} t_{res,n}}{N_{tot,pp}}, \quad (7.12)$$

where $N_{tot,pp}$ is the total number of primary particles contained in the discharged particles in a specified period of process time.

Meanwhile, the particles fed in any given period of process time can be considered as tracers. Then, the tracer particle mass fraction can be calculated as:

$$X_t(t) = \frac{N_{pp,t}(t)}{N_{dis,pp,tot}(t)}, \quad (7.13)$$

where $N_{pp,t}(t)$ is the number of tracer particles contained in the discharged particles in a given interval of time from $t - \Delta t$ to t , and $N_{dis,pp,tot}$ is the total number of primary particles contained in the discharged particles in the same span.

Then, the E-curve holds

$$E(t) = X_t(t) \frac{N_{feed,pp}}{\Delta t N_{pp,t,tot}}, \quad (7.14)$$

where $N_{pp,t,tot}$ is the total number of tracer particles.

7.2 Simulation plan

In this chapter, all experiments presented in [Chapter 5](#) are simulated by the Monte Carlo model. At first, the collision frequency prefactor is derived by fitting the simulation results to the reference experiment Exp. Ref. The collision frequency prefactor is then kept constant and used in all simulations. Similar to the experimental plan, the simulations are divided into two series. In the first series, different process parameters are varied. In correspondence to the varied parameters in experiments, the fluidization air temperature (Sim. T1 and T2), primary particle feed rate (Sim. F1 and F2), binder flow rate (Sim. S1 and S2) and binder concentration (Sim. B1 and B2) are varied in the simulations. In the second series, Sim. W1, W2 and W1-L are conducted by the model with four simulation boxes. The particle flow behavior is controlled according to the particle RTD results achieved from experiments. The varied parameters used in simulations are listed in [Table 7.1](#), and the parameters kept constant are summarized in [Table 7.2](#).

Table 7.1: Varied simulation parameters.

Simulation [-]	$T_{g,in}$ [°C]	\dot{m}_{feed} [kg/min]	\dot{m}_{spray} [g/min]	X_b [%]	d_d [μm]	N_{pos} [-]	N_{sb} [-]	R [-]
Ref	80	0.4	77	4	40	24	2	-
T1	70	0.4	78	4	40	24	2	-
T2	100	0.4	78	4	40	24	2	-
F1	80	0.3	78	4	40	24	2	-
F2	80	0.5	79	4	40	24	2	-
S1	80	0.4	98	4	40	24	2	-
S2	80	0.4	53	4	40	24	2	-
B1	80	0.4	77	5	46	18	2	-
B2	80	0.4	76	3	33	36	2	-
Ref-L	80	0.4	78	4	40	24	2	-
W1	80	0.4	80	4	40	24	4	6.7
W2	80	0.4	79	4	40	24	4	7.1
W1-L	80	0.4	78	4	40	24	4	4.8

Table 7.2: Additional simulation parameters.

Starting number of particles in simulation box	$N_{pp,0}$	4000
Particle surface asperities height	h_a	1 μm
Collision prefactor	F_{coll}	0.03
Particle restitution coefficient	COR	0.8
Breakage rate	-	0.17 %
Particle-binder contact angle	θ	40°

7.3 Simulation results

7.3.1 Simulation of the reference experiment

In [Chapter 6](#), the collision frequency prefactor and the breakage rate of the model have been identified by fitting the simulation results to the experimental results of the reference experiment conducted in batch. Considering that the particles and binder used in the experiments conducted in the cylindrical fluidized bed and the horizontal fluidized bed are identical, the breakage rate is kept the same at 0.17 %. However, the collision prefactor needs to be re-fitted due to the change in the shape of process chambers and the distance from nozzles to the distribution plate. Since there is no batch-wise experiments performed in the horizontal fluidized bed, the reference experiment Exp. Ref is used to obtain the collision frequency prefactor. As illustrated in [Figure 7.3](#), simulations conducted with different collision frequency prefactors of 0.025, 0.030 and 0.035 show the influence of this parameter on the particle growth behavior. By visually fitting the simulation results to the experimental results of Exp. Ref, the collision frequency prefactor is set to 0.030, and then this value is used in all simulations in this chapter. Similar to the model used for the cylindrical fluidized bed, the collision frequency prefactor has a significant influence on the particle size growth rate and final particle size, since the collision times and process time are linked by this factor directly. When the collision frequency prefactor is 0.030, the simulation results match the experimental results in both transient and steady state. After 160 min of process, we see a slight decrease in the particle size for the simulation results, which is caused by the increase in bed mass. However, the increase in bed mass during the late period of the process is usually due to the accumulation of large particles in real experiments. Since the separation effect is kept constant in the simulation, the model cannot simulate the sudden accumulation of large particles, which usually takes place in the late period of the process. That is why the particle size increases with the bed mass in the experiments, whereas it decreases in the simulation.

[Figure 7.4](#) shows the PSDs of selected bed samples from the experiment and simulation at different process time. Due to the limited number of discharged particles, the PSDs of products from the simulation are not compared to the experiment. After 4 min of process time, we see more large particles in the simulated PSD, which is consistent with

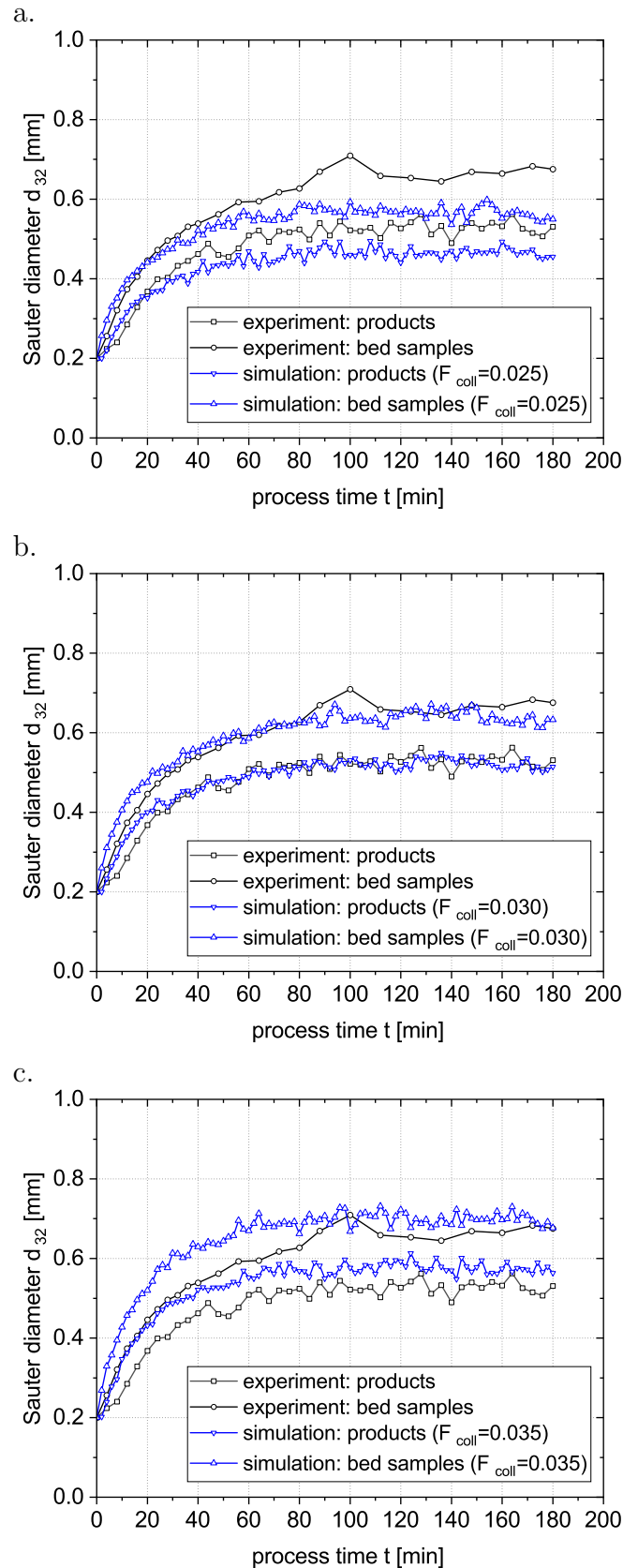


Figure 7.3: Evolution of particle size with different collision frequency prefactor: a. $F_{coll} = 0.025$, b. $F_{coll} = 0.030$, c. $F_{coll} = 0.035$.

the calculated Sauter mean diameter. In the simulation, the particle size growth rate is higher than that in the experiment. This may be caused by the simplification of the drying and particle wetting process in the model. With ongoing process time, the peak at about 0.20 mm becomes lower, which means that there are fewer primary particles. It is also observed that when the particle sizes in simulation and experiment are almost identical, for example, at 64 min and 100 min, the PSDs are also well reproduced.

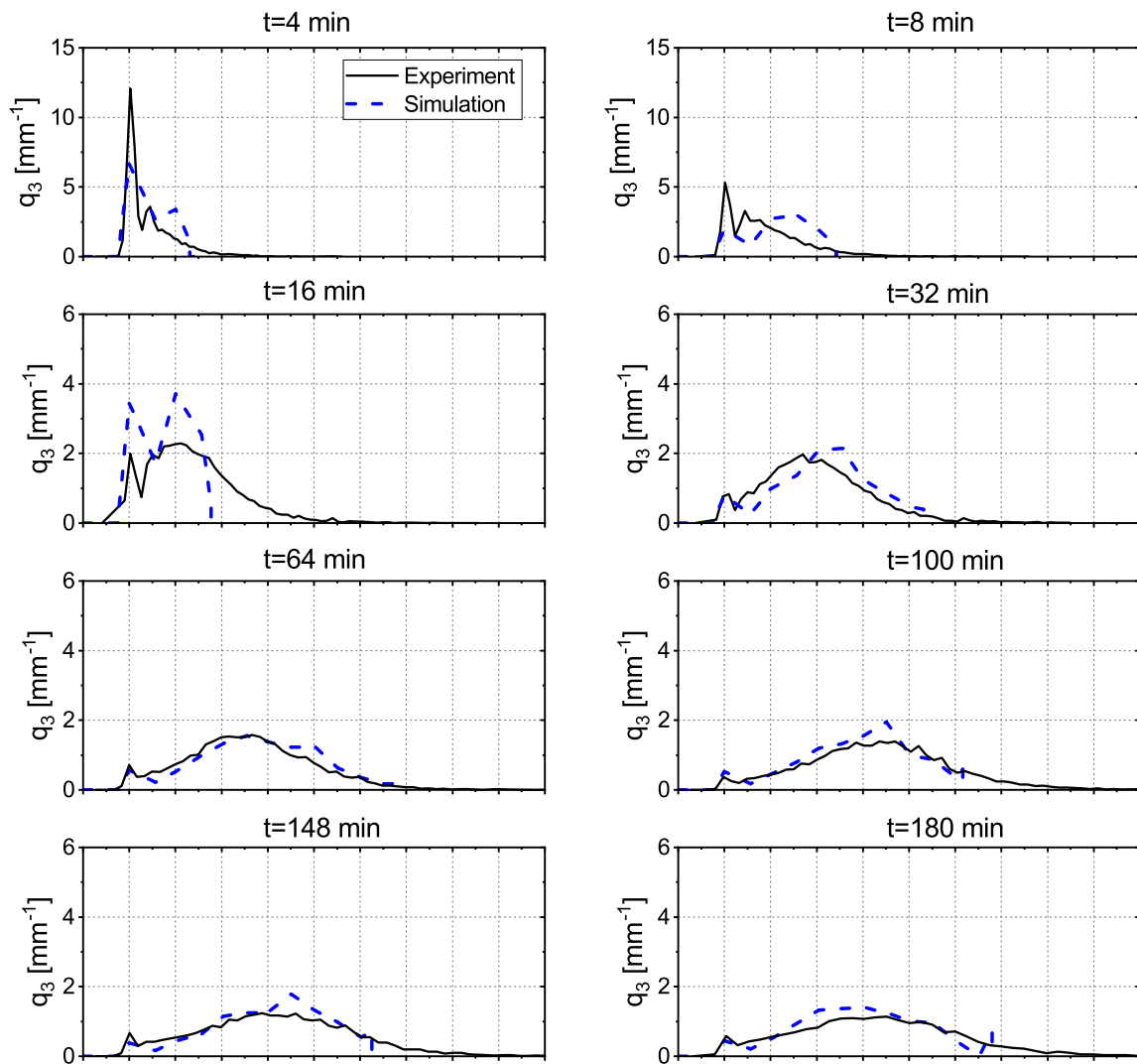


Figure 7.4: PSDs of bed samples from experiment and simulation.

The change in bed mass has a significant influence on the particle growth behavior in the experiment, which means that it can not be neglected in the simulation. The change in bed mass achieved from experiments is used in the corresponding simulation. By controlling the number of particles in the simulation box, the change in bed mass is simulated. Here, a similar algorithm to that used in the model for the cylindrical fluidized bed is employed. As depicted in Figure 7.5, the bed mass in the simulation

result agrees well with the experimental result. In all simulations performed in this chapter, the bed mass from experiments is well reproduced. Since the change in bed mass for each experiment has been shown and described in Chapter 5, the results for other simulations are shown in Appendix C.1.

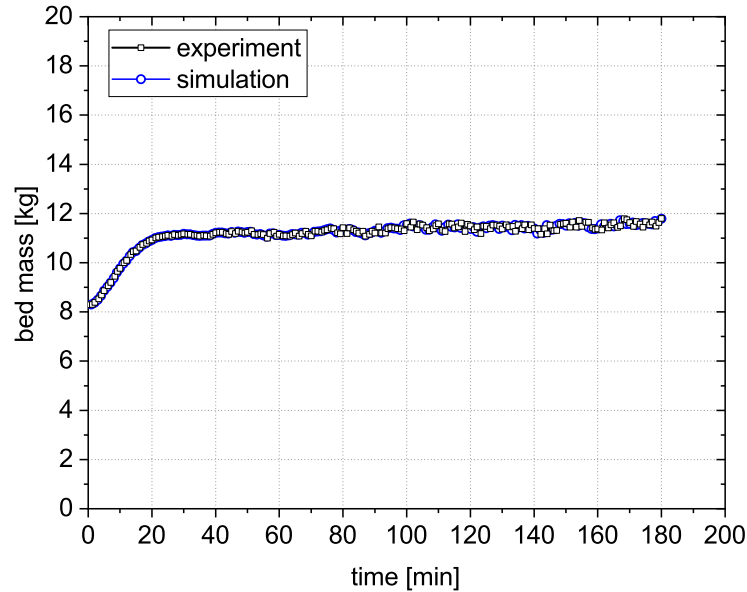


Figure 7.5: Development of bed mass in experiment and simulation.

As has been discussed before, when there are no internal weirs installed, the particles fed at the inlet travel very fast to the outlet due to the existence of jets from nozzles. This results in a rapid dispersion of particles along the process chamber, similar to a well-mixed reactor. To simulate this rapid particle flow behavior in the model, all particles in simulation box 2 are refluxed to simulation box 1 in each particle flow event. The particles that are added to the simulation box at 100 min are considered as tracers, and the residence time of each particle is tracked and calculated. As presented in Figure 7.6, the particle RTD in the simulation is well reproduced. Compared to the experimental results, the peak of the simulated curve comes earlier with a higher value, which indicates a faster movement of particles in the model. The particle mean residence time is 28.58 min, which is very close to the measured value 28.90 min in the experiment.

The total computational time for this simulation is about 25 hours on a 64-bit PC (10-core Intel(R) Core(TM) i9-10900K with 64 GB of RAM) for the simulation of the reference experiment (Exp. Ref). As mentioned before, the computational time of the Monte Carlo model is significantly affected by the primary particle number and the attained particle size (number of doublings). Compared to Sim. C-Ref-BMC conducted for the reference experiment in the cylindrical fluidized bed, this simulation has a higher number of primary particles (4000 to 1000) and a longer process time (180 min to 120 min). Therefore, it takes a longer time for computation.

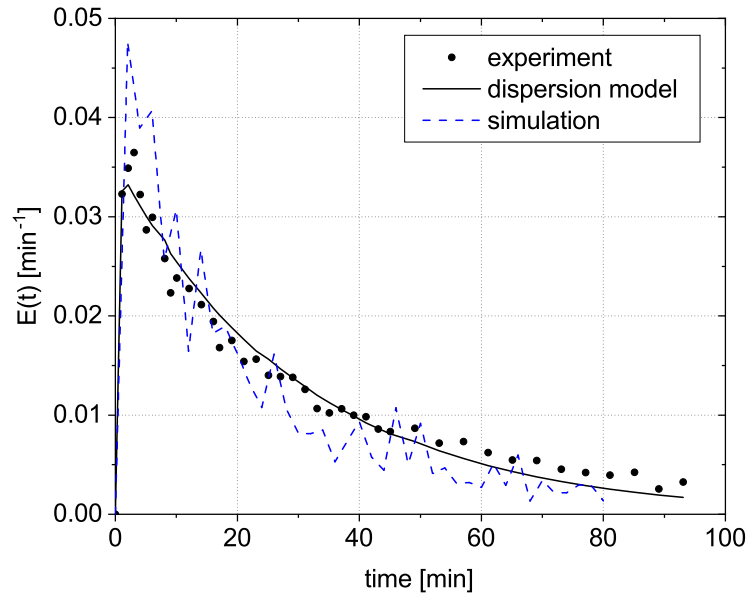


Figure 7.6: RTD results from experiment, dispersion model and simulation.

7.3.2 Effect of air temperature

To simulate the effect of air temperature on the particle growth behavior, Sim. T1 and T2 are conducted with the air temperature at 70 and 100 °C, respectively. As shown in Figure 7.7a, the evolution of particle size in the simulation agrees well with the result from the experiment in the transient period (from the starting to about 24 min). However, the particle size is slightly overestimated from 24 min of process time to the end of the process. With lower air temperature, the deposited droplets are dried more slowly, which provides more opportunities for successful collisions. Therefore, larger agglomerates are achieved. This trend can be observed in both simulation and experimental results. Figure 7.7b presents the PSDs of selected bed samples at 16 min and 180 min of process time. At 16 min of process time, the simulated particle Sauter mean diameter is almost identical to that in the experiment. Comparing the PSDs achieved from simulation and experiment, the PSD in the simulation is steeper. This is due to the discrete nature of the particle system and the assumed mono-dispersity of the primary particles, which result in the equivalent diameter of the agglomerates being limited to specific numbers. At 180 min of process time, more large particles are seen in the simulated PSD, which is consistent with the comparison of Sauter mean diameter. When the air temperature is increased to 100 °C in the simulation, the agglomeration rate is significantly reduced. The increased air temperature dries the droplets faster, which reduces the opportunity of successful collisions. As illustrated in Figure 7.8a, the particle size is slightly overestimated in the first 20 min of process time, while it is slightly underestimated in the steady state. A similar trend is also observed in Figure 7.8b. Much narrower PSDs are achieved in both simulation and experiment.

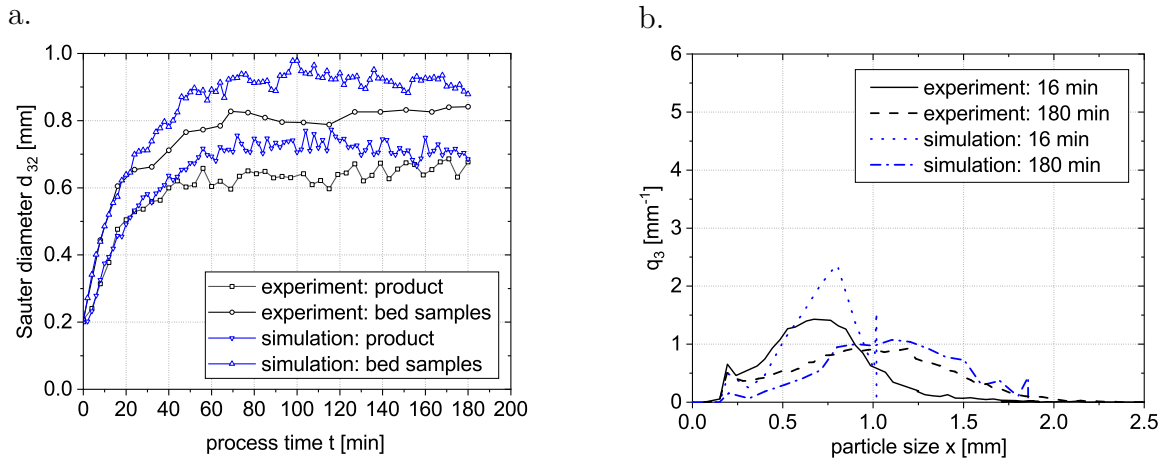


Figure 7.7: Comparison of Exp. T1 and Sim. T1: a. evolution of particle size, b. PSDs of selected samples.

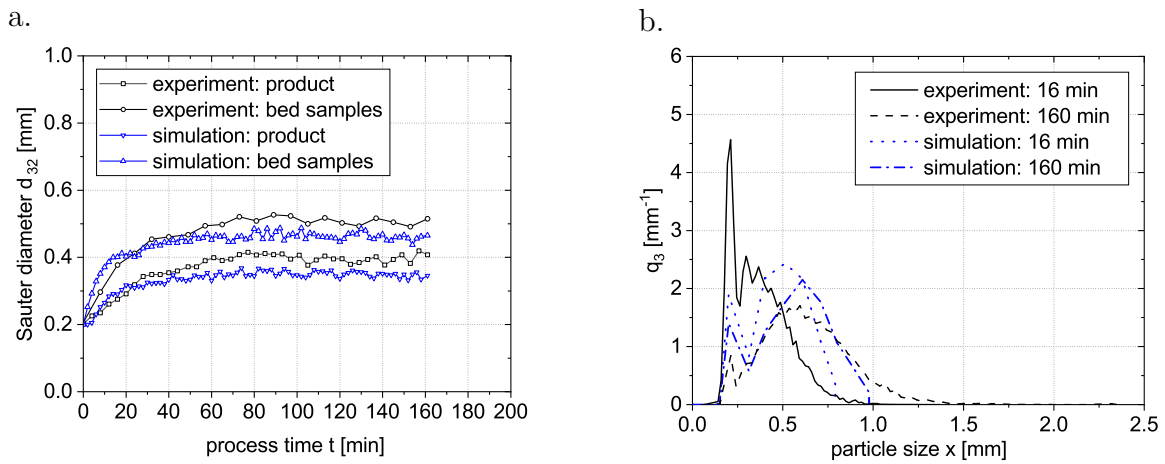


Figure 7.8: Comparison of Exp. T2 and Sim. T2: a. evolution of particle size, b. PSDs of selected samples.

7.3.3 Effect of particle feed rate

To simulate the effect of primary particle feed rate on the growth behavior of particle size, Sim. F1 and F2 are conducted with particle feed rates at 300 and 500 g/min, respectively. Figure 7.9a presents the evolution of particle size in the simulation and the comparison with experimental results. It is seen that lower feed rate results in a larger particle size in both simulation and experiment. In the transient period (the first 120 min of process time) of the simulation results, the predicted particle size is larger than that achieved in the experiment. With ongoing process time, the simulation results match better to the experimental results. As presented in Figure 7.10a, when the particle feed rate is increased, a slower growth rate and smaller particle size are achieved in the simulation. Similar to Sim. F1, the particle size in the transient period is slightly overestimated but agrees well with the experimental results in the steady state. Figure 7.9b and Figure 7.10b show the PSDs of selected bed samples from both experiment and simulation. Here, it is observed again that when the Sauter mean diameters in the simulation and in the experiment are close to each other, the simulated PSDs match well with the experimental PSDs.

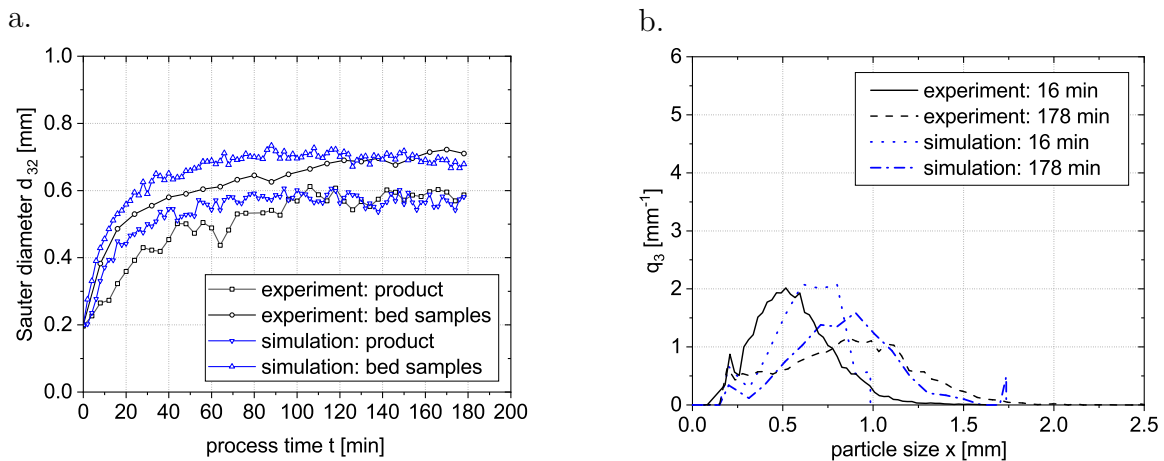


Figure 7.9: Comparison of Exp. F1 and Sim. F1: a. evolution of particle size, b. PSDs of selected samples.

7.3.4 Effect of binder spray rate

To simulate the effect of binder spray rate on the growth behavior of particle size, Sim. S1 and S2 are conducted with the binder spray rate at 98 and 53 g/min, respectively. Figure 7.11a depicts the evolution of particle size with the spray rate increased to 98 g/min. Because the change in bed mass used in the simulation is obtained from the corresponding experiment, the simulation has to be stopped after 88 min of process time. Here, we see that higher spray rate results in higher growth rate of particle size in both simulation and experiment. In the experimental results, we see strong fluctuations (after about 24 min of process time) due to the clogging of spray nozzles and the sticking of particles on the inner surface of the process chamber. In the simulation, we

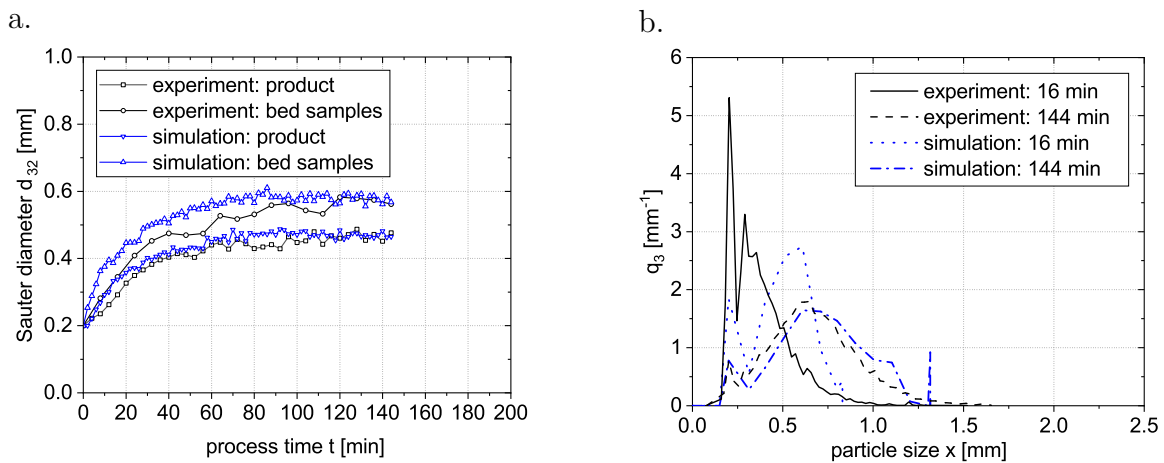


Figure 7.10: Comparison of Exp. F2 and Sim. F2: a. evolution of particle size, b. PSDs of selected samples.

see more fluctuations with larger particle size (after 60 min of process time), which is due to the random breakage of these large particles. Figure 7.11b illustrates the PSDs of selected bed samples. In the transient period, more large particles are seen in the simulated PSD than that achieved in experiment. Again, if the Sauter mean diameters in the simulation and experiment are close, the bed samples have good agreement in the PSDs. When the spray rate is reduced to 53 g/min, a very moderate growth rate and much smaller particle size are seen in the simulation and experiment (shown in Figure 7.12a). In the simulation, the particle size in both transient period and steady state are well reproduced. Although the Sauter mean diameter in the simulation at 16 min matches well with the experimental results, a wider PSD is observed in the experimental results (Figure 7.12b).

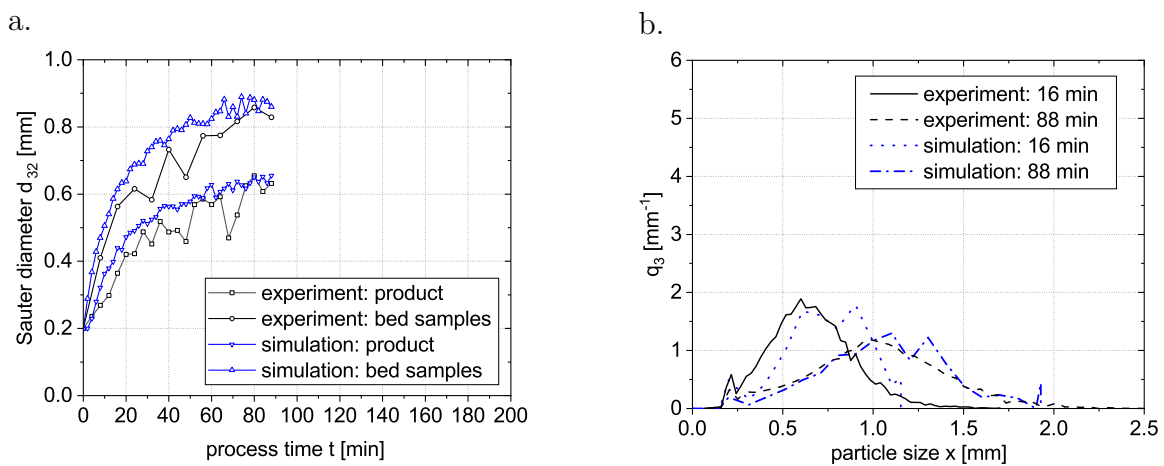


Figure 7.11: Comparison of Exp. S1 and Sim. S1: a. evolution of particle size, b. PSDs of selected samples.

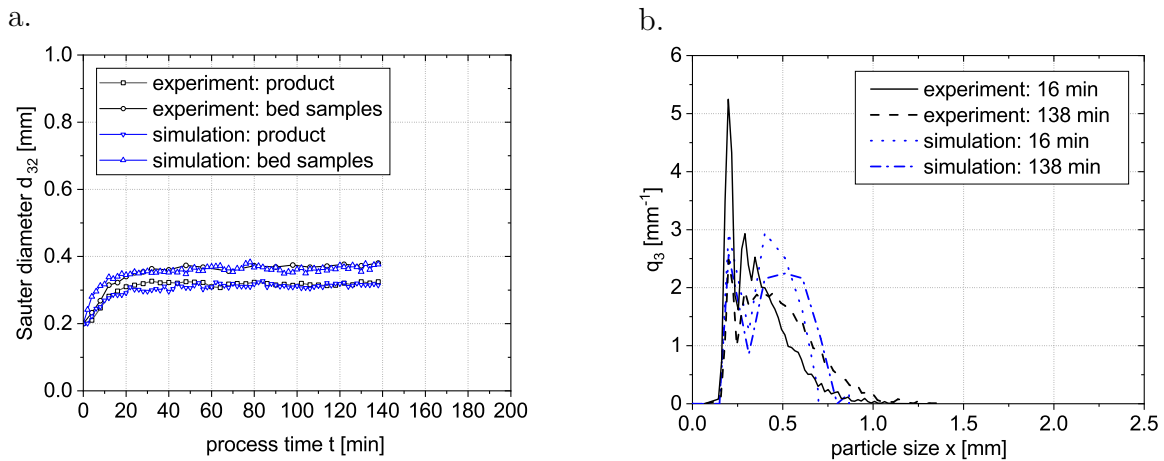


Figure 7.12: Comparison of Exp. S2 and Sim. S2: a. evolution of particle size, b. PSDs of selected samples.

7.3.5 Effect of binder concentration

To simulate the effect of binder concentration on the growth behavior of particle size, Sim. B1 and B2 are conducted with the binder mass fraction at 5 % and 3 %, respectively. The viscosity of binder liquid is determined by its concentration. According to Equations 3.14 and 4.19, the size of spray droplets is significantly influenced by the binder concentration. Thus, the size of droplets as well as the number of positions are varied in these two simulations. As listed in Table 7.1, the droplet size is increased to 46 μm , and the number of positions is decreased to 18 for Sim. B1. Figure 7.13a demonstrates the evolution of particle size achieved from Sim. B1. It can be seen that, the growth rate in simulation is overestimated in the transient period, whereas the size is underestimated in steady state. Due to the decreased position number and increased droplet size, the growth rate at the beginning of the process in simulation is high. However, the particle growth rate in the simulation decreases gradually from about 60 min of process time, and then it reaches to the steady state faster. Comparing the PSDs in the simulation and experiment at 180 min of process time (Figure 7.13b), it is observed that the maximum particle size in the simulation is limited to about 1.3 mm, which is obviously lower than that in experiment. This may be caused by the simplified breakage model. When the binder concentration is reduced to 3 %, the droplet size is decreased to 33 μm , and the number of positions is increased to 36 for Sim. B2. As presented in Figure 7.14a, the particle growth rate is reduced significantly with smaller particles at the end of process. Compared to experimental results, the particle size is overestimated in the transient period (from the beginning to about 40 min), then the particle size in the simulation reaches to steady state with small fluctuations. However, the particle size continues growing in experiment until almost 130 min of process time. Seen from Figure 7.14b, the PSD from the simulation at 178 min has narrower distribution than that achieved in experiment.

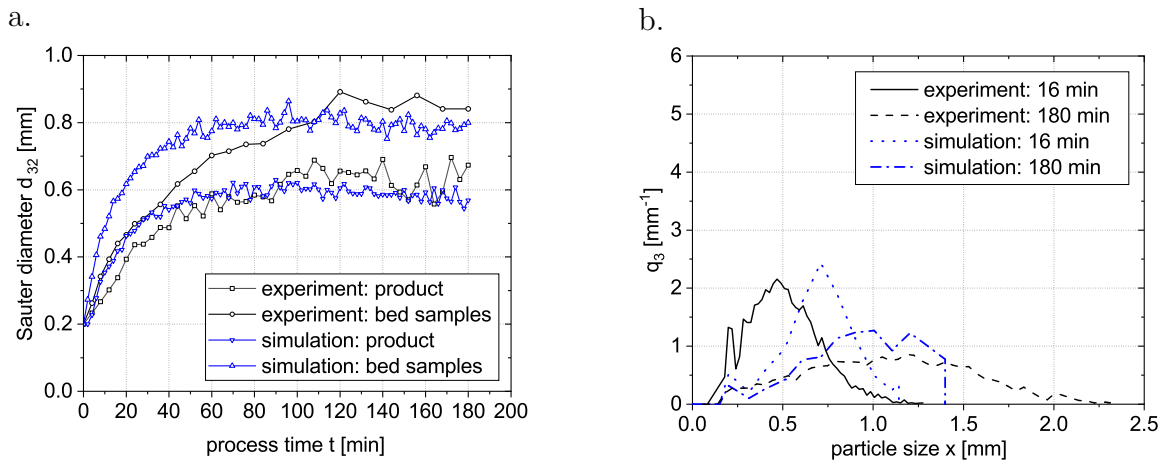


Figure 7.13: Comparison of Exp. B1 and Sim. B1: a. evolution of particle size, b. PSDs of selected samples.

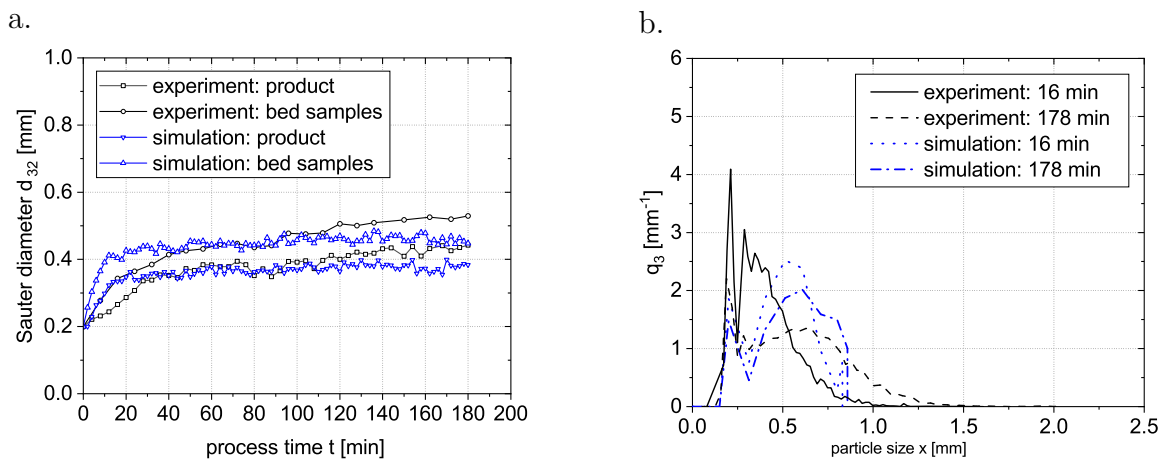


Figure 7.14: Comparison of Exp. B2 and Sim. B2: a. evolution of particle size, b. PSDs of selected samples.

7.3.6 Effect of outlet weir height

As detailed in Chapter 5, when an outlet weir of lower height is used, the bed mass and the separation effect are significantly reduced. To simulate the effect of outlet weir height, Sim. Ref-L is conducted by using the same model that is used for Sim. Ref. Only the change in bed mass and the value of separation effect are varied by using the data retrieved from the corresponding experiment. As illustrated in Figure 7.15a, the particle size is overestimated in the simulation. Due to the lower bed mass from the beginning of the process, the ratio of binder droplet number to particle number is higher compared to Sim. Ref. Therefore, a higher growth rate is observed in this simulation. However, when we check the experimental results, it can be observed that the particle size of bed samples in Exp. Ref-L is quite close to Exp. Ref. When the low outlet weir is used, the overspray and the sticking of binder on the inner surface of process chambers are stronger, which means that less binder can be used to generate liquid and solid bridges. However, these two factors are neglected in the current model. Another reason may be that the breakage rate is kept constant in all simulations due to the simplified breakage model. However, if the bed mass is decreased a lot, the probability of successful collision is higher due to the higher ratio of binder droplets to particles, which means more bridges are formed. Since the breakage rate is kept constant, the number of bridges that break in each collision event will not increase. Therefore, the particle size grows faster in the simulation. Similar trend is also observed in Figure 7.15b, which presents the PSDs of selected samples; the particle size is overestimated in the simulation.

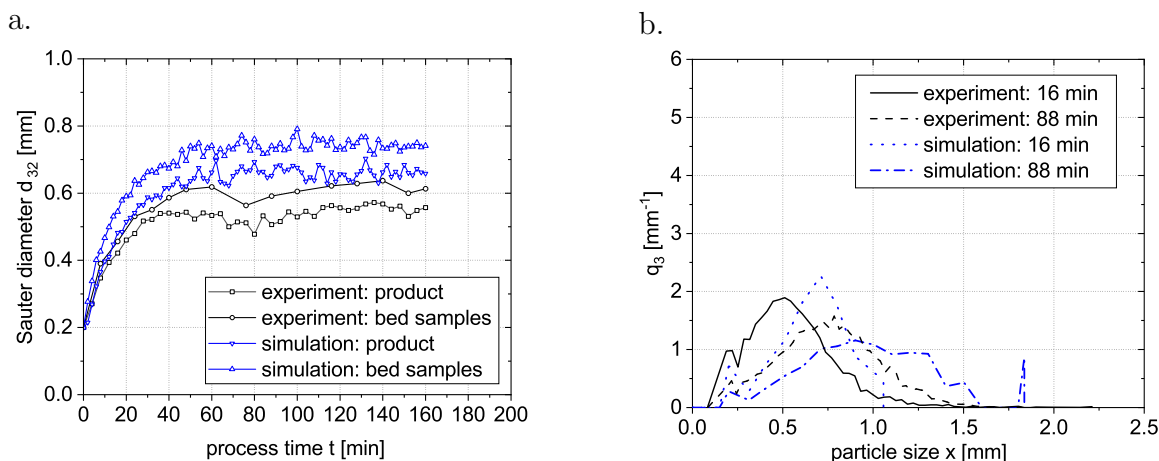


Figure 7.15: Comparison of Exp. Ref-L and Sim. Ref-L: a. evolution of particle size, b. PSDs of selected samples.

7.3.7 Effect of internal weirs

The internal weirs are installed to control the particle flow behavior in the continuous SFBA process. To simulate this process, the Monte Carlo model with four simulation boxes is employed. At first, Sim. W1 and Sim. W2 are conducted with reflux factors R of 6.7 and 7.1, respectively. As presented in Figure 7.16a, the growth of particle size

is slightly overestimated in the simulation from the beginning to the end of the process. However, the growth of particles in Sim. W2 matches better with the experimental results (shown in [Figure 7.17a](#)) compared to Sim. W1. As have been discussed in [Chapter 5](#), the flow of large particles between the process compartments can be restricted due to the smaller gap between the internal weirs and the distribution plate in Exp. W1, which leads to a smaller particle size and more fluctuations compared to Exp. W2. In the model, however, the particles are randomly selected regardless of particle size for each particle flow event, which means the larger particles and the smaller particles have an equal opportunity to flow. Therefore, the particle size is almost identical in Sim. W1 and W2.

Similar to Sim. Ref-L, the model predicts a higher particle growth rate with a lower outlet weir in Sim. W1-L (presented in [Figure 7.18](#)) due to the low bed mass. Differing from Sim. Ref-L, the separation effect is set to zero in this case, according to the experimental results. It is observed that the particle size of bed samples and products in the simulation is almost identical. Compared to Sim. Ref-L, the particle size of bed samples and the difference between products and bed samples are lower, which indicates a weaker accumulation of large particles. Due to the overestimated particle size in the simulation, we see larger particles in the PSDs achieved from simulation than that achieved in the experiment. In terms of particle RTD, the simulation results agree well with the experimental results for all simulations (shown in [Figure 7.16c](#), [Figure 7.17c](#) and [Figure 7.18c](#)). By using the backflow cell model, the particle residence time distribution is successfully represented. The particle mean residence times for Sim. W1, Sim. W2 and Sim. W1-L are 28.80, 28.48 and 19.89 min, respectively.

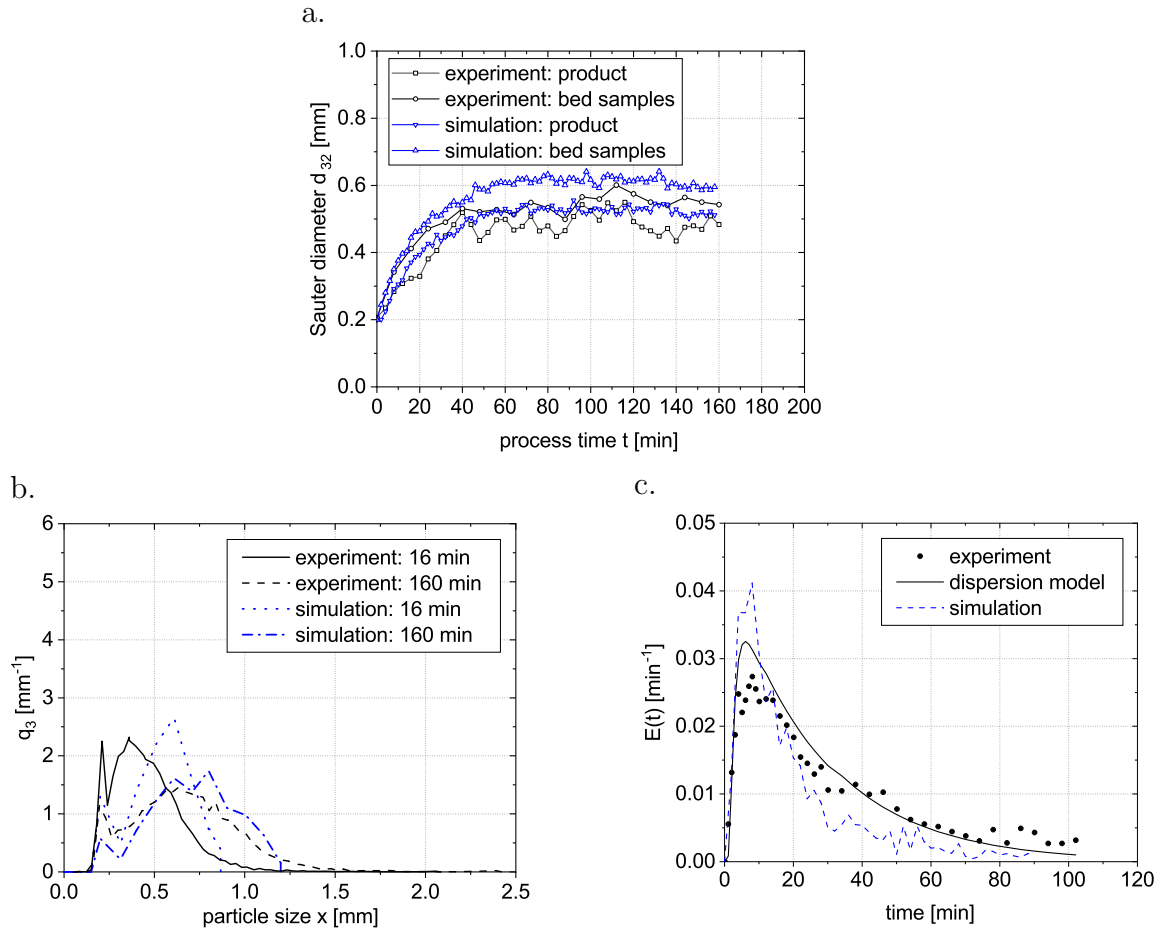


Figure 7.16: Comparison of Exp. W1 and Sim. W1: a. evolution of particle size, b. PSDs of selected samples, c. simulated RTD.

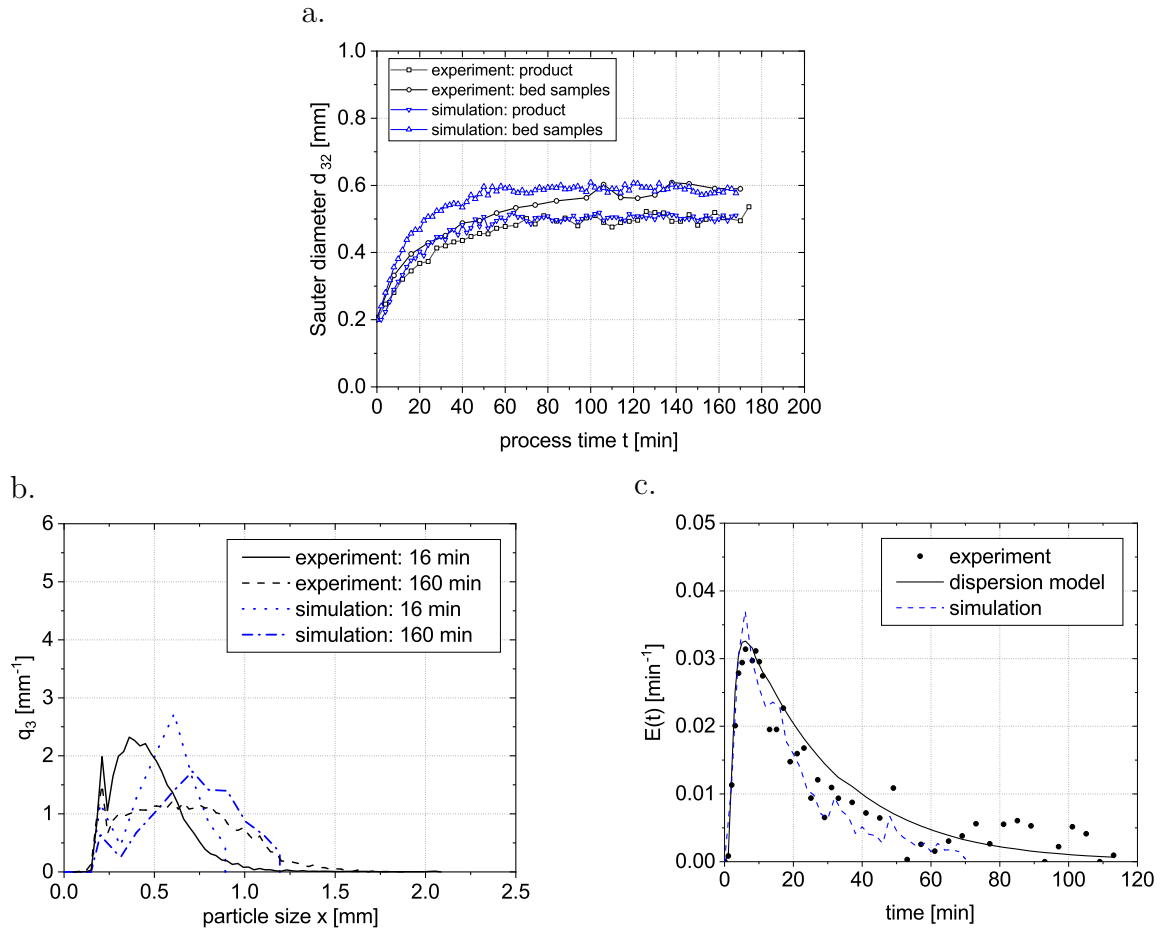


Figure 7.17: Comparison of Exp. W2 and Sim. W2: a. evolution of particle size, b. PSDs of selected samples, c. simulated RTD.

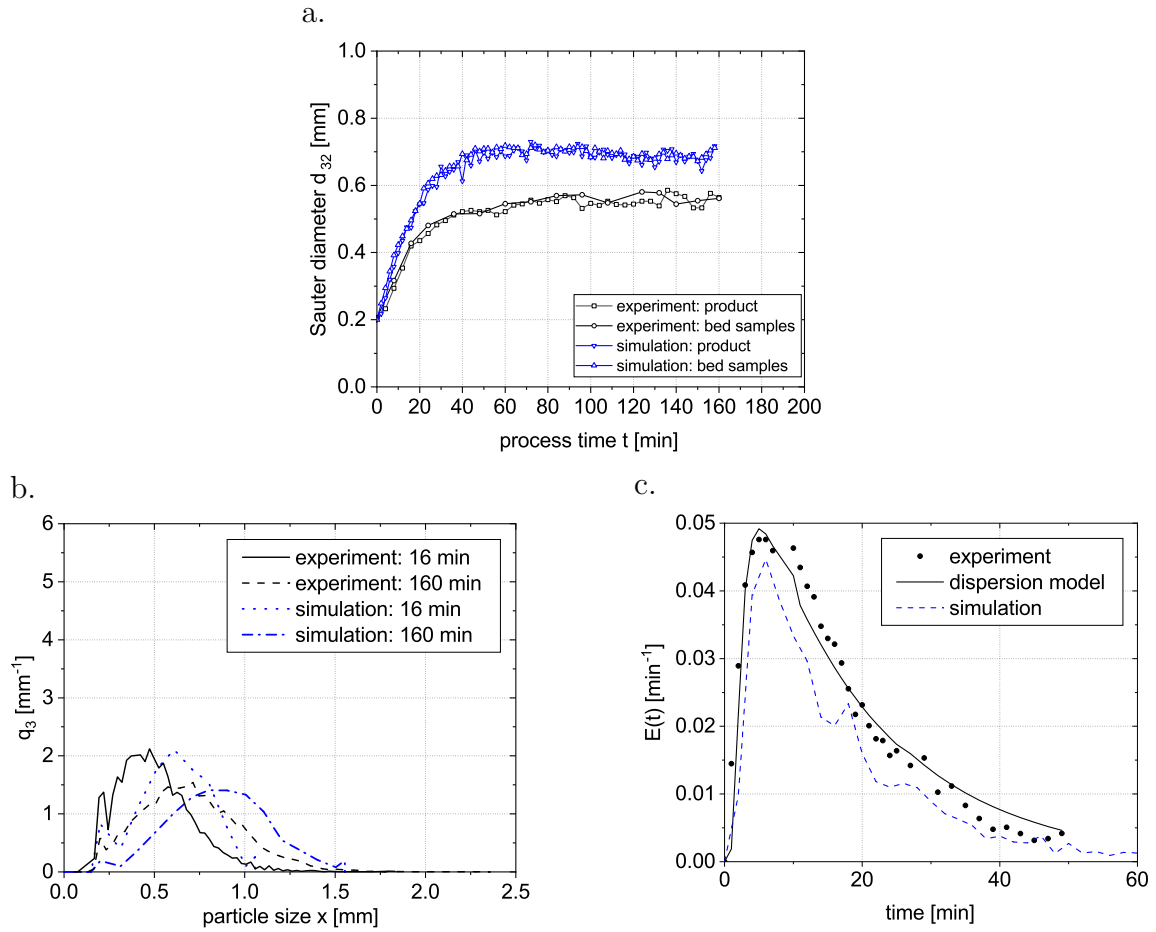


Figure 7.18: Comparison of Exp. W1-L and Sim. W1-L: a. evolution of particle size, b. PSDs of selected samples, c. simulated RTD.

7.3.8 Conclusions

In this chapter, the continuously operated SFBA process in a horizontal fluidized bed with multiple process chambers has been simulated by two Monte Carlo models with different numbers of simulation boxes according to the configuration of internal weirs. Specifically, when internal weirs are not installed, the process is simulated by the model with two simulation boxes with rapid particle exchange between them. When three internal weirs are installed, the process is simulated by the model with four simulation boxes. The particle exchange between different simulation boxes is controlled by the backflow cell model based on RTD data achieved from corresponding experiment. Meanwhile, in each particle flow event, particles are randomly removed from the simulation box according to a predetermined value, and new primary particles are added to the simulation box according to the feed rate.

At first, the collision frequency prefactor is identified by visually fitting the simulation results to the reference experimental results, and then it is used in all simulations. For the reference experiment, the evolution of particle size, the PSDs of selected samples and the particle RTD are well reproduced in the simulation. To further validate the model, two series of simulations are conducted, which correspond to the experiments shown in Chapter 5. In the first series of simulations, the process parameters are varied. The model is able to correctly describe the influence of different process parameters, and the same trends as in the experiments are achieved in all simulations. When the temperature is decreased, the particle size is slightly overestimated by the simulation. Whereas, the particle size is slightly underestimated with lower air temperature. For the simulations with varied particle feed rate and binder spray rate, the simulation results agree well with experimental results. When the binder concentration is increased or decreased, the particle size is overestimated in the transient period, but slightly underestimated in the steady state in both simulations. In the second series of simulations, the configurations of internal weirs or outlet weir is changed. In both simulations with lower outlet weir (Sim. Ref-L and W1-L), the model predicts higher agglomeration rate compared to the experimental results. For the simulation with internal weirs, the particle size is slightly overestimated with lower gap between the internal weirs and distribution plate (Sim. W1), while the simulation results agree well with the experimental results with higher gap between the internal weirs and distribution plate (Sim. W2). Again, the particle RTD is well reproduced with internal weirs.

Chapter 8

Summary and outlook

8.1 Summary

Continuously operated horizontal fluidized beds have been successfully used to perform different processes, such as drying, coating and granulation. However, investigations of the continuously operated agglomeration process in such equipment are missing. In the present work, the continuous agglomeration process conducted in a pilot scale horizontal fluidized bed is systemically investigated with varied parameters and different weir configurations. The particle growth behavior, RTD, process stability and operation window are presented. Meanwhile, the Monte Carlo method is successfully applied to represent the continuous agglomeration process for the first time. The new proposed model can be either used to simulate the process performed in a cylindrical fluidized bed with a single process chamber or used to simulate the process performed in a horizontal fluidized bed with multiple process chambers. In the simulation, a particle flow event that takes place periodically is used to simulate the feed of particles and the discharge of products. Furthermore, the backflow cell model is used to control the particle exchange between different simulation boxes if the model is employed to simulate the process in the horizontal fluidized bed with internal weirs installed.

Experimental investigations on the continuous agglomeration process help us understand the process behavior. It is observed that the process behavior is significantly influenced by process parameters. To be specific, the decrease in air temperature and particle feed rate promotes the agglomeration rate, whereas the decrease in binder concentration and spray rate reduces the agglomeration rate. Meanwhile, internal weirs can be used to control the dispersion of particles and decrease the separation effect. With the installation of internal weirs, the separation effect is reduced, which means that the size difference between the bed particles and the products is smaller. Finally, with the installation of internal weirs and low outlet weir, the separation effect can be eliminated. It is also observed that the fluctuations of particle size and the stability of the process heavily depend on the agglomeration rate. At a higher agglomeration rate, larger agglomerates are achieved with more fluctuations, and their accumulation increases the risk of defluidization. Instead of oscillations in the evolution of particle

size, a continual increase in particle size is frequently seen. Although most experiments in this work have reached a steady state, operation parameters need to be chosen carefully, and the process needs to be controlled attentively to avoid the collapse of the bed, especially when the plant is used to produce large agglomerates.

To simulate the continuous SBFA process, the Monte Carlo method is used by adding a particle flow event. The particle flow event is considered as an extra event that takes place periodically, which is used to control the particle flow behavior and the change in bed mass. When the model is applied to simulate the process in a cylindrical fluidized bed with a single process chamber, the feed of particles and the discharge of products are included in this event. By comparing with experimental results, the Monte Carlo model was found able to simulate the continuous SFBA process performed in the cylindrical fluidized bed. The evolution of particle size, PSDs and change in bed mass are well reproduced in the simulation. Further on, for the simulation of the continuous SFBA process performed in a horizontal fluidized bed with multiple process chambers, a model version with multiple simulation boxes is proposed. Without internal weirs, the fluidized bed is simulated by two simulation boxes with a rapid exchange of particles between them. With three internal weirs, the process is simulated by four simulation boxes. The backflow cell model is used to control the particle exchange between different simulation boxes. Same trends are observed in the simulations and experiments when the process parameters are changed. Although the simulation speed may restrict the usage of these models in the field of process control, they can still be used to predict the process behavior with given parameters, which may reduce the effort necessary for future development.

8.2 Outlook

Concerning the continuous SFBA process, it has been proved that the horizontal fluidized bed is capable of performing this process, and the steady state could be reached with appropriate parameters. In future work, experiments should be performed with amorphous particles such as maltodextrin and lactose as primary particles and water as binder liquid. In order to decrease the accumulation of large particles, the plant could be modified by the installation of an internal classifier or an external classifier with a reflux system to separate and discharge the large particles. For the development of control concepts, experiments with varied parameters during the process should be performed to test its response to different parameters. With multiple process chambers, the horizontal fluidized bed has the possibility to run different processes in different chambers simultaneously, which may be an option to improve the process efficiency further.

Regarding the Monte Carlo method, the new proposed model has shown its potential for the simulation of continuous SFBA processes performed either in a cylindrical fluidized bed or in a horizontal fluidized bed. However, due to the complexity of the micro-events, there are still many assumptions and simplifications in the present model, which need to be relaxed and improved in future work, especially regarding the collision frequency

and agglomerate breakage. The real process time is directly linked to the event number in the simulation by the collision frequency. Therefore, this parameter can significantly influence process behavior in the simulation. As has been proposed by Jiang et al. [118], the coupling of CFD-DEM with the Monte Carlo method may provide additional opportunities. Concerning the breakage of agglomerates, the simplified breakage model ignores the distribution of particle size, bridges (wet or dry) and collision velocity. To improve the breakage model, different types of breakage such as fragmentation and attrition shall be considered for different collision energies and sizes.

References

- [1] J. Litster, Design and Processing of Particulate Products, Cambridge University Press, Cambridge, 2016.
- [2] B. Cuq, R. Jeantet, K. Saleh, T. Ruiz, Chapter 7: Agglomeration/granulation in food powder production, in: B. Bhandari, N. Bansal, M. Zhang, P. Schuck (Eds.), Handbook of Food Powders, Woodhead Publishing Series in Food Science, Technology and Nutrition, Woodhead Publishing, 150–177, 2013.
- [3] S. M. Iveson, J. D. Litster, K. Hapgood, B. J. Ennis, Nucleation, growth and breakage phenomena in agitated wet granulation processes: A review, Powder Technology 117 (1-2) (2001) 3–39.
- [4] K. Chen, P. Bachmann, A. Bück, M. Jacob, E. Tsotsas, Experimental study and modeling of particle drying in a continuously-operated horizontal fluidized bed, Particuology 34 (2017) 134–146.
- [5] P. Bachmann, K. Chen, A. Bück, E. Tsotsas, Prediction of particle size and layer-thickness distributions in a continuous horizontal fluidized-bed coating process, Particuology 50 (2020) 1–12.
- [6] M. Schmidt, C. Rieck, A. Bück, E. Tsotsas, Experimental investigation of process stability of continuous spray fluidized bed layering with external product separation, Chemical Engineering Science 137 (2015) 466–475.
- [7] M. Schmidt, A. Bück, E. Tsotsas, Experimental investigation of process stability of continuous spray fluidized bed layering with internal separation, Chemical Engineering Science 126 (2015) 55–66.
- [8] H. Uhlemann, J. Schmoll, M. Bucheler, Apparatus for continuous fluidized bed agglomeration, US 5480617A, USA, 1996.
- [9] M. Schmidt, Process dynamics and structure formation in continuous spray fluidized bed processes, Ph.D. thesis, Otto von Guericke University Magdeburg, 2018.

-
- [10] G. Strenzke, R. Dürr, A. Bück, E. Tsotsas, Influence of operating parameters on process behavior and product quality in continuous spray fluidized bed agglomeration, *Powder Technology* 375 (2020) 210–220.
- [11] F. Winkler, Verfahren zum Herstellen von Wassergas, DE437970C, 1922.
- [12] J. R. Grace, X. Bi, N. Ellis, *Essentials of Fluidization Technology*, John Wiley & Sons, 2020.
- [13] J. R. Grace, Contacting modes and behaviour classification of gas-solid and other two-phase suspensions, *The Canadian Journal of Chemical Engineering* 64 (3) (1986) 353–363.
- [14] D. Geldart, Types of gas fluidization, *Powder Technology* 7 (5) (1973) 285–292.
- [15] L. Mörl, S. Heinrich, M. Peglow, Chapter 2 - Fluidized bed spray granulation, in: A. Salman, M. Hounslow, J. Seville (Eds.), *Granulation*, vol. 11 of *Handbook of Powder Technology*, Elsevier Science B.V., 21–188, 2007.
- [16] B. J. Ennis, Agglomeration and size enlargement session summary paper, *Powder Technology* 88 (3) (1996) 203–225.
- [17] K. Saleh, R. Cherif, M. Hemati, An experimental study of fluidized-bed coating: Influence of operating conditions on growth rate and mechanism, *Advanced Powder Technology* 10 (3) (1999) 255–277.
- [18] M. Schmidt, A. Bück, E. Tsotsas, Experimental investigation of the influence of drying conditions on process stability of continuous spray fluidized bed layering granulation with external product separation, *Powder Technology* 320 (2017) 474–482.
- [19] H. Tan, A. Salman, M. Hounslow, Kinetics of fluidised bed melt granulation, Part 1: The effect of process variables, *Chemical Engineering Science* 61 (5) (2006) 1585–1601.
- [20] P. M. Wong, L. W. Chan, P. W. S. Heng, Investigation on side-spray fluidized bed granulation with swirling airflow, *AAPS PharmSciTech* 14 (1) (2013) 211–221.
- [21] D. Z. L. Er, C. V. Liew, P. W. S. Heng, Layered growth with bottom-spray granulation for spray deposition of drug, *International Journal of Pharmaceutics* 377 (1) (2009) 16–24.
- [22] M. E. Aulton, Drying, in: *Aulton's pharmaceuticals: The design and manufacture of medicines*, Elsevier Health Sciences, 487–503, 2013.
- [23] D. E. Wurster, Air-suspension technique of coating drug particles: A preliminary report, *Journal of the American Pharmaceutical Association* 48 (8) (1959) 451–454.

- [24] D. E. Wurster, Particle-coating methods, *Pharmaceutical dosage forms: Tablets* 3 (1990) 161–197.
- [25] M. Xu, P. W. S. Heng, C. V. Liew, Evaluation of coat uniformity and taste-masking efficiency of irregular-shaped drug particles coated in a modified tangential spray fluidized bed processor, *Expert Opinion on Drug Delivery* 12 (10) (2015) 1597–1606.
- [26] R. N. Elsergany, L. W. Chan, P. W. S. Heng, Application of the modified tangential spray-fluidized bed to produce nonpareils from primary crystals, *AAPS PharmSciTech* 20 (3) (2019) 1–13.
- [27] C. Vecchio, F. Fabiani, M. E. Sangalli, L. Zema, A. Gazzaniga, Rotary tangential spray technique for aqueous film coating of indobufen pellets, *Drug Development and Industrial Pharmacy* 24 (3) (1998) 269–274, PMID: 9876584.
- [28] J. Bouffard, H. Dumont, F. Bertrand, R. Legros, Optimization and scale-up of a fluid bed tangential spray roto granulation process, *International Journal of Pharmaceutics* 335 (1) (2007) 54–62.
- [29] M. Peglow, S. Antonyuk, M. Jacob, S. Palzer, S. Heinrich, E. Tsotsas, Chapter 7: Particle formulation in spray fluidized beds, in: E. Tsotsas, A. S. Mujumdar (Eds.), *Modern Drying Technology*, Wiley-VCH, Weinheim, 295–378, 2011.
- [30] G. Wang, L. Yang, R. Lan, T. Wang, Y. Jin, Granulation by spray coating aqueous solution of ammonium sulfate to produce large spherical granules in a fluidized bed, *Particuology* 11 (5) (2013) 483–489.
- [31] I. M. Cotabarren, D. Bertín, S. Veliz, L. Mirazú, J. Piña, V. Bucalá, Chapter 1: Production of granular urea as nitrogenous fertilizer, in: C. M. Muñoz, A. M. Fernández (Eds.), *Urea: Synthesis, Properties and Uses*, Nova Science Publishers, New York, 1–63, 2012.
- [32] M. Capece, R. Dave, Application of fluidized bed film coating for membrane encapsulation of catalysts, *Powder Technology* 211 (2) (2011) 199–206.
- [33] C. P. Coronel-Aguilera, M. F. San Martín-González, Encapsulation of spray dried β -carotene emulsion by fluidized bed coating technology, *LWT - Food Science and Technology* 62 (1) (2015) 187–193.
- [34] A. Maroni, L. Zema, G. Loreti, L. Palugan, A. Gazzaniga, Film coatings for oral pulsatile release, *International Journal of Pharmaceutics* 457 (2) (2013) 362–371.
- [35] S. Bose, R. H. Bogner, Solventless pharmaceutical coating processes: A Review, *Pharmaceutical Development and Technology* 12 (2) (2007) 115–131.
- [36] A. Madene, M. Jacquot, J. Scher, S. Desobry, Flavour encapsulation and controlled release: A review, *International Journal of Food Science & Technology* 41 (1) (2006) 1–21.

- [37] A. Burggraeve, T. Monteyne, C. Vervaet, J. P. Remon, T. D. Beer, Process analytical tools for monitoring, understanding, and control of pharmaceutical fluidized bed granulation: A review, *European Journal of Pharmaceutics and Biopharmaceutics* 83 (1) (2013) 2–15.
- [38] S. Palzer, Agglomeration of pharmaceutical, detergent, chemical and food powders - Similarities and differences of materials and processes, *Powder Technology* 206 (1) (2011) 2–17.
- [39] N. Jinapong, M. Suphantharika, P. Jamnong, Production of instant soymilk powders by ultrafiltration, spray drying and fluidized bed agglomeration, *Journal of Food Engineering* 84 (2) (2008) 194–205.
- [40] R. Boerefijn, M. Hounslow, Studies of fluid bed granulation in an industrial R&D context, *Chemical Engineering Science* 60 (14) (2005) 3879 – 3890.
- [41] M. Hemati, R. Cherif, K. Saleh, V. Pont, Fluidized bed coating and granulation: Influence of process-related variables and physicochemical properties on the growth kinetics, *Powder Technology* 130 (1-3) (2003) 18–34.
- [42] J. Du, A. Bück, E. Tsotsas, Investigation of spray agglomeration process in continuously operated horizontal fluidized bed, in: *Proceedings of 21st International Drying Symposium, Valencia, Spain, 1855–1862, 2018*.
- [43] K. Dewettinck, L. Deroo, W. Messens, A. Huyghebaert, Agglomeration tendency during top-spray fluidized bed coating with gums, *LWT - Food Science and Technology* 31 (6) (1998) 576–584.
- [44] G. Barnocky, R. H. Davis, Elastohydrodynamic collision and rebound of spheres: Experimental verification, *The Physics of Fluids* 31 (6) (1988) 1324–1329.
- [45] B. J. Ennis, G. Tardos, R. Pfeffer, A microlevel-based characterization of granulation phenomena, *Powder Technology* 65 (1-3) (1991) 257–272.
- [46] J. Akkermans, M. Edwards, A. Groot, C. Montanus, R. van Pomeran, K. Yüregir, Production of detergent granulates, *International Patent WO9858046*, 1998.
- [47] P. D. Hede, P. Bach, A. D. Jensen, Validation of the flux number as scaling parameter for top-spray fluidised bed systems, *Chemical Engineering Science* 63 (3) (2008) 815–828.
- [48] C. Rieck, A. Bück, E. Tsotsas, Estimation of the dominant size enlargement mechanism in spray fluidized bed processes, *AIChE Journal* 66 (5) (2020) 576–594.
- [49] H. Rumpf, Grundlagen und Methoden des Granulierens, *Chemie Ingenieur Technik* 30 (3) (1958) 144–158.

- [50] A. Bück, E. Tsotsas, K. Sommer, Size Enlargement, in: Ullmann's Encyclopedia of Industrial Chemistry, Wiley-VCH, Weinheim, 1–47, 2014.
- [51] C. Rieck, Microscopic and macroscopic modeling of particle formation processes in spray fluidized beds, Ph.D. thesis, Otto von Guericke University Magdeburg, 2020.
- [52] A. Bück, E. Tsotsas, Chapter 12: Agglomeration, in: B. Caballero, P. Finglas, F. Toldrá (Eds.), Encyclopedia of food and health, Academic Press, Waltham, MA., 73–81, 2015.
- [53] W. Pietsch, Agglomeration processes: Phenomena, technologies, equipment, Wiley-VCH, Weinheim, 2001.
- [54] G. Reynolds, J. Fu, Y. Cheong, M. Hounslow, A. Salman, Breakage in granulation: A review, Chemical Engineering Science 60 (14) (2005) 3969–3992.
- [55] C. Turchiuli, Z. Eloualia, N. El Mansouri, E. Dumoulin, Fluidised bed agglomeration: Agglomerates shape and end-use properties, Powder Technology 157 (1) (2005) 168–175.
- [56] S. Watano, T. Fukushima, K. Miyanami, Heat transfer and granule growth rate in fluidized bed granulation, Chemical and Pharmaceutical Bulletin 44 (3) (1996) 572–576.
- [57] R. Turton, G. I. Tardos, B. J. Ennis, Chapter 6: Fluidized bed coating and granulation, in: W.-C. Yang (Ed.), Fluidization, Solids Handling, and Processing, William Andrew Publishing, Westwood, NJ, 331–434, 1999.
- [58] K. Saleh, D. Steinmetz, M. Hemati, Experimental study and modeling of fluidized bed coating and agglomeration, Powder Technology 130 (1) (2003) 116–123.
- [59] H. Tan, A. Salman, M. Hounslow, Kinetics of fluidised bed melt granulation, Part 3: Tracer studies, Chemical Engineering Science 60 (14) (2005) 3835–3845.
- [60] M. Peglow, J. Kumar, S. Heinrich, G. Warnecke, E. Tsotsas, L. Mörl, B. Wolf, A generic population balance model for simultaneous agglomeration and drying in fluidized beds, Chemical Engineering Science 62 (1) (2007) 513–532.
- [61] F. Thielmann, M. Naderi, M. A. Ansari, F. Stepanek, The effect of primary particle surface energy on agglomeration rate in fluidised bed wet granulation, Powder Technology 181 (2) (2008) 160–168.
- [62] R. Hampel, Beitrag zur Analyse von kinetischen Einflüssen auf die Wirbelschicht-Sprühagglomeration, Ph.D. thesis, Otto von Guericke University Magdeburg, 2010.

- [63] M. Dadkhah, M. Peglow, E. Tsotsas, Characterization of the internal morphology of agglomerates produced in a spray fluidized bed by X-ray tomography, *Powder Technology* 228 (2012) 349–358.
- [64] M. Dadkhah, E. Tsotsas, Influence of process variables on internal particle structure in spray fluidized bed agglomeration, *Powder Technology* 258 (2014) 165–173.
- [65] M. Dadkhah, E. Tsotsas, Study of the morphology of solidified binder in spray fluidized bed agglomerates by X-ray tomography, *Powder Technology* 264 (2014) 256–264.
- [66] R. Pashminehazar, A. Kharaghani, E. Tsotsas, Three dimensional characterization of morphology and internal structure of soft material agglomerates produced in spray fluidized bed by X-ray tomography, *Powder Technology* 300 (2016) 46–60.
- [67] R. Pashminehazar, S. J. Ahmed, A. Kharaghani, E. Tsotsas, Spatial morphology of maltodextrin agglomerates from X-ray microtomographic data: Real structure evaluation vs. spherical primary particle model, *Powder Technology* 331 (2018) 204–217.
- [68] I. Atalar, F. Yazici, Effect of different binders on reconstitution behaviors and physical, structural, and morphological properties of fluidized bed agglomerated yoghurt powder, *Drying Technology* 37 (13) (2019) 1656–1664.
- [69] H. Uhlemann, L. Mörl, *Wirbelschicht-Sprühgranulation*, Springer, 2013.
- [70] N. Hampel, A. Bück, M. Peglow, E. Tsotsas, Continuous pellet coating in a Wurster fluidized bed process, *Chemical Engineering Science* 86 (2013) 87–98.
- [71] L. Nilson, R. Wimmerstedt, Drying in longitudinal-flow vibrating fluid-beds, *Drying Technology* 5 (3) (1987) 337–361.
- [72] S. Wetchacama, S. Soponronnarit, W. Jariyatontivait, Development of a commercial scale vibro-fluidized bed paddy dryer, *Agriculture and Natural Resources* 34 (3) (2000) 423–430.
- [73] M. Khanali, S. Rafiee, A. Jafari, A. Banisharif, Study of residence time distribution of rough rice in a plug flow fluid bed dryer, *International Journal of Advanced Science and Technology* 48 (2012) 103–114.
- [74] P. Bachmann, A. Bück, E. Tsotsas, Investigation of the residence time behavior of particulate products and correlation for the Bodenstein number in horizontal fluidized beds, *Powder Technology* 301 (2016) 1067–1076.
- [75] P. Bachmann, A. Bück, E. Tsotsas, Experimental investigation and correlation of the Bodenstein number in horizontal fluidized beds with internal baffles, *Powder Technology* 308 (2017) 378–387.

- [76] K. Chen, P. Bachmann, A. Bück, M. Jacob, E. Tsotsas, CFD simulation of particle residence time distribution in industrial scale horizontal fluidized bed, *Powder Technology* 345 (2019) 129–139.
- [77] S. Pietsch, M. Schönherr, F. Kleine Jäger, S. Heinrich, Measurement of residence time distributions in a continuously operated spouted bed, *Chemical Engineering & Technology* 43 (5) (2020) 804–812.
- [78] S. Heinrich, M. Peglow, L. Mörl, Unsteady and steady-state particle size distributions in batch and continuous fluidized bed granulation systems, *Chemical Engineering Journal* 86 (1) (2002) 223–231.
- [79] A. Bück, S. Palis, E. Tsotsas, Model-based control of particle properties in fluidised bed spray granulation, *Powder Technology* 270 (2015) 575–583.
- [80] D. Müller, A. Bück, E. Tsotsas, Influence of separation properties and processing strategies on product characteristics in continuous fluidized bed spray granulation, *Powder Technology* 342 (2019) 572–584.
- [81] J. Du, A. Bück, E. Tsotsas, Influence of process variables on spray agglomeration process in a continuously operated horizontal fluidized bed, *Powder Technology* 363 (2020) 195–206.
- [82] E. Diez, K. Meyer, A. Bück, E. Tsotsas, S. Heinrich, Influence of process conditions on the product properties in a continuous fluidized bed spray granulation process, *Chemical Engineering Research and Design* 139 (2018) 104–115.
- [83] K. Chen, Modeling and validation of particle drying and coating in a continuously operated horizontal fluidized bed, Ph.D. thesis, Otto von Guericke University Magdeburg, 2020.
- [84] R. Mac Mullin, M. Weber, The theory of short-circuiting in continuous-flow mixing vessels in series and kinetics of chemical reactions in such systems, *Transactions of American Institute of Chemical Engineers* 31 (1935) 409–458.
- [85] M. H. Roemer, L. D. Durbin, Transient response and moments analysis of back-flow cell model for flow systems with longitudinal mixing, *Industrial & Engineering Chemistry Fundamentals* 6 (1) (1967) 120–129.
- [86] K. Terrazas-Velarde, M. Peglow, E. Tsotsas, Stochastic simulation of agglomerate formation in fluidized bed spray drying: A micro-scale approach, *Chemical Engineering Science* 64 (11) (2009) 2631–2643.
- [87] M. Dervedde, M. Peglow, E. Tsotsas, A novel, structure-tracking Monte Carlo algorithm for spray fluidized bed agglomeration, *AIChE Journal* 58 (10) (2012) 3016–3029.

-
- [88] C. Rieck, M. Schmidt, A. Bück, E. Tsotsas, Monte Carlo modeling of binder-less spray agglomeration in fluidized beds, *AIChE Journal* 64 (10) (2018) 3582–3594.
- [89] M. Hounslow, The population balance as a tool for understanding particle rate processes, *KONA Powder and Particle Journal* 16 (1998) 179–193.
- [90] H. Hulburt, S. Katz, Some problems in particle technology: A statistical mechanical formulation, *Chemical Engineering Science* 19 (8) (1964) 555–574.
- [91] J. Li, B. Freireich, C. Wassgren, J. D. Litster, A general compartment-based population balance model for particle coating and layered granulation, *AIChE Journal* 58 (5) (2012) 1397–1408.
- [92] S. Heinrich, M. Peglow, M. Ihlow, M. Henneberg, L. Mörl, Analysis of the start-up process in continuous fluidized bed spray granulation by population balance modelling, *Chemical Engineering Science* 57 (20) (2002) 4369–4390.
- [93] A. Vreman, C. van Lare, M. Hounslow, A basic population balance model for fluid bed spray granulation, *Chemical Engineering Science* 64 (21) (2009) 4389–4398.
- [94] D. Ramkrishna, *Population balances: Theory and Applications to Particulate Systems in Engineering*, Elsevier, 2000.
- [95] M. Capece, E. Bilgili, R. Dave, Identification of the breakage rate and distribution parameters in a non-linear population balance model for batch milling, *Powder Technology* 208 (1) (2011) 195–204.
- [96] T. J. Crowley, E. S. Meadows, E. Kostoulas, F. J. Doyle III, Control of particle size distribution described by a population balance model of semibatch emulsion polymerization, *Journal of Process Control* 10 (5) (2000) 419–432.
- [97] C. B. B. Costa, M. R. W. Maciel, R. M. Filho, Considerations on the crystallization modeling: Population balance solution, *Computers & Chemical Engineering* 31 (3) (2007) 206–218.
- [98] A. D. Randolph, M. A. Larson (Eds.), *Theory of Particulate Processes*, Academic Press, 1971.
- [99] M. J. Hounslow, R. L. Ryall, V. R. Marshall, A discretized population balance for nucleation, growth, and aggregation, *AIChE Journal* 34 (11) (1988) 1821–1832.
- [100] M. Hussain, J. Kumar, M. Peglow, E. Tsotsas, Modeling spray fluidized bed aggregation kinetics on the basis of Monte-Carlo simulation results, *Chemical Engineering Science* 101 (2013) 35–45.
- [101] P. Kapur, Kinetics of granulation by non-random coalescence mechanism, *Chemical Engineering Science* 27 (10) (1972) 1863–1869.

-
- [102] P. A. L. Wauters, B. Scarlett, L. X. Liu, J. D. Litster, G. M. H. Meesters, A population balance model for high shear granulation, *Chemical Engineering Communications* 190 (10) (2003) 1309–1334.
- [103] P. Rajniak, F. Stepanek, K. Dhanasekharan, R. Fan, C. Mancinelli, R. Chern, A combined experimental and computational study of wet granulation in a Wurster fluid bed granulator, *Powder Technology* 189 (2) (2009) 190–201.
- [104] M. Hussain, J. Kumar, E. Tsotsas, A new framework for population balance modeling of spray fluidized bed agglomeration, *Particuology* 19 (2015) 141–154.
- [105] I. Golovin, G. Strenzke, R. Dürr, S. Palis, A. Bück, E. Tsotsas, A. Kienle, Parameter identification for continuous fluidized bed spray agglomeration, *Processes* 6 (12) (2018) 1–14.
- [106] E. Otto, R. Dürr, G. Strenzke, S. Palis, A. Bück, E. Tsotsas, A. Kienle, Kernel identification in continuous fluidized bed spray agglomeration from steady state data, *Advanced Powder Technology* 32 (7) (2021) 2517–2529.
- [107] J. Kumar, M. Peglow, G. Warnecke, S. Heinrich, An efficient numerical technique for solving population balance equation involving aggregation, breakage, growth and nucleation, *Powder Technology* 182 (1) (2008) 81–104.
- [108] M. Singh, J. Kumar, A. Bück, E. Tsotsas, A volume-consistent discrete formulation of aggregation population balance equations, *Mathematical Methods in the Applied Sciences* 39 (9) (2016) 2275–2286.
- [109] M. Singh, J. Kumar, A. Bück, E. Tsotsas, An improved and efficient finite volume scheme for bivariate aggregation population balance equation, *Journal of Computational and Applied Mathematics* 308 (2016) 83–97.
- [110] R. L. Harrison, Introduction to Monte Carlo simulation, *AIP Conference Proceedings* 1204 (1) (2010) 17–21.
- [111] K. Binder, D. W. Heermann, *Monte Carlo Simulations in Statistical Physics*, Springer, New York, 2009.
- [112] M. Lísal, M. Bendová, W. R. Smith, Monte Carlo adiabatic simulation of equilibrium reacting systems: The ammonia synthesis reaction, *Fluid Phase Equilibria* 235 (1) (2005) 50–57.
- [113] G. Falope, A. Jones, R. Zauner, On modelling continuous agglomerative crystal precipitation via Monte Carlo simulation, *Chemical Engineering Science* 56 (7) (2001) 2567–2574.
- [114] Y. H. Kwak, L. Ingall, Exploring Monte Carlo simulation applications for project management, *Risk Management* 9 (1) (2007) 44–57.

- [115] D. L. McLeish, *Monte Carlo Simulation and Finance*, John Wiley & Sons, 2011.
- [116] H. Zhao, A. Maisels, T. Matsoukas, C. Zheng, Analysis of four Monte Carlo methods for the solution of population balances in dispersed systems, *Powder Technology* 173 (1) (2007) 38–50.
- [117] C. Rieck, A. Bück, E. Tsotsas, Stochastic modelling of particle coating in fluidized beds, *Procedia Engineering* 102 (2015) 996–1005.
- [118] Z. Jiang, C. Rieck, A. Bück, E. Tsotsas, Modeling of inter- and intra-particle coating uniformity in a Wurster fluidized bed by a coupled CFD-DEM-Monte Carlo approach, *Chemical Engineering Science* 211 (2020) 115289.
- [119] K. Terrazas-Velarde, M. Peglow, E. Tsotsas, Investigation of the kinetics of fluidized bed spray agglomeration based on stochastic methods, *AIChE Journal* 57 (11) (2011) 3012–3026.
- [120] K. Terrazas-Velarde, M. Peglow, E. Tsotsas, Kinetics of fluidized bed spray agglomeration for compact and porous particles, *Chemical Engineering Science* 66 (9) (2011) 1866–1878.
- [121] M. Dervede, M. Peglow, E. Tsotsas, Stochastic modeling of fluidized bed granulation: Influence of droplet pre-drying, *Chemical Engineering and Technology* 34 (7) (2011) 1177–1184.
- [122] A. K. Singh, E. Tsotsas, Stochastic model to simulate spray fluidized bed agglomeration: A morphological approach, *Powder Technology* 355 (2019) 449–460.
- [123] A. K. Singh, E. Tsotsas, A tunable aggregation model incorporated in Monte Carlo simulations of spray fluidized bed agglomeration, *Powder Technology* 364 (2020) 417–428.
- [124] Y. Lin, K. Lee, T. Matsoukas, Solution of the population balance equation using constant-number Monte Carlo, *Chemical Engineering Science* 57 (12) (2002) 2241–2252.
- [125] A. Das, J. Kumar, Population balance modeling of volume and time dependent spray fluidized bed aggregation kernel using Monte Carlo simulation results, *Applied Mathematical Modelling* 92 (2021) 748–769.
- [126] K. Terrazas-Velarde, Monte Carlo simulation of fluidized bed spray agglomeration, Ph.D. thesis, Otto von Guericke University Magdeburg, 2010.
- [127] W. Hintz, S. Antonyuk, W. Schubert, B. Ebenau, A. Haack, J. Tomas, Chapter 6: Determination of physical properties of fine particles, nanoparticles and particle beds, in: E. Tsotsas, A. S. Mujumdar (Eds.), *Modern Drying Technology*, John Wiley & Sons, Ltd, 279–362, 2014.

- [128] P. Danckwerts, Continuous flow systems: Distribution of residence times, *Chemical Engineering Science* 2 (1) (1953) 1–13.
- [129] P. Bachmann, E. Tsotsas, Analysis of residence time distribution data in horizontal fluidized beds, *Procedia Engineering* 102 (2015) 790–798.
- [130] B. Oesterle, A. Petitjean, Simulation of particle-to-particle interactions in gas solid flows, *International Journal of Multiphase Flow* 19 (1) (1993) 199–211.
- [131] P. Buffière, R. Moletta, Collision frequency and collisional particle pressure in three-phase fluidized beds, *Chemical Engineering Science* 55 (22) (2000) 5555–5563.
- [132] T. Hagemeyer, C. Roloff, A. Bück, E. Tsotsas, Estimation of particle dynamics in 2-D fluidized beds using particle tracking velocimetry, *Particuology* 22 (2015) 39–51.
- [133] Z. Jiang, T. Hagemeyer, A. Bück, E. Tsotsas, Experimental measurements of particle collision dynamics in a pseudo-2D gas-solid fluidized bed, *Chemical Engineering Science* 167 (2017) 297–316.
- [134] M. Dervede, Modellierung der Wirbelschicht-Sprühagglomeration unter Berücksichtigung der Partikelstrukturbildung, Ph.D. thesis, Otto von Guericke University Magdeburg, 2013.
- [135] D. T. Gillespie, An exact method for numerically simulating the stochastic coalescence process in a cloud, *Journal of Atmospheric Sciences* 32 (10) (1975) 1977–1989.
- [136] A. H. Lefebvre, V. G. McDonell, *Atomization and sprays*, CRC press, Boca Raton, 2017.
- [137] H. Tan, A. Salman, M. Hounslow, Kinetics of fluidised bed melt granulation, Part 4: Selecting the breakage model, *Powder Technology* 143-144 (2004) 65–83.
- [138] G. I. Tardos, M. I. Khan, P. R. Mort, Critical parameters and limiting conditions in binder granulation of fine powders, *Powder Technology* 94 (3) (1997) 245–258.
- [139] A. K. Singh, E. Tsotsas, Influence of polydispersity and breakage on stochastic simulations of spray fluidized bed agglomeration, *Chemical Engineering Science* 247 (2022) 117022.
- [140] S. Satija, I. Zucker, Hydrodynamics of vibro-fluidized beds, *Drying Technology* 4 (1) (1986) 19–43.
- [141] D. Reay, Particle residence time distributions in "plug flow" fluid bed dryers, in: *Proceedings of 1st International Drying Symposium*, Montreal, Canada, 136–144, 1978.

-
- [142] J. Du, G. Strenzke, A. Bück, E. Tsotsas, Monte Carlo modeling of spray agglomeration in a cylindrical fluidized bed: From batch-wise to continuous processes, *Powder Technology* 396 (2022) 113–126.
- [143] R. Span, Chapter D2.2: Properties of dry air, in: VDI-GVC (Ed.), *VDI Heat Atlas*, Springer-Verlag Berlin Heidelberg, 2010.
- [144] B. Glück, *Zustands- und Stoffwerte - Wasser, Dampf, Luft - Verbrennungsrechnung*, Verlag für Bauwesen, Berlin, 1986.
- [145] B. E. Poling, J. M. Prausnitz, J. P. O'Connell, *The Properties of Gases and Liquids* (5th Edition), McGraw-Hill, 2000.

Appendices

Appendix A

Material properties

A.1 Properties of dry air

Molecular mass ([143])

$$\tilde{M}_g = 28.9583 \quad (\text{A.1})$$

Unit: kg/kmol

Density:

$$\rho_g = \frac{P_{tot} \tilde{M}_g}{\tilde{R}(T + 273.15)} \quad (\text{A.2})$$

$\tilde{R} = 8314.4 \text{ Jkmol}^{-1}\text{K}^{-1}$

Unit: kg/m³

Dynamic viscosity ([144])

$$\mu_g = a_1 + a_2 T_g + a_3 T_g^2 + a_4 T_g^3 \quad (\text{A.3})$$

$$a_1 = +1.705568 \cdot 10^{-5}$$

$$a_2 = +4.511012 \cdot 10^{-8}$$

$$a_3 = -8.766234 \cdot 10^{-12}$$

$$a_4 = -3.382035 \cdot 10^{-15}$$

Unit: Pa s

Range of application: $p = 0.1 \text{ MPa}$; $-20^\circ\text{C} \leq T_g \leq 200^\circ\text{C}$

Maximum error: 0.6%

Kinematic viscosity

$$\nu_g = \frac{\mu_g}{\rho_g} \quad (\text{A.4})$$

Unit: m²/s

Specific heat capacity ([144])

$$s_g = a_1 + a_2 T_g + a_3 T_g^2 + a_4 T_g^3 \quad (\text{A.5})$$

with

$$\begin{aligned} a_1 &= +1006.256 \\ a_2 &= -2.120536 \cdot 10^{-2} \\ a_3 &= -4.180195 \cdot 10^{-4} \\ a_4 &= +1.521916 \cdot 10^{-7} \end{aligned}$$

Unit: J/(kgK)

Range of application: $p = 0.1 \text{ MPa}$; $-20^\circ\text{C} \leq T_g \leq 200^\circ\text{C}$

Maximum error: 0.05%

A.2 Properties of water

Molecular mass of water ([145])

$$\tilde{M}_w = 18.015 \quad (\text{A.6})$$

Unit: kg/kmol

Specific heat capacity of water ([144])

$$s_w = a_1 + a_2 T + a_3 T^2 + a_4 T^3 \quad (\text{A.7})$$

$$\begin{aligned} a_1 &= +4174.785 \\ a_2 &= +1.785308 \cdot 10^{-2} \\ a_3 &= -5.097403 \cdot 10^{-4} \\ a_4 &= +4.216721 \cdot 10^{-5} \end{aligned}$$

Unit: J/(kgK)

Range of application: $-20^\circ\text{C} \leq T \leq T_{sat}(p)$ or 200°C

Maximum error: 0.43%

Saturated pressure of water vapor ([144])

The saturated pressure of water vapor is a function of saturated gas temperature:

$$p_{sat} = a_1 \exp(a_2 T_{sat} + a_3 T_{sat}^2 + a_4 T_{sat}^3 + a_5 T_{sat}^4) \quad (\text{A.8})$$

$$\begin{aligned}
 a_1 &= +611 \\
 a_2 &= +7.257 \cdot 10^{-2} \\
 a_3 &= -2.937 \cdot 10^{-4} \\
 a_4 &= +9.810 \cdot 10^{-7} \\
 a_5 &= -1.901 \cdot 10^{-9}
 \end{aligned}$$

Unit: Pa

Range of application: $0^\circ\text{C} \leq T_{sat} \leq 100^\circ\text{C}$

Maximum error: 0.2%

Specific heat capacity of water vapor ([144])

$$s_v = a_1 + a_2T + a_3T^2 + a_4T^3 \quad (\text{A.9})$$

$$\begin{aligned}
 a_1 &= +1862 \\
 a_2 &= +2.858485 \cdot 10^{-1} \\
 a_3 &= +6.148483 \cdot 10^{-4} \\
 a_4 &= -2.060606 \cdot 10^{-7}
 \end{aligned}$$

Unit: J/(kgK)

Range of application: $0.001 \text{ MPa} \leq p \leq 0.01 \text{ MPa}$; $25^\circ\text{C} \leq T_g \leq 400^\circ\text{C}$

Maximum error: 0.06%

Appendix B

Additional experimental results

B.1 Measured and calculated RTD

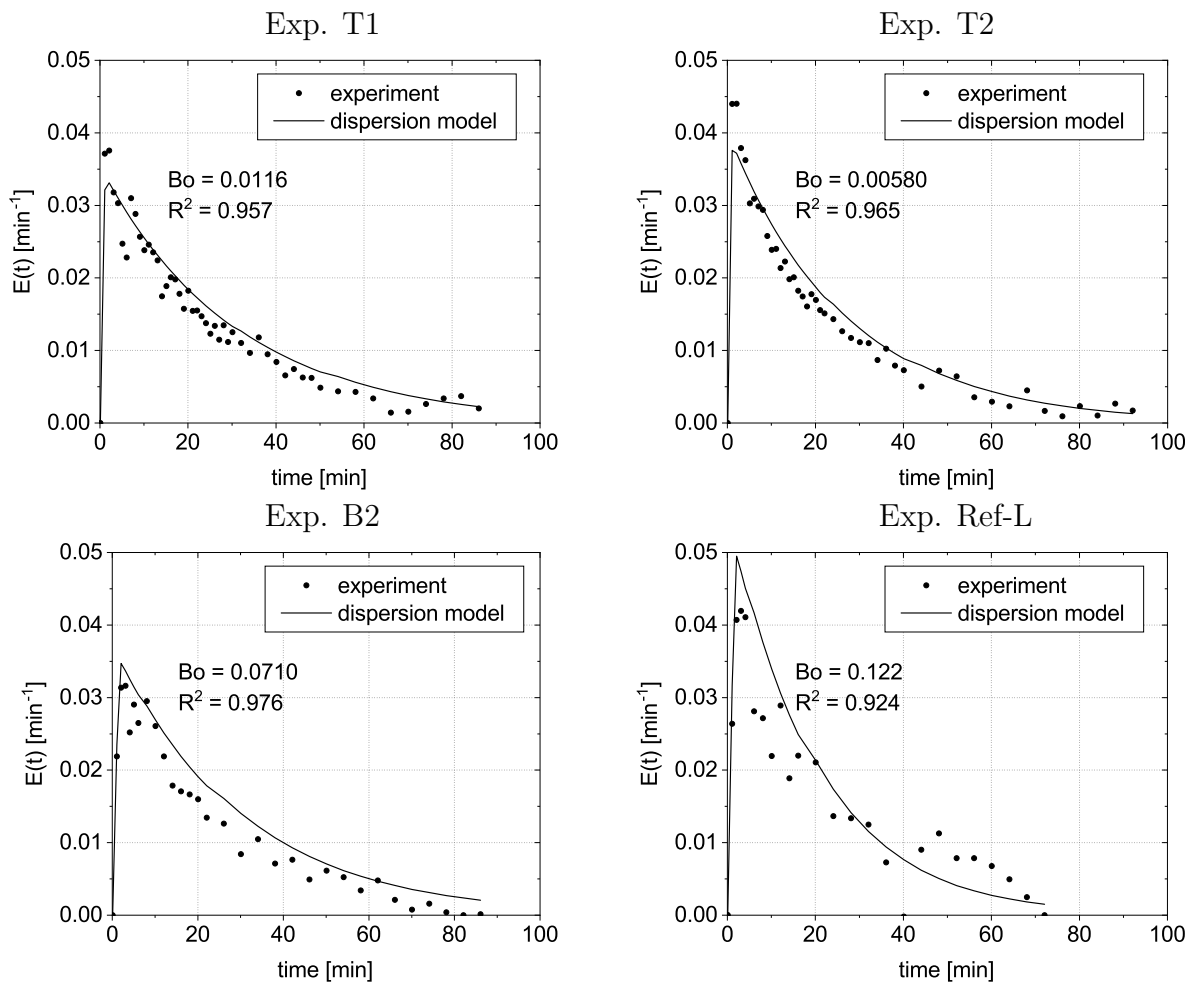


Figure B.1: Measured and calculated RTD.

B.2 Results of experiment with air temperature at 60 °C

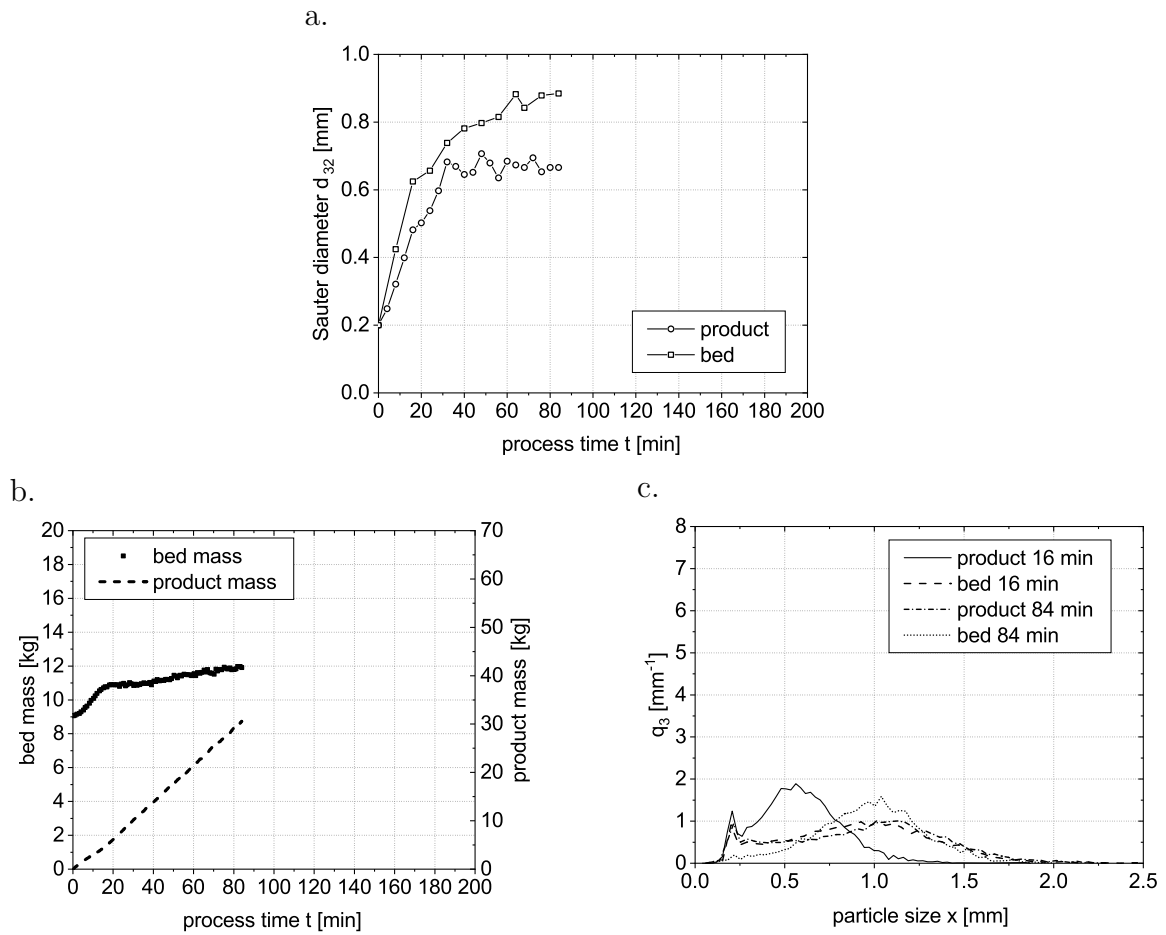


Figure B.2: Results of experiment with air temperature at 60 °C: a. evolution of particle size; b. development of bed and product mass; c. PSDs of selected samples.

B.3 Results of experiment with binder mass fraction at 6%

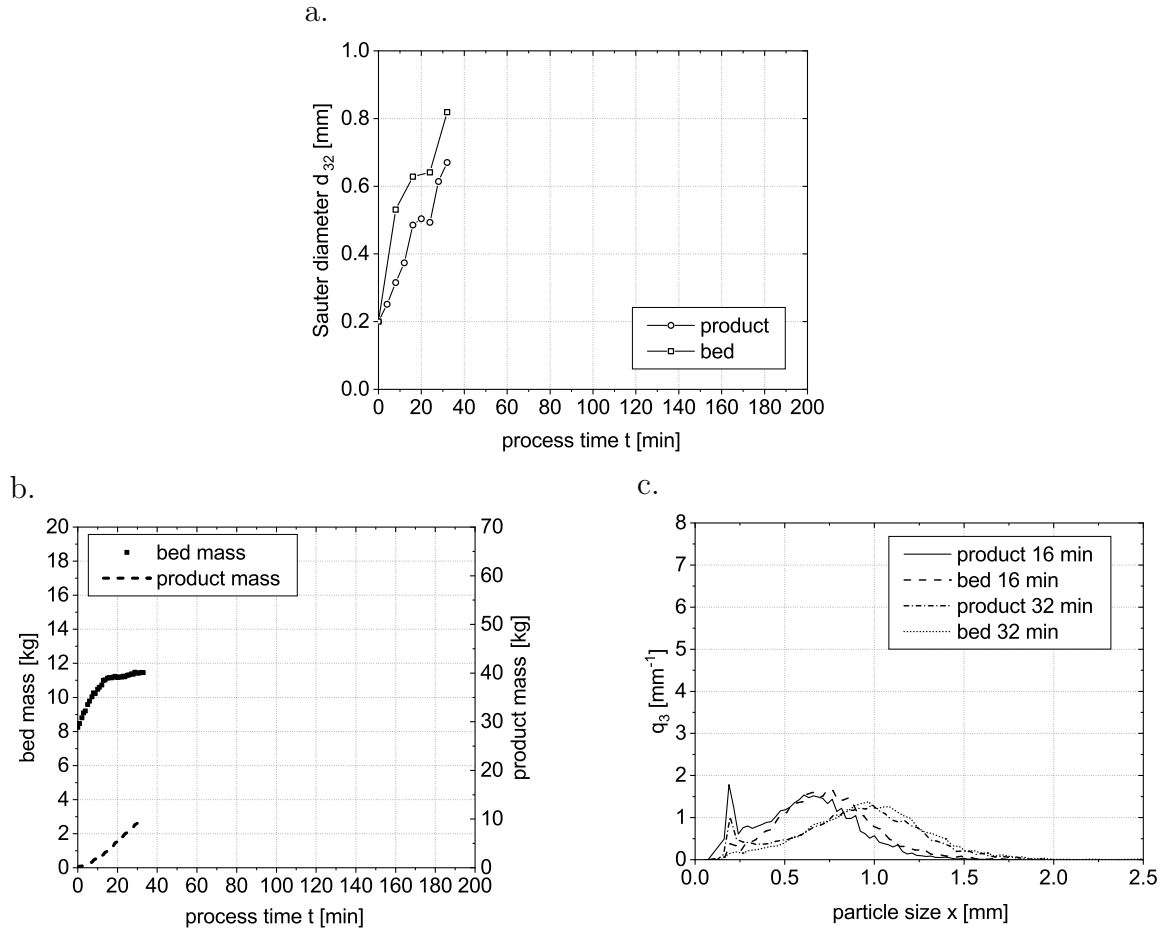


Figure B.3: Results of experiment with binder mass fraction at 6%: a. evolution of particle size; b. development of bed and product mass; c. PSDs of selected samples.

Appendix C

Additional simulation results

C.1 Comparison of the development of bed mass in simulation and experiment

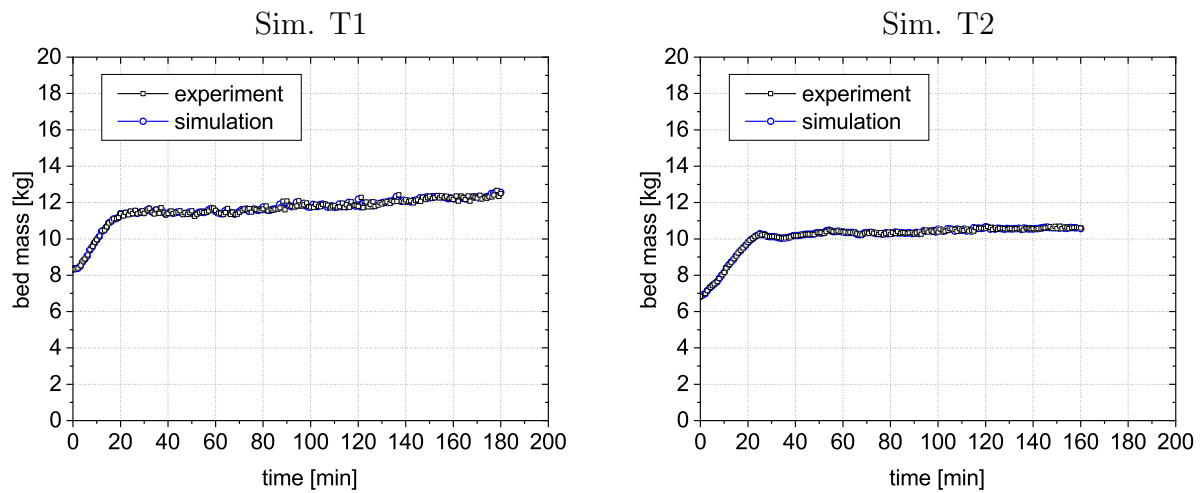


Figure C.1: Development of bed mass with varied air temperature.

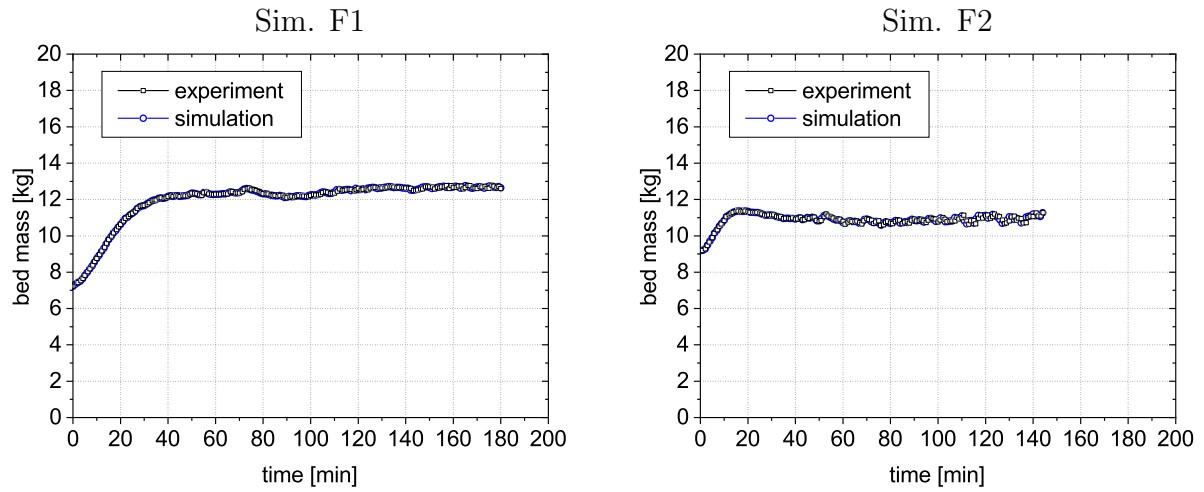


Figure C.2: Development of bed mass with varied particle feed rate.

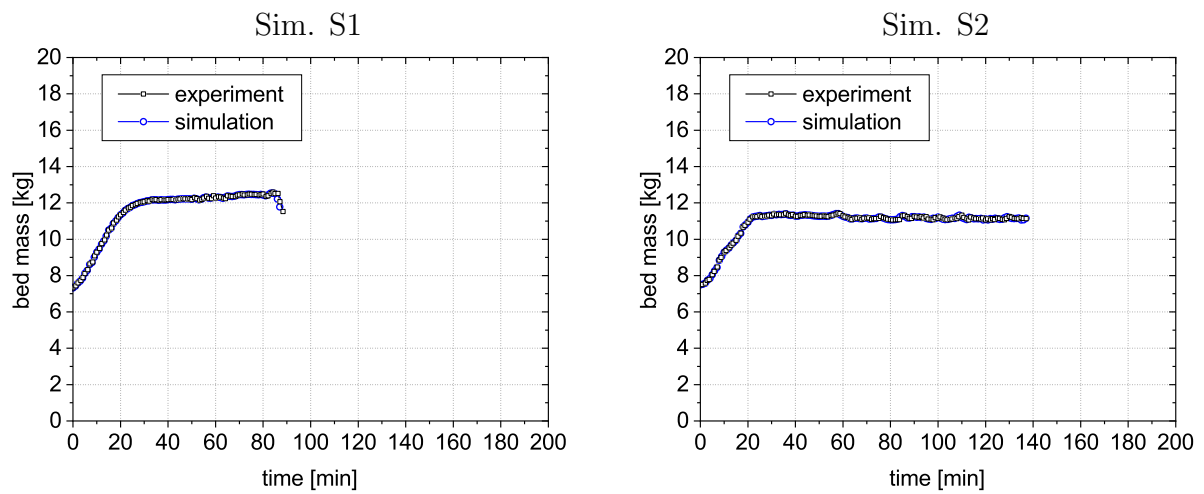


Figure C.3: Development of bed mass with varied binder spray rate.

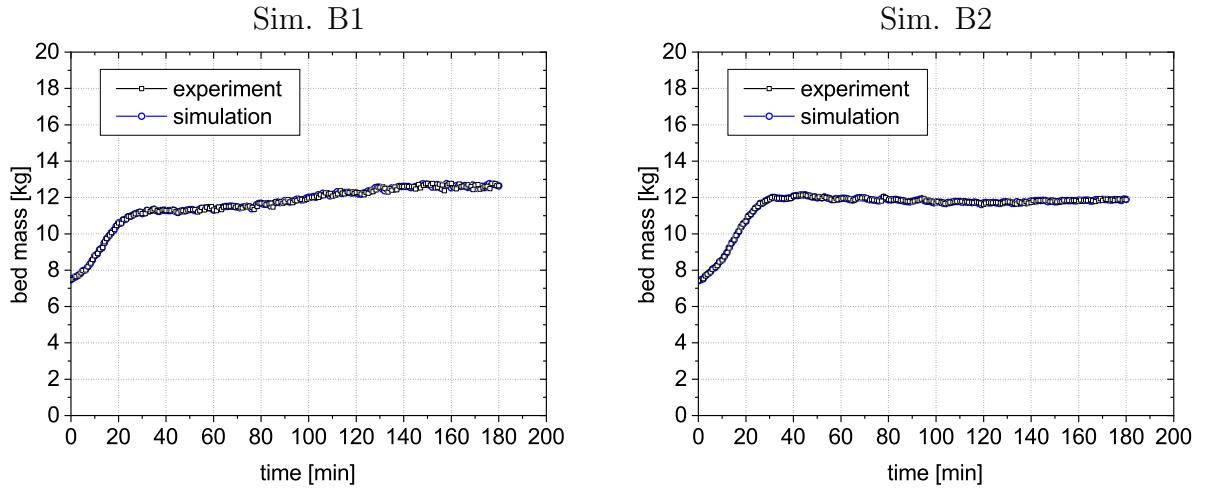


Figure C.4: Development of bed mass with varied binder concentration.

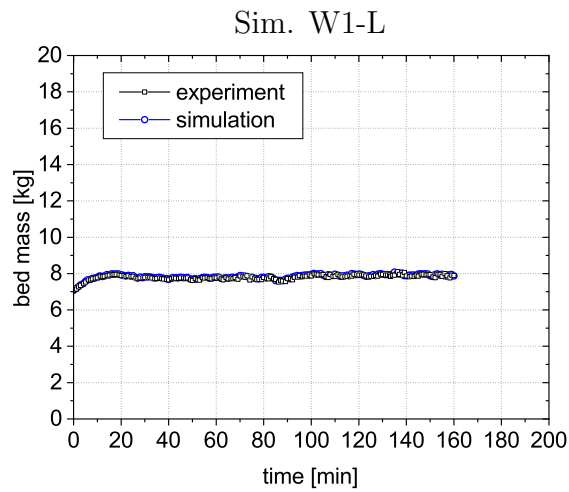


Figure C.5: Development of bed mass with lower outlet weir.

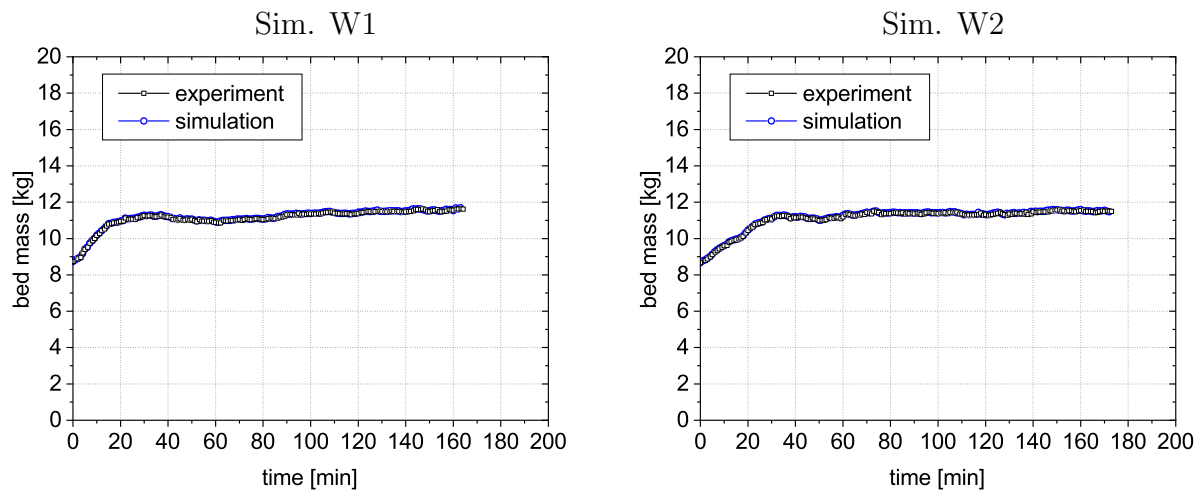


Figure C.6: Development of bed mass with varied internal weirs.

Publication list

2016.10 - 2022.09

Journal Papers

1. Z. Jiang, **J. Du**, C. Rieck, A. Bück, E. Tsotsas, *PTV experiments and DEM simulations of the coefficient of restitution for irregular particles impacting on horizontal substrates*, Powder Technology 360 (2020), 352-365. [10.1016/j.powtec.2019.10.072](https://doi.org/10.1016/j.powtec.2019.10.072)
2. **J. Du**, A. Bück, E. Tsotsas, *Influence of process variables on spray agglomeration process in a continuously operated horizontal fluidized bed*, Powder Technology 363 (2020), 195-206. [10.1016/j.powtec.2020.01.008](https://doi.org/10.1016/j.powtec.2020.01.008)
3. **J. Du**, G. Strenzke, A. Bück, E. Tsotsas, *Monte Carlo modeling of spray agglomeration in a cylindrical fluidized bed: From batch-wise to continuous processes*, Powder Technology 396 (2022), 113-126. [10.1016/j.powtec.2021.10.051](https://doi.org/10.1016/j.powtec.2021.10.051)
4. **J. Du**, A. Bück, E. Tsotsas, *Monte Carlo modeling of spray agglomeration in a continuously operated horizontal fluidized bed*. [in preparation]

Conference Proceedings

1. **J. Du**, G. Strenzke, A. Bück, E. Tsotsas, *Investigation of spray agglomeration process in continuously operated horizontal fluidized bed*, In: 21st International Drying Symposium, Valencia (Spain), September, 2018
2. **J. Du**, K. Chen, A. Bück, E. Tsotsas, *Stochastic simulation of spray agglomeration process in a continuously operated horizontal fluidized bed by Monte Carlo method*, In: 13th International Conference on Fluidized Bed Technology, Vancouver (Canada), May, 2021
3. **J. Du**, A.K. Singh, A. Bück, E. Tsotsas, *Monte Carlo simulation of the influence of drying conditions on the spray agglomeration process in a continuously operated horizontal fluidized bed*, In: 22nd International Drying Symposium, Worcester (US), June, 2022

Oral and Poster Presentations

1. **J. Du**, A. Bück, E. Tsotsas, *Investigation of spray agglomeration process in continuously operated horizontal fluidized bed*, In: Jahrestreffen der ProcessNet-Fachgruppen Zerkleinern und Klassieren und Agglomerations- und Schüttguttechnik, Neuss (Germany), March, 2018
2. **J. Du**, G. Strenzke, A. Bück, E. Tsotsas, *Investigation of spray agglomeration process in continuously operated horizontal fluidized bed*, In: 21st International Drying Symposium, Valencia (Spain), September, 2018
3. **J. Du**, G. Strenzke, A. Bück, E. Tsotsas, *Stochastic simulation of spray agglomeration process in a continuously operated horizontal fluidized bed by Monte Carlo method*, In: Jahrestreffen der ProcessNet-Fachgruppen Zerkleinern und Klassieren und Agglomerations- und Schüttguttechnik, Lausanne (Switzerland), March, 2019
4. **J. Du**, N. Vorhauer, A. Bück, E. Tsotsas, *Experimental investigation of process and particle residence time distribution in continuously operated horizontal fluidized bed spray agglomeration*, In: International Congress on Particle Technology, Nuremberg (Germany), April, 2019
5. **J. Du**, A. Bück, E. Tsotsas, *Experimental investigation of particle dispersion in continuous spray agglomeration process in a horizontal fluidized bed*, In: 9th International Granulation Workshop, Lausanne (Switzerland), June, 2019
6. G. Strenzke, **J. Du**, A. Bück, E. Tsotsas, *Experimental investigation of process behavior of continuous fluidized bed spray agglomeration with internal classification*, In: 9th International Granulation Workshop, Lausanne (Switzerland), June, 2019
7. **J. Du**, G. Strenzke, A. Bück, E. Tsotsas, *Monte Carlo simulation of spray agglomeration process in a continuously operated fluidized bed with internal separation*, In: Jahrestreffen der ProcessNet-Fachgruppen Zerkleinern und Klassieren und Agglomerations- und Schüttguttechnik, Online, March, 2021
8. **J. Du**, K. Chen, A. Bück, E. Tsotsas, *Stochastic simulation of spray agglomeration process in a continuously operated horizontal fluidized bed by Monte Carlo method*, In: 13th International Conference on Fluidized Bed Technology, Vancouver (Canada), May, 2021
9. **J. Du**, A.K. Singh, A. Bück, E. Tsotsas, *Monte Carlo simulation of the influence of drying conditions on the spray agglomeration process in a continuously operated horizontal fluidized bed*, In: 22nd International Drying Symposium, Worcester (US), June, 2022

Student theses

1. N.A. Shashwath, Investigation of spray agglomeration process in continuously operated horizontal fluidized bed, Master thesis, Otto von Guericke University Magdeburg, Germany, 2018
2. S.R. Rajendran, Investigation of process variables in spray agglomeration and particle residence time distribution in horizontal fluidized bed, Master thesis, Otto von Guericke University Magdeburg, Germany, 2018
3. U. Wahid, Experimental investigation of spray agglomeration process in a horizontal fluidized bed under steady-state and dynamic conditions, Master thesis, Otto von Guericke University Magdeburg, Germany, 2018
4. J. Zhou, Continuous agglomeration process in a horizontal fluidized bed: Comparison of a stochastic model with experiments, Master thesis, Otto von Guericke University Magdeburg, Germany, 2020

Curriculum vitae

<i>Name</i>	Jiajie Du
Date of birth	July 15th, 1988
Place of birth	Hebei, China
<i>Education</i>	
2004-2007	Hengshui High School, Hebei
<i>Higher Education</i>	
2007-2011	East China University of Science and Technology, Shanghai, Bachelor studies “Chemical Engineering” Academic degree: Bachelor’s Degree
<i>Master Education</i>	
2011-2013	Otto von Guericke University, Magdeburg, Master studies “Chemical and Energy Engineering” Academic degree: Master of Science (M. Sc.)
<i>Work Experience</i>	
2013-2016	The Fourth Research and Design Engineering Corporation of CNNC, Shijiazhuang Engineer
<i>PhD study</i>	
since 2016	Chair of Thermal Process Engineering, Faculty of Process and System Engineering, Otto von Guericke University, Magdeburg Scientific assistant and PhD student

Magdeburg, 28.09.2022

M.Sc. Jiajie Du

